Understanding the Electronic and Thermodynamic Properties of Wide Band Gap Materials

.....

Benjamin A. D. Williamson
UNIVERSITY COLLEGE LONDON

.....

SUPERVISOR
Dr David O. Scanlon

SECONDARY SUPERVISOR
Prof. Claire J. Carmalt

A dissertation submitted in partial fulfilment
of the requirements for the degree of
Doctor of Philosophy

April, 2018

I, *Benjamin Albert Dobson Williamson*, confirm that the work presented in this thesis is my own. Where information has been derived from other sources, I confirm that this has been indicated in the work.

_____

Benjamin Albert Dobson Williamson

APRIL, 2018

Acknowledgements

I would first like to thank my supervisor, Dr David Scanlon, for giving me the opportunity to pursue a PhD in computational chemistry as well as providing the exceptional support, enjoyable working environment, multitude of rewarding projects and the drive to do them throughout the course of my studies. I would also like to thank the Scanlon Materials Theory Group (SMTG) for not only providing fun both in the office as well as at conferences but also for their academic support. In particular, I would like to thank my fellow PhDs: Alex Ganose, Chris Savory, Ian Johnson and Dougal Howard for all the office banter (plus Catan) and also to Dr Adam Jackson who has provided me with much needed help for all the problems I have encountered (even if I didn't realise I had one!).

I would like to thank my experimental collaborators both inside and outside the department of chemistry at UCL. In particular I would like to thank Prof. Ivan Parkin and my secondary supervisor Prof. Claire Carmalt whose guidance has been instrumental in linking theory and experiment. I would also like to thank Dr Sanjayan Sathasivam, Dr Nicholas Chadwick and Sebastian Dixon for their experimental collaborations. I would also like to thank Dr Robert Palgrave and his team for their work on CaCuP. Outside of UCL I would like to acknowledge the fantastic work that Prof. Timothy Veal and his group at the University of Liverpool as well as Dr Geoffrey Hyett's group at the University of Southampton carry out on the various collaborative projects.

Funding for my PhD was organised through Bio Nano Consulting (www.bio-nano-consulting.com) in a collaboration between UCL and King Abdulaziz University, Saudi Arabia. Further to this, I would like to acknowledge the use of the "Donor Design for Maximum Mobility TCOs" grant (EPSRC grant no. EP/N01572X/1) and access to the UK national supercomputing facility, ARCHER (www.archer.ac.uk) via membership of the UK's HEC Materials Chemistry Consortium, funded by EPSRC (grant no. EP/L000202). The use of the Legion (Legion@UCL) and Grace (Grace@UCL) supercomputing facilities which were also used for

the calculations presented in this thesis.

I would also like to thank all my friends who have helped me during my studies, specifically I would like to thank all those in the University of London Chamber Choir who provided me with the (sometimes) much needed breaks from density functional theory!

When it comes to family, I feel that I have been incredibly fortunate in having one that I am so close to and who have been supportive of me throughout my time at university. My father: Roger, brother: George, sister: Alice, grandfather: Roger and above all, my mother: Emma – thank you for supporting me throughout the entirety of my studies and for the constant inspiration you give to me. I am also grateful for the constant encouragement that Hannah-May's parents: Bettina and Wagih have given me since I have known them.

Finally, my love and deepest gratitude to Hannah-May: not only have you encouraged and supported me during my PhD, but your love, infectious optimism and motivation has helped get me to this point.

Thank you.

Abstract

Wide band gap ($E_g > 3.1$ eV) semiconductors are ubiquitous in many present day industrial applications and environmental endeavors. In particular, wide band gap materials find use within photovoltaics, portable electronics, gas sensors, self-cleaning and thermochromic window coatings as well as photocatalysis to name a few. Despite the wide range of current applications, there are still many issues that disrupt advancements in this field.

Within the area of transparent conductors (TCs), the dominant materials are all *n*-type which are themselves dominated by the flagship ITO (Sn-doped In_2O_3). Due to the expense and scarcity of In, finding an alternative earth-abundant material is key to sate the ever growing demand for consumer electronics. Although SnO_2 and ZnO are heralded as alternatives, issues arise such as the failure to realise reproducible ITO-like conductivities as well as a lack of understanding of the limitations that these materials present. Alternatively, *p*-type TCs are held back by the lack of a degenerate high mobility material to match their *n*-type counterparts. This means that the formation of a high transparency p-n junction is not yet possible in addition to hindering the efficiency of devices such as photovoltaics.

Lastly, wide band gap materials are also used in photocatalysis, in particular with TiO_2 which has applications in water splitting as well as antimicrobial surface coatings. Understanding the mechanisms by which TiO_2 undergoes photocatalysis and the effects that the intrinsic and extrinsic defect chemistry has is ongoing despite the decades of dedicated study.

This thesis aims to address these three topics; *n*-type and *n*-type transparent conductors and TiO_2 photocatalysis. By using *ab-initio* density functional theory (DFT) aided by experiment elucidation of the mechanistic shortfalls are carried out providing solutions based on theory and observation.

Publications

Publications produced over the course of this PhD:

Relating to this thesis:

1. *Engineering Valence Band Dispersion for High Mobility p-type Semiconductors*; **B.A.D. Williamson**, J. Buckeridge, J. Brown, S. Ansbro, R.G. Palgrave, D.O. Scanlon; Chemistry of Materials, 29 (6), 2402–2413, *2017*

2. *Self-Compensation in Transparent Conducting F-doped SnO_2*; J.E.N. Swallow, **B.A.D. Williamson** et al.; Advanced Functional Materials, 1701900, *2017*

3. *A Deeper Understanding of Boron-doped Anatase Thin Films as a Multifunctional Layer through Theory and Experiment*; M. Quesada-Gonzalez, **B.A.D. Williamson** et al.; Journal of Physical Chemistry C, 122 (1), 714–726, *2017*

4. *Phosphorus Doped SnO_2 Thin Films with Excellent Optical and Electrical Properties for Transparent Conducting Oxide Applications*; M.J. Powell, **B.A.D. Williamson** et al. ; *in submission*

5. *Enhanced Electrical Properties of Antimony Doped Tin Oxide Thin Films Deposited via Aerosol Assisted Chemical Vapour Deposition*; S.D. Ponja, **B.A.D. Williamson** et al.; *in submission*

6. *Uncovering the Origin of the Enhanced Photocatalytic and Antibacterial Ability of Cu-doped Anatase TiO_2 Thin Films through Theory and Experiment*; A. Alotaibi, **B.A.D. Williamson** et al. *in submission.*

7. *Dispelling the Myth of Compensated Codoping*; N.P. Chadwick, **B.A.D. Williamson** et al.; *in submission*

8. *Computationally Aided Discovery of Layered Quinary Oxychalcogenide p-type Transparent Conductors*; **B.A.D. Williamson**, G. J. Limburn et al.; *in preparation.*

9. *Is Tantalum the Optimum Dopant in SnO_2?*; **B.A.D. Williamson** et al. ; *in preparation.*

Other completed publications:

10. *A Single-Source Precursor Approach to Solution Processed Indium Arsenide Thin Films*; P. Marchand, S. Sathasivam, **B.A.D. Williamson** et al.; Journal of Materials Chemistry C , 4 (28) 6761–6768, *2016*

11. *Chemical Vapor Deposition Synthesis and Optical properties or Nb_2O_5 Thin Films with Hybrid Functional Theoretical Insight into Band Structure and Band Gaps*; S. Sathasivam, **B.A.D. Williamson** et al.; ACS Applied Materials & Interfaces, 9 (21), 18031–18038, *2017*

12. *Computational and Experimental Study of Ta_2O_5 Thin Films*; S. Sathasivam, **B.A.D. Williamson** et al. ; Journal of Physical Chemistry C; 121 (1), 202–210, *2017*

13. *Transparent Conducting n-Type ZnO:Sc - Synthesis, Optoelectronic Properties and Theoretical Insight*; S.C. Dixon, S. Sathasivam, **B.A.D. Williamson** et al. ; Journal of Materials Chemistry C, 5 (30), 7585–7595,*2017*

14. *Chemical Vapor Deposition of Photocatalytically Active Pure Brookite TiO2 Thin films*; A. Alotaibi, S. Sathasivam, A. Kafizas, **B.A.D. Williamson** et al.; Chemistry of Materials, *2018*

15. *Understanding the Doping Effect of Hematite Photoanodes with Nanohybrid Metal Oxide Overlayers for Efficient and Stable Photoelectrochemical Water Splitting*; S. Ho-Kimura, **B.A.D. Williamson** et al.; *in submission.*

16. *Dopant design triples conductivity of In_2O_3 transparent electrodes*; J.E.N. Swallow, **B.A.D. Williamson** et al.; *in preparation*

Contents

Motivation **1**

PART I: Computational Theory and Methodology

1 Computational Theory **6**

1.1 Introduction to Quantum Chemical Approaches 6

1.2 The Many Body Problem 8

1.2.1 Hartree-Fock Theory 8

1.3 Density Functional Theory 10

1.3.1 Early Density Functional Theory 10

1.3.2 Kohn-Sham and Modern Density Functional Theory 11

1.3.3 The Exchange-Correlation Functional 11

2 Computational Methodology **15**

2.1 Periodic Boundary Conditions and Geometry Optimisations 15

2.2 Electronic Structure Optimisations 18

2.2.1 Density of States 18

2.2.2 Band Structures 18

2.2.3 Effective Mass 19

2.2.4 Optical Absorption 20

2.3 Defect Calculations 22

2.3.1 The Supercell Method and Defect Thermodynamics 22

2.3.2 Enthalpy of Formation for a Neutral Defect 22

2.3.3 Enthalpy of Formation for a Charged Defect 23

2.3.4 Post Processing and Correction Schemes 24

2.3.5 Chemical Potential Limits 26

2.4 Thermodynamic Transition Levels . . . 31
2.4.1 Optical Transition Levels . . . 33
2.5 VASP – The Vienna *Ab-Initio* Simulation Package . . . 35

PART II: *n*-Type Transparent Conductors

3 Introduction to *n*-type Transparent Conductors 40
3.1 Transparent Conducting Oxides . . . 40
3.1.1 Selected Applications . . . 41
3.2 Fundamentals of TCOs . . . 44
3.2.1 Electronic Structure . . . 44
3.2.2 Conductivity in TCOs . . . 48
3.3 Doping in SnO_2 . . . 53

4 The Search for the Optimum Dopant in SnO_2 55
4.1 Bulk Electronic Properties and Intrinsic Defects . . . 55
4.1.1 Structural and Electronic Properties . . . 55
4.1.2 Intrinsic Defects . . . 57
4.2 Self-Compensation in F-Doped SnO_2 . . . 60
4.2.1 Understanding the Role of Fluorine Species in SnO_2 . . . 60
4.2.2 Experimental Verification . . . 63
4.3 The Limitations of Antimony . . . 65
4.3.1 The Role of Sb Species in SnO_2 . . . 65
4.4 The Amphoteric Role of Phosphorus . . . 70
4.4.1 Which is the Dominant P Defect? . . . 70
4.5 Is Tantalum the Optimum Dopant for SnO_2 . . . 76
4.5.1 A Comparison of Nb and Ta doped SnO_2 . . . 76
4.5.2 Unfolded Band Structures . . . 81
4.6 Conclusions . . . 85

PART III: *p*-Type Transparent Conductors

5 Introduction to *p*-type Transparent Conductors 90
5.1 Design Strategies of *p*-type Transparent Conductors . . . 91

5.1.1 Acceptor Doping of *n*-type TCOs . . . 91
5.1.2 The Chemical Modulation of the Valence Band . . . 92
5.1.3 Beyond the Transparent Conducting Oxide . . . 94

6 Next Generation *p*-Type Transparent Conductors 97
6.1 Elemental Modulation of $[Cu_2S_2][Sr_3Sc_2O_5]$ . . . 97
6.1.1 Thermodynamic Stability Screening . . . 98
6.1.2 Geometric and Structural Properties . . . 101
6.1.3 Electronic and Optical Properties . . . 106
6.1.4 Experimental Verification . . . 115
6.1.5 Discussion . . . 116
6.2 Engineering Valence Band Dispersion - CaCuP . . . 118
6.2.1 Structural Parameters . . . 119
6.2.2 Electronic Properties . . . 120
6.2.3 Discussion . . . 124
6.2.4 Experimental Verification . . . 126
6.3 Conclusions . . . 128

PART IV: Understanding TiO_2 Photocatalysis

7 Introduction to Bulk TiO_2 Photocatalysis 134
7.1 Ideal Bulk Properties . . . 136
7.1.1 Band Alignment: . . . 136
7.1.2 Electronic Structure: . . . 138
7.2 Doping . . . 140
7.2.1 Passivated Codoping . . . 142

8 Understanding the Role of Defects and Dopants in Anatase 145
8.1 Structural, Electronic Properties and Intrinsic Defects . . . 145
8.1.1 Bulk Structural and Electronic Properties . . . 145
8.1.2 Intrinsic Defects . . . 146
8.1.3 Optical Absorption and Emission . . . 150
8.2 Dispelling the Myth of Passivated Codoping in TiO_2 . . . 153
8.2.1 Mono doping of Anatase with N, Nb and Ta . . . 153

8.2.2 The Realisation of Full Compensation? . . . 156
8.3 Conductivity and Photocatalysis in Boron Doped TiO_2 . . . 160
8.3.1 Defect Thermodynamics of B-Doped TiO_2 . . . 161
8.4 Enhanced Carrier Lifetimes in Copper Doped TiO_2 . . . 166
8.4.1 Cu-doping of TiO_2 . . . 166
8.4.2 Optical Absorption and Photoluminescence in TiO_2:Cu . . . 169
8.5 Conclusions . . . 172

Summary **175**

Appendices

A *n*-Type Transparent Conductors **181**
A.1 Introduction to *n*-Type Transparent Conductors . . . 181
A.2 The Search for the Optimum Dopant in SnO_2 . . . 182
A.2.1 Defect Methodology . . . 182
A.3 F-doped SnO_2 Experimental Methodology . . . 186

B *p*-Type Transparent Conductors **188**
B.1 Elemental Modulation of $[Cu_2S_2][Sr_3Sc_2O_5]$ . . . 188
B.1.1 Computational Methodology . . . 188
B.1.2 Experimental Methodology . . . 190
B.1.3 Supplementary Information: Thermodynamic Stability . . . 192
B.1.4 Supplementary Information: Electronic Properties . . . 201
B.1.5 Supplementary Information: Experimental XRD . . . 201
B.1.6 Supplementary Information: Experimental Optical Absorption . . . 203
B.2 Engineering Valence Band Dispersion - CaCuP . . . 205
B.2.1 Computational Methodology . . . 205
B.2.2 Experimental Methodology . . . 207
B.2.3 Supplementary Information: XRD and XPS results . . . 208
B.2.4 Supplementary Information: Optical Properties . . . 211

C Understanding TiO_2 Photocatalysis **213**
C.1 Understanding the Role of Defects and Dopants in Anatase . . . 213

C.1.1 Defect Methodology 213

Indexes and Bibliography

Acronyms and Abbreviations **220**

List of Equations **224**

List of Figures **227**

List of Tables **230**

Acknowledgement of Resources and Figures **232**

Bibliography **234**

Motivation

Wide band gap semiconductors encompass a large array of applications from electronic displays to antimicrobial coatings and gas sensors. The 'band gap' of a material is fundamentally the difference between the occupied valence bands and the unoccupied conduction bands in semiconductor materials. A *wide* band gap refers to all semiconductors where the energy separation or optical absorption is generally greater than ~ 3.1 eV. This allows for properties that are becoming increasingly desirable in portable electronics, energy generation or sensing applications such as transparency as well as increasing the effectiveness of the reducing and oxidising ability for catalysis.

Although a wealth of wide band gap materials exist, a full understanding of their thermodynamic (intrinsic and extrinsic defects, stabilities, phases) and electronic properties (optical absorption, band structure, defect states) is an ongoing endeavour. With the advent of portable electronics and the need for clean and renewable energy, there is an ever increasing demand for these materials. As such, the requirement that such materials be earth-abundant, non-toxic and possess a cheap and scalable fabrication method is paramount. Atomistic simulations, particularly using density functional theory (DFT), have allowed for a greater in-depth analysis into the properties of compounds, as well as a relatively affordable method for screening and prediction. The advances in processor architecture in the past 10–20 years have permitted supercomputers to reach several hundred petaFLOPS (floating operations per second). Twinning this with the progressing accuracy in advanced simulation methods such as hybrid DFT, computational prediction and analysis is becoming more and more prevalent as a vital tool in modern chemistry.

The motivations of this thesis are to understand the advantages and disadvantages present in wide band gap materials for three industrially significant categories: n-type transparent conductors, p-type transparent conductors and TiO_2 photocatalysis. The key aims are to establish:

- *The geometric and electronic structure:* What are the structure-property relationships that give rise to the desired properties?
- *Materials prediction:* Using 'design rules', can accurate predictions of novel compounds be made that improve upon the current generation of known compounds?
- *Defect equilibria:* What defects exist in key materials and which ones contribute to the electronic or structural properties; can they limit or enhance them?
- *Doping Analysis:* What role does the current generation of doping have on the structural and electronic properties of the material, what are the limitations and/or advantages?
- *Enhanced Doping:* Are there better dopants to use with fewer limitations, beneficial electron/hole transfer mechanisms, optical absorption etc.?

The first part of this thesis will detail the computational theory (Chapter 1) and methodology (Chapter 2) behind the atomistic simulations used within this thesis. The second part of this thesis will investigate the electronic and thermodynamic properties of n-type transparent conductors, in particular, tin dioxide, SnO_2, one of the 'industry-standard' materials. Current doping regimes and limitations will be explored in Chapter 4, and a focused screening of new elements is carried out to find the *optimum* dopant in SnO_2. The third part explores p-type transparent conductors, the counterparts of n-type materials such as SnO_2. The availability of comparable high conductivity p-type wide band gap materials is more or less non-existent and as such Chapter 6 will follow well established design principles in this field and generate new structure-property relationships with the prediction of new layered materials. Finally, an assessment of the role that defects and dopants play in the enhancement of photocatalysis in anatase TiO_2 is carried out in the fourth part. Although a wealth of research has been undertaken on TiO_2 for photocatalysis, the mechanisms of visible light enhancement, extended electron-hole separation times, defect equilibria is still relatively unknown. Chapter 8 evaluates the validity of codoping in TiO_2 and provides an insight into the bulk defect properties of Cu and B doped TiO_2, both of which undergo promising photocatalyst properties in experiment.

Part I

Computational Theory and Methodology

Chapter 1

Computational Theory

1.1 Introduction to Quantum Chemical Approaches

Quantum chemical approaches for the description of chemical systems from first principles or *ab-initio*, involve finding a tractable solution to the time-independent Schrödinger equation[1]:

$$\hat{H}\Psi = E\Psi \tag{1.1.1}$$

Where $\hat{H}$, E and Ψ are the Hamiltonian, system energy and the wavefunction respectively. The Hamiltonian is a sum of the kinetic and potential energy operators which are themselves split into different contributions and interactions:

$$\hat{H} = \overbrace{\hat{K}_n + \hat{K}_e}^{\text{kinetic energy}} + \overbrace{\hat{V}_{n,n} + \hat{V}_{e,e} + \hat{V}_{n,e}}^{\text{potential energy}} \tag{1.1.2}$$

The kinetic energy operator, $\hat{K}$, is broken down to satisfy a nuclear contribution and an electronic contribution ($\hat{K}_n$ and $\hat{K}_e$) whereas the potential energy operator is split into nuclear-nuclear, electron-electron and nuclei-electron interactions ($\hat{V}_{n,n}$, $\hat{V}_{e,e}$ and $\hat{V}_{n,e}$ respectively). The solving of equation 1.1.2 allows for the calculation of the *ground state* wavefunction, electron density and thus a comprehensive understanding of a chemical system. In order to make 1.1.1 more compliant, the *Born-Oppenheimer* approximation is applied which

assumes that electronic movement is more or less instantaneous with respect to the movement of nuclei (a fair assumption considering the mass of an electron is $\sim \frac{1}{1837}$ that of a proton). The *kinetic energy* of the nuclei $\hat{K}_n$ in equation 1.1.2 can therefore be ignored and $\hat{V}_{n,n}$ interactions can be held constant [1] giving:

$$\hat{H} = \hat{K}_e + \hat{V}_{e,e} + \hat{V}_{n,e} \tag{1.1.3}$$

Where, for a system with N electrons (i):

$$\hat{K}_e = -\sum_{i}^{N} \frac{1}{2}\nabla_i^2 \quad \text{and} \quad \hat{V}_{n,e} = -\sum_{A}^{M}\sum_{i}^{n} \frac{Z_A}{|r_{iA}|} \tag{1.1.4}$$

∇_i^2 is the Laplacian kinetic energy operator, r_{iA} refers to the distance between electron 'i' and the nuclei of atom 'A' (within a system of 'M' nuclei (n)) and Z_A is the nuclear charge on atom A.

Despite this simplification, the Born-Oppenheimer approximation fails in the description of systems where there is a distinct difference between electronic and ionic motion, such as H_2. The *variational principle* is used to calculate the ground state wavefunction (Ψ_0) whereby the expectation value of the Hamiltonian can never be lower than the ground state energy: E_0. This involves the incorporation of a trial wavefunction: Ψ_T, which is calculated by incrementally lowering the energy of the wavefunction to get closer to the *true* ground state energy:

$$\langle \Psi_T | \hat{H} | \Psi_T \rangle = E_T \geq E_0 = \langle \Psi_0 | \hat{H} | \Psi_0 \rangle \tag{1.1.5}$$

The most complex part of the Hamiltonian to describe is the electron-electron interactions ($\hat{V}_{e,e}$) due to their substantial contribution to the total energy. In order to make this problem more tractable, the many-electron wave function needs to be simplified.

1.2 The Many Body Problem

It is reasonable to assume that for a chemical system in general, electrostatics dominate. The energy of a system is therefore dependent on the wavefunction, which in turn is dependent on the total energy of the electrons. For a small system this calculation is trivial, but for increasingly larger systems the quantum mechanical problem becomes exponentially more costly and near impossible to calculate. This is known as the '*many-body problem*'.

1.2.1 Hartree-Fock Theory

The Hartree-Fock (HF) method[2] is an attempt at the rectification of the issues surrounding multi-electron systems. The initial approximation in HF is transforming the *many-electron* wavefunctions into the product of *one-electron* wavefunctions, effectively bypassing the electron-electron interactions. Thus the electronic Hamiltonian for a system with N electrons can be described as:

$$H = \sum_{i}^{N} h(i) \tag{1.2.1}$$

where:

$$h(i) = -\frac{1}{2}\nabla_i^2 + \sum_{A}^{M} \frac{1}{r_{iA}} \tag{1.2.2}$$

Solving equation 1.2.1 can be solved using a product of a set of spin-orbitals ($\chi_i(x_i)$) known as the Hartree Product:

$$\Psi(x_1 \dots x_N) = \chi_i(x_1)\chi_j(x_2)\dots\chi_n(x_N) \quad \text{with} \quad h_i\chi_i(x_i) = \epsilon_i\chi_i(x_i) \tag{1.2.3}$$

ϵ_i is the energy of the spin-orbital and the sum of all the energies accounts for the total system energy. Although each one-electron wavefunction acts independently, they each respond to a *mean-field* (the stationary electrons in the system). An iterative procedure is used to solve the system and is deemed to be converged when there is no change between the field generated by the electronic states and that used to predict the electronic states. This is known as the *'self-consistent field'* (SCF) approach.

Electron repulsion is unaccounted for in this formalism (making this approach unrealis-

tic) and secondly, the Pauli antisymmetry principle is disregarded where the interchange between two electrons gives the same wavefunction.[1] In 1929, Slater formed a determinant of a system with N electrons and spin orbitals providing a set of antisymmetric wavefunctions.[3] Its use in HF theory means that an energy can be calculated based upon an electrostatic repulsion between the electrons, $J_{i,j}$, known as the *Coulombic term*:

$$J_{i,j} = \iint \chi_i(x_1)\chi_j^*(x_2)\frac{1}{r_{12}}\chi_i(x_1)\chi_j^*(x_2)\,dx_1\,dx_2 \tag{1.2.4}$$

and an *exchange integral*, $K_{i,j}$:

$$K_{i,j} = \iint \chi_i(x_1)\chi_j^*(x_2)\frac{1}{r_{12}}\chi_j(x_1)\chi_i^*(x_2)\,dx_1\,dx_2 \tag{1.2.5}$$

Where r_{12} refers to the distance between the electrons at x_1 and x_2. When the electrons do not have the same spin, the exchange term ($K_{i,j}$) is zero. This same term, however, makes this a highly expensive computational technique especially when the inclusion of periodic boundary conditions are used. Incorporating this into the total HF energy (E_{HF}) is given by:

$$E_{HF} = \sum_i \langle i|h|j\rangle + \frac{1}{2}\sum_{ij}(J_{i,j} - K_{i,j}) \tag{1.2.6}$$

$\langle i|h|j\rangle$ refers to the one electron integrals as calculated using the spin-orbitals in equations 1.2.3.

The inability of HF theory to calculate the *true* ground state wavefunction energy is also a limitation. The difference in the HF ground state energy and the true energy was termed the *correlation* energy by Lowdin.[4] This definition of the correlation energy is different from *electron* correlation (which HF also fails to describe accurately) as each electron is assumed independent of another as described in equation 1.2.2. This new definition of correlation is described in two ways, *dynamically* and *non-dynamically*. Dynamic correlation is where the probability of finding an electron is determined by the position of the second electron, characteristic of transition-metal systems. *Non*-dynamic correlation occurs in molecular systems where a highest occupied molecular orbital (HOMO) is composed of two or more degenerate states. In total the correlation energy is ~0.1%, leading to substantial errors in larger systems.

1.3 Density Functional Theory

1.3.1 Early Density Functional Theory

A popular and widely applied solution to the *Many-Body Problem* is that of *Density Functional Theory* or DFT. Early pioneers such as Thomas, Fermi and Dirac[5–7] created the original theoretical model which was by nature 'semi-classical'. The original case study was the 'uniform electron gas' (UEG) the aim of which was to form a description of the total energy through its electron density, $\rho(r)$. Similar to HF theory, early DFT was limited through its failure to describe the *correlation* effect of electrons and therefore real-world *non*-homogeneous systems. This model also predicts the dissociation of molecules into their constituent elements due to incorrect calculation of the energies of the system.[8]

Additions to this theory utilised the description of an *inhomogeneous* electron gas in 1964 by Pierre Hohenberg and Walter Kohn.[9] Within this formalism, the Hamiltonian describes the total energy of a system, $E[\rho(r)]$, which is formed from an external potential dependent on the electron density ($\rho(r)$) and calculated using a variational principle. The functional $E[\rho(r)]$ is broken into a kinetic energy function ($T[\rho]$) and functions relating the electron-electron interactions and the nuclei-electron interactions, $E_{e,e}[\rho(r)]$ and $E_{n-e}[\rho(r)]$:

$$E[\rho(r)] = T[\rho(r)] + E_{e,e}[\rho(r)] + E_{n-e}[\rho(r)] \tag{1.3.1}$$

This can be rewritten to show the relationship between the total energy and the electron density (equation 1.3.2) using the *'Hohenburg and Kohn Universal Functional'*, $F[\rho(r)]$ and an external potential (from the nuclei etc.) for the electrons to move around in ($V_{ext}(r)$). $F[\rho(r)]$, arises from the kinetic and electron-electron terms in Equation 1.3.1 and is unfortunately unknown. $F[\rho(r)]$ contains the exact exchange and correlation, thus finding the solution to the universal functional has been dubbed the 'holy grail' of modern DFT.

$$E[\rho(r)] = F[\rho(r)] + \int \rho(r) V_{ext}(r) dr \tag{1.3.2}$$

1.3.2 Kohn-Sham and Modern Density Functional Theory

To attempt a solution to $F[\rho(r)]$, Kohn and Sham split the the kinetic energy term $T[\rho(r)]$ into interacting and non-interacting electron contributions[10]:

$$T[\rho(r)] \rightarrow \underbrace{T_c[\rho(r)]}_{\text{interacting electrons}} + \overbrace{T_s[\rho(r)]}^{\text{non-interacting electrons}} \tag{1.3.3}$$

The total energy of the system can now be shown as:

$$\begin{aligned} E[\rho(r)] &= T_s[\rho(r)] + J[\rho(r)] + E_{XC}[\rho(r)] + E_{n\text{-}e}[\rho(r)] \\ \text{where} \quad E_{XC}[\rho(r)] &= T_c[\rho(r)] + E_{e,e}^{NC} \end{aligned} \tag{1.3.4}$$

where $J[\rho(r)]$, $E_{XC}[\rho(r)]$ and $E_{n-e}[\rho(r)]$ describe the Coulombic interactions of electrons in an external potential, a *non-classical* (denoted by the superscript "NC") electron-electron exchange-correlation interaction and a term to describe the nuclear-electron interactions respectively. In essence this means that density functional theory *is able to calculate the exact ground state energy of a system if* $E_{XC}[\rho(r)]$ *is known.*

1.3.3 The Exchange-Correlation Functional

As the exact solution to the *exchange-correlation functional* is not known, attempts at approximating it are laid out below. Although approximations need to be made to *both* the exchange and correlation, this is preferable to HF where you have exact exchange but *no* correlation. Fairly accurate results can be gained from the most trivial of approximations making DFT the computational tool kit of choice. This is the case with fairly uniform systems such as metals where the valence electrons are free to move and are heavily delocalised over the system. Fairly accurate exchange and correlation energies can be obtained utilising Quantum Monte-Carlo methods.

The Local Density Approximation (LDA):

The local density approximation (LDA) calculates the density at each point in space rather than over the whole system.[11] $\epsilon_{xc}[\rho(r)]$ in Equation 1.3.5 is the same as the exchange-

correlation energy of a UEG at each point (r) in a system. $\epsilon_{xc}[\rho(r)]$ is therefore the exchange and correlation *per* electron, and as such integrating over all points of the system will result in $E_{XC}[\rho(r)]$:

$$E_{XC}[\rho(r)] = \int \rho(r)\epsilon_{xc}[\rho(r)]dr \tag{1.3.5}$$

Reasonably accurate results are given in systems where the density does not fluctuate wildly yet inaccuracies are gained when describing systems with tightly bound valence electrons. LDA also has a distinct *underestimation* of bond lengths and band gaps and binding energies become overestimated. LDA however, is a highly affordable computational approach.

The Generalised Gradient Approximation (GGA):

The generalised gradient approximation (GGA) arisen from LDA, takes into account the electron density at each point in space (r) but also the *gradient* of the density around r. This increased accuracy has made GGA one of the most popular DFT approaches in computational physics and chemistry.[12] Typically GGA functionals are gradient-corrected LDA functionals, however experimentally derived functionals exist such as the Lee-Yang-Parr (LYP) correlation functional.[13] These functionals tend to originate from lighter elements and molecules and have a tendency to break down when applied to heavier atoms. Arguably the most popular GGA functional is the Perdew-Burke-Ernzerhoff functional (PBE)[14] which is based upon the previous Perdew and Wang PW91[15] functional and is not experimentally derived. These systems, including the PBE functional optimised for structural calculations (PBEsol[16]) are notorious for underestimating band gaps despite giving an accurate approach to structural parameters.

The Hubbard 'U' Parameter:

Despite overcoming HF by allowing for interacting electrons, LDA and GGA both suffer from the *self-interaction error* or SIE. This phenomenon is an artefact of these methods whereby an electron interacts with itself due to the poor description of exchange and correlation. For systems where the electrons are in close proximity to each other such as in highly localised orbitals this poses an obvious problem. Incorrect metallic behaviour due to the delocalisation of electrons and holes from GGA or LDA is therefore expected.

To account for this, a Hubbard-like 'U' parameter is added whereby a penalty is enacted for partial occupation at a site localising electrons to atomic centres.[17,18] The addition to the DFT formalism is through:[19]

$$\frac{U-J}{2}\sum_{\sigma,m}(n_{l,m,s}-n_{l,m,s}^2) \tag{1.3.6}$$

where $U-J=U_{\text{eff}}$ with U and J being the on-site Coulomb and exchange interactions respectively for electrons with the same 'l' (angular momentum) for a given atom. $n_{l,m,\sigma}$ is the occupation for an orbital with angular momentum (l), magnetic quantum number (m) and spin (s).

This method is commonly known as *DFT+U* and is typically used in *strongly correlated* systems such as TiO_2 or other transition metal oxides. This definition of correlation is in a different context to that described by Lowdin[20] (Section 1.2.1). It can be said therefore that DFT+U correctly treats on-site Coulomb interactions particularly for d and f electrons. A major caveat, however, is the determination of a suitable value of 'U' which can typically be both geometry and electronically dependent. Materials with inequivalent atomic sites could therefore have different values of 'U'.[21]

Hybrid Functionals:

Hybrid functionals approach the exchange-correlation problem by mixing an amount of exact exchange from non-local HF theory together with the exchange correlation from DFT. As mentioned in Section 1.2.1, HF allows for the calculation of *exact* exchange and thus the formalism when combined with DFT is :

$$E_{XC}^{\text{hybrid}}=\alpha E_X^{\text{HF}}+(1-\alpha)E_{\text{XC}}^{\text{DFT}} \tag{1.3.7}$$

where α is the amount of variable exact exchange from HF. The PBE0 functional[22,23] within the PBE (Perdew Burke Ernzerhoff)[14] formalism uses 25% exact HF exchange ($\alpha=0.25$) together with 100% correlation and 75% PBE exchange thus giving:

$$E_{XC}^{\text{PBE}}=\frac{1}{4}E_X^{\text{HF}}+\frac{3}{4}E_X^{\text{PBE}}+E_C^{\text{PBE}} \tag{1.3.8}$$

PBE0 excels in the description of the electronic properties of SnO_2 and other Sn-based oxides such as $BaSnO_3$.[24–29] PBE0 however, is fairly computationally expensive as it suffers from the slow decay of the exchange interaction in real space. Screening this exchange allows for a more efficient calculation of materials properties and is seen in the HSE functionals such as HSE06[30–32]:

$$E_{XC}^{\mathrm{HSE06}} = \alpha E_X^{\mathrm{HF,SR}}(\omega) + (1-\alpha)E_X^{\mathrm{PBE,SR}} + E_X^{\mathrm{PBE,LR}}(\omega) \tag{1.3.9}$$

where $\alpha = 0.25$ and $\omega = 0.20$ for HSE06 (Heyd-Scuseria-Ernzerhoff). SR and LR refer to the 'short ranged' and 'long ranged' parts of the functional to describe the Coulomb potential and addresses some of the exchange decay seen in PBE0. HSE06 describes the properties of TiO_2 polymorphs well.[33–40]

Chapter 2

Computational Methodology

2.1 Periodic Boundary Conditions and Geometry Optimisations

Calculating the properties of macroscopic crystals directly is not a practical method for probing the properties of a material due to the vast number of electrons contained within. Fortunately, the crystalline nature of a material can be described by repeating units therefore periodic boundary conditions can be applied to a system. Using periodic boundary conditions, a unit cell is repeated in all directions taking into account all the lattice vectors, angles and the space-group symmetry as depicted in Figure 2.1.

Unit cells are geometric arrangements of atoms where the cell parameters and lattice points can be classified by the fourteen Bravais lattices and hence have large symmetry relationships. The *smallest* possible repeat unit is known as a *primitive* cell and contains one lattice point. It usually makes sense computationally to use the primitive cell, however in certain situations where the use of symmetry operations increases the efficiency of a calculation, a conventional unit cell may be used. Examples of the primitive cell, unit cell and supercell under periodic conditions are shown in Figure 2.1.

A linear combination of functions combine to form basis sets which are generally used to create mathematical representations of the wavefunctions in a system. Arguably the most applicable basis sets employed are *plane-waves* of the form e^{ikr} as they translate efficiently into a periodic formalism.[41] Bloch's theorem[42] ($\psi_k = u(r)e^{ikr}$) shows that the wavefunction

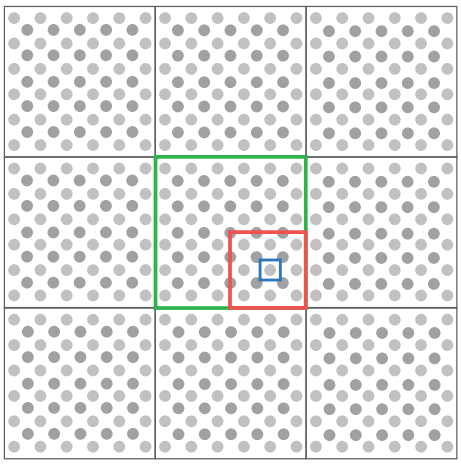

FIGURE 2.1: A schematic diagram displaying three types of calculated cell, the *primitive cell* (blue), the *conventional unit cell* (red) and a *supercell* (green) which is subjected to periodic boundary conditions

of an electron can be made up of a function consistent with the periodicity of the lattice ($u(r)$) and a plane wave part (e^{ikr}). The plane waves are therefore only dependent on the sampling of the reciprocal lattice vectors (k-points) and are only dependent on the size of the cell in question and not on the number of atoms in a system.

An upper bound is applied called the *plane-wave energy cutoff* due to the kinetic energy term present. High and rapid fluctuations of the wavefunction in a system can occur with core electrons near to the nuclei of atoms requiring high energy cutoffs, especially for systems with light atoms.

Pseudopotentials are typically used to offset these rapid fluctuations of the wavefunctions near the nuclei thus decreasing the plane-wave cutoff energy and computational cost. Pseudopotentials do a good job of describing the interactions between the valence electrons and core electrons, as well as the nuclei and core electrons which are replaced by an effective potential. The pseudized wavefunction is smoothed out to match the shape of the valence electrons, thus reducing the number of nodes within the core region(Figure 2.2). Most pseudopotentials are derived from *all electron* calculations and have been shown to possess the same accuracy as such a calculation with a reduction in the computational cost.[43]

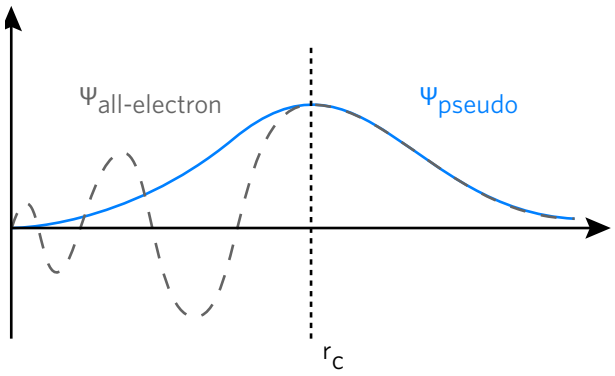

FIGURE 2.2: A schematic diagram showing a *pseudopotential* wavefunction (red) as compared to an *all electron* wavefunction (blue), r_c is the radial cutoff or where the core electrons meet the valence electrons.

The projector augmented wave method (PAW) by Blöchl[44] was developed as an all-electron approach which is used in the work in this thesis. Within the PAW framework, the core electron wavefunction is 'frozen' (meaning they do not participate in bonding) and the smooth wavefunction of the valence electrons (treated explicitly) are projected into the core region.

Geometry optimisation of a structure is best practice in computational materials chemistry due to the difference between the experimental low potential energy well and that calculated in theory. Properties of interest such as the electronic structure or defect thermodynamics will be significantly changed if geometry optimisation is not carried out. In defect supercells (section 2.3), geometry optimisations are slow due to the removal of symmetry optimisation, which, in unit cells of high symmetry reduce the number of degrees of freedom making the calculation more efficient. Iterative algorithms exist for the efficient optimisation of structures which use updated steps within a nested loop to reach a minimum with an acceptable convergence parameter eg. $0.01\,\mathrm{eV\,\AA^{-1}}$ for forces and $1\times10^{-5}\mathrm{eV\,\AA^{-1}}$ for energies. Force calculations are typically carried out within the Hellmann-Feynman theorem which calculates the forces on the ions as the classical electrostatic force on the nucleus when the valence electron wavefunctions are updated.[45,46] The benefits of this methodology is that it only relies on the already calculated wavefunction, however the calculation of the derivative of the basis set relative to the *position* of the ion is overlooked. Without a sufficiently high plane-wave energy cutoff, the force on the ions results in Pulay stress.[47] The Pulay stress arises due to the incomplete convergence of the basis set to the changes in the volume of a system.

2.2 Electronic Structure Optimisations

2.2.1 Density of States

The electronic density of states (typically denoted 'DOS') allows the visualisation and characterisation of the orbital contributions that make up features of the band structure (section 2.2.2). The total DOS is the sum of the band contributions at a particular eigenvalue and is what would be gleaned from integrating a band structure. The DOS can be decomposed into the *partial* DOS (pDOS) based upon either the atom involved or further into specific orbitals. In order to achieve this, the wavefunctions are projected onto each ion using spherical harmonics. Figure 2.3 displays the total and partial density of states for ZnO as an illustrative example. The DOS is aligned to the band structure to show the relationship between the two diagrams, a highly dispersive (curvature) VBM, for example, will have a low DOS intensity; thus it can be said that the intensity of the DOS is inversely proportional to the dispersion seen in the band structure.

Experimental techniques can be compared to a DOS, such as valence-band X-ray photoelectron spectroscopy (VB-XPS) or Hard X-ray Photoelectron spectroscopy (HAXPES). This can be achieved by weighting the DOS with atomic orbital photoionisation cross sections formulated by Yeh and Lindau[48] or Scofield[49], and the application of both Gaussian and Lorentzian broadenings to match experimental apparatus. This method has been used successfully in many studies in order to accurately describe the electronic states that give rise to the XPS data.[50–55]

2.2.2 Band Structures

Band structures are another tool for the vital determination of a material's electronic properties. These plots depict the change in the eigenvalue of a band relative to k. Ideally a band structure would be calculated over the entirety of k-space for a material, but due to computational cost, it is customary to choose a path along the high symmetry points within the first Brillouin zone. The first Brillouin zone for ZnO is shown in Figure 2.3 alongside the associated band structure of ZnO.

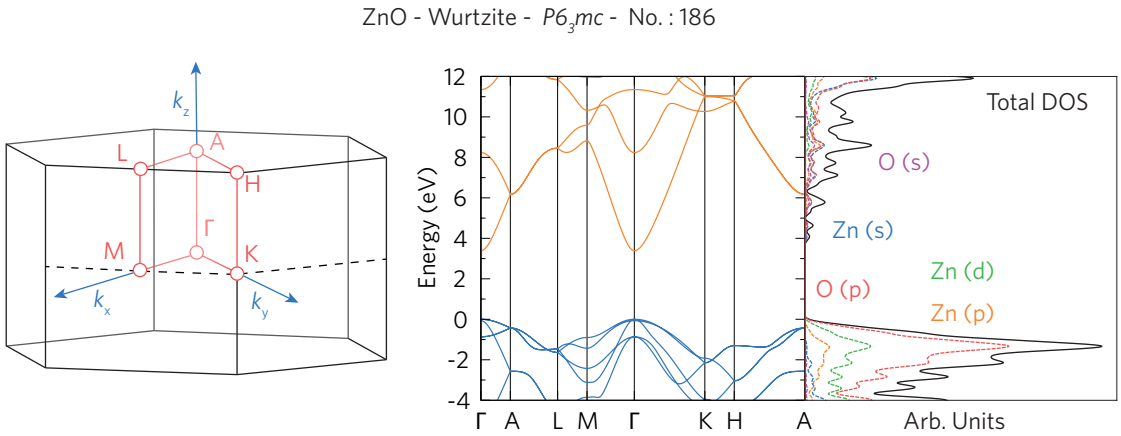

FIGURE 2.3: The first Brillouin zone of wurtzite ZnO ($P6_3mc$, no. 186) and the associated band structure (using the high symmetry points in reciprocal space (Red)) and DOS. In the band structure, the valence bands are depicted in blue (VBM = 0eV) and the conduction bands are in orange. The DOS is aligned to the band structure to show the relation between the two diagrams. The high symmetry points are taken from Bradley and Cracknell[56] and are: Γ = (0,0,0), A = (0,0,$\frac{1}{2}$), H = ($\frac{1}{3}$,$\frac{2}{3}$,$\frac{1}{2}$), K = ($\frac{1}{3}$,$\frac{2}{3}$,0), M = (0 $\frac{1}{2}$,0), L = (0 $\frac{1}{2}$,$\frac{1}{2}$).

At first glance, the band structure can give information about the nature of the fundamental band gap. This can be whether it is *indirect* or *direct* as well as the magnitude. As discussed in Section 3.2.1, it can be important for an idealised *n*-type TCO to have an extra gap between the CBM and the next highest band which can easily be obtained from a band structure. As absolute band energies are not calculated from a typical periodic calculation, the valence band maximum (VBM) is typically set at 0 eV.

2.2.3 Effective Mass

The effective mass (m_0^*) is the mass of a charge carrier in a solid subject to an external electrostatic potential and is given in terms of the rest mass of an electron (9.109×10^{-31} kg). Calculating the effective mass from a band structure is a reliable method of determining the electron or hole mobility and thus the potential conductivity of a material. Judging from the curvature of the CBM (or VBM), one can determine whether a material will have a light or heavy electron (hole) effective mass (m_0^*). A useful assumption and description of the effective mass is through the parabolic model, where it is assumed that the band structure is isotropic at the CBM (VBM) and therefore the electrons (holes) can be treated as a *free elec-*

tron gas. The effective mass tensor is therefore:

$$\frac{1}{m^*_{ij}} = \frac{\delta^2 E(k)}{\delta k_i \delta k_j} \frac{1}{\hbar^2} \tag{2.2.1}$$

Where the energy of an electron at k-point 'k' ($E(k)$) is inversely proportional to the effective mass m^*_0. Generally this approximation is sound for wide band gap semiconductors, where the CBM and VBM are generally parabolic in nature, however non-parabolic approximations exist for systems without this .[57] In this thesis, the parabolic model is assumed.

2.2.4 Optical Absorption

In order to calculate the optical absorption of a material and to further compare to experiment, the absorption coefficient (α) can be calculated and thus the optical band gap can be described. The imaginary part of the dielectric function is obtained using a summation over the unoccupied bands in a method by Furthmüller and coworkers.[58] The real part of the dielectric constant can then be calculated from the imaginary part with a Kramers-Kronig transformation[59]:

$$\epsilon_r(\omega) - 1 = \frac{2}{\pi} P \int_0^\infty \frac{\omega' \epsilon_i(\omega')}{\omega'^2 - \omega^2} d\omega' \tag{2.2.2}$$

Where P is the principal value of the integration, $\epsilon_r(\omega)$, $\epsilon_i(\omega)$ are the real and imaginary parts of the dielectric constant respectively (with respect to the frequency, ω and ω'). The absorption coefficient,α, can then be determined by:

$$N = n_r + i n_i = \frac{(\epsilon_r(\omega) + i\epsilon_i(\omega))}{\epsilon_0} \tag{2.2.3}$$

Where n_r and $i n_i$ are the real and imaginary parts of the refractive index respectively. $\epsilon_r(\omega)$, $\epsilon_i(\omega)$ are the real and imaginary parts of the dielectric constant respectively (with respect to the frequency, ω) and ϵ_0 is the vacuum permittivity. Thus, α can be expressed using the relationship:

$$\alpha = \frac{4\pi n_i}{\lambda_0} \tag{2.2.4}$$

where λ_0 is the incident wavelength. A strong absorption is deemed to be when α is at least $\sim 10^5$. Although this is a powerful method for creating absorption spectra, this only sums transitions between occupied and unoccupied absorptions thus ignoring intra-band and indirect transitions. This method also ignores electron-hole correlations requiring higher levels of theory than standard DFT or hybrid DFT.[58,60,61] The dielectric constant calculated herein is only the high-frequency response, the lattice response contribution to the dielectric function which is used in the *image charge correction* (Section 2.3.4 can be calculated using DFPT, or Density Functional Perturbation Theory.

2.3 Defect Calculations

2.3.1 The Supercell Method and Defect Thermodynamics

The most accessible and versatile method of calculating defects from first principles within a periodic code formalism is through the use of *supercells*. Other methods such as the Mott-Littleton[62,63], QM/MM embedded cluster approach[64–67] have been used as well as quantum MonteCarlo methods.[68–70] The 'supercell' method is widely used due to its simplicity and applicability to different materials and applications (dopants, clusters etc.). A supercell is an expansion of a unit cell (Figure 2.1) ie. 3×3×1 supercell (108 atoms) of the unit cell of anatase TiO_2 is 3 times the *a* and *b* directions and 1 of the *c* direction. This cell is subsequently treated with periodic boundary conditions where the cell shape, volume and lattice parameters are kept constant, leaving only atomic positions to be relaxed to a convergence criterion. Due to computational expense, the supercell is limited to a few hundred atoms, however due to 'finite' size effects present issues arise such as the slow decay of the Coulomb potential with distance[71,72] requiring post-processing corrections which are covered in Section 2.3.4.

2.3.2 Enthalpy of Formation for a Neutral Defect

A basic assumption in the thermodynamic calculation of defects, is the negation of entropic effects due to calculation at the *athermal* limit. This drastically reduces the computational expense of the calculations due to the large concentration of defects present when calculating vibrational entropy terms. The enthalpy of formation for a neutral defect (D) ($\Delta H_f^{(D,q=0)}$, the charge state $q=0$) is dependent on both the total energy of the defective supercell ($E^{(D,q=0)}$) relative to the host supercell ($E^{(H)}$) and the chemical potentials (μ_i) and the elemental reference energies (E_i where i = each constituent element) in the relationship:

$$\Delta H_f^{(D,q=0)} = (E^{(D,q=0)} - E^H) + \sum_i n(E_i + \mu_i) \tag{2.3.1}$$

Where n is positive or negative dependent on whether the element is added to (-n) or removed from the system (+n).

2.3.3 Enthalpy of Formation for a Charged Defect

Due to the number of available electrons, defects can therefore occur in multiple charge states denoted by 'q'. The periodic boundary conditions means that an homogeneous jellium background charge is applied to neutralise the supercell. The defective system now possesses a charge that no longer matches to the neutral supercell and so a dependence arises on the chemical potential of the electrons and thus the enthalpy of formation of a charged defect is[73,74]:

$$\Delta H_f^{(D,q)} = (E^{(D,q)} - E^H) + \sum_i n(E_i + \mu_i) + q(E_f + \epsilon^H_{\mathrm{VBM}} + \Delta v^{\mathrm{pot}}) \tag{2.3.2}$$

The equation is just an extension of equation 2.3.1 where $\mathrm{E}^{(D,q)}$ is the total energy of the defective supercell in charge state q. There is now a dependance on the Fermi energy (E_f) (with reference to the eigenvalue of the VBM in the host supercell, $\epsilon^H_{\mathrm{VBM}}$). An alignment term, Δv^{pot} is applied to account for the difference in the bulk and defect supercells' electrostatic potentials. Δv^{pot} is important as the determination of the total energy being a derivative of the occupied Kohn-Sham eigenvalues.[75] Therefore a restoration of the potentials of the charged defect supercell and the host is necessary (Figure 2.3.4). *Potential alignment* is problematic for charged supercells due to the slow decay of the Coulomb Potential of the defect.[73,76,77] At the most simplistic, a potential alignment involves aligning a core level potential far away from the defect to that in the host, i.e. an O 1s core level in In_2O_3, however large supercells are required for this method to be accurately applied. Other schemes are available such as that by Lany and Zunger, whereby the core levels of the supercell are averaged and compared to the host supercell bar those within the immediate vicinity of the defect in question.[73,77] This method is the one used for all calculated defects within this thesis.

2.3.4 Post Processing and Correction Schemes

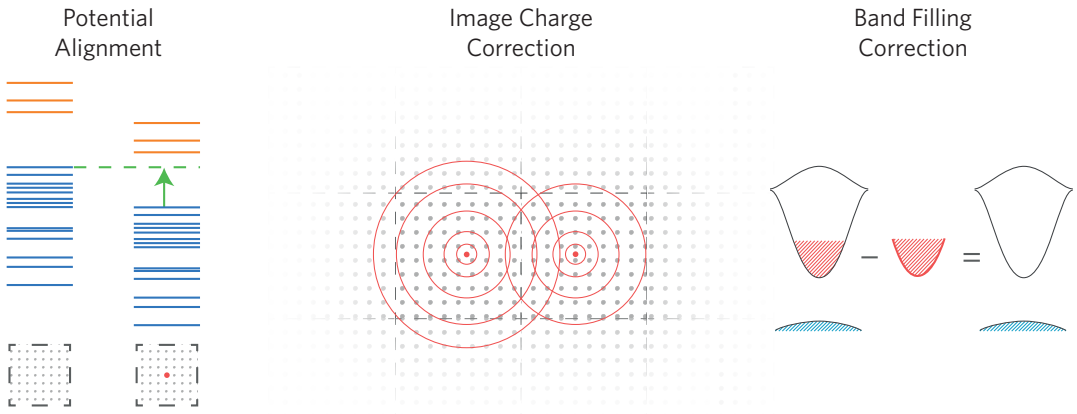

FIGURE 2.4: A depiction of the three commonly used *post-processing* corrections associated with defect formation energies, firstly there is the potential alignment to align the VBM of the host supercell with that of the defective supercell, secondly there is the image charge correction to account for the spurious interaction of a charged defect with its periodic images and lastly the band filling correction to regain the 'dilute' limit.

Despite the great practicality of the supercell calculations, in order to increase computational efficiency and decrease the expense of a single calculation, very large supercells using hybrid DFT are unrealistic on today's computer architecture. Therefore, due to the finite size of a typical supercell (~70-200 atoms) there are necessary corrections applied *a posteriori* to equations 2.3.1 and 2.3.2 in order to obtain accurate formation energies especially when implementing computationally demanding hybrid functionals (Section 1.3.3).

Image Charge Correction:

Due to the long-ranged nature of the Coulomb interaction[71,72], the convergence of the defect energy is very slow and increases asymptotically with $\frac{q^2}{L}$ (where L is the supercell size length). This has led to arguably the most crucial correction, the *image charge correction*. The electrostatic energy of a repeating charged supercell under periodic boundary conditions is compensated for by a uniform electrostatic background charge or *jellium* which is therefore described by the Madelung energy[73,78,79]:

$$E_{\text{corr}}^{\text{Madelung}} = \frac{q^2\alpha}{2\epsilon L} \tag{2.3.3}$$

Where α is the Madelung constant (dependent on the Bravais lattice) and ϵ is the static dielectric constant of the material. The correction in its most simplistic form involves a removal of the Madelung energy. This method works for an array of point charges with a neutralising background, i.e. highly ionic systems, but breaks down with any other system.[80] Makov and Payne[81] elaborated on this system by introducing a second order term that describes the *localised* charge density with the 'jellium':

$$E_{\text{corr}}^{\text{MP}} = \frac{q^2\alpha}{2\epsilon L} - \frac{2\pi qQ}{3\epsilon V} \tag{2.3.4}$$

where Q is the 'second radial moment' of the localised charge distribution[73]:

$$Q = \int r^2 \rho(r) dr \tag{2.3.5}$$

Where $\rho_r(r)$ (r is the radial part) is the density difference between the host cell ($\rho_H(r)$) and the defective cell ($\rho_D(r)$): thus $\rho(r) = \rho_H(r) - \rho_D(r)$. The Makov and Payne correction on its own however has a tendency to greatly overestimate the formation energy for small supercells.[79] Augmentations to this theory have been formalised by various groups, in particular the FNV correction by Freysoldt, Neugebauer and Van de Walle[79] and subsequently an anisotropic extension by Kumagai and Oba[82] which account for higher order long range image charge interactions. The short-range potentials incur issues however, and the schemes, whilst simple and can be generally applied to different cell shapes and sizes become problematic when the defect charge distribution becomes delocalised.[73] The image charge correction used in this work utilises an addition to the formalism described by Lany and Zunger[77,83]:

$$E_{\text{corr}}^{\text{LZ}} = [1 + c_{sh}(1 - \epsilon^{-1})] E_{\text{corr}}^{\text{Madelung}} \tag{2.3.6}$$

Where c_{sh} is the 'shape factor' determined from the shape of the supercell, ϵ is the static dielectric constant. This methodology allows for the application of an image-charge correction to non-cubic cells, and this implemented in a scheme by Hine and Murphy[78] the dielectric tensor can be applied. If the supercell is isotropic and $\epsilon \gg 1$ equation 2.3.6 becomes:

$$E_{\text{corr}}^{\text{LZ}} \approx \frac{2}{3} E_{\text{corr}}^{\text{Madelung}} \tag{2.3.7}$$

Band Filling Correction:

The band filling correction corrects for the unphysical filling of the conduction band at degenerate doping concentrations (of resonant or shallow defects) due to the small size of the simulated supercell.[74,77,84–86] Using the potential alignment ΔV (sec. 2.3.3), all electrons (and corresponding eigenvalues) above a certain energy are shifted towards a *reference* energy taking into consideration the band occupations and k-point weights. Figure 2.4 displays schematically the correction for an n-type semiconductor. The band filling correction[74,76,77,84] and is described for a donor as:

$$\Delta E_{\text{corr}}^{\text{bf}} = -\sum_{n,k} (e_{n,k} - e_{\text{CBM}}^{\text{host}})(\omega_k \eta_{n,k} e_{n,k} - e_{\text{CBM}}^{\text{host}}) \tag{2.3.8}$$

or

$$\Delta E_{\text{corr}}^{\text{bf}} = -\sum_{n,k} (e_{n,k} + e_{\text{VBM}}^{\text{host}})(\omega_k \eta_{n,k} e_{n,k} - e_{\text{host}}^{\text{host}}) \tag{2.3.9}$$

for a shallow acceptor, where $e_{n,k}$ corresponds to the eigenvalue at band n and k-point k, $e_{\text{VBM/CBM}}^{\text{host}}$ is the VBM or CBM eigenvalue of the host. ω_k and $\eta_{n,k}$ are the k-point weighting and occupation at band, n, and k-point, k. For a localised defect state in the band gap the correction will give a value of 0 eV

2.3.5 Chemical Potential Limits

Equations 2.3.1 and 2.3.2 rely on the chemical potentials μ_{x} where X refers to the species added to or taken away from the system. The chemical potentials are also bounded via the formation enthalpy of the host material and by any competing phases. Any dopant species are also affected by these bounds and by the formation enthalpies of any dopant secondary phases. Using TiO_2 doped with Nb as an example, the chemical potentials of the host material are constrained by the enthalpy of formation of TiO_2 ($\Delta H_f^{TiO_2}$) as well as limited by the formation of a secondary phase, Ti_2O_3 ($\Delta H_f^{Ti_2O_3}$). Equations 2.3.10 and 2.3.11 show the for-

mation enthalpies of these two compounds as a function of their chemical potentials.

$$\Delta H_f^{TiO_2} = \mu_{Ti} + 2\mu_O = -9.14\,eV \tag{2.3.10}$$

$$\Delta H_f^{Ti_2O_3} = 2\mu_{Ti} + 3\mu_O = -14.76\,eV \tag{2.3.11}$$

Therefore, solving these equations simultaneously results in upper and lower bounds in the chemical potential limits under *Ti-rich/O-poor*:

$$\mu_{Ti} = -2.11\,eV; \mu_O = -3.51\,eV \tag{2.3.12}$$

and for *Ti-poor/O-rich*:

$$\mu_{Ti} = -9.14\,eV; \mu_O = 0\,eV \tag{2.3.13}$$

Equations 2.3.12 and 2.3.13 show that under the most *O-poor* conditions, the chemical potentials are limited via the formation of Ti_2O_3 and under *O-rich* conditions by the formation of $O_{2(g)}$.

The formation of dopant species, in this example Nb, are also limited by the formation of secondary phases; NbO, NbO_2 and Nb_2O_5. Equations 2.3.14, 2.3.15 and 2.3.16 show the enthalpies of formation of the limiting dopant phases for Nb-doped TiO_2.

$$\Delta H_f^{NbO} = \mu_{Nb} + \mu_O = -4.10\,eV \tag{2.3.14}$$

$$\Delta H_f^{NbO_2} = \mu_{Nb} + 2\mu_O = -7.64\,eV \tag{2.3.15}$$

$$\Delta H_f^{Nb_2O_5} = 2\mu_{Nb} + 5\mu_O = -18.48\,eV \tag{2.3.16}$$

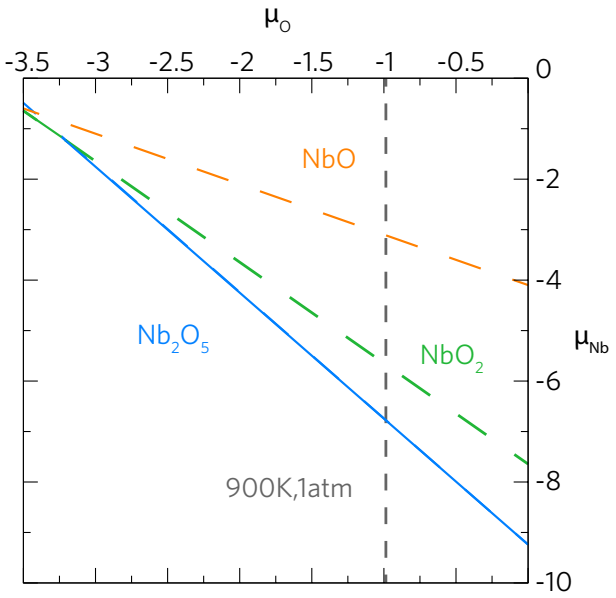

FIGURE 2.5: The evolution of the formation of secondary phases in terms of O chemical potential (μ_O and Nb chemical potential (μ_O). Under *Ti-rich/O-poor* conditions (μ_O = -3.51 eV) the limiting phase is NbO_2 and under *Ti-poor/O-rich* conditions (μ_O = 0 eV) by Nb_2O_5. The dashed grey line corresponds to a μ_O =0.97 eV under 900K, 1atm conditions showing the limiting phase to be Nb_2O_5.

Figure 2.5 displays the evolution of the formation of each Nb-related phase within the chemical potential limits of anatase TiO_2 (from equation 2.3.12 and 2.3.13). The limiting phase is the one with the lowest chemical potential thus under *Ti-rich/O-poor* and *Ti-poor/O-rich* conditions, μ_{Nb} will be determined via the formation of NbO_2 and Nb_2O_5 respectively thus μ_{Nb} is:

$$\begin{aligned} &\textit{Ti-rich/O-poor}: \mu_{Nb} = -0.62\,eV \\ &\textit{Ti-poor/O-rich}: \mu_{Nb} = -9.24\,eV \end{aligned} \tag{2.3.17}$$

Simulation of Experimental Conditions:

In order to simulate the experimental growth conditions typically used in thin film deposition, μ_O can be determined by the oxygen partial pressure at a specified temperature and

pressure. This method uses the equation as outlined by Reuter and Scheffler:[87]

$$\mu_O(T,p^0) = \frac{1}{2}[H(T,p^0,O_2) - H(0K,p^0,O_2)] - \frac{1}{2}T[S(T,p^0,O_2) - S(0K,p^0,O_2)] \quad (2.3.18)$$

Where T, H and S correspond to temperature, enthalpy and entropy respectively. p^0 = 1 atm with reference to a zero state ; $\mu_O(0K,p^0)=\frac{1}{2}E_{O_2}^{total}$ = 0 (i.e. the total energy of oxygen in an isolated molecule).[88,89]

Using thermochemical tables[90] μ_O can be determined for a range of temperatures and pressures. Ideal scalable deposition methods such as chemical vapour deposition (CVD) typically used in industry[91], are carried out at atmospheric pressure, p^0 = 1 atm.

TABLE 2.1: The oxygen chemical potentials at varying temperatures (500K–1200K) at atmospheric pressure (p^0 = 1 atm) using equation 2.3.18 and thermochemical data tables.[90]

Temp (K)	μ_O (eV)
500	-0.49
600	-0.61
700	-0.73
800	-0.85
900	-0.97
1000	-1.10
1100	-1.23
1200	-1.36

For completeness, if one were to calculate the dependency on varying partial pressures at a specific temperature (i.e. not just at 1 atm) equation 2.3.19 can be used:

$$\mu_O(T,p) = \mu_O(T,p^0) + \frac{1}{2}kT\ln(\frac{p}{p^0}) \quad (2.3.19)$$

Where k refers to the Boltzmann constant. Thus for a typical deposition temperature of 900 K and a pressure range of 0.001-1000 atm μ_O is now:

TABLE 2.2: The oxygen chemical potentials at varying *oxygen partial pressures* (0.001–1000 atm) at 900K using equation 2.3.19.

p (atm)	μ_O (eV)
1×10^{-3}	-1.24
1×10^{-2}	-1.15
1×10^{-1}	-1.06
1×10^{0}	-0.97
1×10^{1}	-0.89
1×10^{2}	-0.80
1×10^{3}	-0.71

From this analysis, at 900K and 1 atm, the Nb chemical potential will be limited via the formation of Nb_2O_5 with μ_{Nb} = -6.80 eV as shown in Figure 2.5.

2.4 Thermodynamic Transition Levels

Transition level diagrams are an ideal choice for displaying the vital thermodynamic properties of defective systems with their respective charge states. The addition of defects and dopants into a system usually create levels present in the band gap of a material which can usually be detected experimentally. There are three levels associated with defects, the 'single particle levels' (SPLs), thermodynamic transition levels and optical transition levels. SPLs are the raw Kohn-Sham eigenvalues which describe the position of occupied defect levels in the band structure of a material. These levels, although instructive to the defect properties, cannot be related to experiment as the thermodynamic and optical transition levels can. Thermodynamic transition levels are the equilibrium transitions between different charge states (in the case of DFT: at 0K). The optical transition levels, however are the optically excited transitions between different charge states with respect to the CBM or VBM. The relaxation towards an equilibrium configuration between $q\prime$ and q can be seen experimentally in techniques such as deep level transient spectroscopy (DLTS) photoluminescence and temperature-dependent Hall effect measurements.[92]

$$\epsilon_D(q/q') = \frac{\Delta H^f(D,q') - \Delta H^f(D,q)}{q' - q} \tag{2.4.1}$$

Figure 2.6 displays the thermodynamic transition levels for a fictional n-type wide band gap (E_g = 3.1 eV) material. The slopes of each line indicate the type of defect, donor/n-type defect (positive slope) or acceptor/p-type defect (negative slope) with the gradient corresponding to the charge state (i.e. gradient of 2 is a 2+ charge state). The Fermi level ranges from the VBM (0 eV) to the CBM (3.1 eV) and for a defect to be shallow/resonant (i.e. conducting) the transition to the neutral charge state needs to be < 0.03 eV from the band minima/maxima (corresponding to k_BT at room temperature, i.e. ionisation at room temperature). Situation 1 describes a chemical potential range that favours the formation of n-type defects. The donor defect (D) is a low formation energy *resonant* defect with the 1+/0 transition level occurring within the conduction band, meaning that the extra electron is donated readily into the conduction band indicative of high conductivity. An acceptor defect also exists (A) which has a high formation energy ($\Delta H_f^A(q=0)$ = 5 eV) across the range of the band gap. As the two lines (D and A) *do not* intersect, the acceptor defect does not *compensate*

the donor defect. The acceptor defect is *extremely* deep with the 0/1- transition level situated ~ 2 eV *above* the VBM meaning that *thermal excitation* will have a prohibitively high activation energy. A second donor defect exists (D^2) which is a *negative-U* defect[93,94] and transitions directly from the +2 charge state to the neutral charge state. For this defect, the 1+ charge state is unstable and thus disproportionates into the 2+ and 0 charge states. In this instance the 2+/0 transition level is very deep (~ 0.7 eV below the CBM) and so is not expected to contribute to the conductivity of the system.

Situation 2, however, shows a different scenario whereby the acceptor defect is now lower in energy thus the Fermi level becomes 'pinned' in the band gap (~ 2.8 eV above the VBM where D^{1+} intersects A^{1-}). This 'pinning' occurs when the acceptor defect and donor defects cross and thus to Fermi energies below this point donor defect 'D' is the most likely to form, and above this point acceptor defects (A) are most prevalent . We also notice that donor defect D has a transition level that occurs *below* the CBM, however this transition level is within 0.03 eV of the band minima and thus can readily undergo room-temperature ionisation making this a *shallow* donor.

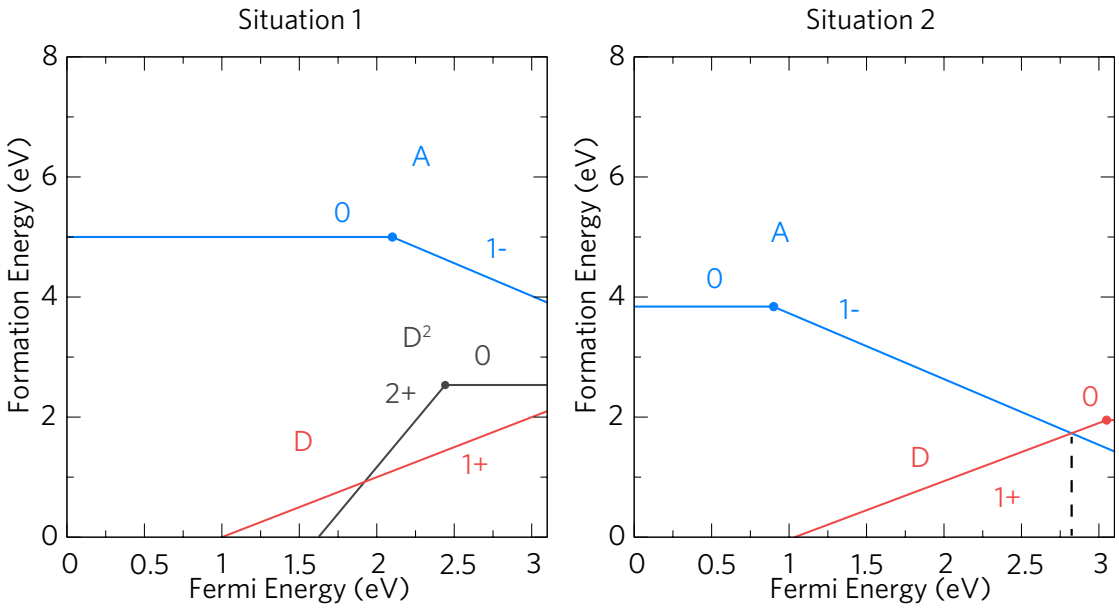

FIGURE 2.6: Examples of *transition level diagrams* under two situations. In each example the Fermi level ranges from the VBM (0 eV) to the CBM, which, in this fictional material is 3.1 eV. The red line corresponds to a *donor* defect (D), the blue line to an *acceptor* defect (A) and the black line to a second donor (D^2). In situation 2 the Fermi level is pinned at the intersection of the two opposing defects.

2.4.1 Optical Transition Levels

The ability to analyse the optical absorption and emission processes of a defective system is hugely important in the analysis of defects both in terms of a 'fingerprint' and application specific optical properties. The optical transitions can aid explanations of complex defect systems such as the well known DX centre (a deep donor defect with large lattice relaxations) in AlN and GaN[95], the visible light excitation mechanism in N doped TiO_2[96] or aid the role of defects in quantum computing.[97] Probing the properties of defects using photons occurs at the femtosecond to picosecond time-scale (10^{-15} s - 10^{-12} s) offering a "high resolution" picture of the defect landscape. Experimentally the absorption can be evaluated using the Beer-Lambert Law[98,99] which gives the optical transmission (T):

$$T = \frac{I}{I_0} = e^{-\alpha x} \tag{2.4.2}$$

Where I_0 is the initial intensity of the incoming photon beam, I is the detected intensity having passed through the film, x is the thickness of the film and α is the absorption coefficient.

Photoluminescence is perhaps the most sensitive-to-defects method of probing the optical emission of a film. Photoluminescence spectroscopy (PL) probes the spontaneous emission of light following an optical excitation of a material. Typically the monochromatic wavelength of light used is slightly greater than the band gap of the material in order to create electron-hole pairs.[100] After photo excitation of an electron from a defect or valence band to the conduction band, the electron will recombine with the associated hole and emit a photon, the intensity of which is detected by a spectrometer. The associated absorption can be measured using *photoluminescence excitation* (PLE) which measures the intensity of the emission at varying wavelengths from the absorption edge of the material to the expected absorption of a particular emission peak.[101]

Calculation of Optical Transition Levels:

It is possible to evaluate the optical transition levels $\epsilon^{opt}(q/q')$ for a given defect in a system. In optical absorption it is assumed that for a defect in charge state q, an electron is excited from the defect to the CBM (or from the VBM to the defect) forming charge state q'. As optical excitations happen on the femto to picosecond time-scale,[101] it is assumed that optical

excitation is more or less instant (as per the Franck-Condon principle [102,103]) and that lattice relaxation is much slower in comparison. In order to calculate $\epsilon^{opt}(q/q')$, the same method detailed in Section 2.3.3 can be applied except that $D^{q'}$ is locked into the equilibrium geometry of D^{q}. Equations 2.4.3(a),(b),(c) and (d) detail the excitation (and subsequent capture) of an electron from a defect ($D(q)$) to the conduction band as an example. $R(q)$ and $R(q')$ refer to the *equilibrium* geometries of D^{q} and $D^{q'}$ respectively, i.e. $D(q)[R(q')]$ is a defect in charge state q but in the relaxed *equilibrium* geometry of charge state q'. Once optical excitation (E_{abs} - equation 2.4.3(a)) has occurred, the defect relaxes into its equilibrium geometry, $D(q')[R(q')]$ (equation 2.4.3(b)), of which the relaxation energy (E^{1}_{rel}) is usually released as phonons into the system. In equation 2.4.3(c), the excited charge state ($D(q')[R(q')]$) can then *accept* an electron from the CBM emitting a photon (E_{em}) (radiative emission) or phonons (non-radiative emission). $D(q)[R(q')]$ can then relax back into its equilibrium ground state configuration ($D(q)[R(q)]$) with a relaxation energy (E^{1}_{rel}) typically released as phonons.

$$D(q)[R(q)] \xrightarrow{E_{abs}} D(q')[R(q)] \,(+e^{-}_{CBM}) \tag{2.4.3a}$$

$$D(q')[R(q)] \xrightarrow{E^{1}_{rel}} D(q')[R(q')] \,(+phonons) \tag{2.4.3b}$$

$$D(q')[R(q')] \,(+e^{-}_{CBM}) \xrightarrow{E_{em}} D(q)[R(q')] \tag{2.4.3c}$$

$$D(q)[R(q')] \xrightarrow{E^{2}_{rel}} D(q)[R(q)] \,(+phonons) \tag{2.4.3d}$$

The distance between the thermal equilibrium geometries (minima) results in the *zero-phonon line* which roughly translates to the *thermodynamic* transition level relative to the CBM (or VBM for electron capture). [97,104] In certain circumstances, the optically excited electron can be captured by a positively charged defect such as a donor resulting in *donor-acceptor pairs* the strength of which is dependent on the distance between the two defects. [101] Electron capture from the VBM works in much the same way as electron excitation to the CBM.

Configurational Coordinate Diagrams:

Typically the optical transitions are displayed using configurational coordinate diagrams, examples of which are shown in Figure 2.7. Typically these diagrams show energy versus a generalised coordinate (Q) which is a physical difference (displacement etc.) between the different charge states. Each charge state has its own parabola, the minima of which corresponds to the equilibrium geometry ($D(q)[R(q)]$ or $D(q')[R(q')]$). Due to the Franck-Condon principle, the absorption or emission processes are vertical transitions. In Figure 2.7, two situations are given: situation 1 details the excitation of an electron (with a photon of energy E_{abs}) from an acceptor defect, A in charge state $q = 1-$, to the CBM. A^0 (charge state $q = 0$) then relaxes into its *equilibrium* geometry (E^1_{rel}) then subsequently emits a photon (E_{em}) forming A^{1-} (in the equilibrium geometry of A^0. A^{1-} then relaxes into its equilibrium geometry (E^2_{rel}) emitting phonons. Situation 2 shows the *capture* of an electron by a donor defect (D in charge state $q = 1+$) from the VBM. After a relaxation (E^1_{rel}) to the equilibrium geometry of D in charge state $q = 0$ (D^0), the defect then undergoes a *non-radiative* emission, usually through the release of phonons, relaxing into the equilibrium geometry of D^{1+} via a relaxation energy: E^2_{rel}.

2.5 VASP – The Vienna *Ab-Initio* Simulation Package

All calculations used in this thesis were carried out using the Vienna *ab-initio* Simulation Package, VASP.[105–108] The code is a plane-wave, periodic boundary conditions code implementing a wide range of computational physics and chemistry applications. DFT, DFT+U, hybrid functionals and PAW pseudopotentials which add to its flexibility. The code also allows the calculation of band structures, density of states, optical properties and the simulation of large systems such as supercells with efficient parallelisation over k-points or bands.

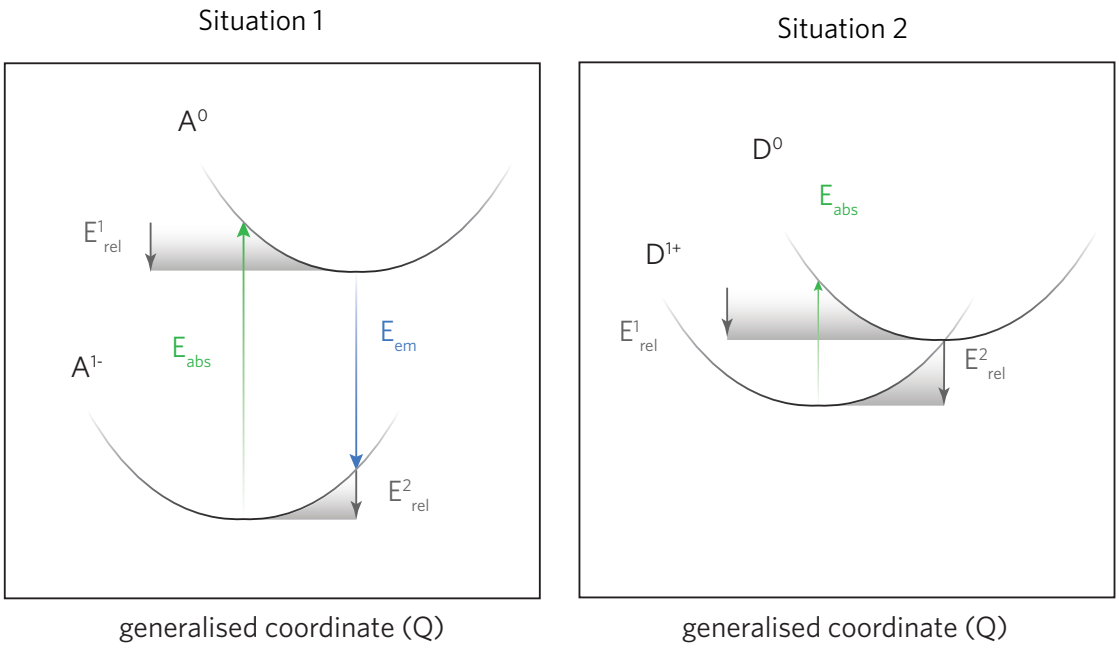

FIGURE 2.7: Configurational coordinate diagrams for two different situations showing the optical transition levels . Situation 1 shows the excitement of an electron from an acceptor defect (A) to the conduction band, whilst situation 2 shows the capture of an electron by a donor (D) from the valence band.

Part II

n-Type Transparent Conductors

Chapter 3

Introduction to *n*-type Transparent Conductors

3.1 Transparent Conducting Oxides

Transparent Conductors (TCs) are a class of semiconductor that are transparent to the highest wavelength of visible light (wavelengths > 3.1 eV) whilst possessing degenerate conductivities. These materials allow for a vast array of applications benefiting modern optoelectronics such as LCD/LED displays for consumer electronics, photovoltaics, self-cleaning windows, gas sensors to name a few. TCs combine two generally mutually exclusive properties; optical transparency usually indicates insulating behaviour i.e. glass (SiO_2) with high resistivities of the order of $10^{10}\,\Omega\,\text{cm}$. The other property is *degenerate* conductivity, such as those seen in metals which are known to have low resistivities ($\sim 10^{-7}\,\Omega\,\text{cm}$) and exhibit opaqueness.[109,110]

The first documented report of a transparent conducting oxide (TCO) was by Karl Bädeker in 1907 with thin films of cadmium oxide (CdO), which were found to possess conductivities of $\sim 10^3\,\text{S}\,\text{cm}^{-1}$.[111] Although research is still carried out on CdO,[112] the high toxicity of Cd means it is unsuitable for industrial production. Other binary TCOs are now known to exist in particular: In_2O_3, SnO_2 and ZnO which have all possess highly desirable properties that make them typically referred to as the '*industry standard*' TCOs.[113–118] TCOs are not limited to binary metal oxides, more recently, $BaSnO_3$ was identified as a high conductivity transparent conductor, which, when doped with La is capable of producing resistivities as low as $5.9 \times 10^{-4}\,\Omega\,\text{cm}$ and high mobilities of $320\,\text{cm}^2\,\text{V}^{-1}\,\text{s}^{-1}$.[26,119,120]

The performance of these materials are measured in terms of their conductivities (σ), resistivities (ρ), carrier mobilities (μ), carrier concentrations (n) and optical transparencies. In_2O_3. For example, when doped with Sn (ITO) or Mo (IMO), In_2O_3 possesses excellent electronic and optical properties such as: resistivities of $\sim 10^{-5}\,\Omega\,cm$, carrier concentrations of $10^{21}\,cm^{-3}$ and optical transparencies $>80\%$.[113–118,121,122] Due to the scarce nature of indium in the earth's crust coupled with its high demand in consumer electronics, concerns have been made about the use of ITO as a viable TCO material for future applications.[123] A recent European report highlighted the supply risk due to $\sim$75% of the Indium originating from China and the fact that it is obtained as a by-product from zinc production, adding concern to price fluctuations and a dependence on imports of indium.[123] A research drive has been led into other more 'earth abundant' materials SnO_2 where Sn is 15 times more abundant than indium and the price is 0.3% of the price per Kg of indium (Figure 3.1).[117,123,124]

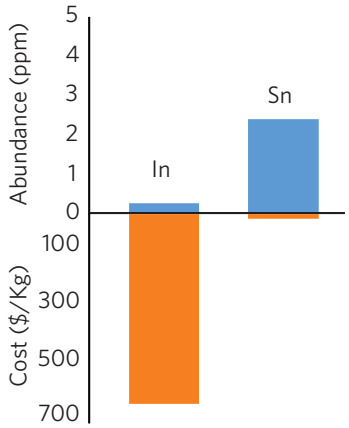

FIGURE 3.1: A graph showing the cost versus abundance of In and Sn. Data is taken from the London Metal Exchange.[124]

3.1.1 Selected Applications

Electronic Displays and Capacitive Touch Screens:

One of the major transparent conductor applications is in portable electronics. The use of transparent conductors as transparent electrodes is the highest value market worth 115.3 billion USD in 2017 and is expected to rise to 177.3 billion by 2027.[125] Ever since the advent of the flat-screen display in the mid-1980s, devices which utilise TCOs have become ubiquitous in everyday life. Figure 3.2 shows a schematic diagram for a liquid crystal display (LCD)

where two TCO electrode layers sandwich the liquid crystal section of the display architecture allowing light to pass through. Other display technologies exist such as light emitting diode (LED) or *organic* light emitting diode (OLED) displays, however, the use of TCOs remains constant as either an electrode or as a vital part of the user input of devices such as tablets or smart-phones. Figure 3.2 also shows a simplified schematic for a *capacitive* touch panel allowing for direct touch input of a display. The main feature of this system is the use of two TCO layers *etched* into lines aligned perpendicularly to each other forming a grid (TCO x axis and TCO y axis). These TCO layers are separated by a separator or dielectric material and can be protected by a glass layer. The device works by detecting the change in capacitance at certain points on the TCO grid and allows for multi-finger input. ITO or Sn-doped In_2O_3 is the material of choice for this application due to the high conductivities, transparency, mobilities and its facile etchability.[114] An alternative to Sn-doped In_2O_3 would need to retain or surpass the optical transparency, conductivities and mobilities of ITO. Such a material would also need to be highly etchable such as ZnO.[114] The amorphous quaternary indium gallium zinc oxide (IGZO) has begun to be seen in new displays within the electronic market.[126,127]

Photovoltaics:

A typical solar cell (photovoltaic) consists of an *n*-type TCO layer coated on glass which is usually Sn-doped In_2O_3 or F-doped SnO_2[115,128,129] allowing light to pass through, a solar absorber material with a band gap of 1–1.6 eV usually consisting of a p-n junction of crystalline silicon doped with B (*p*) or P (*n*) and finally a metal anode contact. Due to the poor absorption coefficients resulting from the indirect band gap of silicon[130,131] new technologies are being sought that increase the efficiencies of the photovoltaic cell. The most recent developments in photovoltaic materials is in the hybrid halide perovskites such as the solution-processable $Ch_3NH_4PbI_3$ or MAPI which has gained efficiencies of 22.1%.[132] The cheap manufacturing and materials cost of the new hybrid halide perovskites requires a similar cheap and facile route to producing the TCO layer and hence is still a major drive of research.

Low Emittance Glass:

The last and arguably the most widely used application is in low-emittance or 'low-E' glass.[115] This technology is widely used in commercial window glass and oven doors allowing heat to be retained whilst retaining optical transparency (Figure 3.2). This works inversely when keeping a room cool by keeping heat out, and absorbing UV light. The use of low-E glass is

also required by current US and European legislation on all new buildings.[115] Passing a current through the TCO layer avoids the condensation of water in the air on a fridge/freezer door. This application was first used in WWII for defrosting the windows of high-altitude bombers.[114] Typically F-doped SnO_2 is used as it can easily be applied in the float glass process[133] and can reduce the heat process by around 75% making it highly desirable for all-glass designed buildings.[91]

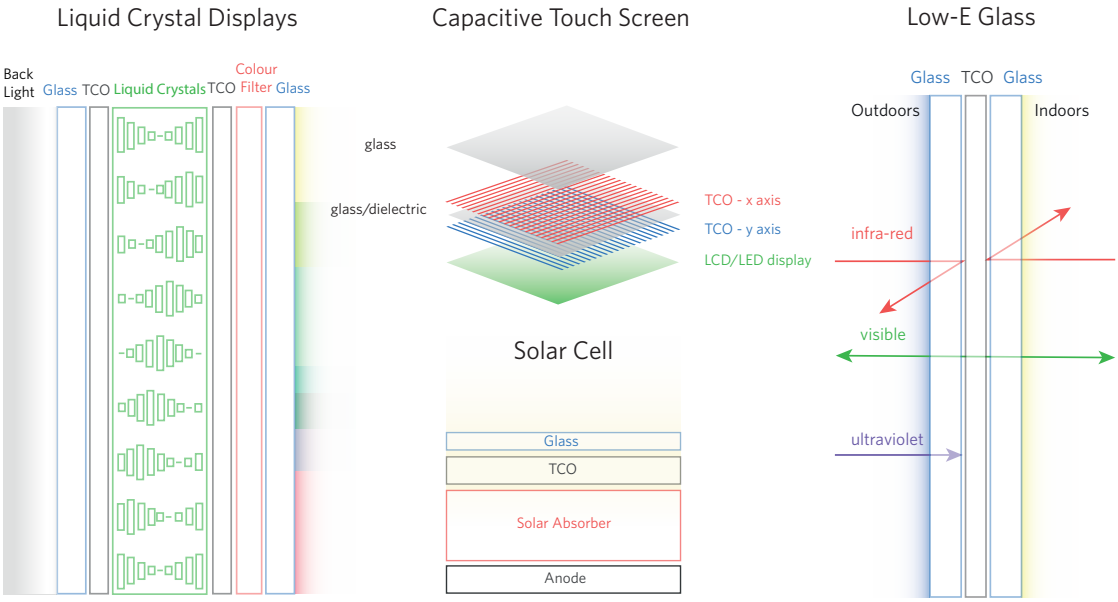

FIGURE 3.2: The common applications of TCOs in the consumer market. These include liquid crystal displays (LCD), capacitive touch screens as used in many portable electronics, solar cells and low-emissivity ('low-E') glass.

3.2 Fundamentals of TCOs

3.2.1 Electronic Structure

Fundamental and Optical Band Gap:

One of the most important parameters in a TC is the magnitude of the optical band gap, E_g^{opt}. The optical band gap is required to have an energy *larger* than the highest wavelength of visible light (3.1 eV) in order to avoid solar absorption and thus haze or colouring; small amounts of haze have been seen to be preferable in photovoltaic devices however.[134–136]

The *optical* band gap of a material is different from the *fundamental* band gap (Figure 3.3(a)) which is classed as the smallest distance between the valence band maximum (VBM) and the conduction band minimum (CBM) . The fundamental band gap can be either *direct* or *indirect* describing the positions of the band minima and maxima in relation to each other in reciprocal space (or *k*-space). An indirect band gap requires additional energy such as a phonon for the promotion of an electron to the conduction band and has been seen to limit the absorption in materials such as Si in photovoltaics.[131] Due to the wide band gap of transparent conductors however, the *nature* of the band gap, whether *direct* or *indirect* is not a major consideration for transparent conductors as photoexcitation of an electron is not as necessary as it is in photovoltaics or photocatalysis.[131,137] Correct band alignment of the CBM and VBM of both the TC and photovoltaic material, however, generally prefers a direct fundamental band gap especially if the difference between the direct and indirect gaps is large. Two notable examples occur in the literature where the fundamental band gap is smaller than the optical band gap; In_2O_3 and CdO. The former, In_2O_3, has an optical band gap of ~3.5-3.73 eV (undoped),[138–140] yet it was shown by Walsh et al. together with a range of X-ray spectroscopies that the fundamental band gap is a forbidden transition.[138] The fundamental band gap (VBM→CBM) was determined to be ~ 2.9 eV with the *optical* dipole-allowed transition occurring from around 0.8 eV below the VBM.[138] A schematic of this is shown in Figure 3.3(b). The dipole-allowed optical transition can also occur just off the VBM to a conduction band directly above which can be seen in Nb_2O_5 polymorphs.[141]

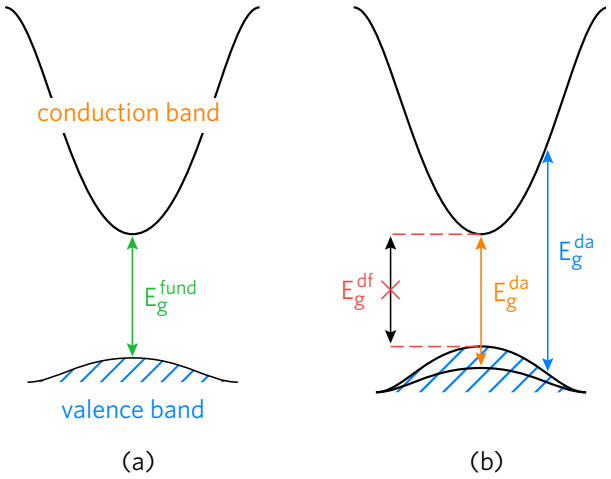

FIGURE 3.3: Two schematics displaying the possible optical band gap. (a) shows a *dipole allowed* transition (E_g^{da}) between the VBM and CBM corresponding to the fundamental band gap . (b) shows the situation where the direct fundamental band gap is symmetry forbidden (E_g^{df}) transitions therefore occur from either below the CBM or from a symmetry point close to the VBM.

Moss-Burstein Shift:

CdO possesses a narrow *indirect* band gap of ~0.84-0.90 eV and a *direct* allowed band gap of ~2.16–2.20 eV.[142–144] These has been verified through HSE06 DFT calculations.[109] When donor-doped, however, CdO possesses a band gap between 3.44–3.61 eV[145–148] due to a 'Moss-Burstein shift'.[149,150] A schematic diagram for this is shown in Figure 3.4 showing the dependence on the optical band gap due to a filling of the conduction band by free carriers. The Moss-Burstein shift can be estimated using free electron theory:

$$E^{\mathrm{BM}} = \frac{\hbar^2}{2m^*}(3\pi^2 n_e)^{\frac{2}{3}} \tag{3.2.1}$$

Where n_e is the electron carrier concentration, $\hbar$ is the reduced Planck constant and m^* is described by:

$$\frac{1}{m^*} = \frac{1}{m^{\mathrm{VBM}}} + \frac{1}{m^{\mathrm{CBM}}} \tag{3.2.2}$$

Where m^{VBM} and m^{CBM} are the effective masses at the valence band maximum (VBM)

and the conduction band minimum (CBM) respectively. The optical band gap is thus:

$$E_g^{\text{opt}} = E_g^{\text{fund}} + E^{\text{MB}} \tag{3.2.3}$$

It was calculated by Burbano et al. that the maximum carrier concentration for CdO was around $4.34 - 5.25 \times 10^{20}\,\text{cm}^{-3}$ matching experimental values of $\sim 5.25 \times 10^{20}\,\text{cm}^{-3}$.[109,145] Similarly it has been shown through theory by Walsh et al. that PbO_2, whilst possessing an indirect band gap of 0.23 eV can be made transparent through high carrier concentrations of the order 10^{21} cm^{-3} and an optical transition from around 0.7 eV *below* the VBM similar to In_2O_3.[151]

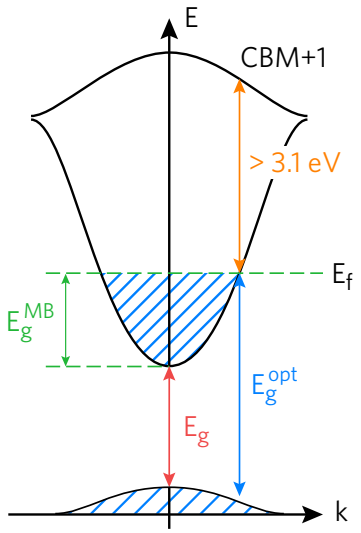

FIGURE 3.4: An illustration of the Moss-Burstein shift (E_g^{MB} whereby the filling of the conduction band with free carriers facilitates a larger optical band gap (E_g^{opt}) than the fundamental one (E_g). E_f is the Fermi level.

Limitations on the Optical Band Gap Due to Free Carriers:

Due to the filling of the conduction band when donor doping, it is important that there is a large enough *secondary gap* (from the CBM to the CBM+1) to avoid intra-band absorptions and thus maintain a high optical transparency (Figure 3.4). The 'industry standard' TCO materials, In_2O_3, SnO_2 and ZnO and $BaSnO_3$ all have large secondary gaps (~4 eV)[152] and can be seen in Figure 3.5. In a recent study by Hautier et al. it was deemed that, whilst beneficial, the absence of a second gap does not cause a significant loss in visible light transmission than

the optical band gap.[152]

The absorption and reflection of free carriers in the conduction band also places a limit on the carrier concentration before visible light excitation occurs. Most TCOs absorb or reflect infrared light due to the free carriers which can be described by the plasmon frequency (ω_p):

$$\omega_p^2 = \frac{ne^2}{m^{CBM}\epsilon_\infty\epsilon_0} \tag{3.2.4}$$

where n and e is the density of free carriers and charge on an electron respectively, m^{CBM} is the effective mass at the CBM (for electrons). ϵ_0 is the permittivity of free space and ϵ_∞ is the high frequency dielectric permittivity of the material. ω_p is thus directly proportional to the carrier concentration n; thus at carrier concentrations towards 10^{22} cm^{-3}, a TCO will incur significant visible light absorption.[116,153,154]

Band Structure:

Other features typical of a high performance TCO can be gleaned from their band structures. Figure 3.5 displays the calculated band structures of the four main TCOs: In_2O_3, SnO_2, ZnO and $BaSnO_3$ as examples (calculation details can be found in Appendix A.1). Aside from the wide optical band gap and second gap (CBM – CBM+1)required for optical transparency, a transparent conductor requires a high conductivity thus highly mobile charge carriers. Equation 3.2.5 shows the dependence on the conductivity (σ) on the mobility (μ) the elementary charge on an electron (e) and the carrier concentration (n).

$$\sigma = \mu e n \quad ; \quad \rho = \frac{1}{\sigma} \tag{3.2.5}$$

The *resistivity* (ρ) of a material is a typically used as a benchmark within transparent conductors which can be determined from the inverse of the conductivity (σ) (Equation 3.2.5).

The mobility of a material depends on the carrier effective mass, m* (see Chapter 2.2.3) which can be determined directly from the band structure. For a TCO to be successfully *n*-type, it must possess *low* effective masses at the conduction band minimum ($\sim 0.3\, m_e$). Figure 3.5 also displays the electron effective masses at the CBM in each direction by the green arrows, and the *mean* electron and hole effective masses are given in Table 3.1. These TCOs all possess large secondary gaps (CBM – CBM+1) of around 4.6 eV, 5.2 eV, 4.9 eV and 4.1 eV

for In_2O_3, SnO_2, ZnO and $BaSnO_3$ respectively meaning that optical transparency is retained with high doping levels.

In Table 3.1, it is clear that the valence band *hole* effective masses are several orders of magnitude larger than the effective masses of electrons at the CBM. This can be explained by the bonding and states that comprise the VBM and the CBM.

TABLE 3.1: The averaged calculated effective masses of electrons and holes at the CBM and VBM respectively for In_2O_3, SnO_2, ZnO and $BaSnO_3$.

	In_2O_3	SnO_2	ZnO	$BaSnO_3$
m_0^{CBM} (m_e)	0.22	0.30	0.33	0.20
m_0^{VBM} (m_e)	14.70	4.82	2.96	4.00

Figure 3.6 show schematic molecular orbital diagrams for each TCO based upon the MO_6 (MO_4 in the case of ZnO) octahedra (tetrahedra) than make up the three-dimensional crystal lattice. In most cases, the VBM is made up of highly localised *non-bonding* O $2p$ states that appear very low in energy giving rise to the high hole effective masses at the VBM, and also limits the ability of *n*-type TCOs in forming high mobility *p*-type TCOs.[25,116,155] The metal d states typically lie very deep in energy, however in TCOs such as ZnO and CdO, the Zn and Cd d orbitals are shallower resulting in a slightly raised VBM and dispersion due to a p–d repulsion.[156] For In_2O_3, SnO_2, ZnO, and $BaSnO_3$ the CBM is made up of metal s states mixing with O $2p$ states giving rise to highly disperse band minima resulting in the low effective masses seen in Table 3.1 and the high conductivities seen in experiment.[120,157] In $BaSnO_3$, the Ba states do not contribute to the CBM, and result in a non-bonding Ba $5d$ band above the CBM.[26]

The resulting electronic structures of the *n*-type TCOs mean that they have very high ionisation potentials and high electron affinities and as such create a defect and doping *asymmetry* and thus cannot be made *p*-type.[25]

3.2.2 Conductivity in TCOs

As the band gap in transparent conductors is too wide for visible light absorption, conductivity is therefore dominated by the formation of point defects, or through doping. A fully

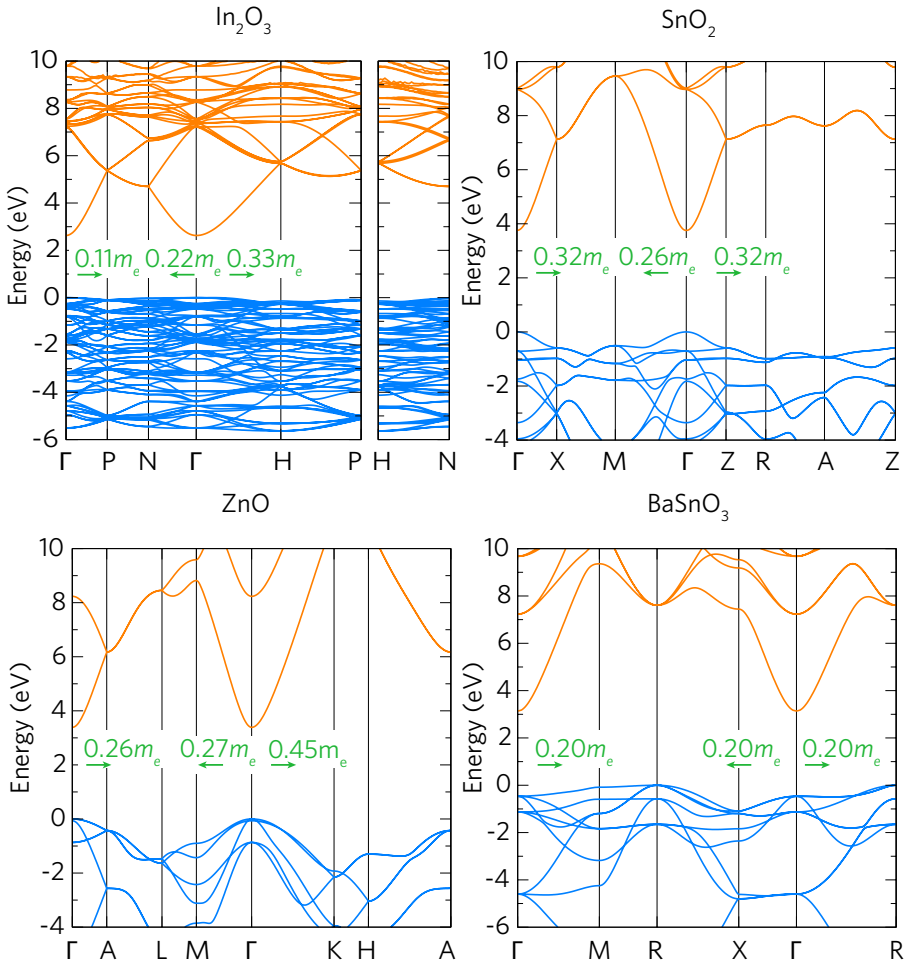

FIGURE 3.5: The calculated band structures of the 'industry standard' TCOs: In_2O_3, SnO_2, ZnO and $BaSnO_3$ (details of the calculations can be found in Appendix A.1). In each case the VBM is set at 0 eV and the valence and conduction bands are depicted in blue and orange respectively. Parabolic effective masses are provided in green for each direction in the Brillouin zone.

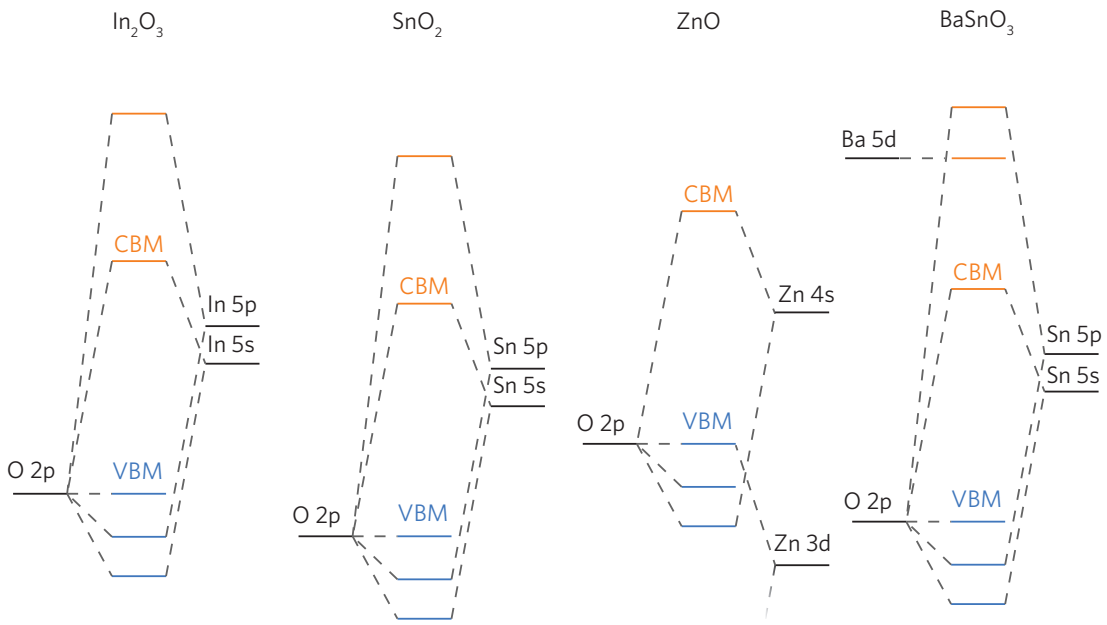

FIGURE 3.6: Simplified molecular orbital diagrams for In_2O_3, SnO_2, ZnO and $BaSnO_3$ showing the mostly non-bonding nature of the VBM and the predominantly Metal *s* states hybridised with O 2*p* states at the CBM giving rise to the high dispersion and low effective masses.

stoichiometric or 'pure' TCO is therefore highly insulating, however in reality the TCOs involve a major degree of *non-stoichiometry*. Defects can be classified firstly as *n* or *p* type defects and secondly as intrinsic or extrinsic. Intrinsic or 'native' defects arise from the inherent non-stoichiometry of a material, and in this case involve vacancies, interstitials or clusters of defects such as Schottky (anion and cation vacancies) or Frenkel pairs (vacancy and an interstitial). Extrinsic defects arise from doping with aliovalent cations or anions. Such examples of highly successful *n*-type doped materials are: F-doped SnO_2 [158], Sn-doped In_2O_3 [159], Al-doped ZnO [160] and La-doped $BaSnO_3$.[27]

In order for a large concentration of a defect to be formed, it must possess a low formation energy, and the enhancement to the conductivity is based upon the ability of the defect to ionise within or close to the appropriate band edges (the VBM for *p*-type defects and the CBM for *n*-type defects). Figure 3.7 shows a schematic for the positions of defect states relative to the band edges. A *deep* defect is highly unfavourable and means that the defect will not be thermally ionised within the lattice of the material. This occurs when the transition level is >0.03 eV of the CBM(VBM) for *n*(p)-type defects which corresponds to $\sim k_B T$ at room tem-

perature. If a defect is deep it can be polaronic in nature (where the charge carrier is bound to lattice relaxations) and as such will follow a hopping mechanism with an activation which determines the conductivity (σ):

$$\sigma \propto \exp(\frac{-E_a}{k_B T}) \tag{3.2.6}$$

where E_a is the activation energy, k_B is Boltzmann's constant and T is the temperature. Conversely, a *shallow* defect is one where the transition level occurs within 0.03 eV of the band edges and thus undergoes *room-temperature* ionisation. The ideal doping situation is where the defect is *resonant* within the conduction band (donors) or the valence band (acceptors) thus ionisation is spontaneous.

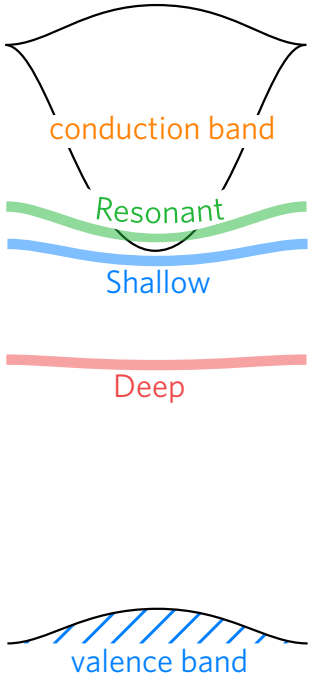

FIGURE 3.7: A schematic diagram displaying the relative positions of the different defect states. A deep defect will occur > ~ 0.03 eV in the band gap and will be difficult to thermally ionise. A shallow defect occurs within room temperature ionisation (~ 0.03 eV) of the CBM (if donor) and a resonant defect occurs within the conduction band so will need no activation energy.

In TCOs the sources of the intrinsic conductivity was thought to exist due to oxygen vacancies (V_O) based upon indirect experimental variations of conductivity oxygen partial pres-

sure.[29,161–165] With the increasing advancement of DFT, it has been found, however, that in In_2O_3, SnO_2 and ZnO that oxygen vacancies are *deep* defects and are thus not likely to account for the high conductivities present in these wide band gap semiconductors.[25,29,161,166,167] Likewise, cation interstitials have been found to be high in formation energy[25,29,168–170], however relatively high carrier concentrations and resistivities of the order of $\sim 10^{-3}\,\Omega\,\mathrm{cm}$ exist when undoped.[117,171,172] As to the reason behind this, it is that fortuitous hydrogen defects, present from fabrication and annealing processes.[25,166,173,174] Density functional theory calculations have proven substitutional (oxygen site) and interstitial hydrogen defects to possess low formation energies and indeed resonant within the conduction band for In_2O_3[175], SnO_2[25] and ZnO[166,173,174]; although hard to detect due to its small size, the presence of hydrogen in In_2O_3 and SnO_2 has since been proven using muon spectroscopy.[176]

In these wide band gap semiconductors there exists a insulator-metal transition with increasing carrier concentration. The critical point for this transition is defined by the Mott criterion (n_c)[177] where:

$$n_c^{\frac{1}{3}}\, a_0^* > 0.26 \tag{3.2.7}$$

where a_0^* is the Bohr radius:

$$a_0^* = \frac{4\pi\epsilon_0\epsilon\hbar^2}{m_e^* e^2} \tag{3.2.8}$$

where ϵ is the dielectric constant of the material, m_e^* is the electron effective mass, $\hbar$ is the reduced Planck's constant, and e is the elementary charge of an electron. The value of 0.26 is calculated from the screened Coulomb potential and is the value at which point the valence electrons are no longer bound by the nuclei. Therefore taking SnO_2 as an example (ϵ=9.86 (ref=178), m_e^*=0.3 m_e), a_0^*=1.74 nm and thus n_c=3.34×10^{18} cm^{-3}. When donor doped (as with fluorine or antimony), however, carrier concentrations of $\sim 10^{20}$ are typically achievable.[115] High carrier concentrations are important for high conductivities in TCOs as shown in equation 3.2.5.

3.3 Doping in SnO_2

SnO_2 crystallises in the rutile ($P4_2/nmn$) structure and possesses both high optical transparency and conductivities when donor doped as well as desirable qualities such as earth abundance, high chemical and thermal stability as well as high infra-red reflectivity.[153,179–181] These properties combine to make SnO_2 highly attractive for use in optoelectronic applications such as low-emissivity windows, solar cells and electronic displays.[115,133,182–188] Compared to indium, Sn is both cheaper and more abundant making the possibility of low cost efficient electronics (Figure 3.1). In order to compete with Sn-doped In_2O_3, doped SnO_2 must be capable of producing figures of merit as low as $\sim 10^{-5}\,\Omega$cm, carrier concentrations exceeding 10^{21} cm^{-3} and high visible light transparency (>90 %).[189–192]

When undoped, non-stoichiometric SnO_2 has resistivities of $\sim 10^{-2} - 10^{-3}\,\Omega$cm[172], whereas when donor doped, resistivities of $\sim 10^{-4}\Omega$cm[115,193–198] are achievable. Successful *n*-type doping via a substitution at either the six-coordinate Sn site or the three-coordinate O site by an element with a higher oxidation state (5+ for Sn site and 1- for O site) should allow for an increase in mobilities and conductivities.

Thin films doped with with fluorine or antimony display resistivities of $\sim 10^{-4}\,\Omega$cm and mobilities of 10-25 cm^2 V^{-1} s^{-1}[188,199–207] and can be made by a variety of experimental deposition processes such as: pulsed laser deposition[208–210],spray pyrolysis[211–214], sol-gel[215–219] and commercially via chemical vapour deposition (CVD) techniques.[188,201–203,220] However, despite their versatility, these dopants are inherently self-limiting.

The high levels of conductivity in both FTO (fluorine doped tin oxide) and ATO (antimony doped tin oxide) is due to the dominant *n*-type defect being substitutional F or Sb (F_O[221] and Sb_{Sn}[38,222]). By increasing the dopant concentration it is expected that there will be a linear increase in the conductivity due to the excess electrons in the system, however, towards higher doping levels the conductivity is reported to decrease.[180,195,203,214,221,223] It is debated in the scientific literature that that interstitial fluorine (F_i) is the reasoning behind this, thereby making F a *self-limiting* dopant.[221,224–227]

Sb doped SnO_2 undergoes a similar self compensation mechanism arising from the observed multivalency of Sb (Sb^{3+} and Sb^{5+}). From both Mössbauer spectroscopy[228–230] and XPS studies,[231,232] both 3+ and 5+ oxidation states are observed. The lower resistivities seen ($\sim 6\times10^{-4}\,\Omega$cm *eg.*[204]) are only possible when the majority of Sb dopant is in the 5+ oxidation state. It is thought that upon increased incorporation, Sb^{3+} segregates to the surface act-

ing as an acceptor, whilst the majority of Sb^{5+} remains in the bulk acting as a donor.[228,229,233] DFT studies have explored the multivalency of ATO showing that ~0.4-0.9eV above the CBM Sb_{Sn}^{1-} forms (indicative of Sb^{3+}), effectively trapping charge.[222] Additionally, extended X-ray absorption fine structure (EXAFS) has suggested the clustering of Sb^{3+} and an oxygen vacancy leading to a similar trapping of electrons.[234,235]

An intuitive way of choosing new dopants is to assess other elements of both group 15 and 17 in the periodic table. These have been studied, but not extensively and involve P, Bi and As[38,222] and the remaining halides; Cl, Br and I.[195,236–239] A successful replacement requires a similar ionic radii to Sn or O for a low formation energy, be a *resonant* donor and not suffer from oxidation state ambiguity or self compensation via competing interstitial defects. Despite unintentional Cl doping in thin films of SnO_2 through the use of $SnCl_2$ or $SnCl_4$ precursors, intentionally Cl-doped SnO_2 suffers higher resistivities to FTO, similarly with Br.[195,238] This is to be expected due to the size difference between the halides and oxygen (the ionic radii of Cl, Br and I are 33% 44% and 62% larger than O respectively)[240] and can be seen in the longer growth rates required.[236] Other group 15 dopants than Sb have been explored *n*-type donors in SnO_2. P has been explored as such a dopant[236,241] however, the resistivities are of the order $7 \times 10^{-3}\,\Omega\,\text{cm}$. P is known to be amphoteric thus it is possible under certain conditions for P to act as an acceptor.

Nb is a 5+ dopant that proves to be a highly conductive dopant in transparent anatase TiO_2 thin films.[33] In SnO_2, however, Nb doping gives rise to high resistivities ($\sim 10^{-2} - 10^{-3}\,\Omega\,\text{cm}$) and low carrier concentrations ($\sim 10^{19}\,\text{cm}^{-3}$) despite the array of different deposition techniques used.[242–254]

Recently, Ta doped SnO_2 have gained an interest as thin films have shown resistivities as low as $1.1 \times 10^{-4}\,\Omega\,\text{cm}$ (comparable to In_2O_3) and much higher electron mobilities 50-84 $\text{cm}^2\,\text{V}^{-1}\,\text{s}^{-1}$.[194,255] Highly conductive thin films of SnO_2:Ta has been made via MOCVD[193,256,257] (metal-organic chemical vapour deposition) and PLD[194,255,258] (pulsed laser deposition), spray-coatings[259], magnetron sputtering[260,261] and sputtering techniques.[262,263] A recent screening on dopants in SnO_2 has shown that both Nb and Ta are resonant donors, donating a valence electron into the conduction band,[264] however as to the reasoning behind the vastly different electronic properties seen in experiment between the two dopants (both with ionic radii of 0.69 Å[240]) has yet to be elucidated.

Chapter 4

The Search for the Optimum Dopant in SnO_2

4.1 Bulk Electronic Properties and Intrinsic Defects

4.1.1 Structural and Electronic Properties

Rutile SnO_2 crystallises in the $P4_2/mnm$ crystal structure (Figure 4.1) and consists of an array of edge sharing SnO_6 octahedra where the oxygen atoms have a trigonal planar coordination (to three Sn atoms). Table 4.1 displays the structural properties and fundamental band gap of SnO_2 as calculated in this work and elsewhere using the PBE0 hybrid functional[23,265] and compared to experiment. Full calculation details are found in Appendix A.1.

TABLE 4.1: The calculated lattice parameters, bond lengths and direct fundamental band gap (E_g^{dir}) of rutile SnO_2 as calculated using the PBE0 functional[23,265] and compared to previous theory[24,25,264,266] and experiment.[267–270]

	a=b (Å)	c (Å)	Sn-O (Å)	E_g^{dir}
This Work	4.74	3.19	2.05, 2.06	3.64
PBE0 (prev.)	4.74–4.76[25,264]	3.19[25,264,266]	.....	3.60[25,264], 3.59, 3.67[24,266]
Experiment	4.74[267,268]	3.19[267,268]	2.05,2.06[267,268]	3.60,3.68[269,270]

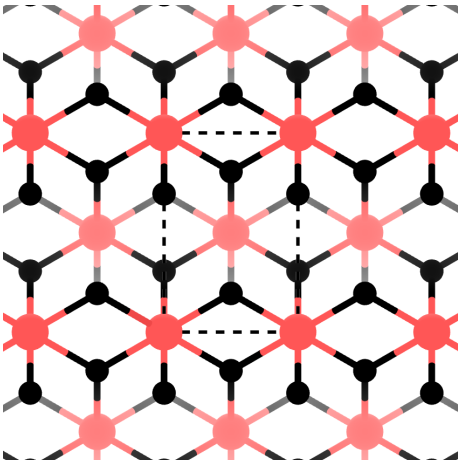

FIGURE 4.1: The conventional cell of SnO_2 as viewed along (010). Sn and O are portrayed as the red and black spheres respectively.

Figures 4.2(a) and (b) show the calculated total and partial electronic density of states (DOS) and the band structure of rutile SnO_2 respectively. In Figure 4.2(a), the VBM is made up primarily of O $2p$ states mixed with some Sn $4d$ states as is typical of the non bonding nature of most binary TCOs (see Chapter 3.2.1). The CBM (inset), however, is formed primarily of Sn $5s$ states mixing with O s and p states. These results are in keeping with other hybrid DOS calculations in the literature.[25,271]

The band structure of SnO_2 in Figure 4.2(b) displays the flat bands of the valence band echoing the localised nature of the O $2p$ states that dominate the VBM with effective masses of 5.16, 4.13 and 5.16 m_e from Γ–X, Γ–M and Γ–Z respectively. The fundamental band gap of SnO_2 is a direct transition at Γ with a magnitude of 3.64 eV matching well to previous hybrid calculations and experimental values (Table 4.1.[24,266,269,270] A further gap of around 5.22 eV is present between the CBM and the next highest band at Γ (CBM+1) allowing for the retention of optical transparency when heavily donor doped.[152] The effective masses at the CBM, are 0.32, 0.26 and 0.32 m_e for the $\Gamma - X$, $\Gamma - M$ and $\Gamma - Z$ directions respectively. This results in a mean electron effective mass of 0.3 m_e which matches experimental determinations of the effective mass of SnO_2 ($\sim$ 0.30–0.33 m_e).[272–274]

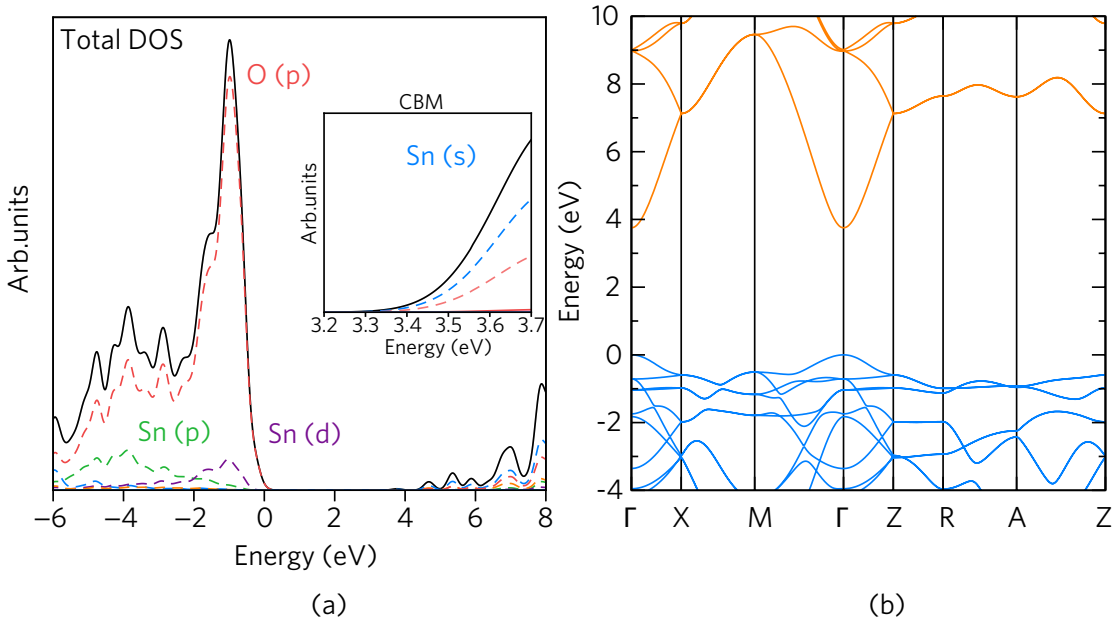

FIGURE 4.2: The bulk density of states of SnO_2 and the band structure. In each panel the VBM is set at 0 eV and in the DOS, a zoomed in section of the CBM is shown inset. In the band structure, the valence bands are depicted in blue and the conduction bands in orange.

4.1.2 Intrinsic Defects

The dominant intrinsic defects in SnO_2 (as determined from previous theory[25]) were calculated using a $2 \times 2 \times 2$ supercell expansion of the SnO_2 conventional cell. Within the SnO_2 lattice, the dominant acceptor and donor defects were found to be V_{Sn} and V_O respectively and are shown with their corresponding transition levels in Figure 4.3.

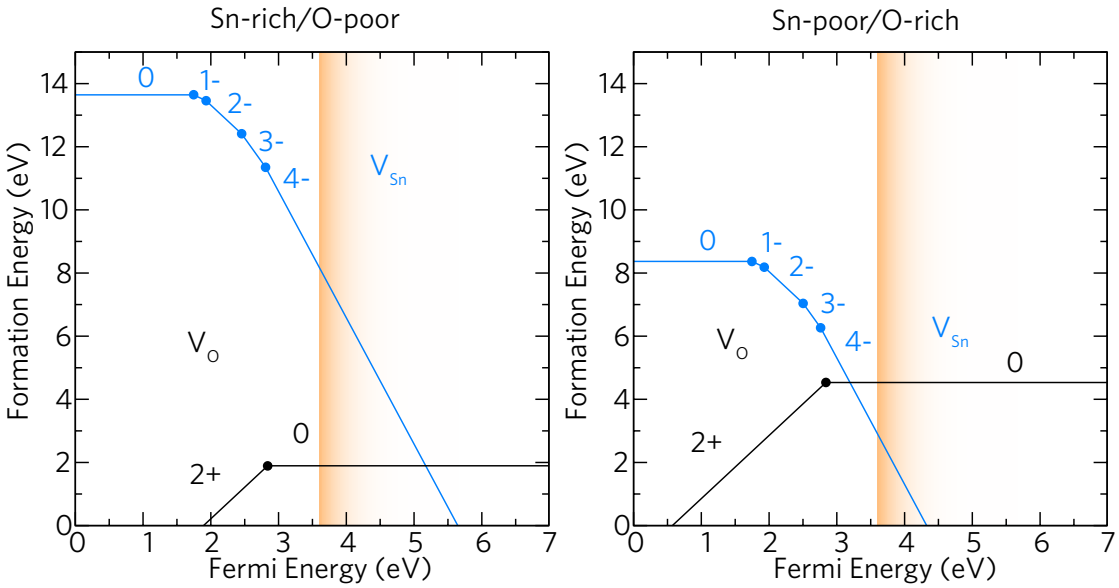

FIGURE 4.3: The thermodynamic transition levels for the dominant intrinsic defects, V_{Sn} and V_O under *Sn-rich/O-poor* and *Sn-poor/O-rich* conditions. In each panel, the Fermi level ranges from the VBM (0 eV) to around 3.4 eV above the CBM (at 3.6 eV). The conduction band is portrayed by the graded orange area.

V_O:

V_O acts as a *deep* donor under both growth conditions. When in the neutral charge state, V_O incurs formation energies of 1.89 eV and 4.53 eV under *Sn-rich/O-poor* and *Sn-poor/O-rich* conditions respectively. V_O is a 'negative-U' defect (see Section 2.4) transitioning from the +2 charge state to the 0 (neutral) charge state around 0.76 eV *below* the CBM. As such, V_O is not expected to contribute largely to the conductivity in nominally undoped SnO_2 and is consistent with previous hybrid theory calculations[28,29,161,275] and experimental observations.[164,176] The negative-U behaviour of V_O is observed in other wide band gap metal oxides such as ZnO[29,276–278] and $BaSnO_3$.[26] The partial electron charge density for V_O in the neutral charge state is shown in Figure 4.4(a). Here, the electron density is shown to be highly localised at the vacancy centre as expected from the deep nature of the defect.

V_{Sn}:

V_{Sn} acts as an *ultra deep* p-type defect which can trap four electrons. The neutral charge state of V_{Sn} possesses a high formation energy of 13.64 eV and 8.37 eV under *Sn-rich/O-poor* and *Sn-poor/O-rich* conditions respectively. Figure 4.4(b) shows the partial charge *hole* density

of the neutral charge state of V_{Sn} depicting the localisation of four holes in surrounding O $2p$ orbitals. A similar localisation can be seen hybrid calculations on V_{Zn} in ZnO.[277,279] The 0/1-, 1-/2-, 2-/3-, 3-/4- transition levels occur in the band gap of SnO_2 at Fermi energies of 1.75 eV, 1.93 eV, 2.45 eV and 2.81 eV above the VBM respectively. The *ultra deep* nature and high formation energies present mean that V_{Sn} does not contribute to *any* intrinsic *p*-type conductivity in SnO_2. These results are consistent with previous theory.[28,29,161,275] V_{Sn}^{4-} compensates V_O around 1.57 eV above the CBM under *Sn-rich/O-poor* conditions and around 0.40 eV *below* the CBM under *Sn-poor/O-rich* conditions.

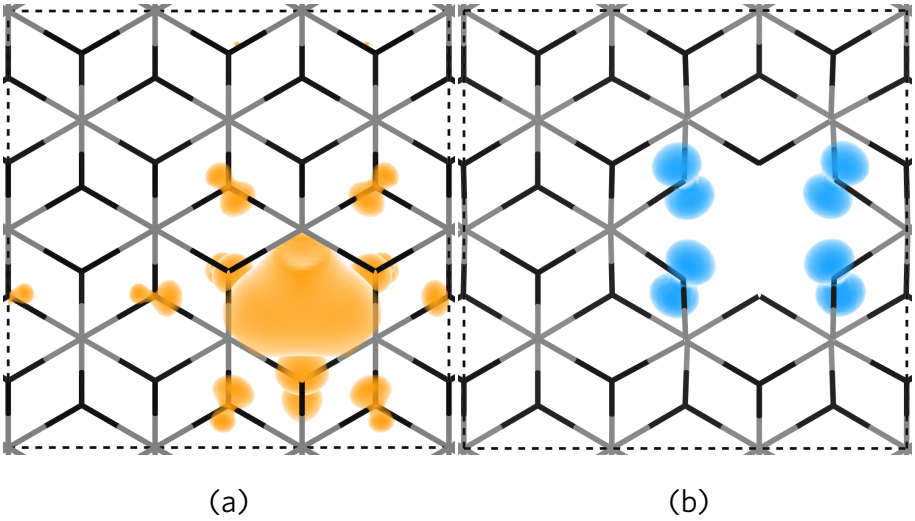

FIGURE 4.4: The partial charge densities for (a) V_O and (b) V_{Sn} as viewed along (010). The SnO_2 lattice is depicted with a wire-frame model with Sn=grey and O=black whilst the electron and hole partial charge densities are shown in orange and blue respectively. The hole density is plotted from 0-0.02 eV Å^{-3} whilst the electron density is plotted from 0-0.005 eV Å^{-3}.

4.2 Self-Compensation in F-Doped SnO_2

Experimental Fabrication of F-doped SnO_2 thin films were obtained by NSG Group.[91] The subsequent analysis was carried out by Mr Jack E. N. Swallow in the Group of Prof. Timothy D. Veal at the University of Liverpool. The experimental work has been reproduced with their permission. Details of the experimental and theoretical methodologies are included in Appendix A.2.
This work has been accepted and published in Advanced Functional Materials. Figures from this paper have been adapted for use in this section.

Fluorine is arguably the most widely used *n*-type dopant in SnO_2 due to its high conductivity large range of deposition methods ; in particular, facile and scalable methods such as chemical vapour deposition.[188,199–203] as used in industry. Fluorine-doped SnO_2 (FTO) is a material which consists of a heavy incorporation of F into SnO_2 whilst retaining the rutile SnO_2 structure. Despite the resulting low resistivity values of $< 4\times10^{-4}\,\Omega\,cm$[188,199–203], above a certain doping concentration, the resistivity increases. This has been postulated through DFT and X-ray diffraction studies to be due to the formation of interstitial fluorine.[221,224–227] This section will focus on the thermodynamic basis behind the degradation mechanism in F-doped SnO_2.

4.2.1 Understanding the Role of Fluorine Species in SnO_2

The calculation of the defect formation energies of a plausible range of fluorine related species were considered alongside the dominant intrinsic defects within the SnO_2 lattice. The transition level diagram for FTO is shown in Figure 4.5 for the *Sn-rich/O-poor* and *Sn-poor/O-rich* chemical potential limits; included in this diagram is the simulation of the defects at the experimental synthesis temperatures and pressures using the oxygen partial pressures at *900K,1atm*. The fluorine species considered in this study were substitutional F (F_O), interstitial F (F_i) and a fluorine substitutional-interstitial pair ($[F\text{-}F]_O$). The latter species ($[F\text{-}F]_O$) has been postulated through theory at high concentrations and through differences in the lattice parameters in experiment.[221,224,225]

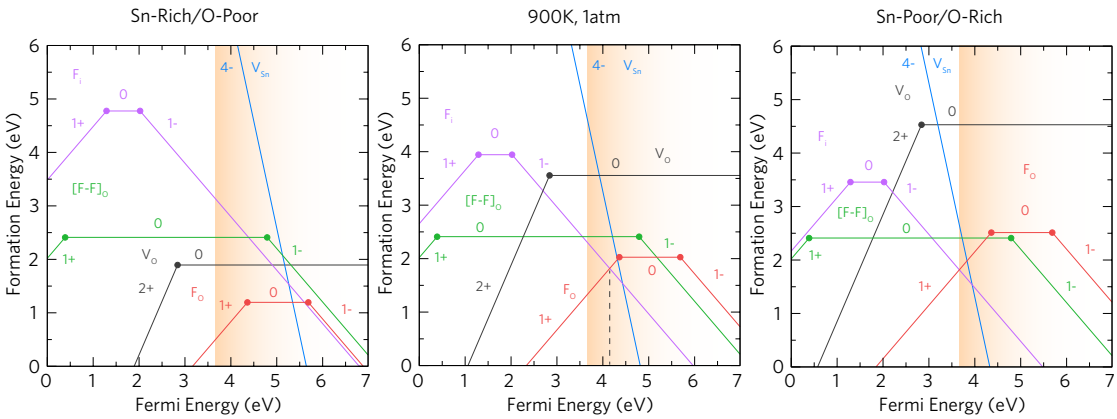

FIGURE 4.5: The transition levels for fluorine doped SnO_2 under *Sn-rich/O-poor*, *900K,1atm* and *Sn-poor/O-rich* growth conditions. The Fermi level ranges from the VBM (0 eV) to ~ 3.4 eV above the CBM. The graded orange area depicts the conduction band.

F_O:

Under all growth conditions, substitutional fluorine (F_O) possesses a low formation energy and acts as a *resonant* donor with the 1+/0 transition level occurring ~ 0.76 eV above the CBM. In the neutral charge state, F_O has formation energies of 1.19 eV, 2.03 eV and 2.51 eV under *Sn-rich/O-poor*, *900K,1atm* and *Sn-poor/O-rich* conditions respectively. F_O is thus expected to be highly soluble under a range of fabrication conditions due to the low formation energies under thermodynamic equilibrium. Figure 4.6(a) shows the partial charge electron density for F_O^0 showing the delocalisation of electron density in the conduction band, consistent with its thermodynamically *resonant* behaviour in tin dioxide. Negligible distortions to the rutile lattice are observed accounting for the low formation energies. F_O undergoes a further transition level (0/1-) around 2.09 eV above the CBM. In this scenario, the 1- charge state corresponds to an extra electron *donated* to the conduction band and thus is not expected to be a 'true' charge state. It is not likely that the 1- charge state will be reached, however, due to compensation from V_{Sn} around 1.75 eV above the CBM under *Sn-rich/O-poor* conditions or by F_i under *900K,1atm* and *Sn-poor/O-rich* conditions. Under the most *Sn-rich/O-poor* conditions it is likely that the Fermi level will be trapped around 0.76 eV above the CBM where the 1+/0 transition level occurs, however these conditions are likely not to be achievable in real-life situations.[28,90]

F_i:

From our calculations, interstitial fluorine (F_i) was found to be an *ultra deep* donor and acceptor species under all growth regimes with a 1+/0 transition level and 0/1- transition level occurring ~ 2.30 eV below the CBM and 2.02 eV *above* the VBM respectively. Upon relaxation of the supercell, F_i was found to distort from the 'ideal' interstitial site towards a lattice oxygen position thereby displacing it (this can be seen for F_i^{1-} in Figure 4.6(b)). F_i^0 possesses reasonably high formation energies of 4.78 eV, 3.94 eV and 3.46 eV under *Sn-rich/O-poor*, *900K,1atm* and *Sn-poor/O-rich* conditions respectively. Under the experimental growth conditions at *900K,1atm* and under the extreme *Sn-poor/O-rich* limit, interstitial F (F_i^{1-}) begins to compensate substitutional F (F_O^{1+}) at 0.50 eV (shown by the dashed black line) and 0.02 eV *above* the CBM respectively. Fluorine in SnO_2 thus follows a *self-compensation* mechanism. Thus at the Fermi level, each electron donated by substitutional F is accepted by interstitial F and is thus malignant to the conductivity. Figure 4.6(b) also displays the partial electron charge density of F_i^{1-} showing the highly localised electron density in a *p*-orbital on the F_i and on the two opposite O *p*-orbitals thus trapping charge. A similar self compensation mechanism has been seen in F-doped anatase TiO_2.[280]

$[F\text{-}F]_O$:

$[F\text{-}F]_O$ is a substitutional-interstitial pair, which has been postulated theoretically at high concentrations and through simple changes in the lattice parameters observed in experiment.[221,224,225] From our calculations, this defect complex possesses a relatively high formation energy and acts as an ultra deep donor and acceptor with 1+/0 and 0/1- transition levels lying around 3.2 eV *below* the CBM and 3.9 eV *above* the VBM respectively. A recent paper by Yang et al.[281] proposed that the rise in resistivity seen in FTO is due to the formation of $[F\text{-}F]_O$ and not due to a self-compensation mechanism by F_i as predicted here. However, in this work the use of the HSE[31] functional with 32% of HF exchange is used and a Γ-point only sampling was used. The authors also only consider the defect states at the chemical potential extremes (i.e. *Sn-rich/O-poor* and *Sn-poor/O-rich*) which is rarely a truthful description of the experimentally achievable conditions.[28,90]

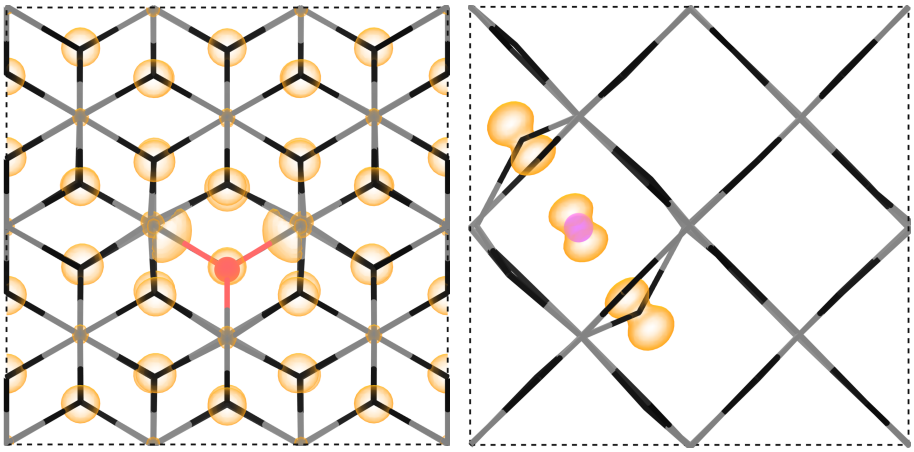

FIGURE 4.6: The partial charge electron density for (a) F_O^{1+} showing the delocalisation of electron density (orange) as viewed along (010) and (b) F_i^{1-} showing the *localisation* of electron density in *p*-orbitals around the interstitial F as viewed along (001) . The SnO_2 lattice is depicted using a wire-frame lattice where Sn=grey and O=black whilst substitutional and interstitial F are depicted as red and pink spheres respectively. The electron density isosurface is plotted from 0-0.001 and 0-0.02 eV Å^{-1} for (a) and (b) respectively.

4.2.2 Experimental Verification

Experimental thin films were fabricated by Pilkington NSG group[91] via atmospheric pressure chemical vapour deposition (APCVD) on glass at *900K,1atm* with varying doping concentrations. Figure 4.7(a) shows the transport mobilities of the FTO samples as a function of carrier concentrations. The dominant mobility reduction mechanism in degenerately doped semiconductors is due to *ionised* impurity scattering.[282,283] Other scattering mechanisms (described Appendix A.3) are taken into account producing a 'combined scattering' limit as shown by the dashed green line in Figure 4.7(a). What is seen from the FTO samples is that the measured mobility is roughly *three times* lower than the theoretical limit, suggestive of a compensation mechanism. These results are in keeping with other Hall effect mobility modelling by Haitzema et al.[284] The compensation ratio, K, is simply the ratio between the number of acceptors to dopants present in the system. This is incorporated into the combined scattering model resulting in a value of ~0.49. This value corresponds well to the assumption that a donor is compensated for by an acceptor with charge Z_D=+1 and Z_A=-1 respectively (where Z_A and Z_D equal the overall charge on the acceptor and donor defect respectively). Figure 4.7(b)

details the measured optical absorption coefficient of the FTO thin film with a carrier concentration, $n = 4.27 \times 10^{20}\,\mathrm{cm}^{-3}$. The optical band gap is determined to be ~ 4.20 eV through a linear extrapolation of α^2 versus the photon energy (blue line). By including the effects of valence band dispersion on the absorption, the Fermi level is calculated to be found around 4.10 eV above the VBM. This point is in excellent agreement with the crossing point of F_O^{1+} and F_i^{1-} at *900K,1atm* in Figure 4.5 calculated using PBE0. These experimental results confirm the theoretical prediction of defects in F-doped SnO_2 and the self-compensation mechanism.

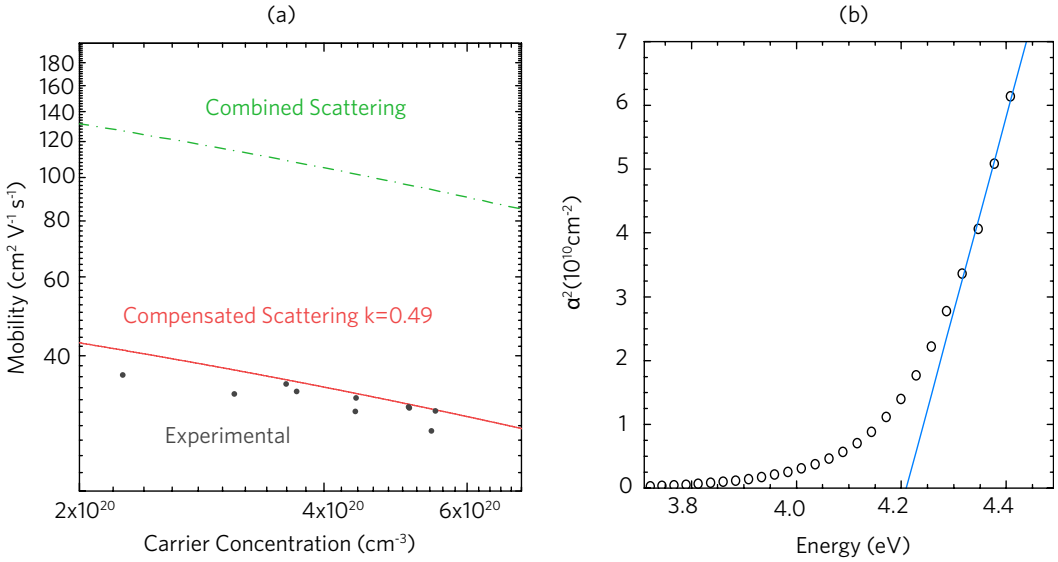

FIGURE 4.7: (a) shows the transport data and simulation for Hall mobility vs carrier concentration in F-doped SnO_2. The data shows that the experimental data follows a *compensated scattering* route (red line) indicating self compensation. (b) shows the optical absorption data with a linear extrapolation estimating the absorption onset. The optical gap of 4.21 eV corresponds to a Fermi level position of 4.10 eV above the VBM.

4.3 The Limitations of Antimony

Details of the theoretical methodology are included in Appendix A.2.
The work in this section is in preparation for publication.

From the self-compensation of FTO it is clear that to find a new dopant two logical steps exist. Firstly the oxygen site in SnO_2 can be doped with other halides such as Cl, Br or I. Due to the larger ionic radii of Cl, Br and I, however it is expected that these dopants will be less soluble than F and is seen in the lower carrier concentrations and higher resistivities[195,236–239] The second solution is to dope the Sn site, in particular with Sb (ATO) which has produced highly favourable resistivities and mobilities competitive with FTO.[204–207] As with FTO, numerous deposition methods are achievable for producing thin films of ATO such as magnetron sputtering[207], aerosol-assisted CVD[205] (AACVD) and spray-pyrolysis[285] producing resistivities as low as 5.8×10^{-5}.[285] As with FTO, however, at high doping concentrations the resistivity rises and an increasing incorporation of Sb^{3+} is seen alongside Sb^{5+}. To date, there has been speculation in the experimental literature as to the mechanisms that harm the conductivities and mobilities of Sb-doped SnO_2 citing surface segregation and the formation of defect complexes such as $[Sb_{Sn}+V_O]$.[228,229,233–235] In this section, the thermodynamic properties of likely Sb-related defect species are calculated in order to aide the search for the optimum dopant in SnO_2.

4.3.1 The Role of Sb Species in SnO_2

The thermodynamic transition levels for Sb-doped SnO_2 are shown in Figure 4.8 under *Sn-rich/O-poor* and *Sn-poor/O-rich* conditions taking into account the transitions in the conduction band. V_{Sn} and V_O are included in this analysis in order to understand any intrinsic compensation mechanisms.

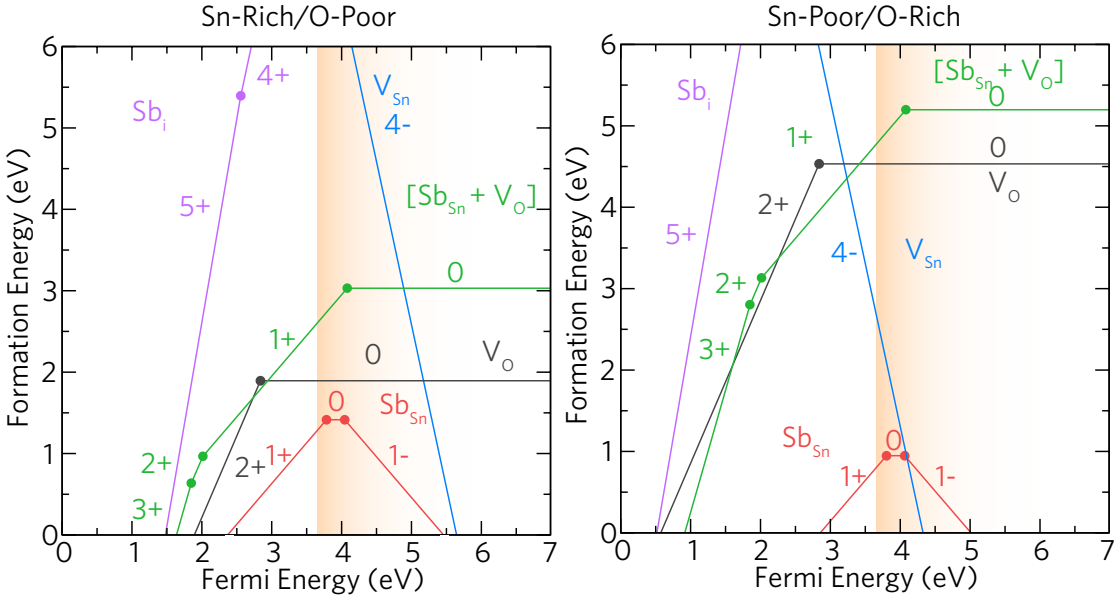

FIGURE 4.8: The transition level diagrams for Sb-doped SnO_2 under *Sn-rich/O-poor* and *Sn-poor/O-rich* conditions. The Fermi level ranges from the VBM (0 eV) to around 3.4 eV above the CBM (3.6 eV). The conduction band region is depicted as the graded orange area.

Sb_{Sn}:

Sb_{Sn} incorporates into the SnO_2 lattice as a low formation energy *resonant* one electron donor as expected by replacing Sn^{4+} with Sb^{5+}. The 1+/0 transition level occurs around 0.15 eV above the CBM and possesses formation energies of 1.42 eV and 0.95 eV (in the neutral charge state) under *Sn-rich/O-poor* and *Sn-poor/O-rich* conditions respectively. Interestingly, these results show that under typically *n*-type preferable conditions (*Sn-rich/O-poor*), Sb_{Sn} is *higher* in energy than under the usually *p*-type favourable conditions (*Sn-poor/O-rich*). The reason behind this is due to the lower μ_{Sb} under *O-rich* conditions and therefore the availability of free Sn sites. Comparing substitutional Sb to substitutional F, it is clear that Sb_{Sn} has a lower formation energy than F_O and is thus likely to be more soluble than fluorine. This is to be expected due to the similarity in ionic radii of Sb to Sn (Sn=0.69 Å; Sb^{5+}=0.6 Å; Sb^{3+}=0.79 Å).[240] Minimal distortions to the rutile lattice are also seen to occur over all charge states with Sb-O bond lengths increasing by just 1.5% (from ~2.0 Å to ~2.03 Å) from the neutral to the 1- charge state. Sb_{Sn} also undergoes a further transition level, 0/1- around 0.41 eV above the CBM which involves an extra electron being trapped in the Sb 5*s* orbital forming Sb^{3+}. Figure 4.9(a) and b display the partial electron charge density for Sb^{0}_{Sn} and Sb^{1-}_{Sn}. In

the neutral charge (Sb^0_{Sn}) state a delocalisation of electron density is present on the lattice oxygens and in the 5*s* orbital on Sb. When in the 1- charge state, Sb_{Sn} the extra electron localised in the 5*s* orbital on Sb is clearly visible alongside the delocalisation of electron density on the O and Sn states that make up the CBM. Previous hybrid DFT calculations on SnO_2:Sb support the low formation energy *resonant* donor nature of substitutional Sb.[38,222,246] Lany and coworkers, however, propose that Sb is in fact a negative-U defect whereby the neutral charge state disproportionates into the 1+ and 1- charge states in contrast to this work.[222] The differefnce between this work and that done by Lany and coworkers could be due to the use of HSE06 functional to describe SnO_2 as well as the lack of band filling correction which can lower the energies of resonant defects such as Sb_{Sn}.

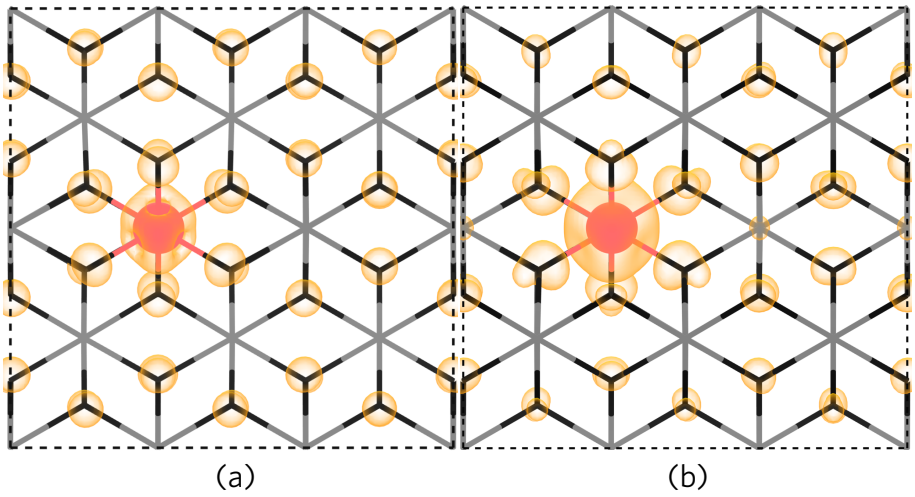

FIGURE 4.9: The partial charge electron densities for (a) Sb^0_{Sn} and (b) Sb^{1-}_{Sn} as viewed along (010). The SnO_2 lattice is depicted by the wire-frame model where grey=Sn and black=O, whilst Sb is shown as a red sphere. The electron charge isosurface (orange) is plotted from 0-0.005 eV atom^{-1}.

It is expected that no compensation from intrinsic defects will occur as under *Sn-poor/O-rich* conditions, V^{4-}_{Sn} crosses Sb^0_{Sn} around 2.05 eV above the CBM. It is therefore likely at chemical potentials realisable in experiment that the conductivity and mobility in ATO will be limited via the formation of the neutral and 1- charge states.

Sb_i:

Under both extreme chemical potential limits it is unlikely that any interstitial Sb will be seen to form. This is due to the very high formation energies where, under *Sn-rich/O-poor* and *Sn-poor/O-rich* conditions, Sb_i^0 possesses formation energies of 9.40 eV and 14.20 eV respectively. Sb_i, is however, a resonant donor defect with a 1+/0 transition level occurring around 0.60 eV above the CBM. Further transition levels are present within the band gap at Fermi levels of 1.08 eV, 0.75 eV, 0.30 eV and 0.03 eV *below* the CBM for the 5+/4+, 4+/3+, 3+/2+ and 2+/1+ transitions respectively.

[Sb_{Sn}+V_O]:

The clustering of Sb_{Sn} and V_O has been suggested through extended X-ray absorption fine structure (EXAFS) experiments thus producing Sb^{3+} (two electrons in a lone pair) and a trapped electron in the oxygen vacancy.[234,235] In order to determine whether these two *n*-type defects do in fact cluster, two configurations of [Sb_{Sn}+V_O] were calculated in a 'near' (both defects neighbouring each other) and a 'far' (both defects ~ 8 Å apart) configuration. It was found from our PBE0 calculations that the 'near' configuration attained the lowest formation energy (by ~ 0.40 eV) and a binding energy (E_{BE}) of 0.78 eV was calculated through:

$$E_{BE} = E^{[Sb_{Sn}+V_O]} + E^{host} - E^{Sb_{Sn}} - E^{V_O} \tag{4.3.1}$$

With increasing dopant incorporation, it is therefore likely that the association of a substitutional Sb with an oxygen vacancy will be facilitated. Usually, Coulombic effects would dictate that two *n*-type defects such as these would repel each other, however, this configuration is favourable due to the stabilisation of a lone pair on the Sb_{Sn}. Under both *Sn-rich/O-poor* and *Sn-poor/O-rich* regimes, [Sb_{Sn} + V_O] acts as a shallow donor with a formation energy 3.03 eV and 5.20 eV respectively. The defect complex acts as a one electron donor with the 1+/0 transition level occurring at 0.48 eV above the CBM. Two further transition levels exist in the band gap: the 3+/2+ and 2+/1+ at 1.75 eV and 1.59 eV below the CBM respectively. Figure 4.10(a), (b) and (c) depicts the partial charge electron density for $[Sb_{Sn} + V_O]^0$, $[Sb_{Sn} + V_O]^{1+}$ and $[Sb_{Sn} + V_O]^{2+}$ respectively. In the neutral charge state ($[Sb_{Sn} + V_O]^0$), two electrons are stabilised in a lone pair on Sb with the additional electron localised in V_O. These results are consistent with the EXAFS studies carried out on ATO in which 5-coordinate Sb is seen indicating

the removal of a neighbouring lattice oxygen.[234,235] The first electron to be ionised originates from the vacancy site and can be seen in the difference between the 0 and 1+ charge states (Figure 4.10(a) and (b)). This leaves two electrons in the lone-pair on Sb which are subsequently removed in the 2+ and 3+ charge states. As these charge states occur deep in the band gap, it is likely they will not be seen and as such will have a negligible effect on the optical transparency. Despite Sb initially distorting towards the oxygen vacancy, over all three charge states Sb_{Sn} shifts a maximum of 2% in all dimensions.

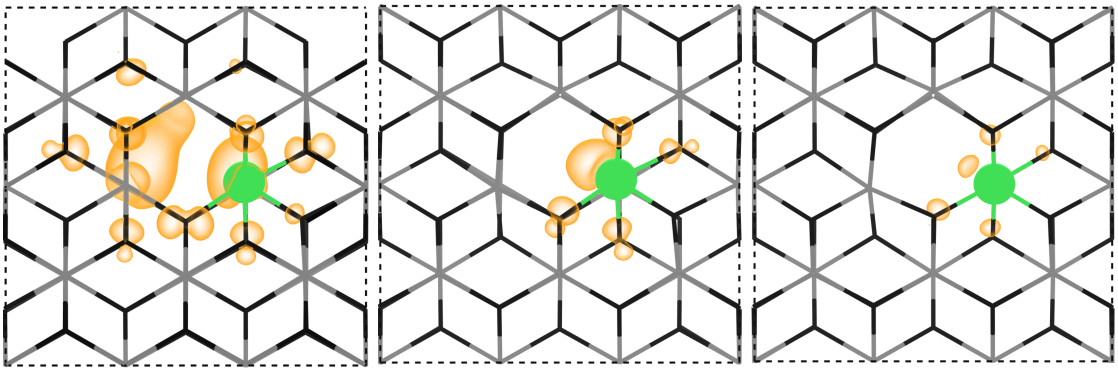

FIGURE 4.10: The partial charge electron densities for $[Sb_{Sn} + V_O]$ in the (a) neutral charge state, (b) the 1+ charge state and (c) the 2+ charge state as viewed along (010). The electron charge density is plotted from 0-0.02 eV atom^{-1} whilst the SnO_2 lattice is displayed by the grey (Sn) and black (O) wire-frame lattice. Sb is portrayed by the green spheres wihlst the electron charge is shown by the orange isosurfaces.

4.4 The Amphoteric Role of Phosphorus

Details of the theoretical methodology are included in Appendix A.2.
The work in this section is in submission for publication.
The figures in this section are adapted from this paper.

Despite the relatively high conductivities seen with F and Sb doping of SnO_2, it is clear that these doped systems are far from optimal with each having their own form of self-compensation. The next logical step is to find an alternative dopant to Sb within group 15. Nitrogen acts as an acceptor in SnO_2 [25,38] as it does in other wide band gap materials such as ZnO [286] or TiO_2 [96], whilst arsenic is highly toxic and bismuth is prefers to be trivalent meaning it will act as an acceptor. [222] P has been sparsely studied as such a dopant in both the theoretical and experimental literature [38,222,236,241] however, with the only resistivities to date being of the order of $7 \times 10^{-3}\,\Omega\,\text{cm}$. Interestingly, P is known to be amphoteric (acting as both an acceptor and donor) and has a small ionic radius (~ 0.38Å) [240] thus it is possible that phosphorus will sit favourably in both substitutional and interstitial positions. To date, only a handful of DFT studies on P-doped SnO_2 exist in the literature yet suggest substitutional phosphorus should be a resonant donor. [38,222,264] Despite this, a comprehensive study of all P-related defect species has yet to be carried out. This section will determine the viability of P-doped SnO_2 as the next generation donor dopant in SnO_2.

4.4.1 Which is the Dominant P Defect?

The thermodynamic transition levels for P-doped SnO_2 are shown in Figure 4.11 under *Sn-rich/O-poor* and *Sn-poor/O-rich* conditions. Each phosphorus related species, P_{Sn}, P_O, P_i and $[P_{Sn}+V_O]$ have been calculated alongside the dominant intrinsic acceptor (V_{Sn}) and donor (V_O) defects.

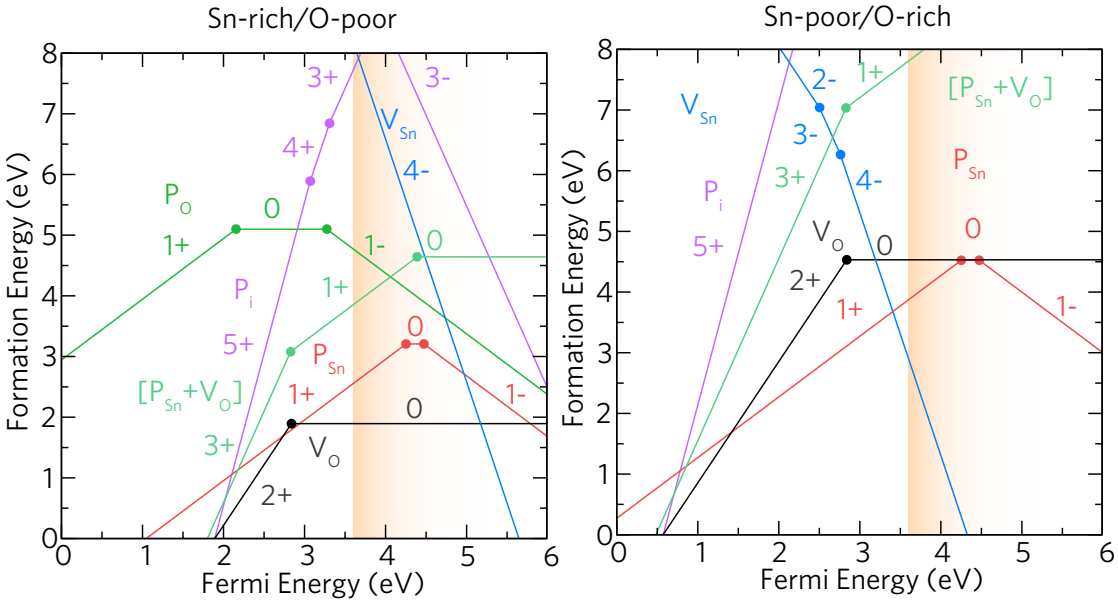

FIGURE 4.11: The transition level diagrams for P-doped SnO_2 under *Sn-rich/O-poor*, *Sn-poor/O-rich* conditions. The Fermi level ranges from the VBM (0 eV) to ~3.4 eV above the CBM (3.6 eV). The conduction band region is taken into account and is shown by the graded orange area.

P_{Sn}:

Across the entirety of the chemical potential landscape, Sn-substitutional P (P_{Sn}) is the dominant phosphorus donor defect. In the neutral charge state, P_{Sn} possesses a relatively high formation energy under *Sn-rich/O-poor* conditions of 3.21 eV which rises to 4.53 eV under *Sn-poor/O-rich* conditions. The incorporation of high concentrations of P_{Sn} in SnO_2 may require the use of non-equilibrium processes such as MBE (molecular beam epitaxy) due to the high formation energies at thermodynamic *equilibrium*. Large lattice relaxations can be seen (rationalised from the reduced P radii to Sn by ~50%)[240] and are likely to account for the relatively high formation energies. The P–O bond lengths see a reduction of ~14% as compared to Sn–O, in keeping with previous theoretical calculations by Varley et al.[38] From our calculations, P_{Sn} acts as a resonant donor with the 1+/0 transition level occurring around 0.61 eV above the CBM, higher than both F (Figure 4.5 and Sb (Figure 4.8). Varley et al. and also see P_{Sn} acting as a resonant donor with the electron occupying a 'conduction-band-like' state which is echoed by Lany et al. and Graužinytė et al.[38,222,264] Lany and coworkers (using HSE06 combined with GW (green's function)) show that P_{Sn} is a negative-U defect with the

1+/1- transition level occurring around 0.9 eV above the CBM.[222] Although we see all charge states, the 0/1- transition level occurs around 0.87 eV above the CBM. From our calculations, the 1- charge state shows a delocalisation of the electron charge in the conduction band (Figure 4.12(a)) with some localisation on P similar to Sb (Figure 4.9(b)). Under *Sn-rich/O-poor* conditions, V_{Sn}^{4-} becomes the dominant defect around 1.37 eV above the CBM where it crosses P_{Sn}^{1-}. Under *Sn-poor/O-rich* conditions, V_{Sn}^{4-} crosses P_{Sn}^{1+} around 0.2 eV below the CBM thus degenerate conductivity will not be expected at this extreme growth regime. Any experimental conditions, will likely lie in between these two limits, thus expecting an increase in conductivity due to P doping.

P_O:

P_O acts as both a *deep* donor and *deep* acceptor defect where a 1+/0 transition level occurs at 1.45 eV *below* the CBM and the 0/1- transition level occurs at 3.27 eV above the VBM in agreement with previous HSE06 studies on P-SnO_2.[38] From our calculations, the neutral charge state of P_O occurs high in energy under both growth conditions with formation energies of 5.10 eV and 14.32 eV under *Sn-rich/O-poor* and *Sn-poor/O-rich* conditions respectively. The rationalisation of these energies could be due to the larger size of P to O. In the neutral charge state, a distortion off the lattice oxygen site by ~ 3% in the *ab* directions occurs. This increases by a further 4% from the 0 to the 1- charge state due to the increased electron localisation. Figure 4.12(b) and (c) show the partial electron charge density for P_O^0 and P_O^{1-} respectively showing the distortion and electron localisation existing in this substitutional defect.

P_i:

P_i (interstitial phosphorus), acts as a highly unfavourable shallow *three electron* donor under all growth conditions. Transition levels of 5+/4+ and 4+/3+ occur in the band gap around 0.58 eV and 0.34 eV below the CBM respectively. A further 3+/1+ transition level occurs around 0.08 eV above the CBM. The formation energies of P_i under *n*-type favourable *Sn-rich/O-poor* conditions are 9.30 eV and under *Sn-poor/O-rich* conditions this rises to 14.24 eV. At Fermi levels below 2.10 eV and 0.78 eV above the VBM under *Sn-rich/O-poor* and *Sn-poor/O-rich* conditions respectively, P_i becomes the dominant phosphorus defect in SnO_2. It is likely, however, that the Fermi energies under both conditions will lie within, or close to the CBM due to the formation of P_{Sn}. As an *amphoteric* defect, P_i can act as an accep-

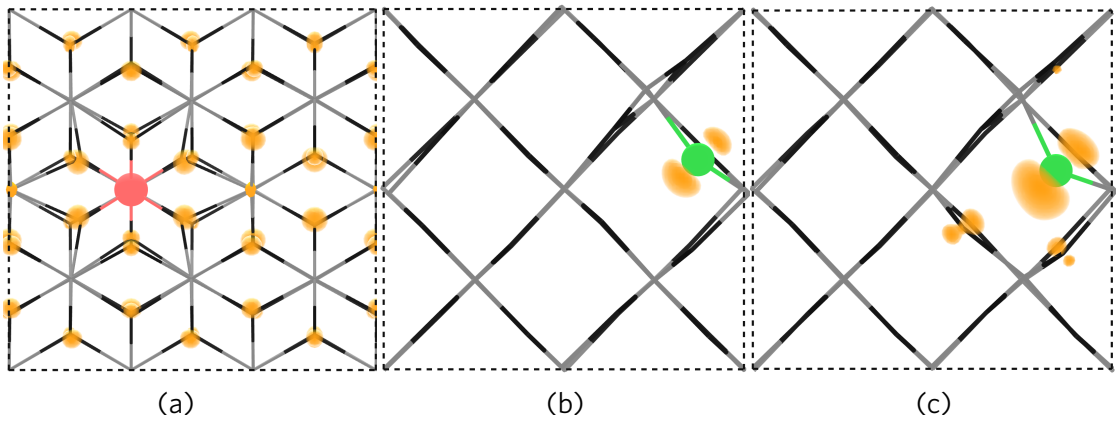

FIGURE 4.12: The partial electron charge densities for (a) P_{Sn}^{1-} as viewed along (010) (b) and (c) correspond to P_O^0 and P_O^{1-} respectively as viewed down (001). In each example, the electron charge density is shown in orange and plotted from 0-0.005 eV Å^{-3} in (a) and 0-0.02 eV Å^{-3} in (b) and (c). The SnO_2 lattice is depicted by the grey (Sn) and black (O) wire-frame whilst P is shown in red (a) and green (b and c).

tor, however, the 1+/1- and 1-/3- transition levels occur in the conduction band at 0.31 eV and 0.44 eV, and due to the high formation energies, any self-compensation will occur well above the CBM. Figure 4.13(a) displays the partial electron charge density for P_i^{3+}, in this charge state the delocalised electron charge is seen . Figures 4.13(b) and show the electron charge density and displacement for P_i^{3-} respectively. In this charge state a highly localised triple polaron forms on the interstitial P making it highly unfavourable. P also distorts from the perfect interstitial site (shown by the dashed circle in Figure 4.13(c)) to a lattice oxygen site displacing the oxygen ion to the interstitial position.

[P_{Sn}+V_O]:

A similar analysis to Sb-doped SnO_2 in Section 4.3.1 can be carried out by assessing the formation of a [P_{Sn} + V_O] cluster. Both a 'near' and 'far' configuration was set up as before where it was found that the 'near' configuration was more stable than the 'far' configuration by ~ 0.14 eV. A binding energy of 0.45 eV was calculated using equation 4.3.1 which is lower than the 0.78 eV that was calculated for [Sb_{Sn} + V_O]. This defect complex undergoes two transition levels: a 3+/1+ transition level around 0.82 eV below the CBM and a +1/0 transition level around 0.74 eV *above* the CBM making [P_{Sn} + V_O] a one-electron donor. Figure 4.14(a) shows the partial electron charge density for [P_{Sn} + V_O] in the neutral charge state and in the 1+

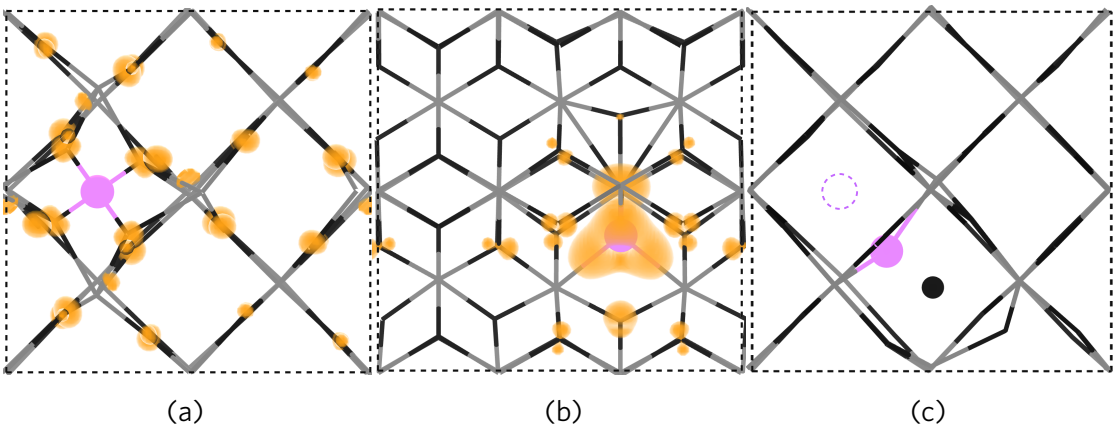

FIGURE 4.13: The partial electron charge densities for (a) P_i^{3+} as viewed along (001) (b) P_i^{3-} as viewed along (010). (c) depicts the displacement of a lattice oxygen by P_i^{3-} as viewed along (001). In each example, the electron charge density is shown in orange and plotted from 0-0.008 eV Å^{-3} in (a) and 0-0.02 eV Å^{-3} in (b). The SnO_2 lattice is depicted by the grey (Sn) and black (O) wire-frame whilst P is shown as a pink sphere. The displaced oxygen in (c) is shown as a black sphere, whilst the 'perfect' interstitial position is depicted by the dashed pink circle.

charge state in Figure 4.14(b). When in the neutral charge state, the defect complex shows a localisation of the electron density on the P and in the vacancy site. In the 1+ charge state the electron is first removed from the P leaving two electrons in the vacancy. This leaves the reasoning that in this situation P is in the 5+ oxidation state, unlike Sb which facilitates the formation of a lone pair on Sb forming Sb^{3+}. The likely explanation for the formation of this defect cluster is to ease strain on the lattice which can be seen clearly in Figures 4.14(a) and (b). Despite the binding energy of 0.45 eV, the formation energy of [P_{Sn}+V_O] in the neutral charge state is 4.64 eV and 8.60 eV under *Sn-rich/O-poor* and *Sn-poor/O-rich* conditions respectively. This defect complex will only be dominant around 2.03 eV and 0.71 eV above the VBM for *Sn-rich/O-poor* and *Sn-poor/O-rich* respectively. However, as with [Sb_{Sn} + V_O] it is likely that at high concentrations of P incorporation that this defect complex could be seen in experiment. EXAFS studies are therefore required to prove the prediction of this.

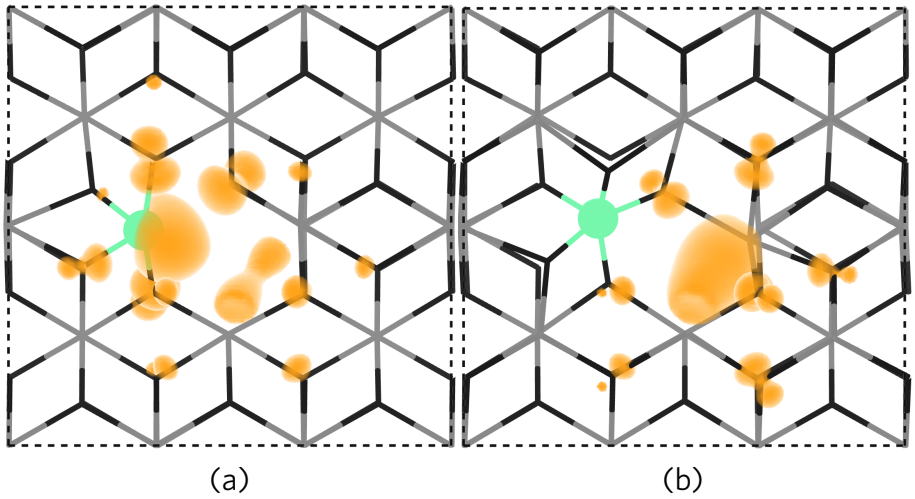

FIGURE 4.14: The partial electron charge density for $[P_{Sn} + V_O]$ in the (a) neutral and (b) 1+ charge state as viewed along (010). The partial charge density is plotted from 0-0.01 eV Å^{-3} and is shown in orange. The SnO_2 lattice is depicted by the grey (Sn) and black (O) wire-frame lattice. P is shown by the turquoise sphere.

4.5 Is Tantalum the Optimum Dopant for SnO_2

Details of the theoretical methodology are included in Appendix A.2.
The work in this section is in preparation for publication.

The conventional choice of dopant in either groups 15 or 17 in the periodic table has therefore shown to be problematic in terms of realising the full potential of highly *n*-type doped SnO_2. From self-compensation to issues with multivalency and ionic radii it is clear that the search for an optimum dopant is ongoing. Extremely high mobilities (50-84 $cm^2\,V^{-1}\,s^{-1}$) and low resistivities ($1.1\times10^{-4}\,\Omega\,cm$) have been reported recently in Ta-doped SnO_2.[194,255] Ta has an ionic radius of 0.69 Å similar to that of Sn (0.60 Å).[240] Nb-doped SnO_2 on the other hand possesses high resistivities and low mobilities[242–254] despite having the same ionic radius to Ta (0.69 Å).f[240] In this section, the thermodynamic and electronic properties of both Nb and Ta defects will be analysed to understand the vast differences in conductivities as well as to determine whether Ta is the optimum dopant for SnO_2 in terms of mobilities, conductivities and carrier concentrations.

4.5.1 A Comparison of Nb and Ta doped SnO_2

Figure 4.15 displays the thermodynamic transition levels for the both Nb and Ta doped SnO_2 together with the *dominant* intrinsic defects under *Sn-rich/O-poor* and *Sn-poor/O-rich* conditions.

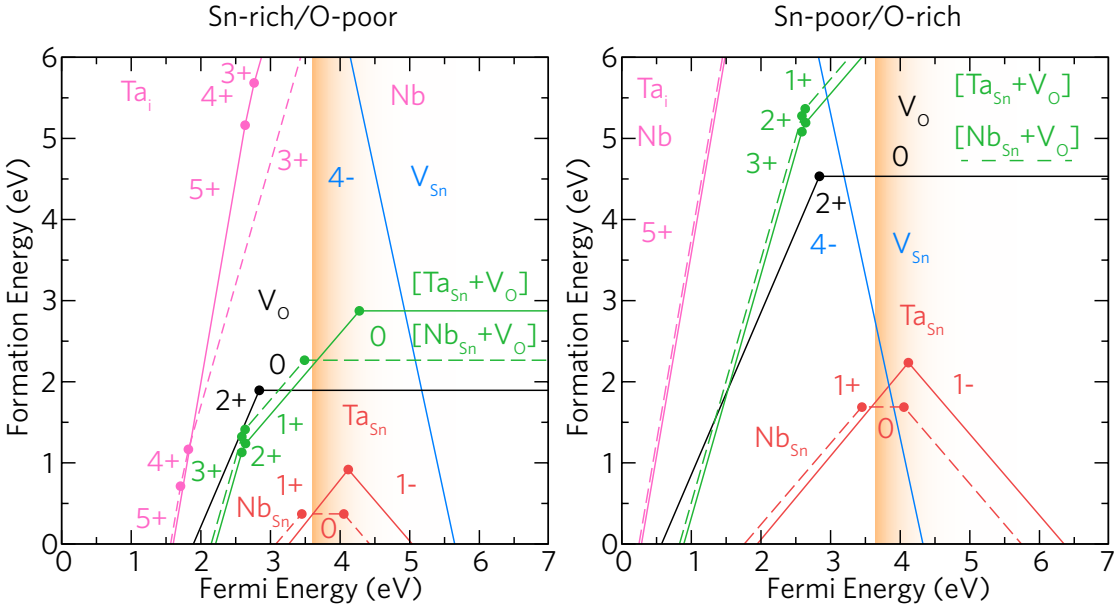

FIGURE 4.15: The thermodynamic transition levels for SnO_2:Nb and SnO_2:Ta under *Sn-rich/O-poor*, and *Sn-poor/O-rich* growth conditions. The Fermi energy ranges from the VBM (0 eV) to ~ 3.4 eV above the CBM (3.6 eV). The conduction band is depicted by the graded orange area, and the Nb dopant related species are shown with the dashed lines.

Nb_{Sn} and Ta_{Sn}:

The effects of substitutional Nb and Ta doping of SnO_2 were evaluated to determine the reasoning behind the vastly different electronic properties. Nb_{Sn} is a low formation energy dopant under the entire range of chemical potentials. Under each regime, the neutral charge state has formation energies of 0.37 eV and 1.68 eV for *Sn-rich/O-poor*, and *Sn-poor/O-rich* growth conditions respectively. These low formation energies mean that high dopant solubilities of Nb will be realisable in SnO_2. Nb_{Sn}, however, is a *deep* donor with a 1+/0 transition level situated around 0.20 eV *below* the CBM requiring a very big excitation energy. Substitutional Nb does not therefore contribute to the conductivity of SnO_2 correlating to the lack of conductivity seen in experiment.[242–254] Figure 4.16(a) shows the partial charge density for Nb^0_{Sn} showing the localised electron situated in the 4*d* orbital on Nb indicating Nb^{4+}. Nb_{Sn} undergoes a second transition level (0/1-) ~0.4 eV above the CBM, however it is not likely that the Fermi level will reach this point and thus the 1- charge state (Nb^{3+}) will not be seen. Nb has a negligible effect on the rutile lattice over all the charge states indicative of the low formation energies. Few DFT studies on Nb doped SnO_2 have been carried out, agreement with

a study by Behtash et al. who, using the HSE06 functional see filled Nb 4*d* states in the band gap of SnO_2 concluding the incorporation of Nb^{4+} into the SnO_2 lattice.[246] A recent review of *n*-type defects in SnO_2 using the PBE0 functional similar to this work, show that Nb is a *resonant* defect with the 1+/0 transition level around 0.5 eV above the CBM suggesting that thin films of SnO_2:Nb will provide high conductivities with larger doping concentrations.[264] This study however relaxed with PBE[14] then *shifted* the lattice parameters using PBE0 thus not fully relaxing the defect supercells likely giving the different results.

Ta_{Sn} is also a low formation energy donor in SnO_2 which, when in the neutral charge state (Ta^0_{Sn}) has energies of 0.89 eV and 2.2 eV under *Ti-rich/O-poor* and *Ti-poor/O-rich* conditions respectively. Ta_{Sn} acts as a *resonant* one-electron donor incorporating into the Sn sublattice as Ta^{5+} and can be seen in the increase in conductivity in experiment.[193,194,255–263] Ta_{Sn} undergoes a transition from the 1+/1- transition state at around 0.5 eV above the CBM allowing for high doping concentrations. Figure 4.16(b) shows the partial charge density of the neutral and 1- charge state of Ta_{Sn} displaying the localised electron(s) in the Ta 5*d* orbital similar to Nb. In this configuration Ta acts as Ta^{4+} (for $q = 0$) or Ta^{5+} (for $q = 1-$) not donating any electrons. As Ta^0_{Sn} disproportionates into Ta^{1+}_{Sn} and Ta^{1-}_{Sn} it is not likely that much Ta^{4+} will be observed. In the 1+ charge state, as with Nb^{1+}_{Sn}, Ta has a minimal effect on the SnO_2 lattice with a slight expansion of the TaO_6 octahedra (<3%) which re-contracts in the 1- charge state explaining the low formation energies of Ta_{Sn}. Under *Sn-poor/O-rich* conditions the Fermi level is trapped just below 0.25 eV above the CBM where V^{4-}_{Sn} crosses Ta^{1+}_{Sn} showing that conductivity will be realised across the whole range of chemical potentials in SnO_2. It is important to note however, that *O-rich* conditions are the *absolute* limits of the formation of SnO_2 and is not likely to be seen experimentally. The only theoretical studies on Ta-doped SnO_2 comes from Graužinytė et al. who show that Ta undergoes the same 1+/1- transition level, however at ~0.1 eV above the CBM.[264] The difference to the present study is likely due to the lack of hybrid PBE0 relaxation carried out in ref. [264] which is important for the optimal structural and electronic convergence of the doped supercell. However it is important to note that the authors acknowledged Ta as a high conductivity dopant in SnO_2 using hybrid screening techniques.

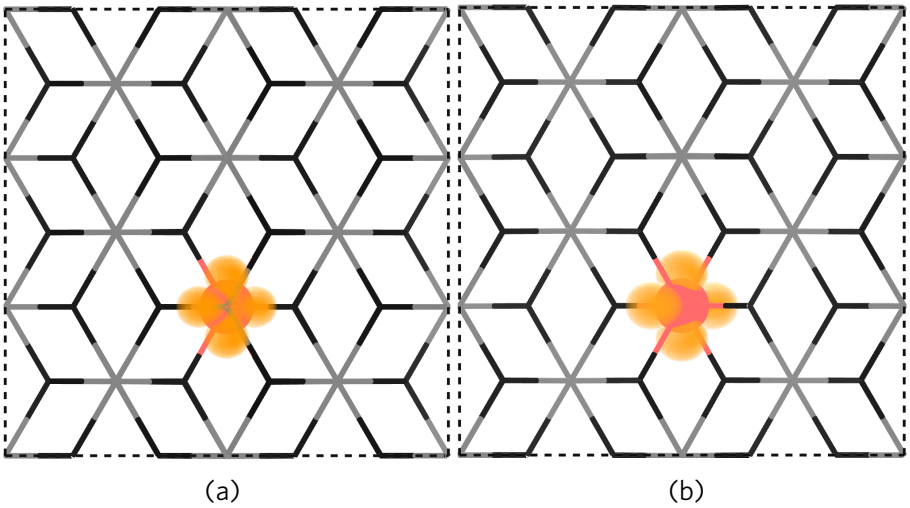

FIGURE 4.16: The partial charge densities of Nb^{0}_{Sn} (a) and $Ta^{0\text{ or }1-}_{Sn}$ (b) as viewed along (010) showing the electron localisation on Nb and Ta in a *d* orbital. In both examples the rutile SnO_2 lattice is displayed using a wire-frame lattice with Sn=grey and O=black whilst Nb/Ta is depicted in red. The partial electron charge density is shown in orange and is plotted from 0-0.03 eV Å^{-3}.

Nb_i and Ta_i:

Interstitial Nb and Ta were assessed as potential donors in SnO_2. In fluorine doped SnO_2 (FTO), interstitial F is a cause of self-compensation and has been proven both theoretically and experimentally.[275] In the case of Nb and Ta, both dopants (when interstitial) act as multi electron *donors* thus no self compensation is expected to occur. Nb_i acts as a three electron *resonant* donor under both growth regimes with a 0/3+ transition level around 0.51 eV above the CBM. The neutral charge state has formation energies of 8.04 eV and 14.64 eV under *Sn-rich/O-poor* and *Sn-poor/O-rich* conditions respectively making the formation of interstitial Nb unlikely to occur at Fermi levels in the conduction band. Nb_i undergoes transition levels of 5+/4+ and 4+/3+ at 1.89 eV and 1.78 eV *below* the CBM. Due to the high formation energies of Nb_i at energies close to the CBM, the Fermi level is likely to be trapped around 0.20 eV below the CBM due to the formation of substitutional Nb (Nb_{Sn}). Ta_i is also a resonant three electron donor in SnO_2 acting in much the same way as Nb_i with 3+/1+ and 1+/0 transition levels occurring around 0.18 eV and 0.50 eV above the CBM. The neutral charge state of Ta_i also has a very high formation energy across the chemical potential range of SnO_2 incurring values of 9.07 eV and 15.66 eV for *Sn-rich/O-poor* and *Sn-poor/O-rich* growth potentials respectively. The 5+/4+ and 4+/3+ transition levels occur in the band gap around 0.97 eV and

0.83 eV below the CBM. As with Nb_i, it is likely then that when the Fermi level is trapped around 0.5 eV above the CBM from substitutional Ta (Ta_{Sn}), quantities of interstitial Ta will be negligible.

[Nb_{Sn}+V_O] and [Ta_{Sn}+V_O]:

As seen in Section 4.3 and 4.4, Sb and P both have the capacity to form a [M_{Sn}+V_O] (where M=P or Sb) cluster. For Sb-doped SnO_2, this has been observed through X-ray absorption fine structure (EXAFS) that substitutional Sb (Sb_{Sn}) clusters with an oxygen vacancy (V_O) leading to the formation of Sb^{3+} and a trapped electron in V_O.[234,235] This behaviour is seen to limit the conductivity in heavily doped SnO_2:Sb. We have proposed the same configuration for Nb and Ta doped SnO_2 in both an 'associated' (ie. $Nb(Ta)_{Sn}$ and V_O neighbouring each other) and a 'dissociated' configuration. From our calculations we find that both [Nb_{Sn}+V_O] and [Ta_{Sn}+V_O] prefer to dissociate from each other with the associated formation energies being ~0.39 eV and ~0.38 eV *higher* for [Nb_{Sn}+V_O] and [Ta_{Sn}+V_O] respectively. Under all growth conditions, [Nb_{Sn}+V_O] (dissociated) has a formation energies of 2.26 eV and 6.22 eV respectively under *Sn-rich/O-poor* and *Sn-poor/O-rich* growth conditions respectively. The defect complex undergoes transition levels of 3+/2+, 2+/1+ and 1+/0 in the band gap at Fermi energies of 1.01 eV, 0.97 eV and 0.11 eV below the CBM respectively meaning that this cluster will not partake in any thermodynamic conductivity in Nb-doped SnO_2. [Ta_{Sn}+V_O], however has two transition levels in the band gap (3+/2+ and 2+/1+ = 1.01 eV and 0.96 eV below the CBM) and the 1+/0 transition level around 0.68 eV above the CBM, making the defect cluster a one-electron donor. $[Ta_{Sn}+V_O]^0$ has higher formation energies than $[Nb_{Sn}+V_O]^0$ at 2.87 eV and 6.82 eV under *Sn-rich/O-poor* and *Sn-poor/O-rich* conditions respectively. The partial charge densities for $[Nb(Ta)_{Sn}+V_O]^0$ and $[Nb(Ta)_{Sn}+V_O]^{1+}$ is shown in Figure 4.17(a) and (b) respectively. In the neutral charge state ($q = 0$) the electron density is localised in V_O and in a *d* orbital on the metal dopant (similar to Figure 4.16). In the 1+ charge state, the electron is removed from the Nb(Ta) independently leaving the two electrons in the oxygen vacancy. This shows that the two defects work independently from each other and thus should not cause limitations in the same way that this defect cluster does in Sb-doped SnO_2. An analysis as to whether the formation energies of either $Nb(Ta)_{Sn}$ or V_O are lowered within the presence of the other defect can be carried out using:

$$\Delta H_f(D, q = 0) = E[\mathrm{Nb(Ta)_{Sn}} + V_O] - E[V_O] + (E_{Sn} + \mu_{Sn}) - (E_{Nb(Ta)} + \mu_{Nb(Ta)}) \qquad (4.5.1)$$

for the formation energy of $Nb(Ta)_{Sn}$ in the presence of an oxygen vacancy, or:

$$\Delta H_f(D, q = 0) = E[\mathrm{Nb(Ta)_{Sn}} + V_O] - E[\mathrm{Nb(Ta)_{Sn}}] + (E_O + \mu_O) \tag{4.5.2}$$

for the formation energy of V_O with $Nb(Ta)_{Sn}$.

From our calculations it can be shown that for both Nb and Ta doping, that an increase in formation energy for V_O occurs. For Nb this value is 0.002 eV higher than undoped SnO_2 making it likely that oxygen vacancies will form, however this value is 0.05 eV higher in Ta-doped SnO_2. Both Nb_{Sn} and Ta_{Sn} also see small increases in formation energies (0.002 eV and 0.05 eV). These values, however, correspond to temperatures of 17-580K, thus making the coexistence of V_O and $Nb(Ta)_{Sn}$ likely within the typical synthesis temperatures of Nb or Ta doped SnO_2. Compensation of $[Ta_{Sn}+V_O]^{1+}$ from V_{Sn}^{4-} occurs around 0.73 eV *below* the CBM under *Sn-poor/O-rich* growth conditions. Towards increasingly *Sn-rich/O-poor* conditions, $[Ta_{Sn}+V_O]$ reaches the neutral charge state before compensation occurs, which, together with the decreased formation energy means that a higher Fermi level may be reached with increased Ta incorporation.

4.5.2 Unfolded Band Structures

The band structures of undoped (host), Nb-doped and Ta-doped SnO_2 were calculated using the PBE0 hybrid functional and with the band-unfolding code BandUP[287,288] in order to determine the origin of the differing conductivities of Nb and Ta and the high mobilities seen in SnO_2:Ta thin films.[194,255] The unfolded band structures for SnO_2:Nb and SnO_2:Ta are shown in Figures 4.18 and 4.19 respectively.

SnO_2:Nb:

SnO_2, when doped with Nb incurs a localised gap state as shown in Figure 4.16(a). The same *filled* gap state can be seen in the spin-up (α) component of the band structure of SnO_2:Nb by the flat localised band around 2.5 eV above the VBM. This band is made up of predominantly Nb *d* states ($\sim$80%) with some Sn *s* and O *p* states. Two further bands are seen ca. 6 eV ($\sim$2.4 eV above the CBM) which are made up of 80% Nb *d* character. Three more bands

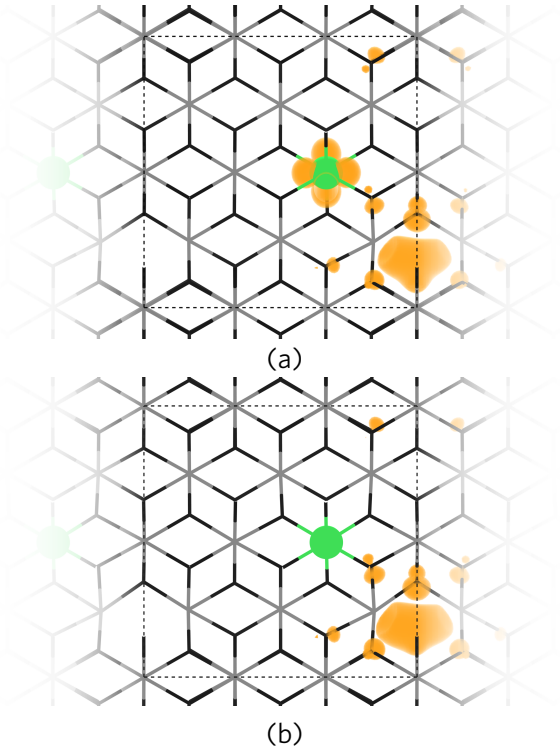

FIGURE 4.17: The partial charge densities for $[Nb(Ta)_{Sn}+V_O]^0$ (a) and $[Nb(Ta)_{Sn}+V_O]^{1+}$ (b) defect species. Here it is shown that the two *n*-type defects act independently to each other with the donated electron in the 1+ charge state coming from the localised d orbital on the Nb(Ta). In both examples the rutile SnO_2 lattice is viewed along the (010) direction with Sn and O displayed in grey and black with a wire-frame model for clarity. Nb/Ta are shown by the green spheres and the electron charge density is plotted from 0-0.015 eV Å^{-3} in orange. The supercell boundary is shown by the dashed black box.

are seen in the spin-down component (β) from ~6-7 eV which are also predominantly Nb *d* states. The conduction band minimum of undoped SnO_2 is made up of mostly Sn *s* states with some O *s* mixing consistent with PBE0 calculated density of states measurements on SnO_2.[25] In Nb-doped SnO_2 the CBM composition is retained, with <1% Nb *s* mixing likely to be due to the finite size of the supercell. These results, conclude why SnO_2:Nb does not produce highly conductive thin films.

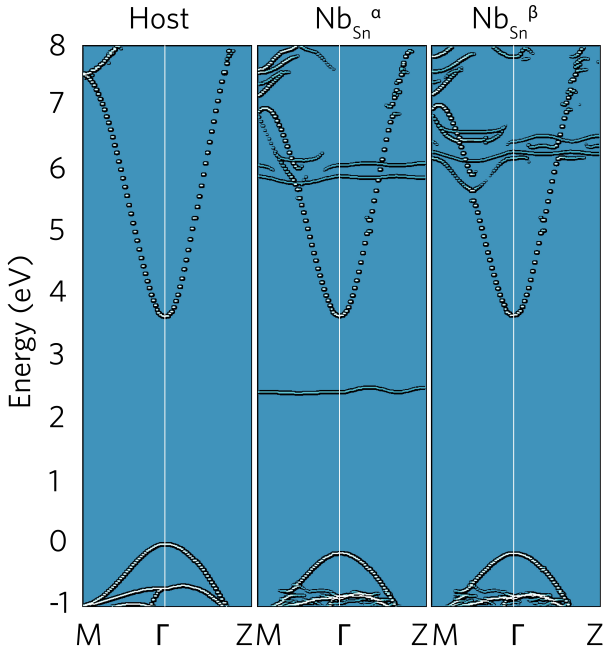

FIGURE 4.18: The unfolded band structures for Nb_{Sn}^{0} and undoped SnO_2. α and β refer to refer to the spin state of the defect.

SnO_2:Ta:

The unfolded band structures for Ta-doped SnO_2 holds many similarities to Nb-doped SnO_2, however Ta's 5*d* bands appear higher in energy than Nb's 4*d* bands in SnO_2. In the 'spin-up' (α) band structure, the filled Ta *d* orbital appears ~0.46-0.5 eV above the CBM consistent with the thermodynamic 1+/1- transition level seen in Figure 4.15. This band is predominantly 70 % Ta *d* character mixed with some Sn *s* and O *s* states typical of the conduction band of SnO_2. As with Nb-doped SnO_2 the mixing is likely to be due to the finite size of the supercell used for our calculations. Further bands appear at around 7 eV and also appear in the spin-down (β) band structure from 6-8 eV. As with Nb, <1% of Ta *s* states hybridise with the Sn *s* and O*s* states at the CBM. This is likely the effect of the high mobility seen in Ta-doped SnO_2 thin films[194] as the states do not *perturb* the dispersion of the conduction band and thus normal impurity-electron scattering is avoided. A similar effect is seen in Mo-doped In_2O_3.[122]

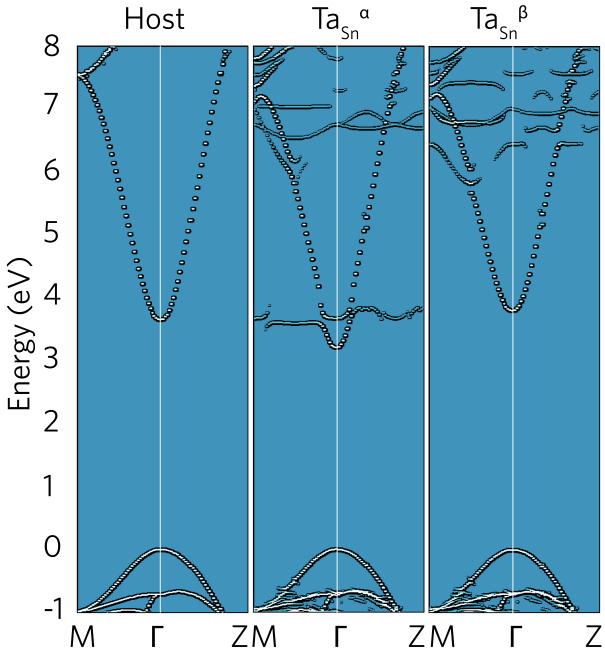

FIGURE 4.19: The unfolded band structures for Ta^{0}_{Sn} and undoped SnO_2. α and β refer to refer to the spin state of the defect.

4.6 Conclusions

The ability to produce high carrier concentrations, low resistivities and high mobilities is vitally important for creating an *n*-type TCO that is capable of replacing the industry standard Sn-doped In_2O_3. Such a material will allow for highly efficient and cost-effective electronic devices. From our work on doped SnO_2, we have provided the theory behind the self-compensation mechanism in the industry leading stannic oxide dopant, fluorine. At high degenerate doping levels ($\sim 10^{20}$ cm^{-3}), interstitial fluorine (F_i) begins to form alongside substitutional fluorine (F_O) forming a direct compensation. Hybrid density functional theory twinned with mobility measurements in FTO thin films prove (with excellent agreement) the self-compensation mechanism. Antimony-doped SnO_2 (ATO) has been shown to be a *lower* formation energy resonant donor in SnO_2 than FTO. A similar limitation, however, occurs with increased doping in that an association with a lattice oxygen vacancy occurs forming Sb^{3+}. Further speculation in the experimental literature have also suggested the segregation of Sb^{3+} to the surface of the material which requires further analysis.[233] Calculations on P-doped SnO_2 show that whilst phosphorus does not incur self-compensation like FTO, it does however, possess a relatively high formation energy. The likely reasoning behind this is the small ionic radii of P^{5+} which allows for an inducement of an oxygen vacancy at high doping concentrations, as with ATO. It is also likely that the use of non-equilibrium techniques such as MBE are likely due to the high formation energies of P_{Sn}. Moving away from choosing one-electron dopants from groups 15 and 17 in the periodic table gave rise to Nb and Ta as suitable *n*-type dopants. Despite being physically similar, Nb and Ta produce vastly different electronic effects when incorporated into SnO_2. Through hybrid DFT, we have shown the difference to be due to Nb incorporating as Nb^{4+} producing a localised electron state in the band gap, whilst Ta incorporates as Ta^{5+}. In Ta-doped SnO_2 (TaTO), the Fermi level can be pushed further into the conduction band than either F or Sb and does not undergo self compensation from interstitials. Ta also does not associate with oxygen vacancies and thus does not readily form Ta^{3+} further limiting the conductivity. The most remarkable aspect of TaTO is its ability to supply high mobilities ($\sim$ 50-84 $cm^2\,V^{-1}\,s^{-1}$) as well as high conductivities. The reasoning behind this has been deduced to be due to the Ta states appearing *above* the CBM and thus does not interfere with the states that make up the CBM. When this happens, the dispersion of bulk SnO_2 is retained resulting in higher mobilities as seen in experiment. It is clear, therefore that Ta is the optimum one-electron dopant in SnO_2. New 'high-mobility'

dopant design rules can be gained from this work which can be applied to other wide band gap materials such as ZnO and even In_2O_3.

Part III

p-Type Transparent Conductors

Chapter 5

Introduction to *p*-type Transparent Conductors

Whilst *n*-type TCOs display high doping concentrations ($\sim 10^{21}\,cm^{-1}$), mobilities ($\sim 20-100\,cm^2\,V^{-1}\,s^{-1}$) and conductivities ($\sim 10^{20}\,S\,cm^{-1}$) with almost total optical transparency (80-90%) [115,289,290], there is a distinct paucity in comparable *p*-type transparent conductors (TCs). There has been a growing need for high mobility, *degenerate p*-type TCs for applications such as photovoltaics, gas sensing and photocatalysis where more efficient hole separation is needed. [116,291–293] A highly conductive *p*-type TC would also allow the realisation of transparent electronics when twinned with an *n*-type counterpart to create an efficient and transparent *p*-*n* junction. One of the first reported *p*-type TCOs was NiO which crystallises in the rock salt structure with octahedral Ni and O and typically has a band gap in the range 3.4-4.0eV [116,294] displaying a maximum conductivity of $7.1\,S\,cm^{-1}$ when doped with Li. [295] This value is far removed from *n*-type Sn-doped In_2O_3 (ITO), which has values nearing $10^5\,S\,cm^{-1}$. [296–299] The average mobility values for NiO are also $<1\,cm^2\,V^{-1}\,s^{-1}$ [116] and thus a major hindrance in the development of a comparable *p*-type TCO.

5.1 Design Strategies of *p*-type Transparent Conductors

5.1.1 Acceptor Doping of *n*-type TCOs

Multiple design strategies have been employed in order to overcome the bottleneck associated with *p*-type TCs; a common approach is to acceptor dope the highly successful *n*-type TCOs (In_2O_3, SnO_2 and ZnO). The ability to introduce mobile holes into an *n*-type TCO would benefit from being able to form a *p-n homojunction* with no issues with lattice matching as well as using materials which already have decades of research and industrial architecture available. In the literature, however, the results of acceptor doping are hugely unreliable and tend to amount to very low hole concentrations, low conductivities as well as poor mobilities.[300–309] *n*-type TCs are inherently unsuited for *p*-type defects due to the positioning of the conduction band and valence band (electron affinity and ionisation potentials respectively) which favour the formation of *electron-donating* defects such as oxygen vacancies and cation interstitials. Most *n*-type TCOs involve post-transition metal cations (ie. In, Sn, Cd) and thus are susceptible to the *d*-block 'contraction' whereby the *d* states occur much lower in energy (relative to the vacuum level) and thus the cation *s* states that make up the conduction band minima are also lower in energy.[25,116] The effect of this is two fold, firstly, any acceptor defect will be a *deep* defect meaning that holes will be largely polaronic in nature and secondly, due to the high formation energies, any *p*-type defect will be compensated for by the *low* formation energy donor defects present, even under the most preferential growth conditions.[25]

As previously mentioned in Section 3.2.1, valence band maxima (VBMs) of *n*-type TCOs are predominantly of O $2p$ character and thus holes are highly localised and polaronic due to the highly electronegative nature of O and large ionicity of TCOs.[310,311] This leads to the characteristically 'flat' valence band maxima as seen, for example, in In_2O_3 (Figure 5.1) and thus any generated holes would be very heavy and immobile. The effective mass of In_2O_3 for electrons and holes are 0.22-0.24 m_e and 16.14 m_e[155] respectively highlighting further the difference in electron and hole preference in *n*-type TCOs. Despite the reproducibility and issues highlighted above, acceptor doping of *n*-type TCOs is still in fact attempted, to no success.[308,312–316,316–321]

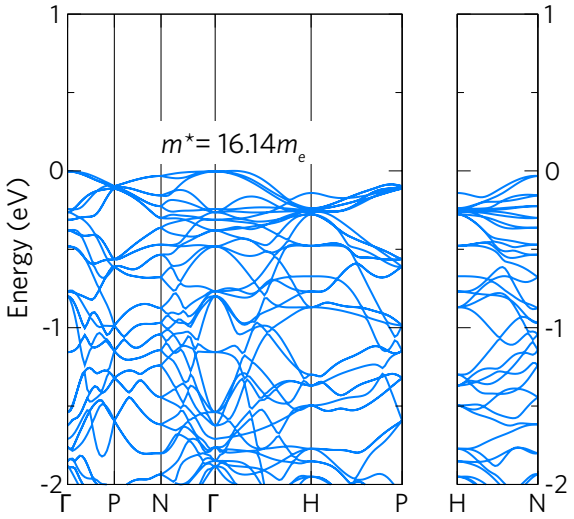

FIGURE 5.1: The upper valence band of In_2O_3 (calculated using HSE06) displaying the 'flat' bands and therefore heavy holes ($m^* = 16.14 m_e$) associated with the localised polaronic O $2p$ character of the *n*-type TCOs. Calculation details are provided in Appendix A.1.

5.1.2 The Chemical Modulation of the Valence Band

A set of rules based upon reducing the lack of O $2p$ localisation at the VBM were pioneered by Hosono and coworkers.[322] The principles of this design method was based in part on the known *p*-type ability of the cubic Cu_2O (Figure 5.2) whereby Cu^{1+} cations hybridise with O $2p$ anions in a O-Cu-O dumbbell motif. This has the effect of substantially reducing the localisation of holes at the VBM. Although extremely high hole mobilities have been reported ($256\,cm^2\,V^{-1}\,s^{-1}$)[323], copper (1+) oxide however, has a band gap of 2.17 eV discounting it from use as a TCO.[116] It is thought that the relatively small distance between neighbouring Cu d^{10} electrons accounts for the lack of transparency to visible light.[324,325]

Hosono and coworkers coined the phrase 'chemical modulation of the valence band' (CMVB) for his *p*-type TCO design principles, based on features seen in Cu_2O and the wide band gap of Al_2O_3. This resulted in identifying the delafossite $CuAlO_2$ (Figure 5.2 as a new *p*-type TCO.[322,326] The design rules gained from $CuAlO_2$ were that a closed shell metal cation such as Cu^{1+} ($3d^{10}$) be hybridised with O $2p$ in such as manner as to bring about dispersion at the VBM. This occurs in the unusual 1D coordination of the O-Cu-O dumbbell motif that Cu_2O and $CuAlO_2$ possess. The benefit of this is two fold, firstly an increased overlap between Cu $3d$ and O $2p$ is present (Figure 5.2) resulting in a raised VBM, an increased dispersion and thus a greater accommodation of *p*-type defects and more mobile holes. Lastly this hybridi-

sation results in a greater separation between the d^{10} electrons on the Cu^{1+} cations. The increased separation allows for fewer d-d transitions that will lower the band gap as seen in Cu_2O ($E_g = 2.17$ eV). The oxygen anions are also *tetrahedrally* coordinated, such that the electrons are distributed along four σ bonds thus removing the non-bonding states altogether.[312]

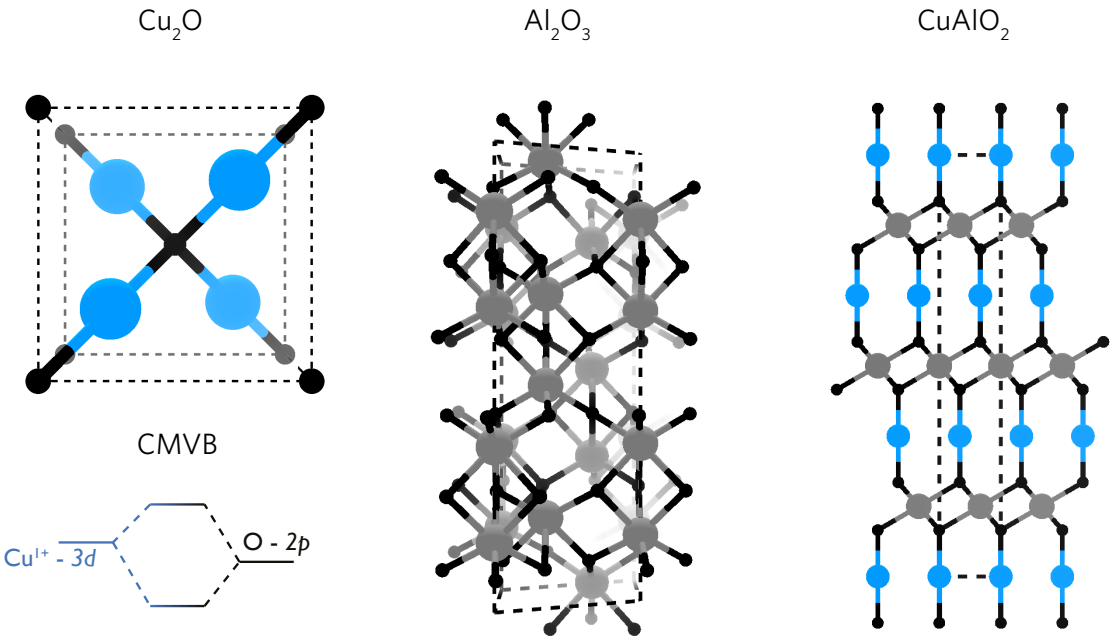

FIGURE 5.2: The crystal structures of Cu_2O, Al_2O_3, $CuAlO_2$ and the schematic molecular orbital diagram showing the overlap of Cu 3d and O 2p orbitals at the VBM, breaking the localisation seen in n-type TCOs. In each structure, Cu = blue, Al = grey and O = black.

Other materials with a similar valence band electronic structure exit such as $CuGaO_2$[327,328], $CuInO_2$[327], $CuCrO_2$[329], $CuBO_2$[330,331], $CuScO_2$[327,332] and $SrCu_2O_2$[333,334] (to name a few). In each case, despite being transparent the p-type hole conductivities were typically several orders of magnitude lower than n-type TCOs. Acceptor defects in these materials have been shown to be fairly deep in nature and as such degenerate conductivity is not realisable in these materials.[330] Indeed the highest reported electrical conductivity has been shown for $CuCrO_2$ doped with Mg (220 S cm^{-1}).[329]

Other potential p-type materials with similar characteristics have been suggested that combine a pseudo closed-shell cation such as a group of spinel oxides with the $ZnM_2^{3+}O_4$ configuration (where M = Co, Rh or Ir). It was Hosono and coworkers who again showed that $ZnRh_2O_4$ was a transparent p-type semiconductor with a conductivity of 0.7 S cm^{-1}.[335] The

direct *fundamental* band gap of $ZnRh_2O_4$ was found to be 2.1 eV with a VBM consisting of Rh d^6 with some O $2p$ mixing due to the octahedral configuration of Rh. The same octahedral coordination of Rh means that the fundamental band gap, however, is forbidden due to the d-d character of the band gap.[336]

Arguably the most studied of the *p*-type spinels is $ZnCo_2O_4$ which has reported conductivities in the range 0.39-21 $S\,cm^{-1}$ [337,338] and a fundamental band gap of 2.63 eV.[336] In general there is a distinct lack of dispersion at the VBM in these materials suggesting that conductivity will be determined by *small* polarons as well as having poor optical transparency and are thus not a viable competitor to *n*-type TCOs.[336,339]

Materials with ns^2-O $2p$ bonding at the VBM can also provide the possibility of high mobility *p*-type TCOs. *s* orbitals are known to be more spatially extended than *p* or *d* orbitals and thus a greater hybridisation and dispersion is expected at the VBM. This is the case for materials with ns^2 cations such as SnO and Ba_2BiTaO_6.[340] SnO however, is readily oxidised to SnO_2 and the ability to create a high mobility TCO is still unreliable as average mobilities are of the order 5 $cm^2\,V^{-1}\,s^{-1}$ and possesses fairly low optical transmissions <80%.[116,340]

Ba_2BiTaO_6 is a more promising addition to the ns^2 based *p*-type TCOs combining a higher optical transparency ($\sim$ 90%) and a mobility of $\sim$ 30 $cm^2\,V^{-1}\,s^{-1}$ yet low hole concentrations $\sim 10^{13}\,cm^{-3}$ [340] have been realisable. Even when high doping concentrations with potassium ($\sim$ 35 at.%) low hole concentrations of $\sim 10^{14}\,cm^{-3}$ and low mobilities (in the kΩ cm range) are seen.[340]

5.1.3 Beyond the Transparent Conducting Oxide

It has been shown that the CMVB can be extended beyond oxide materials to other chalcogenides: S,Se and Te. Comparing Cu_2O to Cu_2S and Cu_2Se, an increase in *p*-type conductivity occurs yet with a red shift of the band gap.[324,341,342] The reasoning behind this is the existence of a greater hybridisation of Cu $3d$ with chalcogen np as you proceed down the group.[343,344] The effect of this means that dispersion of the valence band increases and the ionisation potentials decrease. A group of layered oxychalcogenides, LaCuOCh (Figure 5.3; where Ch=S, Se, Te), with *p*-type conductive layers of $[Cu_2Ch_2]^{2-}$ sandwiched between two $[LaO]^{1+}$ layers have been shown to display the same trends as the binary copper chalcogenides.[345] LaCuOS, LaCuOSe and LaCuOTe display band gaps of 3.1 eV, 2.8 eV and 2.3 eV respectively however with associated conductivities and mobilities (undoped) of 6.4×10^{-5}, 24 and 1.65 $S\,cm^{-1}$ and 0.20, 8 and 80.6 $cm^2\,V^{-1}\,s^{-1}$.[344,346–348] When acceptor doped, LaCuOS:Sr and LaCuOSe:Mg

reach conductivities of 2.6×10^{-1} S cm^{-1} [349] and 910 S cm^{-1} [346] respectively demonstrating the increase in *degenerate* doping from S to Se to Te.

Both polyatomic compounds and layered systems offer a much wider phase space than simple binary or ternary systems.[350] Layered systems offer the ability to accommodate different sized atoms without changing the initial parent structure. Through this, correlations between atomic effects can be gained to enhance specific electronic properties such as band gap, dispersion, ionisation potentials etc.[350] An alternative wide band gap layered oxychalcogenide was been discovered with the formula: $[Cu_2S_2][Sr_3Sc_2O_5]$ [351,352] (*SCSOS*) which comprises of alternating $Cu_2S_2^{2-}$ layers and perovskite-like $[Sr_3Sc_2O_5]^{2+}$ layers and possesses a 3.1 eV band gap (Figure 5.3). It was first synthesised by Otzschi and coworkers in 1999[352] and subsequently reinvestigated by Liu et al. in 2007.[351] The latter displayed undoped conductivities of 2.8 S cm^{-1} and extremely high mobilities of 150 cm^2 V^{-1} s^{-1} despite relatively low carrier concentrations of 10^{17} cm^{-3}.[351] Further to this, hybrid DFT calculations were carried out on SCSOS[330] whereby the electronic structure of the VBM was confirmed to be made up of 50:50 Cu 3*d* and S 3*p* and the large band gap brought about by the perovskite-like layer. It was found that whilst a small Cu-Cu distance is desirable in the delafossites to aide the polaronic hole hopping mechanism, the same effect does not apply to the layered oxychalcogenides (LaCuOCh and SCSOS).[330]

The CMVB can also be extended beyond the chalcogenides towards the *pnictides* and is seen in the metastable compound Cu_3N with the anti-ReO_3 structure.[353–356] As with the *p*-type delafossite oxides, nitrogen prefers a linear 'dumbbell' motif with both Cu_3N and $CuTaN_2$ displaying N–Cu–N coordination. Most copper nitride semiconductors display low band gaps (E_g = 1.4 and 1.5 eV for Cu_3N and $CuTaN_2$ respectively[353,357]) making them ideal for solar absorption. Cu_3N is also identified as *defect tolerant* due to the antibonding character of its band maxima and minima aiding the efficiency of a photovoltaic device.[355,358]

Going beyond copper oxides for pellucid *p*-type conductivity provides a much bigger phase space and thus greater potential for success in designing low hole effective mass, degenerately dopable materials. Technological breakthroughs in thin film and solid state synthesis procedures allow for the fabrication of 'designer' layered compounds. Through this, greater control is achievable allowing previously unobtainable metastable or hard-to-synthesise layered compounds to be realised.[359–361] In the next few chapters, emphasis will be on structure-property relationships based upon the CMVB and post oxide TCs. In particular, the prediction of new layered oxychalcogenides based on the SCSOS structure (Figure

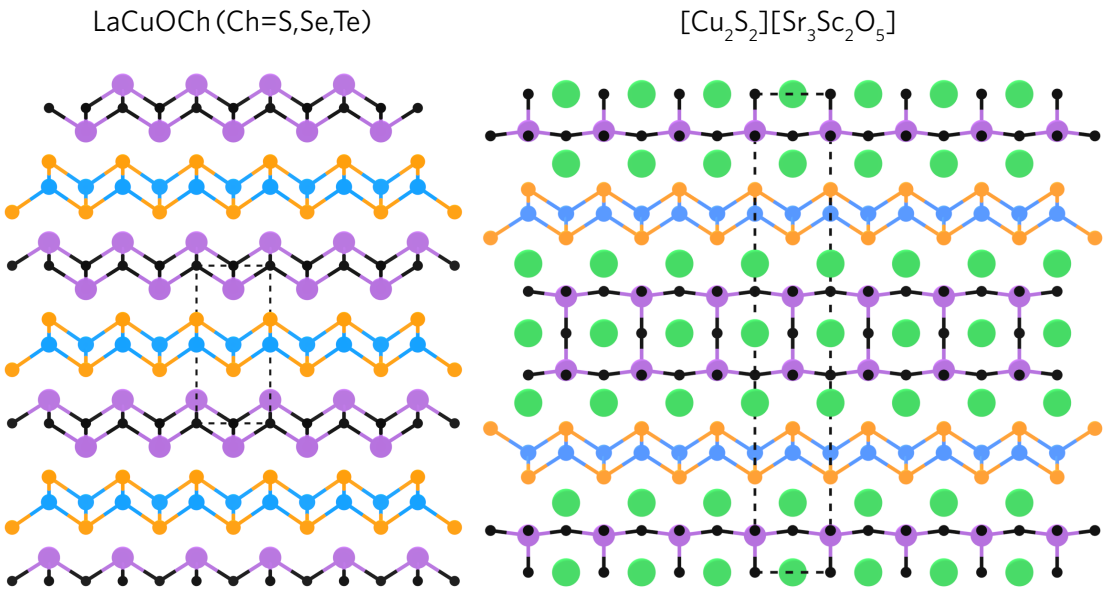

FIGURE 5.3: The crystal structures of LaCuOCh (Ch = S,Se,Te) (*P4nmn*) and $[Cu_2S_2][Sr_3Sc_2O_5]$ (*I4/mmm*) layered oxychalcogenides. Both structures have the same tetrahedral $[Cu_2S_2]^{2-}$] layer responsible for *p*-type conduction. For the two structures: Cu=blue, O=black, Ch/S=orange, La^{3+}/Sc^{3+}=purple and Sr=green.

5.3) with an analysis of the effect of isovalent cations on the electronic and thermodynamic properties. Beyond SCSOS is the extension of the CMVB from chalcogenides and nitrides to copper phosphides illustrating the need for intuitive chemical design for highly dispersive valence band maxima.

Chapter 6

Next Generation *p*-Type Transparent Conductors

6.1 Elemental Modulation of $[Cu_2S_2][Sr_3Sc_2O_5]$

Experimental solid state synthesis of $[Cu_2S_2][Ba_3Sc_2O_5]$ powders and subsequent analysis were carried out by Mr. Gregory J. Limburn in the group of Dr Geoffrey Hyett at the University of Southampton. Details of the experimental and theoretical methodologies are included in Appendix B.1.
The work in this section is in preparation for publication.

$[Cu_2S_2][Sr_3Sc_2O_5]$, denoted 'SCSOS', is a layered oxychalcogenide with a wide band gap suitable for visible light transparency (~ 3.1 eV), which possesses high *undoped* *p*-type conductivity (2.8 $S\,cm^{-1}$) and reported mobilities surpassing that of the industry standard *n*-type TCOs (150 $cm^2\,V^{-1}\,s^{-1}$).[351,352,362] The SCSOS structure consists of an anti-PbO (litharge) $[Cu_2S_2]^{2-}$ layer alternating with perovskite-like $[Sr_3Sc_2O_5]^{2+}$ layers (Figure 6.1). Previous hybrid DFT calculations have found that the VBM is made up of a 1:1 mixing between Cu 3*d* and S 3*p* states typical of the chemical modulation of the valence band (CMVB) as seen in the delafossite $CuAlO_2$.[322] Hole effective masses calculated using HSE06 were found to be

anisotropic with low values of 0.96 m_e. Although this value is lower than the rest mass of an electron, it is still around three times as large as the n-type effective masses seen in Section 3.2.1 causing doubt on the experimental mobility values.[351] As a quinternary material, a large number of potential compounds relating to the SCSOS structure are possible and could provide an insight into the design of a high mobility p-type transparent conductor. Using suitable 'chemical intuition', this space can be narrowed and as such new materials can be screened in terms of their properties. In this section, 24 stoichiometric compounds with the $[Cu_2S_2][A_3B_2O_5]$ structure: where A=Sr,Ca,Ba,Mg and B=Sc,Al,Ga,In,Sc,Y,La were screened in terms of their thermodynamic stability and thereafter in terms of their electronic properties. Each of the 24 compounds is named 'AB' eg. $[Cu_2S_2][Sr_3Sc_2O_5]$ is 'SrSc', $[Cu_2S_2][Ba_3Al_2O_5]$ is 'BaAl' and $[Cu_2S_2][Ca_3Ga_2O_5]$ is 'CaGa' Each structure was relaxed using PBEsol[14,16] to determine the thermodynamic stability and a further relaxation using the hybrid HSE06 functional was utilised to calculate the structural and electronic properties of the stable compounds. Further details of the theoretical methodology is presented in Appendix B.1.

6.1.1 Thermodynamic Stability Screening

The thermodynamic stability of the 24 compounds at 0K was calculated relative to ~313 (geometry relaxed) competing stable phases taken from the Inorganic Crystal Structures Database (ICSD).[363] A stability criterion was established from the energy above the convex hull and ranges from 0–0.07 eV atom^{-1} following work by Ceder and coworkers.[364] An absolute maximum can also applied based upon the synthesis temperature (k_BT, where T = ~ 800°C) in reference [351 which gives an E above Hull of 0.09 eV atom^{-1} (shown by the red line in Figure 6.2). Out of the 24 compounds calculated, 9 compounds were identified within this stability criterion. The energies above the convex hull are tabulated in Appendix B.1; Table B.1 and those within the 0–0.2 eV atom^{-1} range are displayed in Figure 6.2. Using this analysis, SrAl, SrGa, CaAl, CaGa, BaGa and BaSc are predicted to be stable with energies above hull of 0 eV atom^{-1}. The parent compound, SrSc is also predicted to be stable with an energy above the hull of 0.0005 eV atom^{-1}. CaSc and BaAl are predicted to be metastable with energies of 0.05 and 0.07 eV atom^{-1} respectively. CaSc and BaAl are expected to form but may not be phase pure when synthesised and as such other compounds may be present. All the compounds where A^{2+}=Mg and B^{3+}=In,Y,La were found to be unstable.

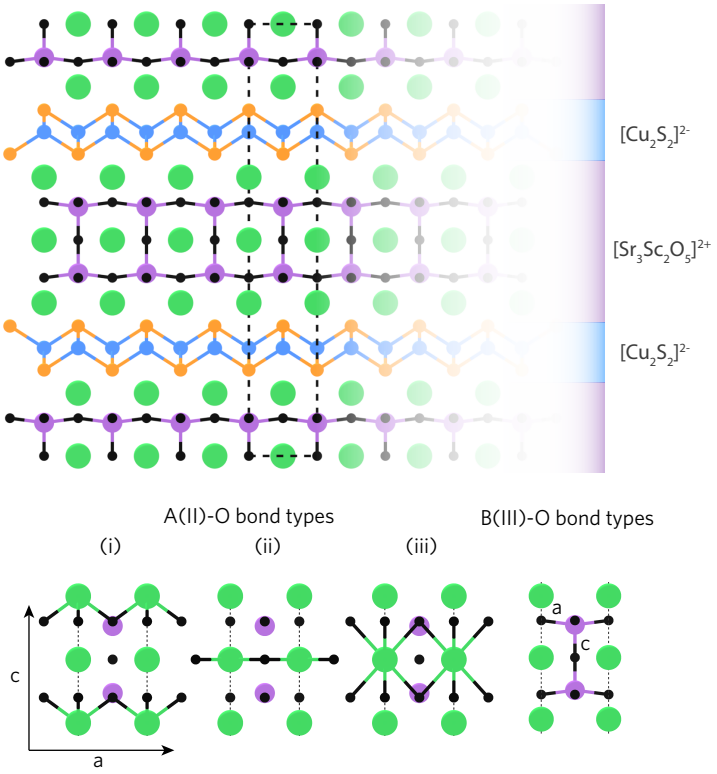

FIGURE 6.1: The $[Cu_2S_2][Sr_3Sc_2O_5]$ crystal structure as viewed along the (100) direction. The different layers are also shown where Cu=blue, S=orange, Sr=green, Sc=purple and O=black. Also shown are the different types of bonds within the $A_3B_2O_5{}^{2+}$ layer, the different bond lengths associated with these types are given in Table 6.2.

The decomposition pathway for SrSc is predicted to be:

$$[Cu_2S_2][Sr_3Sc_2O_5] \rightarrow 8\,Cu + 7\,SrS + 4\,SrSc_2O_4 + SrSO_4; \Delta H = 0.05\,eV \qquad (6.1.1)$$

Where the decomposition energy ($\Delta H = 0.05$ eV) corresponds to a temperature of ~307°C which is far below the synthesis temperatures used by Liu et al. (800°C) and hence will be expected to be formed "phase pure" as is seen from their X-ray diffraction (XRD) patterns.[351] The decomposition products of all the other compounds are tabulated in Appendix B.1; Table B.1.

Another analysis can be undertaken using the synthesis route carried out by Liu et al.[351]

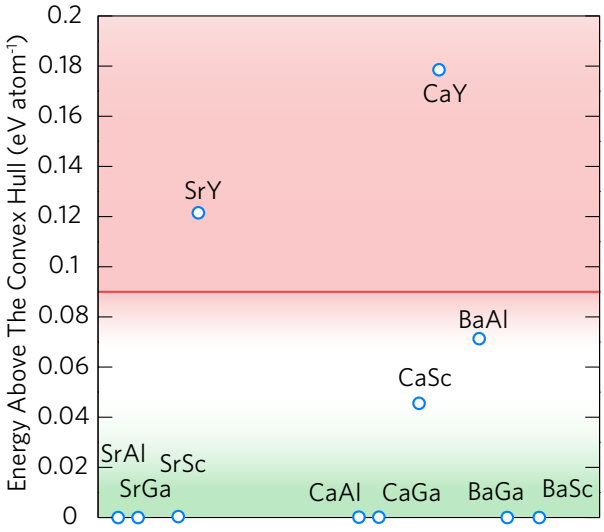

FIGURE 6.2: A depiction of the stable and metastable compounds with respect to the stability criterion 0–0.09 eV atom^{-1}. The green area is the predicted "stable" region (0–0.02,eV atom^{-1}), the white region depicts the area of metastability (0.02–0.09 eV atom^{-1}) and the red region the unstable region (> 0.09 eV atom^{-1})). The graph predicts eight potentially stable variations on the $[Cu_2S_2][Sr_3Sc_2O_5]$ structure.

and is given in equation 6.1.2. The tabulated enthalpies of formation (ΔH_f) are shown for all *stable* compounds in Table 6.1 (and for all compounds in Appendix B.1; Table B.1).

$$AS + Cu_2S + B_2O_3 + 2AO \rightarrow [Cu_2S_2][A_3B_2O_5] \tag{6.1.2}$$

TABLE 6.1: The enthalpies of formation (ΔH_f) generated from equation 6.1.2 for each *stable* compound.

Compound	ΔH_f /eV
CaAl	-12.17
SrAl	-1.10
BaAl	-0.81
CaGa	-12.34
SrGa	-1.83
BaGa	-2.15
CaSc	-8.31
SrSc	-0.61
BaSc	-1.42

In Table 6.1, all stable compounds show a negative formation enthalpy and thus are expected to form via this synthetic route, indeed the Ca-based SCSOS compounds should form easily with enthalpies ranging from ca. -8 to -13 eV. It is important to note, however, that other competing phases may also form in the synthesis.Despite the metastability of both CaSc and BaAl, both compounds are expected to be formed via this synthetic route. In terms of the other compounds (Appendix B.1; Table B.1), this analysis shows that positive formation energies are seen for the majority of unstable compounds (ie. all Mg structures, SrY, SrLa etc.) however, anomalies arise with CaIn, CaY and BaY where negative formation energies are observed despite having energies above hull outside of the stability criterion. For these compounds, the synthesis in reference [351] may not be the intuitive route.

6.1.2 Geometric and Structural Properties

All stable compounds exhibit the same *I4/mmm* crystal structure as the parent compound after relaxation. Each compound consists of the same anti-PbO $[Cu_2S_2{}^{2-}]$ layer alternating with the perovskite-like $[A_3B_2O_5]^{2+}$ as seen in SrSc (SCSOS). The coordination in the copper sulphide layer consists of tetrahedrally bonded Cu ions (with S) in which the S ions are bonded to Cu in a square pyramidal structure and likewise to A^{2+} cations. Within the $[A_3B_2O_5]^{2+}$ layer, there exists tetrahedrally bonded B^{3+} cations to O, which in turn are linearly bonded between two B^{3+} cations and within a square planar motif with adjacent A^{2+} ions. The A^{2+}

cations are generally coordinated in a square anti-prismatic configuration either with 8 oxygens or 4 oxygens and 4 sulphurs.

Cell parameters:

Table 6.2 (page 105) displays the structural parameters for all the stable compounds and are grouped according to increasing cationic radii of the B^{3+} cation (Al→Ga→Sc) and within these groups are ordered by increasing A^{2+} radii (Ca→Sr→Ba). The calculated lattice parameters and bond lengths for the parent compound, SrSc, are in excellent agreement with the experimental values[352] showing the efficacy of HSE06 to reproduce the crystal structure and thus predict the electronic properties of all 24 compounds. As expected when increasing the size of both A^{2+} and B^{3+} cations, the cell parameters, volumes and bond lengths all increase whilst retaining the *I4/mmm* crystal structure. In terms of volume change, within the Al, Ga and Sc compounds (Ca→Ba) an increase in volume by ~ 20%, ~ 18%, and ~ 16%, is seen for each group respectively. The $a(c)$ parameters expand by ~ 5(10)%, ~ 4(10)%, and ~ 3(9)% between Al, Ga and Sc respectively. The greater increase in the c direction is to be expected due to an increase in A^{2+} radii down the group and remains constant between the three different B^{3+}groups (Al,Ga,Sc). The lack of change within the a direction for Sc compared to Ga and Al is likely due to the decreased electronegativity of Sc relative to Al and Ga. The c lattice parameter, whilst extending with increasing *a within* the B^{3+} groups (Al,Ga,Sc), does not increase linearly with increasing a lattice parameter overall. CaSc, displays a smaller c lattice parameter to both CaAl and CaGa, despite the larger atomic radii.[240]

$[Cu_2S_2]^{2-}$ layer:

Previous HSE06 studies carried out on SrSc[362] showed that the $[Cu_2S_2]^{2-}$ layer is responsible for the states that form the VBM and are thus the most important for *p*-type conductivity. The layered oxychalcogenides: LaCuOS and LaCuOSe also possess a $[Cu_2S_2]^{2-}$ layer which give rise to the VBM similar to the SCSOS compounds.[343] Figure 6.3 displays the change in valence band related bond lengths and angles comparative to the increasing basal lattice parameter (a). For each group, it is clear that through increasing the size of the cell there is a proportional increase in Cu–Cu, Cu–S, A^{2+}–S bond lengths as well as S–Cu–S bond angles for each group (Al, Ga, Sc). This allows for a general comparison of the basal lattice parameter (a) to the individual electronic and structural properties of the system. The Cu–Cu bond lengths increase from 2.63 Å for CaAl to 2.94 Å for BaSc due to the increasing A^{2+} and the

B^{3+} cationic radii. An increased Cu–Cu distance is required to avoid $d-d$ transitions which hamper the transparency.[322] The Cu–S distances typically plateau for Sr and Ba in each group (Al,Ga,Sc) and have a minimum bond length of 2.39 Å for CaAl and a maximum of 2.45 Å for BaSc. These results lie within the typical range of other copper sulfide based materials such as CuS (~ 2.10-2.35Å)[365], Cu_2S(~ 2.27-2.35Å)[366,367] as well as the layered oxysulfide LaCuOS (~ 2.42Å).[349] It is likely that the Cu–S bond length *restrains* the systems from expanding further and hence partially dictates the stability of the SCSOS structure to accommodate the different variations. Judging from the increase in bond length from LaCuOS to LaCuOSe and even LaCuOTe[344,349,368] (2.42→ 2.52 →2.66 Å) *selenide* or *telluride* based SCSOS system may be able to accommodate the increasing cell size and hence larger A^{2+} and B^{3+} cations such as Y or La.

The S–Cu–S bond angles increase linearly with increasing *a* as expected from increasing the width of the unit cell producing a 'concertina' effect on the $[Cu_2S_2]^{2-}$ layer. The calculated HSE06 value for SrSc is in reasonable agreement with experiment, overestimating slightly by ~ 5°.[352] The linear trend is broken slightly from SrSc to BaSc and is possible that a limit to the bond angle is occurring; any larger cells would likely become strained favouring either a different crystal structure, or the use of Se or Te within the $[Cu_2S_2]^{2-}$ layer. Cu_2S is known to have a S–Cu–S bond angle of 109.5°[366,367] and LaCuOS possesses one of 108.63°.[349]

The A^{2+}–S bond lengths were also calculated in order to establish an "inter-layer spacing" between the two layers ($[Cu_2S_2]^{2-}$ and $[Sr_3Sc_2O_5]^{2+}$]). Within each B^{3+} (Ca,Sr,Ba) group the increase is linear with respect to *a*, and to an extent *between* the different B^{3+} groups (Al,Ga,Sc). The maximum percentage increase within the Al, Ga and Sc groups is 8%, 7% and 5% respectively. This reduction may be attributed to the increase in electronegativity between Al and Ga over Sc, thus the Al and Ga related bond possess a greater constraint over individual unit cells over the Sc compounds.

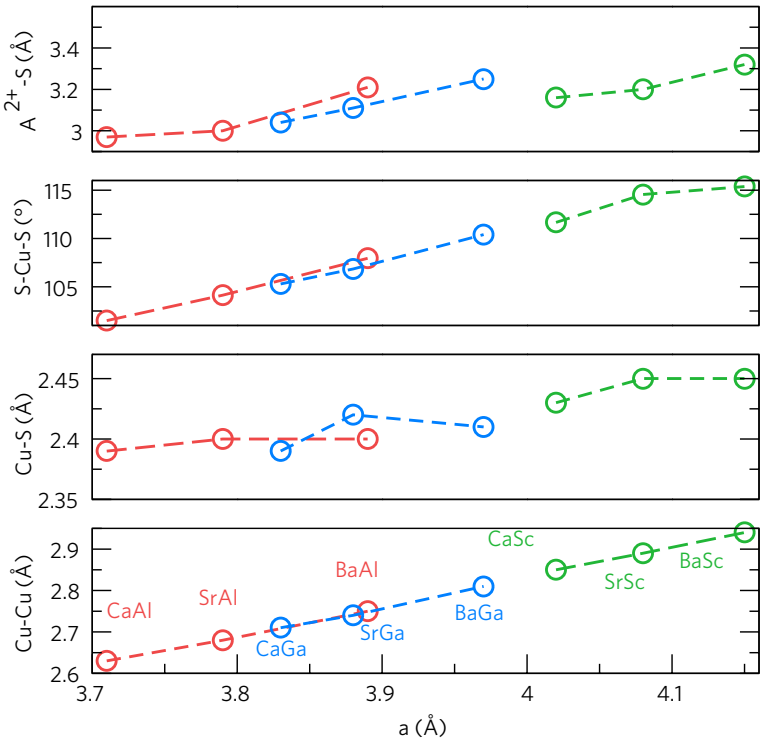

FIGURE 6.3: The bond lengths and angles related to the valence band ($[Cu_2S_2]^{2-}$ layer), Cu–Cu, Cu–S, S–Cu–S and A^{2+}–S with respect to increasing basal lattice parameter.

$[A_3B_2O_5]^{2+}$ layer:

The average B^{3+}–O and A^{2+}–O bond lengths increase relative to both *a* and *c* lattice parameters within each B^{3+} group linearly. For the B^{3+}–O bond lengths, the analysis can be split into the effect of the *a* and *c* directions due to the tetrahedral bonding of B^{3+}. The different bond types are shown in Figure 6.1. Table 6.2 provides the values for both directions, and shows that in the *a* direction the bond length increases linearly with increasing basal lattice parameter. For the Al, Ga and Sc groups the increase in B^{3+}–O is 5%, 4% and 3% respectively (from Ca→Sr→Ba) which is directly proportional to the percentage increase of *a* in section 6.1.2. The bond lengths in the *c* direction however, show very little increase between Ca and Sr for each group however between Sr and Ba this is ~ 1% , 2% and 0.5% within the Al, Ga and Sc groups respectively.

The A^{2+}–O bond lengths show that within the *ab* plane (A^{2+}–O[b]) a linear increase with increasing *a* parameter is seen as expected with an increase of 5%, 4% and 3% within the Al, Ga and Sc groups respectively. A^{2+}–O[a][c] increase as a function of both *a* and *c*.

TABLE 6.2: The structural parameters and bond lengths for all stable predicted compounds calculated using HSE06. The compounds are ordered in groups relating to B^{3+} and within these groups in terms of increasing cell lattice parameter (a)(any experimental results are shown in italics). The different A^{2+}–O and B^{3+}–O bond types are shown in Figure 6.1.

Compound	a /Å	c /Å	vol /Å^3	Cu–Cu /Å	Cu–S /Å	S–Cu–S /°	B^{3+}–O (c,a) /Å	A^{2+}–O (i,ii,iii)/Å	A^{2+}–S /Å
CaAl	3.71	25.66	353.84	2.63	2.39	101.50	1.78,1.88	2.36,2.63,2.78	2.97
SrAl	3.79	26.77	384.47	2.68	2.40	104.13	1.78,1.92	2.51,2.68,2.82	3.00
BaAl	3.89	28.26	427.34	2.75	2.41	107.95	1.80,1.97	2.69,2.75,2.89	3.21
CaGa	3.83	25.66	376.07	2.71	2.39	105.30	1.87,1.93	2.37,2.71,2.90	3.04
SrGa	3.88	26.72	401.88	2.74	2.42	106.85	1.87,1.96	2.53,2.74,2.91	3.11
BaGa	3.97	28.22	445.08	2.81	2.41	110.40	1.91,2.01	2.70,2.81,2.99	3.25
CaSc	4.02	25.25	407.69	2.85	2.43	111.67	1.98,2.03	2.41,2.84,3.01	3.16
SrSc	4.08	26.07	433.45	2.89	2.45	114.55	1.97,2.05	2.55,2.88,3.04	3.20
SrSc[352]	*4.08*	*25.99*	*433.45*	*2.88*	*2.49*	*110.00*	*1.91,2.07*	*2.51,2.88,3.05*	-
BaSc	4.15	27.44	472.11	2.94	2.45	115.37	1.99,2.09	2.70,2.93,3.07	3.32

6.1.3 Electronic and Optical Properties

Density of States:

Figure 6.4(a), (b) and (c) (Page 109) shows the total and partial density of states (DOS) for SrAl, SrGa and SrSc respectively which will be used as representatives of each group in this analysis. Table 6.3 displays the percentage of states at the VBM along with valence band widths and Table 6.4 display the percentage of states at the CBM. Full plots of the partial and total DOS are shown in Appendix B.1 Figure B.1.

Within each B^{3+} group the composition of the upper valence band remains the same with only the valence band widths changing amongst the groups. Figure 6.3a, b and c shows the DOS for SrAl, SrGa and SrSc which can be used to describe each B^{3+} group. In general the valence band widths decrease with increasing A^{2+} cation radius and are inversely proportional to the S–Cu–S angle. A more obtuse S–Cu–S angle therefore results in a smaller valence band width. In the same vein it it would follow that the valence band width would decrease from SrAl→SrGa→SrSc due to the same increase in S–Cu–S angle due to the increasing size of B^{3+}, however this is not the case. As shown in Figure 6.4, both Al and Ga $s+p$ states are present from ~ -10 eV to ~ -7 eV. From -7 eV to ~ -5 eV in SrAl and SrGa, significant mixing between O p, Sp, Cud and Al/Ga p states is seen. In SrSc, from -6 eV to -4 eV the majority of states in the valence band is made up of O p, S p, Cud and Sc d states. From this point the compounds become very similar with a large proportion of the states belonging to Cu d mixed with O p states in a nearly 50:50 ratio from ~ -3 eV to ~ -2 eV. From -2 eV to the VBM (0 eV) Cu d states hybridise with S p states over O p almost exclusively in ~ 55:~ 41 Cu:S ratio with negligible contributions from Cu p, Sr $p+d$ and O p states (Table 6.3). These results are consistent with previous HSE06 calculations on SrSc by Scanlon et al.[362] as well as with the similar layered oxychalcogenides: LaCuOCh (where Ch=S,Se,Te).[345]

The states at the CBM are shown in Table 6.4 where the states vary with each group of compounds. Within the aluminium compounds, it is clear that a hybridisation between both the Cu s, S s and Al s and O s states generally make up the CBM. From Ca→Sr→Ba, the larger cell sizes increases the proportion of Al s states seen at the CBM from 5%→14%→30% respectively. A decrease in overall Cu and S states seen at the CBM is also observed making up 58% in SrAl to just 25% in BaAl. In CaAl, a significant mixing of Ca s states is present at the CBM, which could likely be due to the CaAl possessing the smallest A^{2+}–S bond length (2.97 Å). An

TABLE 6.3: The percentage of states at the VBM in the thermodynamically stable SCSOS compounds together with the width of the valence band. Significant contributions are indicated in bold. The total DOS and partial DOS is displayed in Appendix B.1 Figure B.1.

Compound	Cu:s,p,d /%	S:s,p,d /%	A^{2+}:s,p,d/%	B^{3+}:s,p,d /%	O:s,p,d /%	VB width /eV
CaAl	0,1,**49**	0,**45**,0	0,2,2	0,0,0	0,1,0	9.5
SrAl	0,1,**51**	0,**45**,0	0,1,1	0,0,0	0,1,0	9.2
BaAl	0,1,**52**	0,**43**,0	0,1,1	0,0,0	0,1,0	9.2
CaGa	0,1,**52**	0,**44**,0	0,2,2	0,0,0	0,1,0	10.3
SrGa	0,1,**53**	0,**44**,0	0,1,1	0,0,0	0,1,0	10.0
BaGa	0,1,**53**	0,**42**,0	0,1,1	0,0,0	0,1,0	9.9
CaSc	0,1,**55**	0,**41**,0	0,1,1	0,0,0	0,1,0	5.9
SrSc	0,2,**55**	0,**41**,0	0,1,1	0,0,0	0,2,0	5.5
BaSc	0,2,**55**	0,**41**,0	0,1,1	0,0,0	0,1,0	5.4

increase in O $s+p$ states is observed down group 2. From the CBM to the peak at 4 eV in SrAl, the CBM consists of a hybridisation between the Cu *s*, Cu *d* and O *p* states mixed with predominantly Sr *d* states. From 4 eV to 6 eV the conduction band is primarily Sr *d* states mix with some O *p* and a small amount of Cu *s* states around 5.6 eV.

In the gallium systems, a reduction in the Cu *s* and S *s* states are seen at the CBM, with predominantly Ga $s+$O*s* mixing observed. Down group 2, an increase in the Ga *s* states is observed with a further reduction in the Cu and S states from 19%→14%→5% (from CaGa→SrGa →BaGa respectively). A similar effect is seen in the band alignment of AlN, GaN and InN where, due to the increasingly penetrating *s* orbitals down the group means that the CBM lies lower in energy from AlN to GaN to InN.[95] From ~2.7 eV to the peak at 4 eV, the conduction band of SrGa consists of an increasing hybridisation between the Ga $s+$ O *p* states that make up the CBM and the Sr *d*, Cu $s+d$ and S *p* states. This is consistent with the peak at 4 eV in SrAl (Figure 6.4(a)) which possesses an increased Sr *d* presence. From 4 eV to 6 eV the CBM is predominantly Sr *d* states mixed with some O *p*, Cu *s* and Al *s* states.

The CBM of the scandium compounds consist of negligible quantities of Sc in contrast to the aluminium and gallium compounds. The CBM is predominantly Cu *s* and S$s+p$ with significant mixing from A^{2+} states. From Ca→Sr→Ba, the Cu *s* states increase from 21% to 34% in contrast to the Al and Ga compounds where increasing A^{2+} resulted in *less* Cu and S states at the CBM. Between CaSc and SrSc, a reduction in A^{2+} *s* states is seen from 18% to 13% respectively. BaSc shows that the Ba *d* states dominate at the CBM with no S *s* or *p* states

observed (as with CaSc and SrSc). This is likely due to the decreased Ba–Cu distance over Ca–Sc and Sr–Sc respectively due to the 'concertina' effect of the $[Cu_2S_2]^{2-}$ layer and thus a more compact unit cell. In SrSc, the conduction band from the CBM to 6 eV consists of an increasing proportion of Sr *d* and Sc *d* states. Towards 6 eV an increased hybridisation with O *p*, S *p* and Cu *s* states is seen.

TABLE 6.4: The percentage of states at the CBM in the thermodynamically stable SCSOS compounds. Significant contributions are indicated in bold. The total DOS and partial DOS is displayed in Appendix B.1 Figure B.1.

Compound	Cu:s,p,d /%	S:s,p,d /%	A^{2+}:s,p,d/%	B^{3+}:s,p,d /%	O:s,p,d /%
CaAl	**20**,0,0	**28**,10,0	**22**,4,0	5,1,0	8,2,0
SrAl	**22**,0,1	**29**,5,0	8,2,1	**14**,2,0	**13**,5,0
BaAl	**11**,0,2	**14**,0,0	8,0,9	**30**,3,0	**17**,6,0
CaGa	8,0,1	**11**,0,0	7,1,0	**51**,3,1	**17**,0,0
SrGa	6,0,1	8,0,0	2,0,1	**56**,2,0	**23**,0,0
BaGa	2,0,1	2,0,0	1,0,1	**68**,4,0	**16**,0,0
CaSc	**20**,0,1	**32,11**,0	**18**,1,1	2,0,3	9,0,0
SrSc	**24**,0,1	**33,13**,0	**13**,3,0	3,0,3	6,2,0
BaSc	**34**,0,15	0,0,0	0,0,**47**	0,0,0	2,1,0

Band Structure and Optical Gap:

The band structures of all stable SCSOS compounds are presented in Figure 6.5 (Page 110) and the direct,indirect and optical band gaps together with hole and electron effective masses at the VBM and CBM respectively are shown in Table 6.5. The value for the optical band gap is taken from the α^2 value in the absorption spectra compiled for each of the 9 compounds in Appendix B.1 Figure B.3.

From our calculations, 3 of the 24 SCSOS compounds are found to be transparent: CaAl, SrSc and BaSc with optical band gaps of 3.17 eV, 3.06 eV and 3.24 eV respectively. The optical absorption for SrSc (3.06 eV) is in accordance with the optical band gap seen in experiment by Liu et al. who observed a band gap around 3.1 eV.[351] It is possible that SrAl will be transparent,

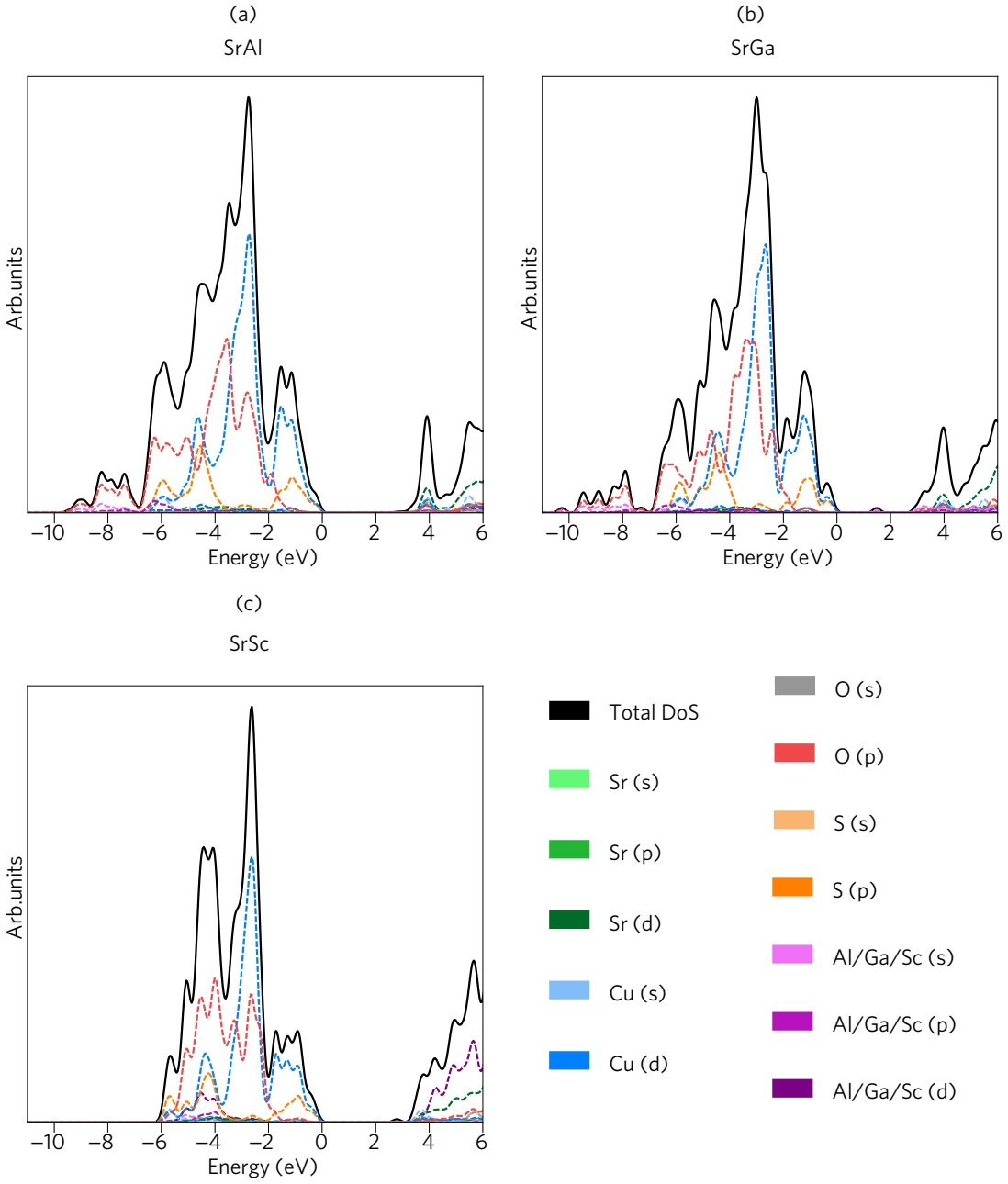

FIGURE 6.4: Representative density of states (DOS) for the different groups, SrAl, SrGa and the parent compound: SrSc. In each example the valence band maximum is set to 0 eV. Full partial and total DOS for all other compounds can be found in Appendix B.1 Figure B.1.

however, colouring or haze may arise due to the 3.00 eV optical band gap. In general the optical band gaps correspond to the direct fundamental band gap at Γ, however CaAl and

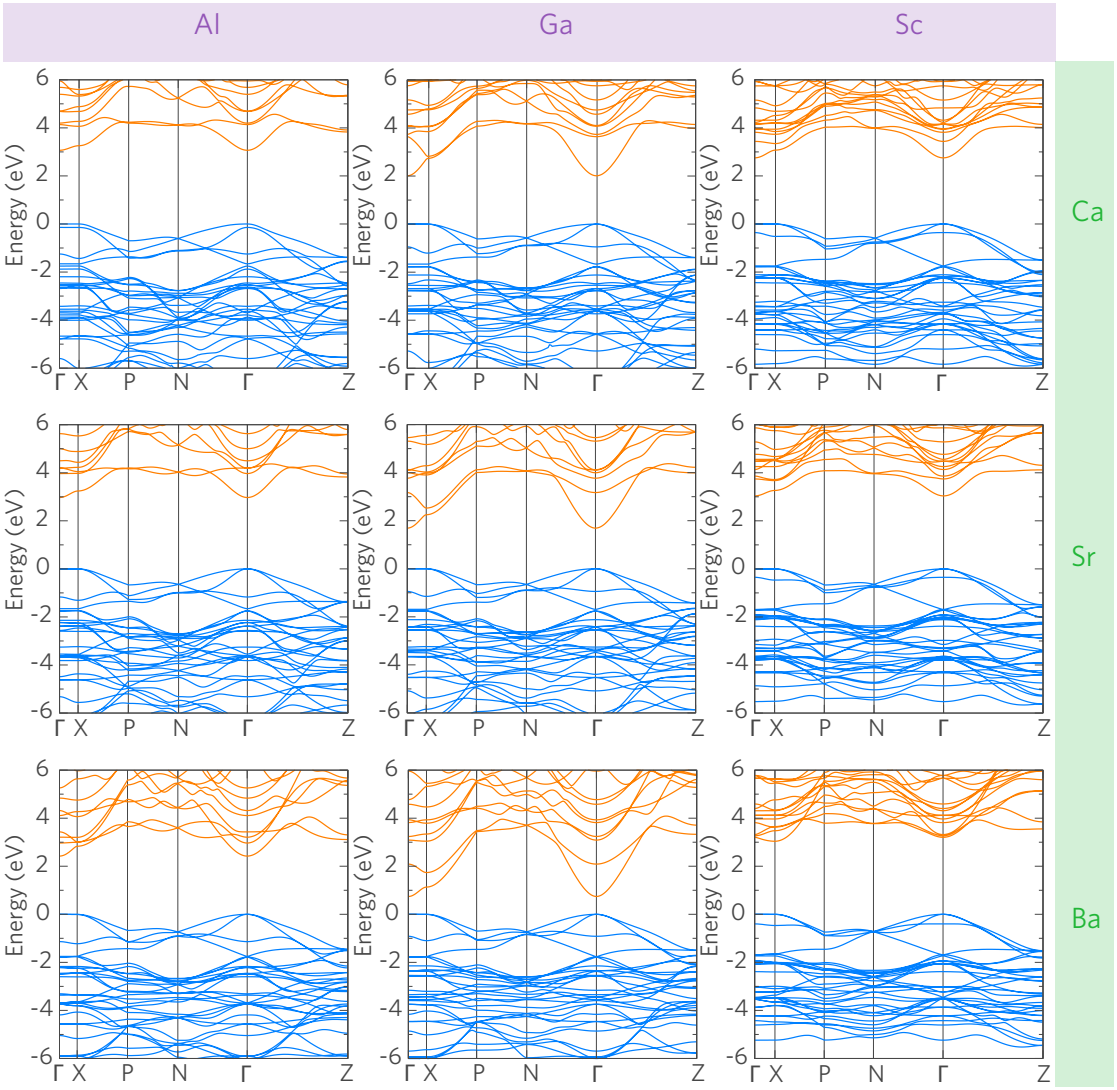

FIGURE 6.5: The combined band structures for the stable and metastable SCSOS compounds calculated using the HSE06 functional. The band structures are arrayed in a grid such that the top left corresponds to CaAl and the bottom right to BaSc. In the stable examples, the valence bands are depicted in blue and the conduction bands in orange, where the VBM is set to 0 eV. The band structures are ordered in terms of increasing A^{2+} cation (Ca→Sr→Ba) and in terms of increasing B^{3+} cation (Al→Ga→Sc).

BaSc this is not the case. BaSc is the only compound to possess an *indirect* fundamental band gap where the VBM and CBM are located at Γ and X respectively. Due to the flat bands from Γ–X, the difference between the two high symmetry points is generally around 0.002 eV for each compound. The indirect and direct band gap at X (BaSc) is, however, a *disallowed*

transition due to the *d* nature of both the VBM (Cu *d*) and CBM (Ba *d*). The direct band gap at Γ (3.20 eV) is, however, an allowed transition. In CaAl, the origin of the optical band gap occurs from the band below the VBM which lies ~ 0.15 eV lower in energy. This accounts for the larger optical band gap to the fundamental band gap.

Figure 6.6(a) shows the change in direct fundamental band gap as a function of *a* parameter. In both Al and Ga compounds the band gap shrinks as a function of increasing cell size. This can be attributed to the increased presence of Al and Ga *s* states at the CBM down from Ca→Sr→Ba from an increased interlayer spacing. Due to the larger penetration of the Ga 4*s* states over Al 3*s*, the CBM is lowered further in the gallium compounds over the aluminium compounds. The lower band gap, however does allow for a greater dispersion at the CBM and thus a lower electron effective mass as seen in both the band structures in Figure 6.5 and the effective masses in Table 6.5.

Conversely, the scandium compounds which see negligible Sc *s* and *d* states at the CBM (and appear around ~ 1 eV above the CBM in SrSc) show a widening of the fundamental band gap with increasing *a* parameter. The band gap, therefore is highly sensitive to the different states at the band maxima and minima and no one rule can be used to describe all compounds.

In order to possess high hole mobilities and thus produce degenerate *p*-type conductivity, the effective masses at the VBM must be low. For 8 out of the 9 compounds (CaAl excluded) there exists two degenerate bands at the VBM allowing for the calculation of a 'heavy' and 'light' effective mass. These values are presented in Table 6.5 and show that in the Γ–N and Γ–Z directions, the parent compound (SrSc) experiences 'heavy' effective masses of 1.70 m_e and 0.68 m_e respectively. In the same directions, *light* hole effective masses of 0.48 m_e and 0.65 m_e are calculated respectively owing to the relatively high (for a *p*-type TC) undoped conductivity seen in experiment of 2.8 S cm^{-1}.[351]

Figure 6.6(b) shows the trends of the hole effective masses as a function of *a* parameter for the Γ–N and Γ–Z directions for each group of compounds. For the aluminium and gallium compounds, the heavy effective masses in the Γ–N direction *decrease* as a function of increasing *a* size with maximum values of 4.54 m_e and 3.45 m_e respectively and minimum values of 2.22 m_e and 2.04 m_e respectively. The scandium compounds possess the lowest 'heavy' hole effective masses in the Γ–N direction. Inverse to the Al and Ga compounds, these effective masses *increase* from 1.34 m_e → 1.70 m_e → 1.72 m_e from CaSc→SrSc→BaSc respectively.

The 'light' hole effective masses in the Γ–N direction remain relatively constant in both

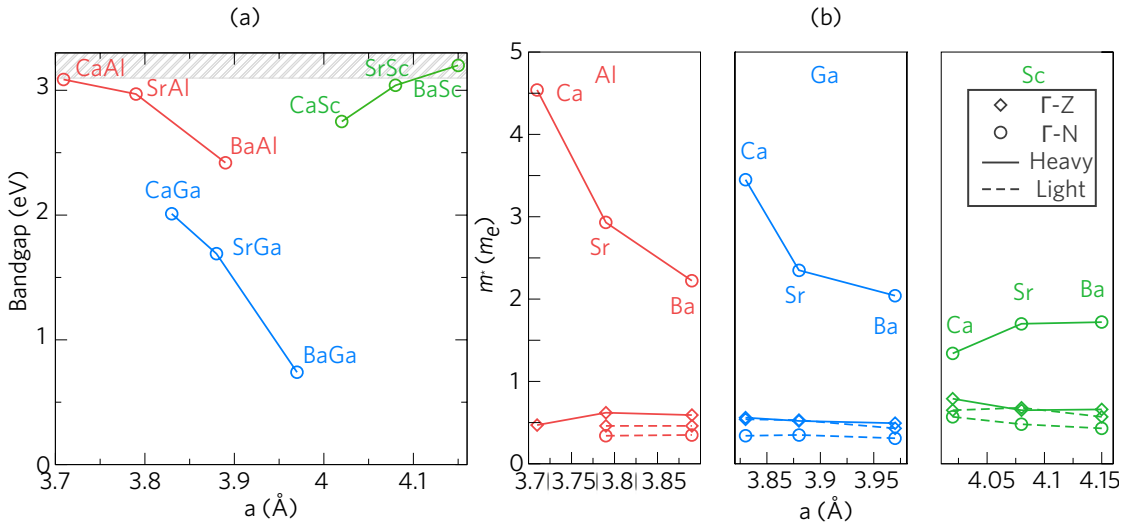

FIGURE 6.6: (a) The direct fundamental band gap as a function of increasing *a* parameter. The hashed grey region corresponds to the visible light transparency region. (b) The VBM hole effective mass as a function of increasing *a* parameter.

the Al and Ga compounds with average effective masses of 0.35 m_e and 0.33 m_e. The scandium compounds experience a slight decrease in magnitude from 0.57 m_e for CaSc to 0.43 m_e for BaSc.

In the Γ–Z direction both heavy and light hole effective masses are low. From CaAl to BaAl, the heavy effective masses increase slightly from 0.47 $m_e \rightarrow 0.59 m_e$ whilst the light hole masses remain constant at 0.46 m_e. In the gallium compounds a slight *decrease* is seen in both the heavy and light effective masses with the highest effective mass being for CaGa (0.56 m_e) and the lowest being for BaGa (0.43 m_e). CaSc, SrSc and BaSc possess the highest effective masses in this direction which decrease with increasing *a* parameter for both the heavy and light holes. The light effective masses for CaSc, SrSc and BaSc are 0.65 m_e, 0.65 m_e and 0.57 m_e respectively.

From Γ–X, however, the hole effective masses are very high (40.38–41.71 m_e) due to the very flat bands as can be seen in the band structure (Figure 6.5). This is likely due to a lack of overlap between the Cu *d* and S *p* tetrahedra in the $[Cu_2S_2]^{2-}$ layers. The Γ–X direction corresponds to the *ab* plane (Appendix B.1 Figure B.2 shows the first Brillouin zone) and hence with an increasing 'flattening' of this layer due to the more obtuse S–Cu–S angles with larger cation sizes, it is expected that a better overlap between Cu and S will occur and thus lower hole effective masses in the Γ–X direction. This effect is certainly the case

for both the aluminium and gallium compounds where the effective masses reduces from 64.40 m_e →15.60 m_e and 45.56 m_e → 25.28 m_e respectively. The scandium compounds, however, do not see the same trend with the largest values seen for SrSc. Due to the very high mobilities (150 $cm^2\,V^{-1}\,s^{-1}$).[351] seen in experiment, it is likely that this effective mass in the Γ–X direction does not limit the mobilities as much as the Γ–N and Γ–Z directions do.

In general the *electron* effective masses in all directions decrease as a function of increasing a parameter. Due to the lower lying CBM in the gallium compounds, the lowest electron effective mass is seen for BaGa with an average effective mass of 0.2 m_e competitive with the industry standard n-type TCOs such as In_2O_3 (0.22 m_e).[369] In the scandium compounds, the trend is broken due to the Ba d states forming an indirect band gap with the CBM at X. BaSc therefore possesses the highest electron effective masses of 0.94 m_e (X–Γ) and 0.57 m_e (X–P) out of the stable compounds.

TABLE 6.5: The fundamental direct and indirect band gaps together with the optical band gap for the SCSOS compounds alongside the various effective masses for both the VBM and CBM. The optical gap value is taken from α^2 as seen in Appendix B Figure B.3. The direct gaps for BaSc are displayed for the direct transition at X and the direct transition at Γ.

Compound	E_g^{dir}/eV	E_g^{ind}/eV	E_g^{opt}/eV	$m^*_{[\Gamma-X]}$ / m_e			$m^*_{[\Gamma-N]}$ / m_e			$m^*_{[\Gamma-Z]}$ / m_e		
				VBM (h)	VBM (l)	CBM	VBM (h)	VBM (l)	CBM	VBM (h)	VBM (l)	CBM
CaAl	3.08	-	3.17	*64.40*	-	0.52	4.54	-	0.40	0.47	-	0.31
SrAl	2.97	-	3.00	*43.93*	*41.46*	0.38	2.93	0.34	0.33	0.62	0.46	0.29
BaAl	2.42	-	2.46	*15.60*	*15.94*	0.31	2.22	0.35	0.33	0.59	0.46	0.29
CaGa	2.01	-	2.03	*45.56*	*49.37*	0.23	3.45	0.34	0.24	0.56	0.54	0.22
SrGa	1.69	-	1.71	*39.67*	*40.19*	0.23	2.35	0.35	0.23	0.53	0.52	0.20
BaGa	0.74	-	0.78	*25.28*	*25.52*	0.24	2.04	0.31	0.19	0.49	0.43	0.17
CaSc	2.75	-	2.78	*22.16*	*22.31*	0.36	1.34	0.57	0.33	0.79	0.65	0.30
SrSc	3.04	-	3.06	*40.38*	*41.71*	0.43	1.70	0.48	0.35	0.68	0.65	0.31
BaSc	3.04 (*X*)/3.24 (Γ)	3.04 (Γ–X)	3.24 (Γ–Γ)	29.55	28.57	0.94 (X–Γ)	1.72	0.43	0.31 (X–P)	0.66	0.57	-

6.1.4 Experimental Verification

It is clear from the analysis that the most promising compound is $[Cu_2S_2][Ba_3Sc_2O_5]$ which possesses the largest optical band gap ($\sim 3.24\,eV$) as well as the lightest overall hole effective masses of the three transparent conductors (CaAl, SrSc and BaSc). For this reasoning, the experimental verification of both the existence of this transparent conductor and its structural and electronic properties is required. Experimental powders of BaSc were produced via a solid-state synthesis, the full details of this and the XRD characterisation and optical absorption is provided in Appendix B.1. Table 6.6 provides the structural parameters, bond lengths and optical band gap calculated using the Kubelka-Munk function, $f(R)$ calculated from the diffuse reflectance data. All structural properties are within excellent agreement with the calculated HSE06 values by <1.17 % with a slight overestimation of the c direction. The experimental optical band gap matches exactly that of the HSE06 results. So far no mobility measurements have been carried out on the powders or thin films made which would be the next step of the experimental analysis.

TABLE 6.6: The structural parameters, bond lengths and optical band gap for the BaSc powders.

Parameters	Experiment	HSE06
a /Å	4.14	4.15
c /Å	27.12	27.44
Cu–Cu /Å	2.93	2.94
Cu–S /Å	2.44	2.45
S–Cu–S /°	116.07	115.37
B^{3+}–O(c, a) /Å	2.00,2.08	1.99,2.09
A^{2+}–O (i,ii,iii) /Å	2.71,2.93,3.04	2.70,2.93,3.07
A^{2+}–S /Å	3.30	3.32
E_g^{opt} /eV	3.24	3.24

6.1.5 Discussion

From our analysis, the discovery of two *novel* *p*-type transparent conductors has been predicted using hybrid density functional theory. These compounds are CaAl and BaSc with optical band gaps of 3.17 eV and 3.24 eV respectively. Recent experimental synthesis of BaSc powders confirm the predictions gained from DFT in particular the wide optical band gap making BaSc a novel *p*-type transparent conductor. From the structural analysis, a clear trend can be seen based on the *a* lattice parameter which directly influences the Cu–Cu and Cu–S bond lengths as well as the S–Cu–S bond angles. With increasing cell size, a narrowing of the $[Cu_2S_2]^{2-}$ layer is seen which influences the curvature and width of the valence band and thus directly affecting the electronic properties. In the delafossite Cu^{1+} oxides, it was found that conductivity can be loosely proportional to the Cu–Cu distances due to the polaronic nature of the VBM. A *small* distance was required to reduce the 'hopping' distance thus high undoped conductivities were seen for $CuBO_2$ over $CuAlO_2$.[324,362] We find that in the SCSOS materials, an increased *a* parameter (corresponding to an extended Cu–Cu bond length) *decreases* the overall effective masses seen in the Γ–Z and Γ–N directions (however with an increase in the heavy hole masses in the scandium compounds). This behaviour is seen to exist in the other layered oxychalcogenides LaCuOS and LaCuOSe where a larger Cu–Cu bond length is not detrimental to the conductivity.[343,362] The larger Cu–Cu distances also inhibit $d-d$ transitions which limit the transparency. Out of the new predicted TCs, the lowest hole effective masses were seen for BaSc making this the most promising discovery from this work.

Optimising the band gap in the SCSOS layered oxychalcogenides is based upon two observations. Firstly, a smaller valence band width could play a role in improving the magnitude of the band gap. In general it was seen that a larger Cu–Cu distance resulted in a smaller VB width which could explain the increase in band gap seen in the scandium compounds (where the CBM is not influenced by B^{3+} states). Secondly, the states that make up the CBM highly influence the position of the conduction band. In the aluminium and gallium compounds, the low lying B^{3+} *s* states cause a sharp reduction in the band gap. The position of the conduction band is highly sensitive to the B^{3+}–O bond length thus larger cells push the CBM lower in energy. Despite this, increasing the cell size reduces the VBM effective mass so a compromise is necessary for a wide band gap, high mobility TC. In both the aluminium and scandium compounds there is significant mixing of the Cu and S states at the CBM which could enhance the transparency which can be seen by the decrease in fundamental band gap

with increasing percentage of Cu and S states at the CBM. The decrease in band gap in the aluminium compounds with increasing *a* is similar to other layered oxychalcogenides such as LaCuOSe (2.82 eV[347]), SmOCuSe (2.60 eV[370]) and YOCuSe (2.58 eV[350]) however the scandium SCSOS compounds see the reverse.

Aside from the parent compound (SrSc), six other compounds were found to be stable albeit without band gaps wide enough to accommodate high optical transparencies. It is possible, however, that these materials could be used in other applications such as photovoltaics or photocatalysis. SrGa displays a band gap in the correct range for a solar absorber (E_g^{opt}=1.71 eV).[131] Despite this, the optical absorption onset is fairly weak. It could be possible, however to create a mixed hybrid material oxychalcogenide such as Sr/BaGa or BaAl/BaGa to reduce the band gap or create a stronger absorption.[24] CaGa and BaAl both have band gaps in the range of a visible light water-splitter[137] (2.01 eV and 2.42 eV respectively), however, due to the metastability of BaAl, only CaGa can be recommended for photocatalytic water splitting. Further work would require band alignment and surface calculation to determine whether CaGa would be successful in this application.

It is likely that the thermodynamic stability of the compounds are restricted by certain structural parameters such as S–Cu–S bond angles and Cu–S bond lengths, thus going from S to Se to Te could help accommodate a smaller or larger cell size such as the Mg or La cells which were found to be unstable from this work. Comparing LaCuOS, LaCuOSe and LaCuOTe, the S–Cu–S bond angles decrease from 111.2° → 107.5° → 103.5° respectively, however the Cu–S bond lengths increase from 2.42 Å →2.52 Å →2.66 Å respectively.[345] It is expected that the VBM dispersion will increase down the chalcogenides as seen with the increased conductivity from LaCuOS to LaCuOSe.[343] Including Se and Te however, may have a detrimental effect on the optical band gap as can be seen in other layered oxychalcogenides such as LaCuOCh[344,346–348] and other layered Cu–Chalcogen structures such as BaFCuS (3.2 eV[371], BaFCuSe (2.9 eV[372]) and BaFCuTe (2.3 eV[373]).[350] It is likely, however, that combining the design rules laid out here that transparency with a selenide or telluride may be possible, ie. $[Cu_2Se_2][Zn/Mg_3Al_2O_5]$. Other layered Cu^{1+} oxychalcogenide structures such as $[CuS][Sr_2GaO_3]$[374] or $[Cu_2S_2][Bi_2YO_4]$[375] could also be explored and the same design rules applied to these systems. Further analysis on $[Cu_2S_2][Ba_3Sc_2O_5]$ would require defect analysis to determine the extent of *p*-type conductivity in terms of compensation and dopability.

6.2 Engineering Valence Band Dispersion - CaCuP

Experimental solid state synthesis of CaCuP powders and subsequent analysis were carried out by the group of Dr Robert G. Palgrave. Details of the experimental and theoretical methodologies are included in Appendix B.2.
This work was published in Chemistry of Materials and the experimental work is reproduced here with permission.
Figures from this paper have been adapted for use in this section.

Section 6.1 brought the prediction of a new *p*-type transparent conductor, $[Cu_2S_2][Ba_3Sc_2O_5]$ confirming the extension of the CMVB to chalcogenides. In this section we show that the effect can be extended further into the *pnictides*. Herein, the effects of Cu–P mixing at the VBM is tested examining the effect on the dispersion (and therefore the hole effective masses) by alternative Cu coordinations. Four compounds have been identified from the Inorganic Crystal Structures Database (ICSD)[363] which are M^{2+}CuP (M^{2+} = Mg, Ca, Sr, Ba) which, possess alkaline earth metals (group 2) that should not hybridise with the VBM. In the CMVB, the VBM should be dominated by Cu 3*d* and P 3*p* states producing highly dispersive bands. MgCuP which crystallises in the *Pnma* crystal structure was first reported in 1979 by Mewis et al.[376] and shows a 3D array of Cu–P tetrahedra. In MgCuP, P is coordinated to four Cu ions and five Mg ions (which displays square pyramidal coordination to P) as shown in Figure 6.7(a).

CaCuP[377], SrCuP[377] and BaCuP[376] which crystallise in the $P6_3/mmc$ structure were also reported by Mewis et al. in the late 1970s and are shown in Figures 6.7(b) and (c). The 'CaCuP' structure consists of planar hexagonal networks of Cu–P layers sandwiching M^{2+} atoms (Ca, Sr or Ba) which are repeated (at lengths of $c/2$) along the *c*-axis. The M^{2+} ions are coordinated to six Cu ions (three above and three below) as well as six P ions (three above and three below) as shown in Figure 6.7b and c. The trigonal planar array of Cu–P form hexagonal networks in the *ab* plane such that for every Cu there is a P atom and vice versa which are stacked along the *c*-axis. In the scientific literature, only crystallographic characterisation exists on these materials without an analysis on their electronic properties or the implications of the structure-property relationships of these copper phosphides.

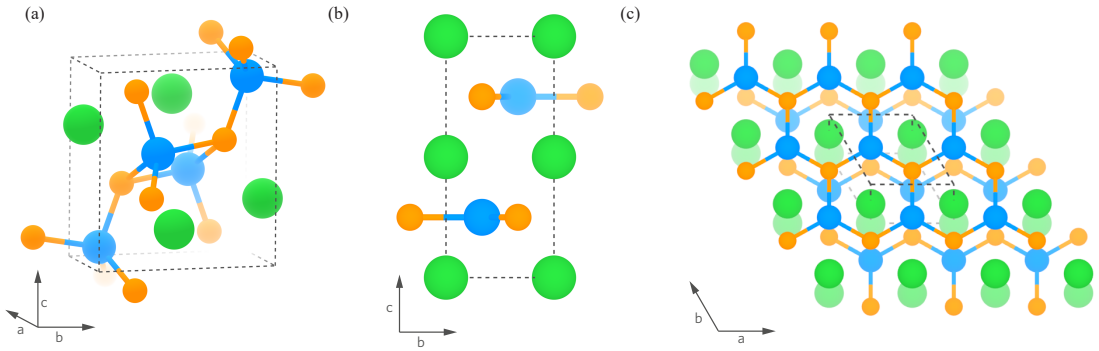

FIGURE 6.7: The crystal structures of MgCuP in the *Pnma* space group (a) and CaCuP, SrCuP and BaCuP ($P6_3/mmc$) as viewed along (100) (b) and down the *c* axis in (c). MgCuP consists of a tetrahedrally coordinated network of Cu–P, whilst CaCuP, SrCuP and BaCuP show a hexagonal layered network of trigonal planar Cu–P. The alkaline earth metals (Mg, Ca, Sr and Ba) are depicted by the green spheres whilst Cu and P are shown by the blue and orange spheres respectively. The unit cell is portrayed by the dashed black black box.

Hybrid density functional theory calculations using the PBE0[23,265] functional (the details of which are provided in Appendix B.2) are used to predict and analyse the electronic properties arising from the different coordination environments of M^{2+}CuP and therefore the implications for designing novel *p*-type transparent conductors.

6.2.1 Structural Parameters

The PBE0 calculated structural parameters (a, b, c, Volume, Cu–P bond length) for MgCuP, CaCuP, SrCuP and BaCuP are shown in Table 6.7. The unit cell parameters and Cu–P bond lengths are in excellent agreement with the experimental values[376,377] (shown in parentheses), with the slight underestimation of the calculated data being due to the experimental analysis being carried out at room temperature, whilst the DFT values are calculated at the athermal limit. Within the $P6_3/mmc$ structures, trends can be observed to occur down group 2 (Ca→Sr→Ba) which, due to the increase in ionic radii account for the increase in *all* lattice parameters and bond lengths down the group. The a/b and c lengths increase by around 5%, and 14% respectively from CaCuP to SrCuP to BaCuP, whilst the Cu–P bond lengths differ by ~5%. In MgCuP (*Pnma*), however, the Cu–P bond lengths are in fact larger than those for CaCuP and therefore do not follow the same trend.

TABLE 6.7: The calculated lattice parameters and Cu–P bond lengths for each M^{2+}CuP compound. Experimental values are show in brackets.[376,377]

System	a / Å	b / Å	c/ Å	Cu-P / Å	Volume / Å^3
MgCuP	3.82 (3.84)	6.50 (6.53)	7.15 (7.17)	2.40 (2.46)	177.48 (179.61)
CaCuP	4.05 (4.06)	4.05 (4.06)	7.83 (7.80)	2.34 (2.34)	111.34 (111.12)
SrCuP	4.14 (4.15)	4.14 (4.15)	8.42 (8.48)	2.39 (2.39)	125.14 (126.18)
BaCuP	4.25 (4.24)	4.25 (4.24)	9.10 (9.01)	2.46 (2.45)	142.59 (140.15)

6.2.2 Electronic Properties

MgCuP (Pnma):

The band structure of MgCuP is displayed in Figure 6.8(a). The VBM is situated at Γ whilst the CBM is located between *Y* and Γ making MgCuP an indirect band gap semiconductor. The magnitude of the indirect band gap is 1.14 eV, whilst the direct fundamental band gap at Γ has a magnitude of 2.06 eV. Table 6.8 presents the effective masses for MgCuP showing that the hole effective mass from Γ–Z is larger than that from Γ–Y as shown by the decreased dispersion. Along Γ–Y the hole effective mass is 0.15 m_e whilst from Γ–Z this rises to 6.30 m_e as seen with the corresponding flat band curvature in Figure 6.8(a). The CBM displays a relatively high dispersion in both the CBM–Γ and CBM–Y with electron effective masses of ca. 0.68 m_e and 0.62 m_e respectively.

The total and partial density of states (DOS) for MgCuP is shown in Figure 6.8 with Table 6.9 displaying the percentage of states at the VBM and CBM as calculated using PBE0. The width of the upper valence band in MgCuP is approximately 8 eV with P $3s+3p$ mixed with Cu $3d+3p$ and Mg $3s$ states seen from -8 eV to -7 eV. The Cu $3d$ states begin to dominate from -6 eV to -4 eV with a large peak occurring at -4.5 eV mixed with some P $3p$ states. Towards the VBM (at 0 eV), a ratio of 42:54 Cu $3d$: P $3p$ states are observed along some slight Cu $3p$ (~ 4%). The CBM is made up of predominantly Cu $d+s$ states mixed with a similar magnitude of Mg *s* and P $s+p$ states. Within the CBM to around 6 eV, a fairly uniform mixing of Cu $p+d$, P $s+p$ and Mg *s* states are seen.

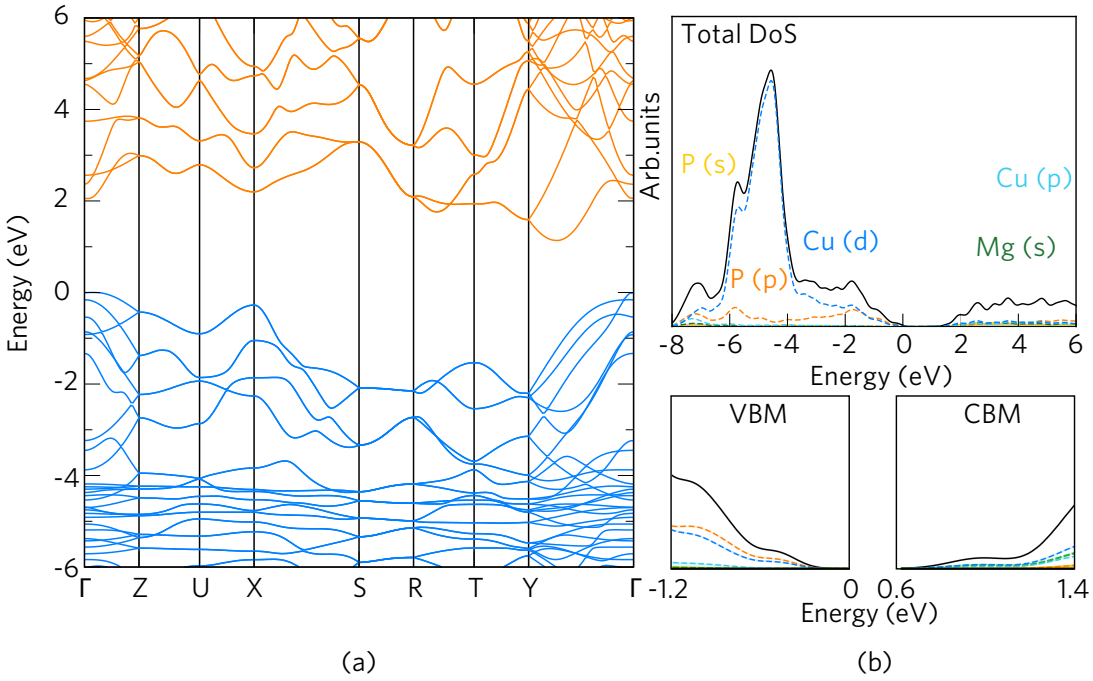

FIGURE 6.8: The band structure (a) and total and partial density of states (DOS) (b) for MgCuP in the *Pnma* space group. In (a) the valence bands and conduction bands are depicted by the blue and orange bands respectively. In both (a) and (b) the VBM is shifted to 0 eV. Expanded views of the VBM and CBM are shown in (b).

CaCuP, SrCuP and BaCuP ($P6_3/mmc$):

The band structures for CaCuP, SrCuP and BaCuP are shown in Figure 6.9(a), (b) and (c) respectively. In all three compounds, the VBM is situated at Γ whilst the CBM occurs between the L and M high symmetry points and shifts towards M down group 2. This incurs indirect band gaps of 1.23 eV, 1.20 eV and 0.80 eV for CaCuP, SrCuP and BaCuP respectively. The direct fundamental band gaps at Γ also decrease down the group with magnitudes of 2.17 eV, 1.86 eV and 1.48 eV respectively.

Two degenerate bands are present at the Γ–M and Γ–K directions which show both extremely low hole effective masses (Table 6.8). The light hole effective masses (0.11 m_e) are insensitive to the increasing size of the group 2 cation, whereas the heavier effective masses increase from Ca→Sr→Ba (0.25 m_e, 0.27 m_e 0.28 m_e respectively). These values are competitive with and even surpass (in terms of the light hole effective masses)the electron effective masses of the industry standard *n*-type TCOs such as In_2O_3, SnO_2, ZnO and $BaSnO_3$ [26,273,378,379] (See Section 3.2.1).

From Γ–A the hole effective masses are limited to ~ 0.79–0.81 m_e showing no particular trend down the group. Despite the higher effective masses from Γ–A, these hole effective masses are superior to some of the top performing *p*-type TCOs such as LaCuOSe and $[Cu_2S_2][Sr_3Sc_2O_5]$ which have hole effective masses of 1.06 m_e and 0.9 m_e respectively.[346,362]

The curvature of the CBM increases from CaCuP to BaCuP resulting in *electron* effective masses as low as ~ 0.22 m_e for BaCuP in the M–Γ direction.

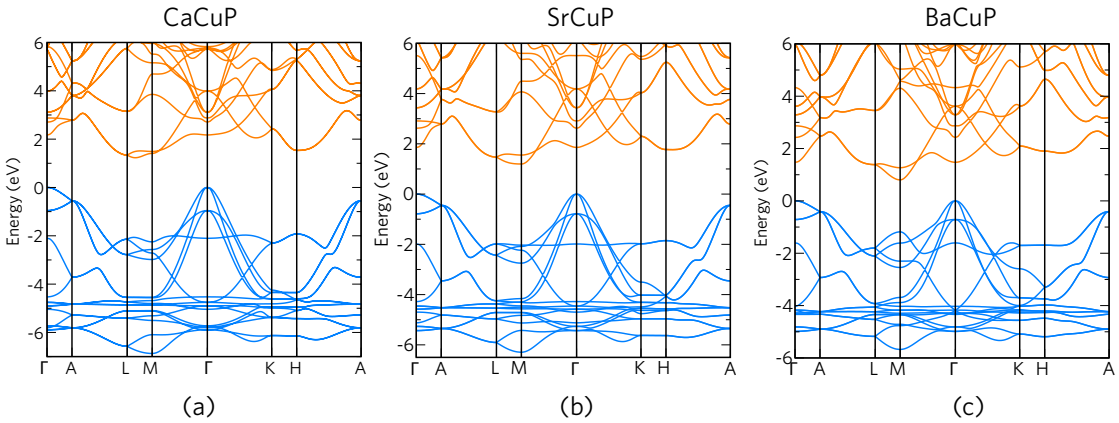

FIGURE 6.9: The PBE0 band structures for (a) CaCuP, (b) SrCuP and (c) BaCuP ($P6_3/mmc$ space group). The valence and conduction bands are coloured in blue and orange respectively and the VBM in each example is set to 0 eV

The density of states for the $P6_3/mmc$ structures are shown in Figure 6.10 whilst the percentage of states at the band maxima, in Table 6.9. The upper valence band widths of CaCuP, SrCuP and BaCuP decrease down the group with values of ca. 7 eV, 6.5 eV and 6 eV respectively. As the DOS is very similar in all compounds, CaCuP can be taken as an example for this analysis. From -7 eV to -4 eV, predominantly Cu 3*d* states mixed with some P 3*p* states occur similar to that seen in MgCuP. The ratio of states decreases substantially from -4 eV to -2 eV where there is almost 1:1 overlap of Cu 3*d* states with P 3*p*, however, with the appearance of some Cu 3*p* states. From -2 eV to the VBM (0 eV) the Cu 3*p* states tail off leaving Cu 3*d* hybridisation with P 3*p* in a consistent 38:48 ratio (from CaCuP to BaCuP) with ~ 14% Cu 3*p*. The CBM is made up of predominantly unoccupied M^{2+} *d* states which increase from Ca→Sr→Ba (~ 50% – 62%). The remainder of states at the CBM involve ~ 35% Cu *p* and some negligible P *p* states. From 2ėV to 4 eV there is a net increase in the M^{2+} *d* states, seen with hybridisation from Cu *p* states. The ~4 eV to 6 eV region is primarily M^{2+} *d* states.

TABLE 6.8: The effective masses of electrons at the CBM and holes at the VBM. The values in *italics* correspond to light hole effective masses.

System	VBM / m_e	CBM / m_e
MgCuP	6.30 (Γ–Z) 0.15 (Γ–Y)	0.68 (CBM–Γ) 0.62 (CBM–Y)
CaCuP	0.25, *0.11* (Γ–M) 0.25, *0.11* (Γ–K) 0.79 (Γ–A)	0.39 (CBM–L) 0.90 (CBM–Γ)
SrCuP	0.27, *0.11* (Γ–M) 0.28, *0.11* (Γ–K) 0.87 (Γ–A)	3.50 (M–L) 0.30 (M–Γ)
BaCuP	0.28, *0.11* (Γ–M) 0.29, *0.11* (Γ–K) 0.81 (Γ–A)	0.39 (M–L) 0.22 (M–Γ)

TABLE 6.9: The approximate percentages of states at the VBM and CBM.

System	VBM / %		CBM / %		
	Cu	P	M(II)	Cu	P
MgCuP	4(p) + 42(d)	54(p)	22(s) + 5(p)	15(s) + 3(p) + 30(d)	19(s)+6(p)
CaCuP	14(p) + 38(d)	48(p)	5(s) + 4(p) + 50(d)	34(p)+2(d)	2(s)+3(p)
SrCuP	14(p) + 38(d)	48(p)	5(s) + 2(p) + 51(d)	35(p) + 1(d)	6(p)
BaCuP	13(p) + 38(d)	49(p)	4(s) + 1(p) + 62(d)	24(p) + 3(d)	6(p)

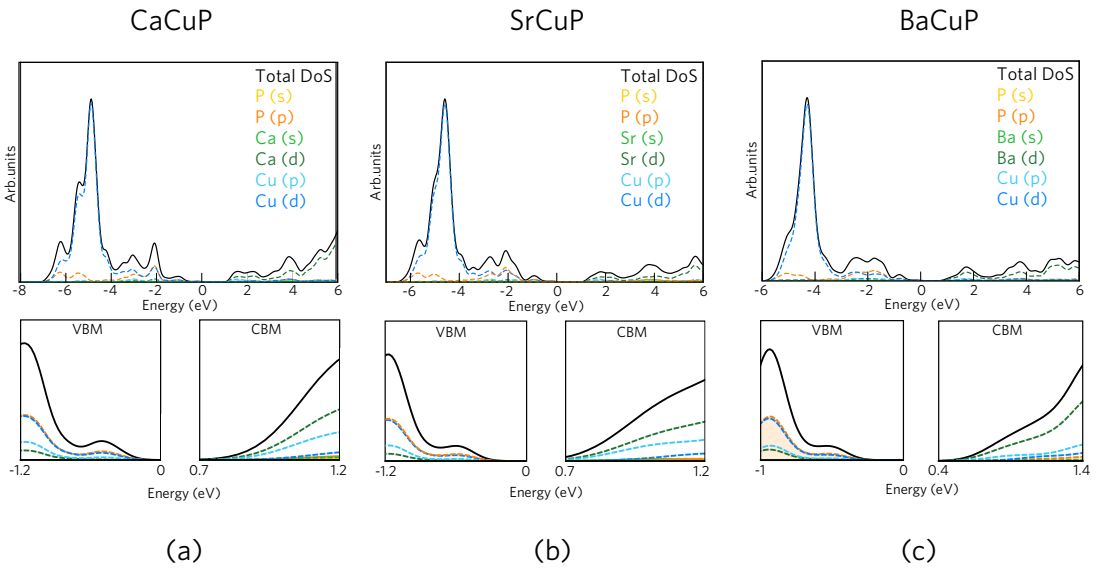

FIGURE 6.10: The total and partial electronic density of states (DOS) for CaCuP (a), SrCuP (b) and BaCuP (c) in the $P6_3/mmc$ space group. For each example, the VBM is set at 0 eV and an expanded view of the VBM and CBM is provided beneath each DOS.

6.2.3 Discussion

In comparing the different electronic structures of the *Pnma* (MgCuP) and $P6_3/mmc$ (CaCuP, SrCuP and BaCuP) structures, it is clear that the difference in Cu coordination plays a significant role in the electronic aspects. Due to the three-dimensional Cu–P array present in MgCuP, the average hole effective mass at the VBM (despite the favourable Γ–Y mass of $0.15\,m_e$) is $3.23\,m_e$. CaCuP, SrCuP and BaCuP however, see *excellent* dispersion in the Γ–M and Γ–K directions which can be attributed to the excellent orbital overlap of the trigonal planar CuP_3 in the hexagonal layers. Far less dispersion is observed in the Γ–A direction which corresponds to the *c* axis. This is to be expected due to the Cu and P atoms being only coordinated in the *ab* plane. MgCuP, on the other hand, is not prone to this anisotropic behaviour due to the three-dimensional Cu–P tetrahedra. The question is raised, therefore, of whether trigonal planar Cu is preferable over tetrahedral Cu in terms of orbital overlap and thus increased valence band dispersion for copper (I) phosphides.

In Cu^+-based systems, the Cu coordination is key to controlling the extent of orbital overlap observed between the cation and anion states and thus the VBM dispersion. For oxygen and nitrogen (first row anions), a linear coordination is typically seen, ie. in Cu_2O[380,381], the delafossite $CuAlO_2$[381] as well as in Cu_3N and $CuTaN_2$.[355,382]f A study by Orgel in 1958 determined the unusually low coordination preference to exist because of the closed shell metal cations (Cu^+, Ag^+ and Hg^{2+}) possessing a low difference in energy between the first excited state, d^9s^1 and the ground state d^{10} energy level.[383] In Cu, this *hybridised* $[3d_{z^2}+4s]$ state can therefore stabilise a *low coordination* environment. This therefore explains the preferential two-coordinate configurations for copper (I) oxides and nitrides. Other d^{10} cations such as Zn^{2+} display a distinctly larger separation between the d^9s^1 state and the d^{10} ground state requiring a higher coordination number. This can be observed in both zinc blende or wurtzite ZnO where ZnO_4 tetrahedra are observed.

β-$CuGaO_2$ (wurtzite-like) has been shown to possess a low band gap (~ 1.5 eV) and as such was considered promising for photovoltaic applications.[384] A subsequent computational study showed that the *tetrahedral* Cu^+ coordination produces a vastly different valence band compared to delafossite $CuGaO_2$ with its linear O–Cu–O coordination.[385] In the delafossites, the Cu $3d$ and O $2p$ states overlap strongly producing favourable dispersion at the VBM.[386–388] Calculations on β-$CuGaO_2$ show that *no* hybridisation is seen at the VBM producing heavy effective masses and 'flat' bands of Cu $3d$ character.[385] The role of coordination is therefore vital in the production of a highly disperse valence band.

Orgel's theory, despite describing the copper (I) oxides and nitrides well, fails to provide an understanding for the preference of higher coordination numbers in copper (I) *chalcogenides*. Examples include the three-coordinate CuS[389] and tetrahedrally coordinated $CuAlS_2$.[382] A transition to a more ionic model down the chalcogenides is therefore necessary.[390] Work by Tossel and Vaughan introduced the effect of ligand interactions into the model pioneered by Orgel.[389] Here, the metal d to chalcogenide (ligand) p energy separation determines the coordination. It is therefore preferable to reduce this energy separation via coordination. Cu_2O for example, has a large energy spacing and thus favours a *low* coordination.

Gaudin and coworkers[390] provided an overview of these models and determined that the Cu $3d$ – O $2p$ interaction is vital in lowering the energy of the main Cu $4s$ – O $2p$ interaction (incorporating Orgel's theory). The polarising influence of the anion over Cu^+ is also a determining factor (Cu is fairly polarisable due to the poor screening of the $3d$ electrons), which for less polarising anions (down the group and from right to left on the periodic table), the weaker the effect is and thus *destabilises* the lower coordination number. From this model, higher coordination numbers are preferred for copper (I) selenides and tellurides. The influence of the third cation in ternary compounds (ie. KCuS, KCuSe and KCuTe[390,391]) also affects the polarisation of the Cu cation. This effect can be seen directly between the different coordinations in Cu_2S (three coordinate) and KCuS (two coordinate) for example. Gaudin noticed a depletion in the electron density of the Cu $3d$ electron cloud for KCuS over Cu_2S which can be attributed to the contribution to the polarisability by the potassium ion.[390]

These explanations can help describe why in M^{2+}CuP, a higher coordination number is preferable over copper oxides, but also to why a *trigonal planar* configuration is stabilised. Taking the polarisability argument described above, P should naturally adopt a higher coordination number due to the low polarisablity of P. The phosphides should also retain a higher coordination due to the decrease in polarising power down group 2 (Ca→Sr→Ba). From our calculations we see that CaCuP, SrCuP and BaCuP all prefer the trigonal planar configuration and fail to adopt the same tetrahedral MgCuP *Pnma* structure. This is most likely a steric effect due to the large phosphorus and the increasing M^2+ ionic radius down the group. The tetrahedral coordination in MgCuP, is an example where there exists a poorer orbital overlap than in the trigonal planar configuration as seen in the increasing Cu–P bond lengths. Comparing MgCuP in the $P6_3/mmc$ space group to MgCuP in the *Pnma* space group shows a decrease in Cu–P bond length (2.28 Å versus 2.40 Å respectively) and lower overall effective

masses.

In comparing the Cu–P bond lengths from CaCuP to BaCuP, an increase is observed down the group and thus a detrimental effect on the hole effective mass and a lowering of the band gap. Despite this, an *increase* in the *electron* effective mass is observed at the CBM and a decrease between the indirect and direct band gaps. The $P6_3/mmc$ compounds also all possess significant contributions from Cu $3p$ at the VBM, specifically from the p_x and p_y orbitals in the ab plane. This adds to the bonding and thus to the high dispersion of the VBM. Relating to the model by Tossel and Vaughan[389], the Cu $3d$ and P $3p$ levels are closer in energy and hence it can be deduced that a tetrahedral or trigonal planar configuration is preferential over a linear configuration. The crystal field splitting for Cu is also increased by moving from a tetrahedral to trigonal planar configuration by pushing the antibonding states higher in energy. This has the two-fold effect of pushing the VBM higher in energy reducing the ionisation potential (favouring hole formation[35,109]) and also increasing the band dispersion.

6.2.4 Experimental Verification

Powders of CaCuP were produced to verify the optical and electronic properties predicted through DFT (details of the experimental methodologies are provided in Appendix B.2 alongside X-ray Diffraction (XRD) and X-ray Photoelectron Spectroscopy (XPS)). The presence of CaCuP is confirmed through the XRD and XPS results. Figure 6.11(a) displays the diffuse reflectance optical spectra showing the Kubelka-Munk function F(R) and $F(R)^2$. The well established Tauc method[392] does not take into account the presence of high carrier concentrations and as such, Poeppelmeier and coworkers proposed a method for the accurate determination of the band gap in degenerately doped semiconductors.[393]

The PBE0 calculated optical absorption (α) in Figure 6.11(b) displays a weak absorption onset at 2.17 eV with a stronger optical absorption occurring ~2.71 eV. These results are in excellent agreement with the experimental optical spectra of the CaCuP powders in Figure 6.11(a) which incurs a value of 2.78 eV.

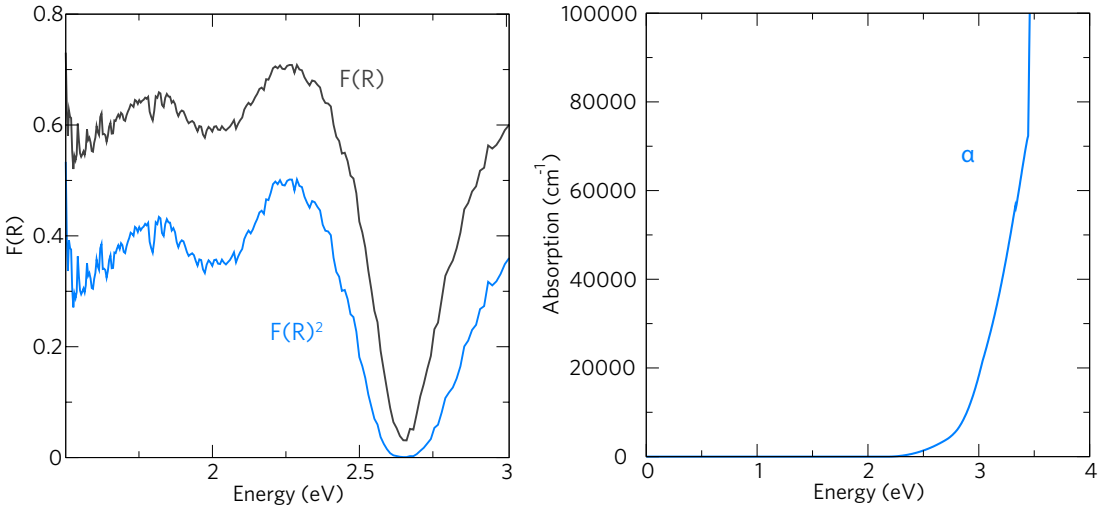

FIGURE 6.11: (a) Shows the diffuse reflectance optical spectra showing the Kubelka-Muk function F(R) and $F(R)^2$. (a) shows that the direct band gap (as calculated using the Poeppelmeier method[393]) is 2.78 eV. (b) displays the calculated optical absorption spectrum from DFT using the PBE0 hybrid functional. In (b) a weak absorption onset is seen at 2.17 eV and a strong absorption at 2.71 eV.

In order to measure the conductivity, the CaCuP powders were formed into a 3 mm thick pellet (density of ~ 70%) which was sintered for 4 hours under $N_{2(g)}$ under an annealing temperature of 300 °C. A four point probe was used to measure the conductivity resulting in a resistivity of $2 \times 10^{-3} \pm 0.2 \times 10^{-3}\,\Omega$cm.

These experimental results on CaCuP support the electronic properties predicted using DFT. The results all indicate that the material is indeed a highly degenerate *p*-type semiconductor possessing high intrinsic conductivities. The most impressive aspect of this is that these results were for a nominally *un-doped* pressed powder pellet, possibly arising from copper vacancies (V_{Cu}). If a single crystal were to be formed, without the limitations of surface and grain boundary effects present in powders, it is likely that the mobility and conductivities would far exceed that presented here. Increases in the hole concentration could also be improved through acceptor doping the 2+ cation site with suitable elements such as Li, Na or K.

6.3 Conclusions

The search for high mobility *p*-type transparent conductors within this chapter has produced results based fundamentally on the extension of the chemical modulation of the valence band (CMVB) used to describe Cu^{1+} oxides such as the delafossite $CuAlO_2$ to Cu^{1+} chalcogenides and pnictides. Using a thermodynamic and electronic structure screening, a novel *p*-type transparent conductor ($[Cu_2S_2][Ba_3Sc_2O_5]$) has been predicted and subsequently proven through experiment. Excellent agreement between the theory and experimental results show the viability of hybrid DFT to predict new compounds and their properties. The benefit of having a quinary layered structure is the ability to tune the band gap and effective mass through an analysis of the physical and electronic structure. This can not only be useful in designing new *p*-type transparent conductors, but also in forming new photovoltaics, thermoelectrics or photocatalysts. Despite the large band gap predicted for $[Cu_2S_2][Ba_3Sc_2O_5]$, the hole effective masses are not competitive with the industry standard *n*-type transparent conducting oxides. Further work would be to enhance this through the incorporation of Se or Te into the SCSOS structure to further decrease the hole effective masses as seen in LaCuOCh (where Ch = S,Se,Te),[344,346–348] however, many selenides and tellurides tend to have *smaller* band gaps.[350] Further work on the 'stable' predicted compounds in this chapter would be to calculate their phonons and thus their dynamic stability. These calculations would also aid the determination of their properties for use in other applications such as thermoelectrics where there is an increased interest in layered structures[394], in particular, layered oxychalcogenides such as LaOBiSSe.[395] Using the design principles gained from this chapter, however, this could be avoided. Other layered oxychalcogenide structures exist such as the $[CuS][Sr_2GaO_3]$[374] or the $[Cu_2S_2][Bi_2YO_4]$[375] structure. The role of defects and dopants in these layered structures would also need to be assessed to evaluate any degenerate conductivity or compensation mechanisms.

The extension of the CMVB to the pnictides, in particular Cu^{1+} phosphides has produced a high hole mobility *p*-type semiconductor, CaCuP. Although CaCuP possesses a large optical band gap (2.71-2.78 eV) it is not transparent to visible light ($E_g > 3.1$ eV). The quest to find a similarly high mobility, high conductivity and also *transparent* semiconductor is still ongoing and can be seen in the wealth of recent literature.[340,396–400] The insights gained from this analysis of CaCuP, SrCuP, BaCuP and MgCuP can act as a stepping stone in understanding the interplay between the structure and electronic properties to provide additional design princi-

ples for this field. The analysis gained from both sections in this chapter can act as a stepping stone in the design of highly *p*-type transparent conductors; the ability to design increasingly complex layered compounds can be fabricated thanks to the technological breakthroughs in experiment.[359–361] Therefore the ability to create materials with a trigonal Cu–P layer in this way could pave the way for materials with the same hole mobilities and conductivities as CaCuP, but with much larger band gaps for transparent conducting applications.[335,401,402]

Part IV

Understanding TiO_2 Photocatalysis

Chapter 7

Introduction to Bulk TiO_2 Photocatalysis

Titanium dioxide, TiO_2, is a wide band gap material that is utilised in a broad range of commercial applications. Examples include its use as a pigment in paints[403,404], an active ingredient in sun creams[405,406], as a whitening agent to food[407,408], superhydrophobic/superhydrophilic coatings[409–412] as well as within the vast scope of photocatalysis.[413–415] TiO_2 therefore, receives a vast amount of research each year with Web of Knowledge[416] displaying >10,000 articles in 2017 alone. Since the publication of *'electrochemical photolysis at a semiconductor electrode'* by Fujishima and Honda in 1972,[417] a multitude of research has been carried out and is still dedicated to the use of TiO_2 as a water splitting photocatalyst. It is the splitting of water into both hydrogen and oxygen that has been seen as the holy grail in terms of the production of alternate sustainable fuels as well as aiding industrial processes such as ammonia synthesis.[418,419] The attractiveness of TiO_2 is in its affordability, earth abundance, high chemical stability (in particular water stability)[420], and ease of fabrication within scalable industrial processes such as chemical vapour deposition (CVD) or solgel methods.[33]

Many polymorphs exist for titania of which the anatase, rutile and brookite polymorphs are widely studied.[35,421,422] Figure 7.1 shows the individual crystal structures for anatase, rutile and brookite. Each polymorph is constructed of differing arrays of distorted TiO_6 octahedra with trigonal planar coordinated oxygen. Whilst rutile is the *thermodynamic equilibrium* phase, anatase and brookite are both metastable. Out of these metastable polymorphs, brookite is difficult to synthesise but anatase is *kinetically* stabilised[419,421] and is used in most major photocatalytic applications.[34,35,423] The changes in local environments between the polymorphs give rise to differing band structures (Figure 7.4) , ionisation potentials and elec-

tron affinities (Figure 7.3).[34,35] TiO_2 in general, still possesses a large band gap which hampers its use in *visible-light* photocatalysis and as such only uses a small portion of sunlight that reaches the surface of the earth (~1-2%).[137] The portion of the solar spectrum that the TiO_2 band gap s utilise is shown in Figure 7.2(a) in red.

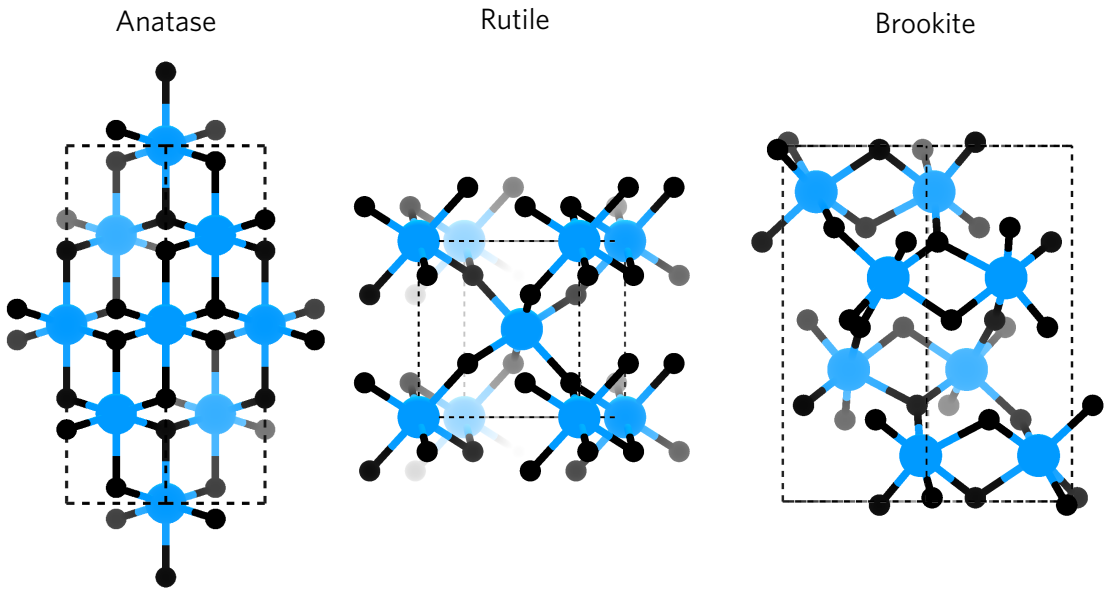

FIGURE 7.1: The unit cells for anatase, rutile and brookite. Anatase crystallises in the *I4/amd* structure, rutile in the *P4/nmn* and brookite in the *Pbca* structure. Ti is depicted in blue and O in black and the unit cell boundaries by the dashed black box.

7.1 Ideal Bulk Properties

Although many photocatalyst mechanisms rely on surface effects[414], idealised photocatalyst behaviour can be gleaned from the *bulk* properties. These involve the magnitude and nature of the band gap as well as the alignment of the CBM and VBM. The correct electronic properties of a material are therefore vital for gaining efficiency in photocatalysis.

7.1.1 Band Alignment:

The schematic in Figure 7.2(b) displays the position of the redox potentials of water relative to the vacuum level. The chemical equations that describe the photocatalytic splitting of water are[424,425]:

$$2\,H_2O_{(l)} + 4\,h^+ \xrightarrow{1.23\,eV} O_{2\,(aq)} + 4\,H^+_{(aq)} \tag{7.1.1}$$

$$4\,H^+_{(aq)} + 4\,e^- \xrightarrow{0.00\,eV} 2\,H_{2\,(g)} \tag{7.1.2}$$

Where equation 7.1.1 refers to the oxidation of water by holes (h^+) in the valence band (denoted O_2/H_2O) forming protons (H^+) and aqueous oxygen O_{2aq} and equation 7.1.2 is the reduction of protons to hydrogen gas (H_{2g}). The redox potentials shown are relative to the standard hydrogen electrode which is itself -4.44 eV relative to the vacuum level.[35] Although the difference between the redox potentials is 1.23 eV, the CBM and VBM of material must have an overpotential of around 0.2-0.3 eV in order to drive the reactions under zero-bias, and thus band gaps in the range of 1.7-2.2 eV are needed.[137] Experiment shows that at least 1.6 eV is needed for photo-induced water splitting.[427] The 1.7-2.2 eV required gap is shown relative to the solar spectrum in Figure 7.2(a) (in blue) showing the much larger portion of solar radiation that is able to be absorbed. Due to to titanium dioxide's large band gap , efficiency is lost due to the lack of visible light harvesting. Figure 7.3 displays the relative positions of the band maxima and minima for anatase, rutile and brookite to the redox potentials of water (as calculated in refs. [34, 35]) and show that in general, the VBM is very low in energy relative to the vacuum and thus forms highly oxidising holes. The calculated band alignments of anatase and rutile both display CBMs *below* the reduction potential of water, whereas brookite does

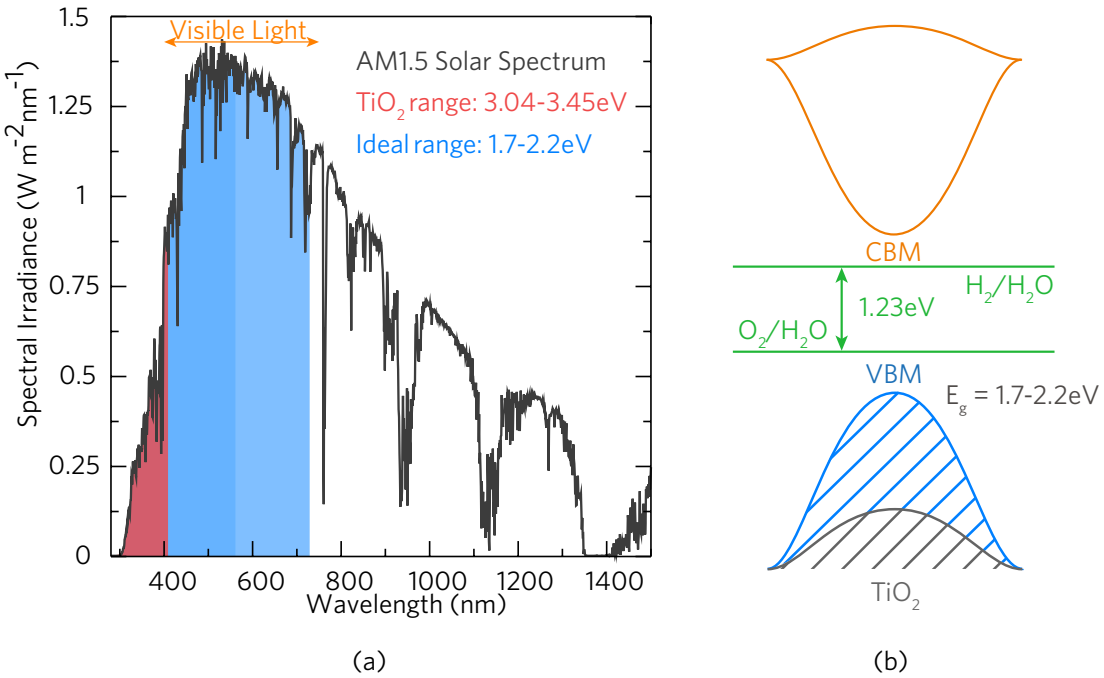

FIGURE 7.2: (a) The AM1.5 solar spectrum[426] showing the portions of light absorption available to different band gaps. The amount of the spectrum absorbed by TiO_2 is shown in red, whilst the ideal photocatalyst band gap range (1.7-2.2 eV) is shown in blue (the darker shade of blue corresponds to the 2.2 eV band gap). (b) The ideal positions of the CBM and VBM relative to the redox potentials of H_2O with suitable over potentials ($\sim 0.2-0.3$ eV) and the position of the TiO_2 VBM.

possess the correct overpotential for reduction to occur.[34,35] It is likely that surface properties of anatase and rutile cause a band bending driving the CBM above the H_2/H_2O potential accounting for the high photocatalytic activity seen in anatase and rutile powders and thin films.[35,414,415,428] Despite stability and doping issues as well as a lack of research carried out on brookite (compared to other polymorphs), experimental thin films have been shown to exceed that of anatase and rutile.[429–432]

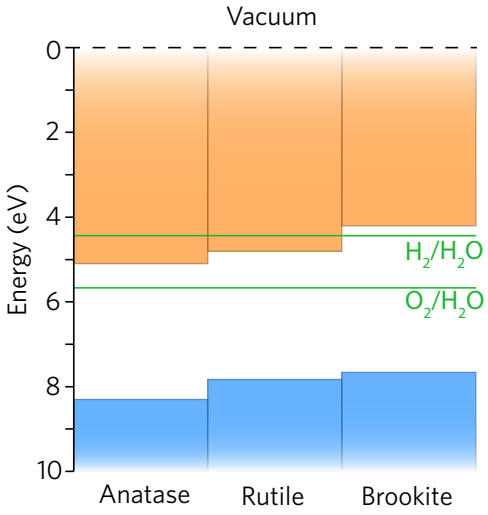

FIGURE 7.3: The band alignment of TiO_2 polymorphs, anatase, rutile and brookite relative to the vacuum level (0 eV). The valence band is blue and the conduction band, orange. The redox potentials for photoelectrochemical water splitting are displayed relative to the vacuum level (NHE = -4.44 eV).

Anatase/rutile mixed powders, in particular Degussa P25 which typically contains ca. 70% anatase and 20-30% rutile allowing for longer electron and hole separation due to the offset between the VBM and CBM.[34] This is particularly important for processes such as water splitting which require both four electrons and four holes for complete splitting as shown in Equations 7.1.1 and 7.1.2.

7.1.2 Electronic Structure:

An enhanced electron-hole pair separation lifetime is another factor towards efficient photocatalysis and can be determined from the band structure. Figure 7.4 show the band structures for anatase, rutile and brookite calculated using the HSE06[30–32] DFT functional. The nature of the fundamental band gap (see Section 3.2.1) is different for each polymorph, however the indirect nature of the anatase band gap (ie. VBM at X and CBM at Γ) is proposed to enhance the separation lifetime. This has been shown by many theoretical DFT studies[34,35,433] and backed up by transient absorption (TAS) studies.[423,434–436] Rutile and brookite on the other hand both have *direct* fundamental band gap s (both band edges occurring at Γ) and as such no additional phonons are needed for excitation of an electron from the valence band to

the conduction band. It is important to note that an indirect band gap that is too far removed from the *direct* fundamental band gap will incur efficiency issues as phonons of larger energy will be needed for excitation, and the absorption coefficient will not be as strong. Anatase has both indirect and direct fundamental band gap s of 3.35 eV and 3.64 eV as calculated by the HSE06 hybrid functional, and so are fairly similar in magnitude.

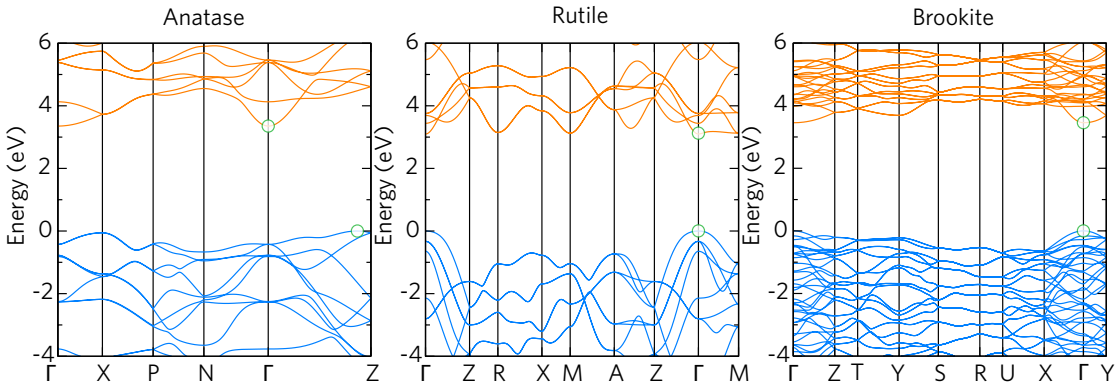

FIGURE 7.4: The band structures of anatase, rutile and brookite TiO_2 as calculated using the HSE06 functional. This displays the varying band structures due to different coordinations of Ti and O in the TiO_2 lattice. In each example the valence bands are depicted in *blue* and set to 0 eV and the conduction bands, in *orange*. The band minima and maxima are highlighted with the *green* circles.

7.2 Doping

Enhancing the photocatalytic properties of TiO_2 comes in the form of doping. Unlike with TCOs (Section 3.3) where doping is carried out to enhance the conductivity, optical transparency and carrier concentrations, extrinsic doping of TiO_2 focuses on improving the electron-hole separation lifetimes as well as increasing the visible light absorption of the material.

TiO_2 is inherently an *n*-type material sharing many of the characteristics of the *n*-type TCOs such as a VBM made up of heavily localised O $2p$ states. Donor doping with Nb, Ta, Sb or W for example gives low resistivities of the order 10^{-2}-10^{-4} Ω cm comparable to doped *n*-type TCOs such as SnO_2,In_2O_3 and ZnO.[33,411,437–440] Despite this, intentional *acceptor*-doping is carried out to 'raise' the VBM towards the oxidation potential of water (equation 7.1.1). This is typically achieved through *non-metal* doping ie. with B[441–444], C[445–448], N[449–452] or P.[449,453,454] In particular, nitrogen has been the 'go-to' dopant for enhanced photocatalysis in TiO_2 since the work of Asahi et al in 2001.[449] The popularity of N-doping in anatase is the reproducibility of results through a range of solution-processed and deposition based techniques such as sol-gel[455,456], CVD[457–459] or sputtering.[460–462] Within the doping framework, it is assumed that the N $2p$ states hybridise with the top of the valence band, lowering the band gap and ionisation potential. However, despite over a decade of research, the exact nitrogen species that forms within the anatase lattice is still scrutinised. The position of N has been suggested to be either substitutional (N_O or N_{Ti}), interstitial (N_i) or part of a complex species with the lattice ions or unintentional dopants such as H (NH_4^-).[96,463–467]) Interestingly, whilst experimental thin films of *anatase* display a red shifting of the band gap , nitrogen doped *rutile* thin films display a blue shift. This has been proposed to be due to the denser crystal structure of rutile forming a wider O $2p$ valence band, and upon nitrogen doping a reduction in Coulombic repulsion is observed causing a widening.[466] In reality, however, the nitrogen states form highly localised hole states just above the VBM corroborated through theoretical studied on both substitutional and interstitial nitrogen species.[96,464–467] Within the DFT literature, multiple groups have managed to show that interstitial N displaces from the preferred interstitial site to form an N-O dumbbell which has also been seen using EPR measurements.[467] Unfortunately these localised N states are a source of e-h recombination especially at the high concentrations typically required for 'band gap reduction'.[424,468] Theoretical studies have also proposed the inducement of oxygen vacancies due to nitro-

gen incorporation providing intrinsic compensation typical of the high ionisation potential of TiO_2 polymorphs (Figure 7.3).[466]

Reports of beneficial carbon doping also exist in the literature, albeit less explored than nitrogen doped TiO_2 in both experiment and theory. Carbon possesses a small ionic radii (~ 0.15-0.16 Å[240]) and generally prefers compounds where it exists as a 4+ cation (CH_4, CO_2 etc.) although it can also exist in the 4- oxidation state as in TiC. Experimental techniques such as XPS[469,470] suggest substitutional carbon (C_O) species or carbonate species (CO_3^{2-}) adsorbed into the lattice. Two theory papers in particular, one by Di Valentin et al[470] and a more recent hybrid DFT paper by Zhang and coworkers[471] elucidate the possible locations and downsides to carbon doping in anatase. Both Di Valentin and Zhang recognise the existence of Ti-substitutional C (C_{Ti}) as a dominant defect whereby it acts as an isovalent dopant neither adding or removing electrons but possibly reducing the band gap at higher doping concentrations.[470,472] Due to the typical coordinations of carbon, it was found that C_{Ti} defects prefer a four-coordinate configuration adding strain to the system due to the six-coordinate environment of Ti (where Ti can hybridise $3d$ orbitals). Due to the small ionic radii, interstitial carbon can also form over the oxygen chemical potential range where it acts as a donor. C_O is only expected to form towards highly *O-poor* regimes where it induces the formation of oxygen vacancies thereby self compensating as with nitrogen defects. The defects that are expected to give states in the band gap suitable for visible light excitation are the C_O related species which do not form as readily as substitutional nitrogen species.[471] Theoretical diffusion studies have also shown that C defects have low barriers for diffusion in the anatase lattice (ca. 600K/327°C) usually lower than the typical synthesis temperatures for anatase thin films.[471,472] Boron doped titania shows promise at enhancing the visible light photoactivity and reaction rates.[441,473,474] Experiment shows that due to the small ionic radii of B (0.27Å[240]) that boron sits interstitially within the anatase lattice and that substitutional boron (B_O) tends to show instability in comparison.[475] Increases in the photocatalytic activity is seen however with just interstitial B, which acts as a donor and no reduction in the magnitude of the band gap .[441,473] B doping also displays an increase in the H_2 production in water splitting aiding the suggestion of a donor defect.[476] Due to the amphoteric nature of B, it can sit substitutionally on both an oxygen and titanium site as well as interstitially, however there is a lack of . DFT studies have been carried out by Yang et al and Finazzi et al. provided a DFT study of B-doped titania[434,444] focussing on the electronic properties of the boron species in anatase (and rutile). Rudimentary thermodynamics have been carried out[477] yet a compre-

hensive thermodynamic and electronic study of the boron species in anatase has yet to be carried out.

Transition metals also provide a source of acceptor dopant and is seen with Ni[478–480], Fe[481–484],Co[485–487], Cr[488–491], and Cu[492–495] for example. It has been proposed that transition metal dopants provide an additional service by acting as an electron (or hole) trap enhancing the efficiency.[414,496–498] Whether this increases or decreases electron-hole separation is still in debate with certain metal cations increasing the rate (Cr) and others decreasing (Cu and Fe).[415,468] Beneficial effects are not just limited to *acceptor doping* as donors such as Nb[33,499], Ta[500–502], Sb[503,504] or W[411,505] also displays an enhancement of the photoactivity of anatase despite no band gap reduction or states within the band gap . The enhanced effects could likely be due to the increased electron concentration and mobility realised through donor doping and thus an increase in reducing electrons, or even an enhanced surface segregation as seen with Sb and Ta.[440,506]

7.2.1 Passivated Codoping

In order to rectify the recombination issues encountered from doping with non-metals, an approach to fully *passivate* the dopant states was proposed by Su-Huai Wei and coworkers whilst retaining the reduced band gap .[424] Within this formalism, the additional incorporation of a *donor* to the anatase lattice should have the effect of annihilating the additional holes brought about by acceptor doping and is shown schematically in Figure 7.5. Thus the beneficial band gap narrowing exhibited by N-doped TiO_2 can be retained whilst alleviating the recombination centres. Due to the location of the anatase CBM relative to the reduction potential (Figure 7.3), a preferable *resonant* donor is required so that no likewise shift downwards of the band gap is seen. This makes Nb, Ta, Mo and W ideal donors for this effect.[424,507] The original study by Gai et al proposed four different systems, [V+N], [Nb+N], [Cr+C] and [Mo+C]. Each of these have been studied extensively ([Nb+N][508–512], [Ta+N][513,514], [Cr+C][515], [Mo+C][516,516–518,518,519]) with notable examples such as [Nb+N] showing promising results such as the 7-fold increase in photocatalytic degradation of methylene blue or the 4-fold increase in decomposition of methyl orange with [Cr+C] codoped anatase.[511,516]

Numerous computational studies have been carried out on codoped systems for band gap engineering[424,507,520–532], in particular a computational screening by Yan and coworkers found that [Nb+N] and [Ta+N] were ideal at a 'high alloying concentration' regime, and

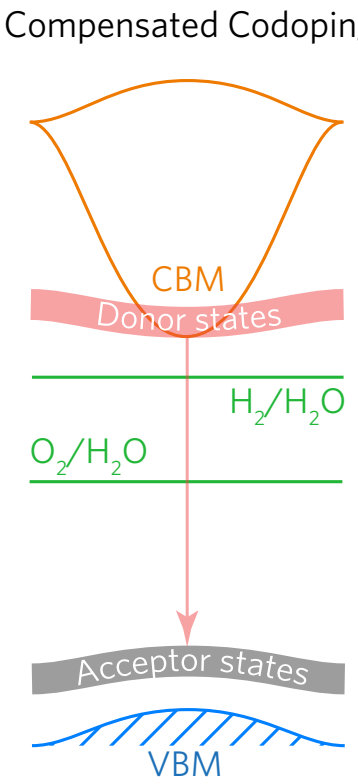

FIGURE 7.5: The schematic diagram for *passivated* co-doping in TiO_2 showing the positions of the band extrema relative to the redox potentials of water and the acceptor (green) and the donor states (red).

that both [Mo+2N] and [W+2N] were ideal in a 'low alloying concentration' regime. Carbon codoped systems were suggested to reduce the band gap too much, which, combined with the problems associated with monodoping of C mean that reproducibility will be an issue in this context, despite a few promising results.[516,518]

Within the codoping literature there exists a lack of distinction between the increased photoactivity seen due to passivated codoping and that seen with simple monodoping with either non-metal or metal aliovalent ions. Spurious claims are also made about the 'increase' in photocatalytic activity such as with the 7-fold increase and 4-fold increase of [Nb+N] and [Mo+C] systems of which the degradation of methylene blue and methyl orange rely on reduction as well as oxidation processes favouring an increased mobility and concentration of conduction band electrons.[511,516] Methylene blue and methyl orange photocatalytic tests also rely on the multi-stage degradation which can proceed via adsorption therefore making the difference between photocatalytic electron/hole transfer indistinguishable from other

processes. Bartlett also remarked that stoichiometric pairing of Nb+N was not achieved, even providing a follow up study on the composition dependence of Nb and N.[512] This work concluded that in fact a larger incorporation of Nb both decreased the optical band gap and increased the photoactivity and is echoed by Chadwick et al.[509,512] Zhang et al. when studying [Mo+C] showed an increase in the codoped system as compared to undoped and carbon-doped TiO_2 for the degradation of methylene blue highlighting again the possibility that the *n*-type donor is preferable in these situations. An analysis of the ionic radii of dopants in TiO_2 shows that for Nb,Ta,W,Cr,Mo and W a range of 0.59-0.64 Å is observed (compared to 0.60 Åfor Ti) making these highly soluble dopants therefore low formation energies would be expected.[240]

Chapter 8

Understanding the Role of Defects and Dopants in Anatase

8.1 Structural, Electronic Properties and Intrinsic Defects

8.1.1 Bulk Structural and Electronic Properties

The calculated structural parameters for anatase TiO_2 are shown in Table 8.1. The cell lengths, angles and bond lengths all match experimental values to within 0.5%[533,534] and within the range of values calculated from previous HSE06 studies.[36,39,535] This shows the efficacy and reliability of the HSE06 functional for the calculation of the geometry of anatase TiO_2, and thus the calculation of doped supercells.

TABLE 8.1: The calculated HSE06 structural parameters for anatase TiO_2 together with previous HSE06 calculated parameters and experimental literature value.

	a=b (Å)	c (Å)	Ti-O (Å)	
This Work	3.77	9.50	90	1.94,1.98
HSE06	3.76[535],3.77[39],3.78[36]	9.45[36],9.50[535],9.60[39]	90[36,39,535]	.....
Experiment[533,534]	3.78	9.50	90	1.93,1.98

Figure 8.1 displays the density of states (8.1(a)) and band structure (8.1(b)) for anatase. The density of states shows that the VBM of TiO_2 is wholly made up of O $2p$ states mixed

with some negligible Ti p and d contribution. The CBM on the other hand is principally Ti $3d$ in character with minor hybridisation with O $2p$ states. These results are consistent with other standard DFT and hybrid DFT studies carried out on anatase TiO_2 and its other polymorphs.[33,34,36–40] The band structure in Figure 8.1(b) confirms the wide *indirect* band gap of anatase, with an indirect band gap of 3.35 eV (VBM = between Γ–Z;CBM = Γ) and a direct fundamental band gap of 3.64 eV at Γ. Previous HSE06 calculations on anatase corroborate these values[536,537], as well as low temperature optical studies (3.3-3.42 eV)[538,539] yet general consensus in experiment places the band gap at ~3.2 eV.[34] GW (Green's function with self energy) calculations place the band gap around 3.6–3.8 eV[540–543] with the overestimation believed to be due to the convergence of the screened interaction in localised systems or from excitonic effects.[541–543] The hole effective masses at the VBM are 3.71 m_e and 1.79 m_e for VBM–Γ and VBM-Z respectively and the electron effective masses are calculated to be 3.61 m_e, 0.48 m_e and 0.61 m_e for Γ–X, Γ–N and Γ–Z respectively. The electron effective masses are noticebly higher than ZnO, SnO_2 or In_2O_3 which explains the lack of a high mobility TiO_2 based TCO.[33,411]

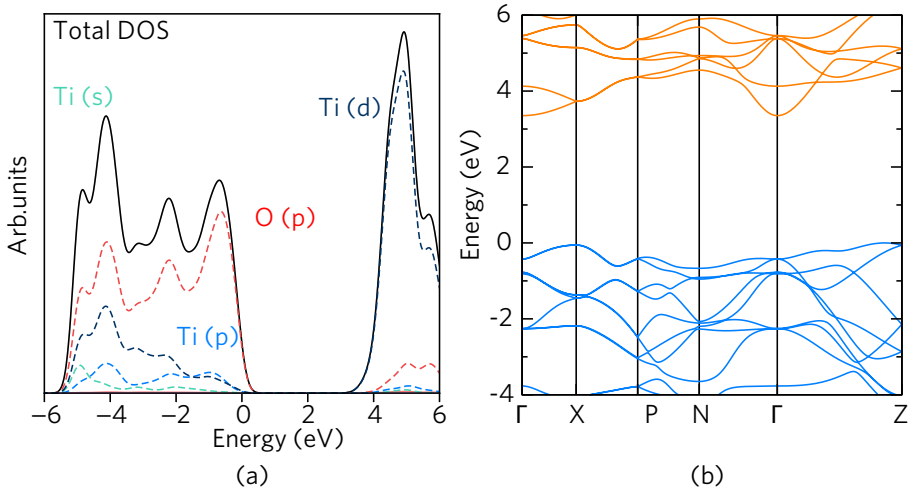

FIGURE 8.1: The density of states (a) and band structure (b) for anatase TiO_2 ($I4_1/amd$). In (b) the valence bands and conduction bands are depicted in blue and orange respectively, and for both (a) and (b) the valence band maximum is set to 0 eV.

8.1.2 Intrinsic Defects

In order to calculate the effect of extrinsic doping in anatase TiO_2, the *dominant* donor and acceptor defects liable to cause intrinsic compensation were evaluated and are included in

all the following sections. The thermodynamic transition levels calculated using the HSE06 hybrid functional are shown in Figure 8.2 under three different growth regimes, *Ti-rich,O-poor, Ti-rich/O-poor*† and *Ti-poor/O-rich* conditions. *Ti-rich/O-poor*† refers to the *O-poor* regime which is within the realms of experimental viability where chemical potentials of $\mu_O = -2$ eV and $\mu_{Ti} = -5.14$ eV making it true for a pressure and temperature of $p_{O_2} < p_{O_2}^{\text{ambient}}$ and $T = 600$ K as rationalised by Agoston et al.[28,90] These chemical potentials will be used in Sections 8.2, 8.3 and 8.4 in place of the *O-poor* boundary. In order to reference our work to previous theory, the intrinsic defects will be analysed over all three growth conditions.

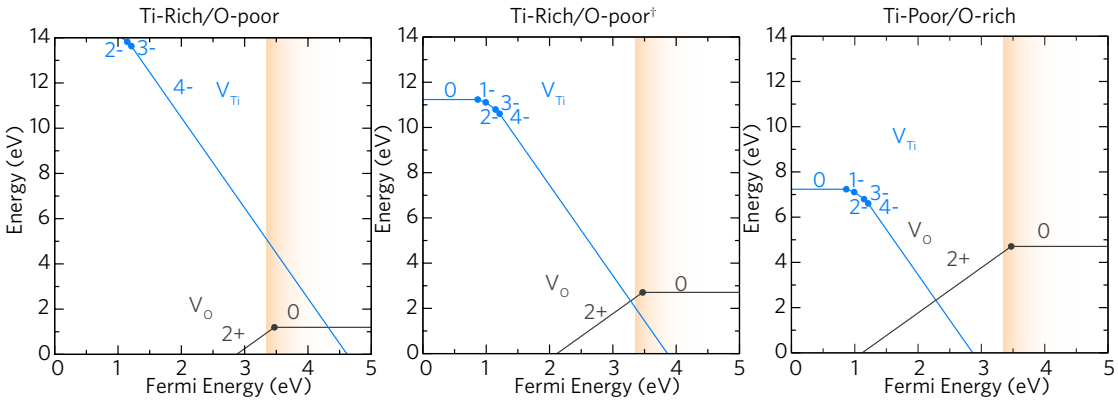

FIGURE 8.2: The transition levels for the dominant intrinsic defects under the most *Ti-rich/O-poor* conditions, experimental poor (*Ti-rich/O-poor*†; μ_O=-2 eV) and the most *Ti-poor/O-rich* conditions. In each example the Fermi level ranges from the VBM (0 eV) to ~ 1.65 eV above the CBM (denoted by the orange graded region).

The dominant acceptor and donor intrinsic defects have been determined to be V_{Ti} and V_{O} respectively based upon previous theoretical calculations on anatase.[38–40,89,386,535,544]

V_O:

Under *n*-type 'favourable' conditions, both *O-poor* and *O-poor*†, V_{O} possesses the lowest formation energy ($V_{\text{O}}^0 =$ 1.19 eV and 2.71 eV respectively) which rises to ~4.71 eV at the *O-rich* limit. Within the anatase lattice, V_{O} is a *resonant* donor with the 2+/0 transition level occurring ~ 0.05 eV above the CBM. This is in contrast to most wide band gap binary oxides such as ZnO[29,276,278,545],SnO_2[25,29,110,161] and $BaSnO_3$[26] where the oxygen vacancy is a *deep* defect. The negative-U behaviour of V_{O} in anatase however is consistent with wide band gap TCOs. The partial charge density of the neutral charge state of V_{O} is displayed in Figure 8.3 showing the localisation of the added electrons onto the two adjacent Ti atoms forming Ti^{3+} and

stabilising the oxygen vacancy. This is in contrast to the oxygen vacancy behaviour shown in SnO_2 (Section 4) where the electron density is localised at the vacancy itself. Our results are consistent with other hybrid and standard DFT studies[38,89] and Ti^{3+} peaks are present in XPS studies on anatase.[468]

V_{Ti}:

Under all growth regimes, V_{Ti} is an *ultra-deep* acceptor with the 1-/0 transition level occurring at ~ 0.87 eV above the VBM. In the neutral charge state (V_{Ti}^{0}), the titanium vacancies have formation energies of 14.26 eV, 11.24 eV and 7.23 eV and under *Ti-rich/O-poor*, *Ti-rich/O-poor*† and the most *p*-type favourable *Ti-poor/O-rich* conditions with the expectation of negligible quantities towards lower Fermi levels. Under *Ti-rich/O-poor*† conditions, V_{Ti}^{4-} begins to compensate V_{O}^{2+} around 0.06 eV below the CBM (0.68 eV *above* the CBM at the most O-poor conditions) and at ~ 2.28 eV *above* the VBM under *Ti-poor/O-rich* chemical potentials. From these calculations, we can show that all charge states appear in the band gap, which differs somewhat from the theoretical literature on V_{Ti}. LDA predicts a quadruple *shallow* acceptor, yet this is likely due to the inadequate description of the band gap and incorrect localisation electrons and holes.[546] Morgan et al. used DFT+U to show that V_{Ti} is in fact a *deep* acceptor yet with an unstable 1- charge state (the 0/2- charge state occurs ~0.85 eV above the VBM). The authors also show that V_{Ti}^{0} has a formation energy that is ~2.5 eV lower than that calculated by our HSE06 study.[89,386] The only other HSE06 calculations on V_{Ti} show that the charge states transition from 0→2-→4- charge states in the band gap.[40] However, this study made use of a single Monkhorst-Pack *k*-point leading to inaccuracies in the calculation of the total energies and uncertainties in the formation energies of defects.[40]

It is also important to correctly describe the localisation and delocalisation of defects when analysing the total energies (this was also pointed out for V_{Sn} in SnO_2 in Section 4). Figure 8.3 shows the partial charge densities for the localisation of holes surrounding the V_{Ti} centre and the evolution over different charge states. For V_{Ti}^{0} , four holes are introduced into the TiO_2 lattice which are situated on adjacent O $2p$ orbitals within the immediate vicinity of the vacancy (two axial and two equatorial). The axial holes are the first to be filled by the 1- and 2- charge states (depicted as p_y orbitals) followed by the equatorial holes by the 3- and 4- (fully ionised) charge states (depicted as p_z orbitals).

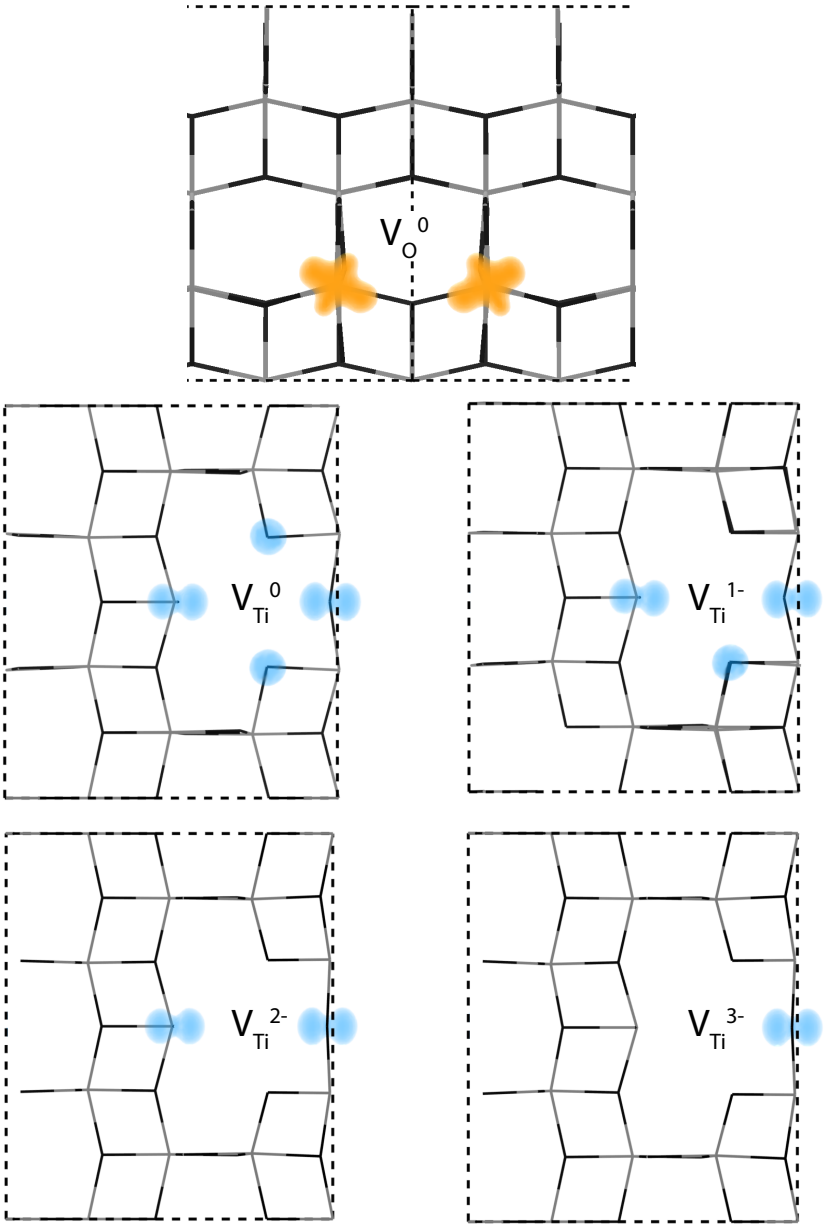

FIGURE 8.3: The partial charges of the dominant intrinsic defects in TiO_2 as calculated with the HSE06 hybrid functional. V_O is viewed along the {100} direction and V_{Ti} is displayed along the {010} direction. In each example the TiO_2 lattice is shown as a wire frame model with grey = Ti and black = O. The electron charge density is shown by the orange isosurface plotted from 0-0.02 eV Å^{-1} and the hole electron density by the blue isosurface (plotted from 0-0.015 eV Å^{-1}) . The supercell is depicted by the dashed black line.

8.1.3 Optical Absorption and Emission

The optical absorption and emission for V_{Ti} and V_{O} are shown using configurational coordinate diagrams in Figure 8.4. The diagrams show the excitation of electrons to the CBM (a and c) and the capture of electrons from the VBM (b and d) (to/from the defect). Each parabola corresponds to a different charge state with the minimum signifying the *equilibrium configuration* of that charge state. As the optical absorption and emissions processes are instantaneous transitions (picoseconds) it is assumed the equilibrium geometry of the ground state does not change.

V_{Ti}:

Figure 8.4(a) shows the absorption of an electron to the CBM for V_{Ti}. Each absorption $q = 4- \rightarrow 3- \rightarrow 2- \rightarrow 1- \rightarrow 0$ that occurs has an associated energy of 2.99 eV, 3.09 eV, 3.33 eV and 3.39 eV corresponding to wavelengths within the range: 366-414nm. These are likely to appear within the absorption edge of anatase TiO_2 and thus will have a negligible effect on the visible light optical transmission. Figure 8.4(b) shows the *capture* of an electron from the VBM and shows that the absorption energies are 2.14 eV, 2.44 eV, 2.61 eV and 2.50 eV for $q = 0 \rightarrow 1- \rightarrow 2- \rightarrow 3- \rightarrow 4-$ corresponding to wavelengths of 496-579nm. Increased visible light absorption is expected with increasing V_{Ti} concentrations. Its possible that these absorption may be present in fine structure absorption spectra.[547]

Infrared photoluminescence also occurs under both electron excitation and capture. Under electron excitation from V_{Ti} to the CBM, energies of 0.92 eV, 0.81 eV, 0.98 eV and 1.28 eV occur corresponding to wavelengths of 969-1344nm (for $q = 4- \rightarrow 3- \rightarrow 2- \rightarrow 1- \rightarrow 0$). The release of an electron to the VBM (Figure 8.4(b)) incurs mostly *non-radiative* emissions of 0.086 eV and 0.033 eV (for $q = 2- \rightarrow 1- \rightarrow 0$) and either non-radiative or IR emissions with energies of 0.43 eV (2903nm) and 0.33 eV (3768nm) (for $q = -4 \rightarrow -3 \rightarrow -2$). Most experimental photoluminescence studies on TiO_2 polymorphs are carried out in the UV/visible portion of the electromagnetic spectrum (<900nm). However, one study on TiO_2 nanoribbons shows a photoluminescence peak at 1.27-1.30 eV for anatase likely to be due to the $1- \rightarrow 0$ emission.[548] Relatively large *Stokes shifts* are calculated for each transition, indicating a broad shift between absorption and emission. These are 2.07 eV for $3- \leftrightarrow 3-$, 2.28 eV for $3- \leftrightarrow 2-$, 2.36 eV for $2- \leftrightarrow 1-$ and 2.11 eV for $1- \leftrightarrow 0$.

V_O:

Figures 8.4(c) and (d) depict the configurational coordinate diagrams for the excitation (c) and capture (d) of an electron from the CBM and VBM respectively. The optical absorption in V_O is a two-photon process displaying very low absorption energies of 0.44 eV (2799nm) making it not likely to be observed. No photoluminescence is seen from this excitation, as the excited electrons are now within the conduction band and the 2+/0 thermodynamic transition level occurs ~0.05 eV above the CBM. Electrons excited from the VBM to V_O have absorption energies of 3.58 and 3.64 eV for $2+ \rightarrow 1+ \rightarrow 0$ corresponding to wavelengths of 340nm and 346nm respectively, likely to be within the strong band gap absorption of anatase TiO_2. Photoluminescence in this process, however, does incur wavelengths of 2.98 eV (416nm) for each transition. The emission of two photons of equal wavelength will likely correspond to a larger photoluminescence intensity. Due to the large associated absorption, most experimental photoluminescence does not excite at energies large enough to see the photoluminescence of V_O as it is typically carried out at wavelengths just larger than the band gap. Wang *et al.* however noticed a photoluminescence excitation (PLE) and associated photoluminescence of 3.65 eV and 2.29 eV respectively.[549] These values match our calculated values well and the measured stokes shift (1.36 eV) between the absorption and emission peaks, corresponds well to the *total* stokes shift calculated from the two photon process (1.26 eV). Numerous room temperature studies see a peak centred around 2.90–2.97 eV which Kernazhitsk *et al.* identify as oxygen vacancies and is close to our calculated value of 2.98 eV (at room temperature a shift is expected).[547,550,551,551–553]

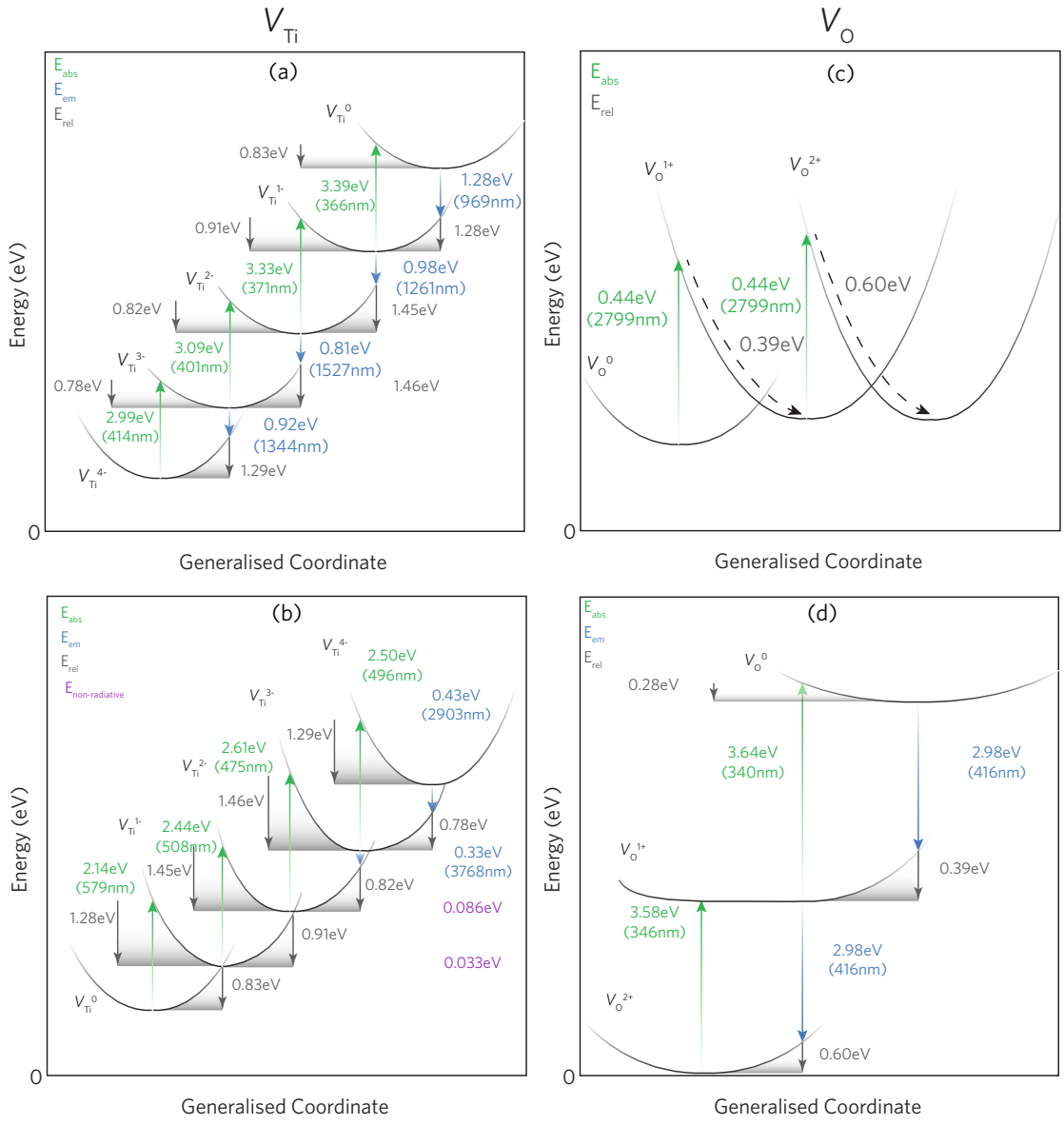

FIGURE 8.4: The configurational coordinate diagrams for V_{Ti} (a and b) and V_O (c and d) showing the optical absorption and emission. Panels (a) and (d) describe the excitement of an electron to the conduction band minimum (CBM), whilst panels (c) and (d) show the excitement of an electron from the valence band maximum (VBM) to the defect. The absorption energies are shown in green, the emission energies in blue and the relaxation energies are shown in grey. The purple values correspond to *non-radiative* transitions.

8.2 Dispelling the Myth of Passivated Codoping in TiO_2

Details of the theoretical methodology is included in Appendix C.1.
The work in this section is in preparation for publication.

In order to assess the ability of fully *passivated* codoping in TiO_2, the defect thermodynamics of the TiO_2:[Nb+N] and TiO_2:[Ta+N] systems were analysed and compared. These systems were chosen due to their abundance in the literature, and from previous theory calculations identifying them as ideal candidates for water splitting.[424,507–513,513,514,523,554,555] Both Nb and Ta have been shown to easily dope into TiO_2[33,437,499–502] and success has been seen in N-doped TiO_2.[449–452] The calculation of these defects were carried out alongside the possible codoped clusters in TiO_2 using the hybrid HSE06[30,31] functional, the details of which are provided in Appendix C.1.

8.2.1 Mono doping of Anatase with N, Nb and Ta

All mono-doped anatase TiO_2 systems were analysed to determine the thermodynamic viability of the chosen defects and any points of unintentional compensation. Figure 8.5 displays the transition levels for the N, Nb and Ta related defects in anatase.

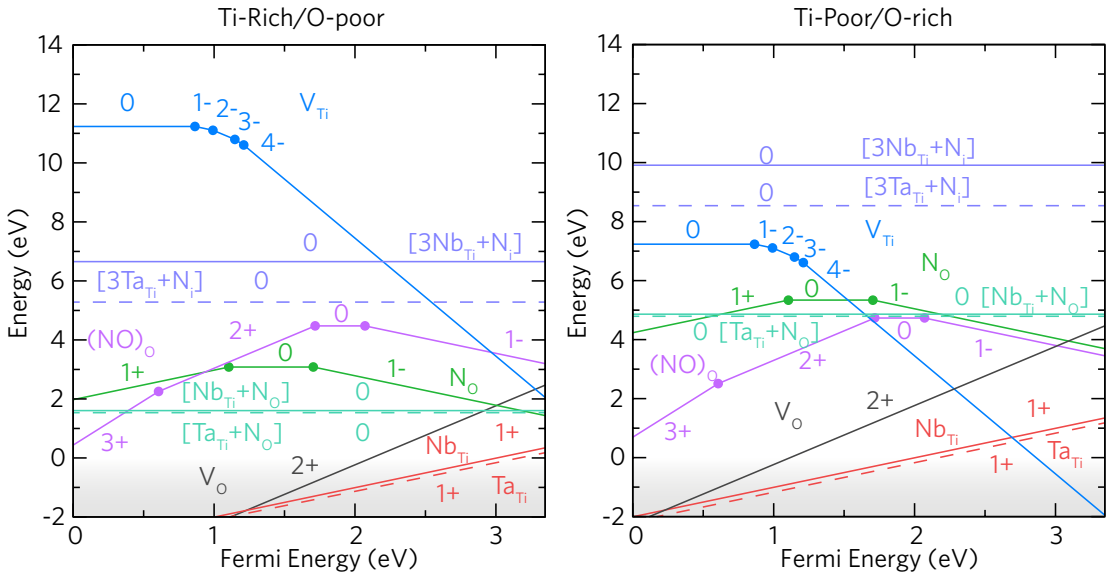

FIGURE 8.5: The thermodynamic transition levels for Nb,Ta,N,[Nb+N] and [Ta+N] doped anatase TiO_2 under *Ti-rich/O-poor* and *Ti-poor/O-rich* conditions. The Fermi level ranges from the VBM (0 eV) to the CBM (3.35 eV).

Substitutional Nitrogen, N_O:

Within the anatase lattice, N can exist both substitutionally and interstitially. Substitutional nitrogen, N_O, acts as an amphoteric defect under both growth regimes with a relatively high formation energy (neutral charge state) of 3.08 eV and 5.34 eV under *Ti-rich/O-poor* and *Ti-poor/O-rich* conditions respectively. Although *O-rich* conditions typically favour the formation of acceptor defects, N_O, is highest in formation energy under this growth regime. This is due to the higher μ_O and thus lack of available oxygen sites reflected in the higher formation energy of V_O. N_O is both an ultra deep acceptor (0/1- transition ~1.70 eV above the VBM) and *donor* defect (1+/0 transition ~2.24 eV below the CBM) contributing no source of *p* or *n* type conductivity in anatase. Due to the intrinsic *n*-type nature of anatase, the Fermi level is likely to exist towards the CBM and as such, N_O will act as an acceptor. Figure 8.6(a) displays the partial charge density for the neutral charge state of N_O showing the hole localised within the N $2p$ orbital. These results are consistent with other HSE06 studies on TiO_2:N.[96,463] Intrinsic compensation occurs from V_O just around 0.34 eV and 0.25 eV below the CBM for *Ti-rich/O-poor* and *Ti-poor/O-rich* conditions respectively. In reality under *O-rich* conditions this point won't be realisable due to the Fermi level being pinned in the band gap around

2.28 eV above the VBM from the crossing of $V_{Ti^{4-}}$ and V_O^{2+}.

Interstitial Nitrogen, $(NO)_O$:

Nitrogen relaxes from the 'ideal' interstitial point to form a "split-interstitial" producing an N–O dumbbell situated on an O atom site (denoted $(NO)_O$). This behaviour is observed in the previous theoretical literature as well as electron paramagnetic resonance (EPR) experiments.[96,463,465–467] The formation energies of $(NO)_O^0$ remain stable across the entirety of the chemical potential range with similar values of 4.48 eV and 4.73 eV under *Ti-rich/O-poor* and *Ti-poor/O-rich* conditions respectively. $(NO)_O$, like N_O, can act as an electron acceptor *and* as a donor. At Fermi energies close to the VBM, $(NO)_O$ acts as a three electron donor and becomes the dominant nitrogen species in TiO_2. $(NO)_O$ undergoes a 3+/2+ and a 2+/0 transition level around 2.82 eV and 1.63 eV below the CBM respectively. In anatase, however, the Fermi level is likely to exist towards the CBM at which point $(NO)_O$ acts as an acceptor. Despite having the ability to produce three holes in TiO_2, $(NO)_O$ only undergoes one transition level in the band gap (0/1- transition at 2.07 eV *above* the VBM). $(NO)_O$ can therefore be said to only accept one hole, consistent with previous theory.[96,465,466] Figure 8.6(b) shows neutral charge state of $(NO)_O$ displaying the localised hole bound to the N–O dumbbell. Under *Ti-poor/O-rich* conditions it is likely that $(NO)_O$ will be the dominant nitrogen species across the entirety of the band gap, and explains the defect's appearance in the experimental literature. Under *Ti-rich/O-poor*, however, it is likely that a greater concentration of substitutional nitrogen will be seen when the Fermi level is trapped just below the CBM.

Nb_{Ti} and Ta_{Ti}:

Nb_{Ti} and Ta_{Ti} are the lowest formation energy defects under both growth regimes having formation energies of 0.38 eV and 0.22 eV respectively under *Ti-rich/O-poor* conditions. Under a *Ti-poor/O-rich* growth regime, the formation energies rise to 1.38 eV and 1.22 eV for Nb_{Ti} and Ta_{Ti} respectively. This is likely due to the similar ionic radii of Nb and Ta (~64pm) to Ti (~61pm)[240] causing minimal strain to the anatase lattice upon incorporation of these dopants (The six surrounding O atoms move ~ 1–1.5% away from the dopant centre). Both substitutional Nb and Ta act as *resonant* donors donating one electron to the conduction band with the 1+/0 transition levels occurring above the CBM. The electron density is therefore delocalised over the Ti 3*d* orbitals that make up the CBM (Figure 8.6(c)). These results are indicative of the high conductivities seen in experiment TiO_2[33,437] and is reproduced in

the theoretical literature.[39,556,557] Under *Ti-poor/O-rich* conditions Nb/Ti_{Ti} is compensated for by V_{Ti}^{4-} ca. 0.66 eV and 0.63 eV below the CBM for Nb and Ta respectively. Under a *Ti-rich/O-poor* growth regime, however, no intrinsic compensation occurs in the band gap.

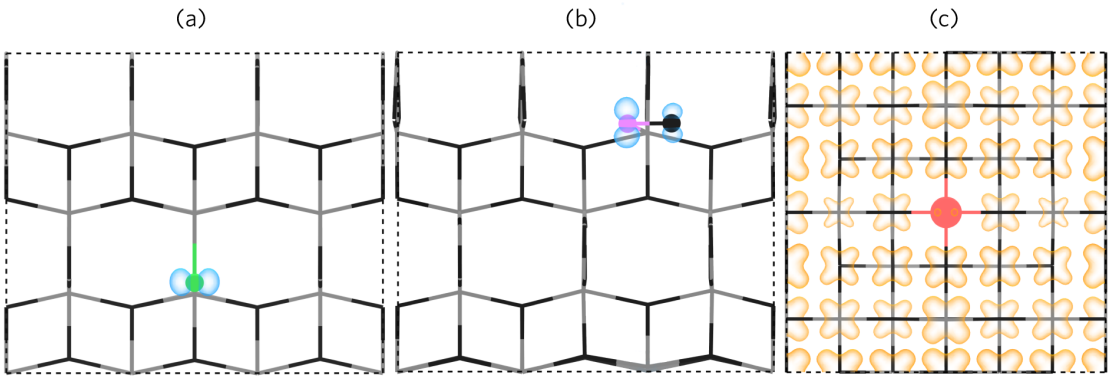

FIGURE 8.6: The partial charge densities of (a) N_O^0 and (b) $(NO)_O^0$ as viewed along the {100} direction and (c) $Nb(Ta)_{Ti}^0$ as viewed along the {001} direction. The anatase lattice (Ti=grey, O=black) is depicted by the wire-frame lattice, and the nitrogen and Nb(Ta) species, by the coloured orbs (colour coded to Figure 8.5). The charge isosurface for holes are shown in blue and plotted from 0-0.02 eV Å^{-1} and the electron charge density in orange and plotted from 0-0.002 eV Å^{-1}

8.2.2 The Realisation of Full Compensation?

In order to assess viability of fully compensated codoping in anatase TiO_2, two different dopant clusters were conceived for this study. The two clusters were: $[M_{Ti}+N_O]$ (where M = Nb or Ta) based on the formation of substitutional nitrogen, and $[3M_{Ti}+(NO)_O]$ based on the formation of *interstitial* nitrogen. These clusters represent fully compensated doped systems under an *O-poor* and *O-rich* regime. The substitutional cluster was calculated in a 'near' and 'far' configuration where the Nb(Ta) dopants are next to or ~8 Å away from the nitrogen defect. These configurations allow for the analysis of the Coulombic (thermodynamic) versus steric (kinetic) interaction of the clusters in the anatase lattice. The interstitial N complex was calculated in the 'near' configuration as the 'far' configuration would require a larger supercell size for an adequate description of this effect.

The transition levels in Figure 8.5 show that under both sets of chemical potentials, the substitutional cluster ($[M_{Ti}+N_O]$) is the lower of the two clusters in terms of formation energy. Under *Ti-poor/O-rich* conditions, the formation energies of $[Nb_{Ti}+N_O]$ and $[Ta_{Ti}+N_O]$ are 1.60 eV and 1.53 eV respectively and under *Ti-poor/O-rich* conditions these are 4.86 eV

and 4.79 eV respectively. Figure 8.7(a) shows the partial charge density for the Nb and Ta substitutional defects whereby the localised hole centred on the N $2p$ orbital is now filled with the donated electron. The likely improvement in visible light activity in TiO_2 is possibly due to the excitation of the electron in the filled N orbital to the conduction band which occurs in the visible light.[96] Calculated binding energies (E_{BE}) were calculated using equation 8.2.1 giving 2.10 eV and 2.01 eV for [Nb+N_O] and [Ta+N_O] respectively.

$$E_{BE} = E^{[Nb(Ta)_{Ti}+N_O]} + E^{host} - E^{Nb(Ta)_{Ti}} - E^{N_O} \tag{8.2.1}$$

Overall, these results show that despite the binding energies present, there is still an overwhelming preference for substitutional Nb and Ta in anatase and thus a doping asymmetry will arise.

The values for both [Nb_{Ti}+N_O] and [Ta_{Ti}+N_O] are similar to those calculated by Gai et al. and Yin et al. via DFT+U calculations both gaining binding energies of 1.97 eV and 1.92 eV respectively.[424,507] Our calculations show a greater preference for [Nb_{Ti}+N_O] binding over [Ta_{Ti}+N_O] and thus a kinetically driven passivation. It is also possible to evaluate the formation of a substitutional N when adjacent to a substitutional Nb or Ta defect. From our calculations we see that the formation of N_O is lowered in this scenario by ~ 2.1 eV and 2.0 eV for Nb and Ta respectively. This is likely to be due to both Coulombic effects and lattice strain. The increase in N content is seen experimentally by Chadwick et al. with increasing Nb incorporation.[509] It is important to note that the formation of Nb_{Ti} and Ta_{Ti} adjacent to a substitutional nitrogen is *also* lowered by 1.86 eV and ~ 1.77 eV respectively, therefore there is still a preference for substitutional Nb and Ta over substitutional N species indicative of the doping asymmetry in TiO_2.

The [3Nb(Ta)$_{Ti}$+$(NO)_O$] clusters occur significantly higher in formation energy than their substitutional counterparts. Under *Ti-poor/O-rich* these are 9.91 eV and 8.54 eV for [3Nb_{Ti}+$(NO)_O$] and [3Ta_{Ti}+$(NO)_O$] respectively. Under Idealised *Ti-rich/O-poor* conditions these formation energies reduce to 6.65 eV and 4.39 eV respectively. Despite the increased distortion to the anatase lattice (as seen in Figure 8.7(b)) only [3Ta_{Ti}+$(NO)_O$] possesses a binding energy of 0.59 eV whereas [3Nb_{Ti}+$(NO)_O$] shows a *dissociation energy* of 0.31 eV as calculated using:

$$E_{BE} = E^{[3Nb(Ta)_{Ti}+(NO)_O]} + 3E^{host} - 3E^{Nb(Ta)_{Ti}} - E^{(NO)_O} \tag{8.2.2}$$

Figure 8.7(b) shows the partial charge density of both Nb and Ta clusters showing the filled N-O hole states associated with full compensation. To the best of our knowledge, the effects of substitutional Nb and Ta with interstitial nitrogen has not been studied theoretically. These results match the appearance of interstitial nitrogen seen in the [Ta+N] codoped systems within the experimental literature.[513,523,554,555] It is important to note, however, that although a binding energy exists for the tantalum and nitrogen codoped system, it may be *entropically* unfavourable due to the large number of species involved.[558] A similar analysis to determine the change in formation energy for interstitial nitrogen can be applied, and it shows that for the Nb cell an increase in formation energy is seen for both substitutional Nb (~ 0.6 eV) and interstitial N (~ 0.3 eV). For the Ta cell however, a decrease in energy of the interstitial N is observed (~ 0.59 eV) with an increase in Ta_{Ti} (~ 0.19 eV) which is to be expected due to the Coulombic repulsion from two other tantalum defects. Despite this, under *Ti-rich/O-poor* conditions, the formation energy for both neutral charge states still favours the formation of Ta_{Ti} over $(NO)_O$ by ~ 3.1 eV.

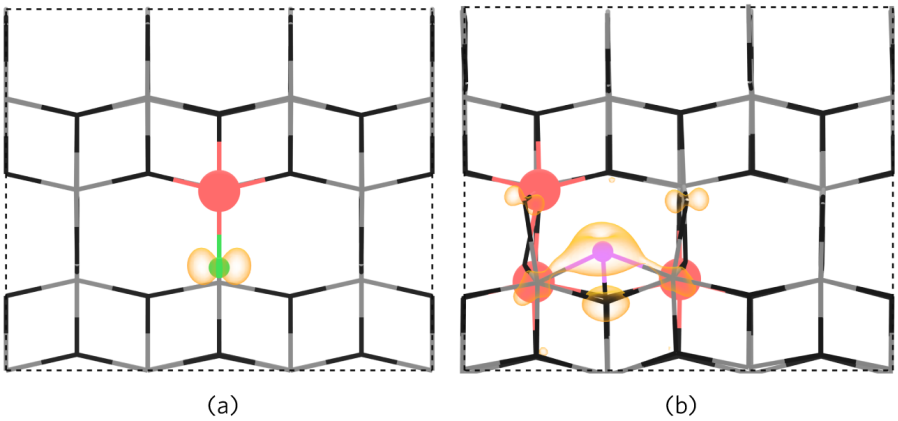

FIGURE 8.7: The partial charge densities for (a) [$Nb(Ta)_{Ti}$+N_O] and (b) [$3Nb(Ta)_{Ti}$+$(NO)_O$] as viewed along the {100} direction. The anatase lattice is portrayed through the wire-frame model (Ti=grey, O=black) and the dopant species by the coloured spheres (coloured coded to Figure 8.5). The electron partial charge density is shown in orange and is plotted from 0-0.02 eV Å^{-3}.

The realisation of *fully* compensated codoping however, is more than certainly unobtainable due to the inherent preference for *n*-type defects and dopants in anatase TiO_2. As seen in Figure 8.5, under both growth regimes, substitutional Nb(Ta) are the dominant defects and

are far lower in energy than any of the nitrogen or cluster species. The implication of this work is that although it is possible for the codoped clusters to form (as shown by the binding energies), there will always be a higher concentration of *n*-type dopant and thus the inability to produce a fully passivated system. The lack of quantitative data on dopant concentrations in the previous experimental literature makes it impossible to ascertain whether full compensation has occurred.[510,513,513,514,523,554,555] Certain studies do, however, acknowledge the lack of full charge parity such as those by Bartlett et al. and Chadwick et al.[509,511,512]

8.3 Conductivity and Photocatalysis in Boron Doped TiO_2

Details of the theoretical methodology is included in Appendix C.
The work in this section has been published in The Journal of Physical Chemistry C. Figures from this section have been adapted from this paper.

The ability to produce fully compensated codoped anatase has been shown to be impossible at thermodynamic equilibrium. It is possible that amphoteric dopants may provide a way of gaining beneficial *self-compensation* in anatase and novel mechanisms for the enhancement of visible light photocatalysis and electron-hole separation. One such dopant is boron, which shows increased rates of photocatalytic activity under both UV and visible light.[441,473,474] In the literature, both red and blue shifts are present[443,559–561] indicating both acceptor and donor defects. Due to its small ionic radii, B is likely to sit interstitially as indicated in experiment[473], yet it can also reside on both the oxygen and titanium sites in the anatase lattice due to its amphoteric nature. XPS studies shows the incorporation of boron interstitially as well as substitutionally on an oxygen site, however B^{3+} can also be an acceptor when incorporated on a titanium site.[444] Numerous theoretical studies have been carried out on TiO_2:B[444,562,563], in particular a study by Finazzi and coworkers[444] which provides a comprehensive electronic overview of various B-related species as found in experiment. The general consensus within the experimental literature (and LDA/GGA DFT studies) rule out the formation of B_{Ti} as a relevant defect due to the lack of associated peak in XPS studies.[444,561,563,564] The small ionic radii of boron (B^{3+} = 0.27 Å)[240] also renders it energetically unfavourable compared to B_O. Finazzi et al also suggest the diffusion of B_O to an interstitial site relating the suggested appearance of interstitial boron in experimental films[473] and ^{11}B NMR (nuclear magnetic resonance).[565] Lin et al.[566] also agreed that substitutional B_O is more preferential than B_{Ti} using GGA+U, however Yu et al.[567] show that B_{Ti} is in fact a lower formation energy defect. The stabilised Ti^{3+} on the anatase surface via boron doping has also been identified due to stabilisation of the distorted structural disorder caused by both B_i and Ti^{3+} proposed to enhance the photocatalytic activity. The lack of confidence in the existing bulk

theoretical data shows the need for a comprehensive thermodynamic study in order to elucidate the species present over different growth conditions and the possible cause of visible light and enhanced photoactivity in boron doped anatase thin films. This section will detail the electronic and thermodynamic formation of all three boron defects: B_i, B_{Ti}, and B_O.

8.3.1 Defect Thermodynamics of B-Doped TiO_2

Figure 8.8 displays the thermodynamic transition levels for the intrinsic defects and boron related species under *Ti-rich/O-poor* and *Ti-poor/O-rich* growth regimes. Boron can enter the anatase lattice both substitutionally (on a titanium, B_{Ti}, or oxygen site, B_O) or interstitially (B_i).

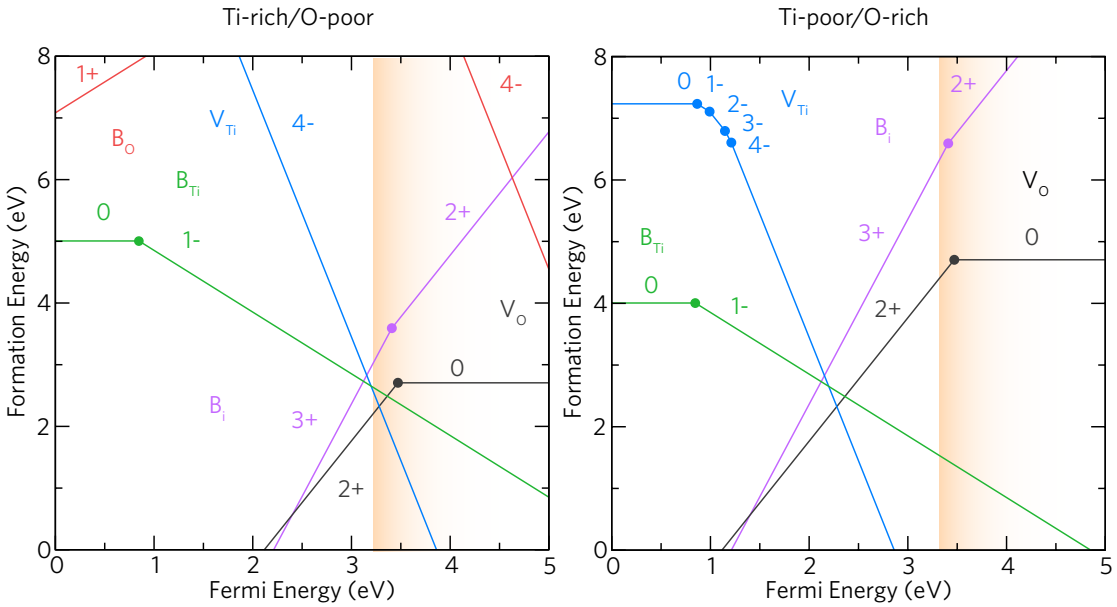

FIGURE 8.8: The transition level diagrams for boron doped TiO_2 (anatase) under both *Ti-rich/O-poor* and *Ti-poor/O-rich* conditions. The Fermi energy ranges from the VBM (0 eV) to 1.7 eV above the CBM (at 3.35 eV). The conduction band region is shown by the graded orange area.

B_i:

Under both *Ti-rich/O-poor* and *Ti-poor/O-rich* conditions, B_i is a three-electron donor. Whilst the formation energy of the neutral charge state is relatively high in energy (*O-poor* = 8.31 eV; *O-rich* = 11.31 eV), the fully ionised charge state (B_i^{3+}) is fairly low in energy and

dominates over the majority of the band gap under *Ti-rich/O-poor* conditions. The 3+/2+ transition level occurs around 0.06 eV above the CBM and the 2+/0 transition occurs around 2.41 eV above the CBM; the Fermi level, however, will not extend this far due to compensation by acceptor defects. Figure 8.9(a),(b) and (c) show the partial charge density for interstitial boron in the neutral, 1+ and 2+ charge states respectively. The neutral charge state (B_i^0) shows the electrons highly localised around the B atom and adjacent O $2p$ and Ti $3d$ orbitals with large distortions to the anatase lattice. This is likely to owe to the high formation energies of this particular charge state. The 1+ charge state (Figure 8.9(b)) shows the removal of an electron from an adjacent Ti^{3+} and thus a further lattice distortion to stabilise the defect charge state. This behaviour has been seen previously by Yang et al..[562] When in the 2+ charge state (Figure 8.9(c)) and the 3+ (not shown) charge state, a delocalisation of the electron charge over Ti $3d$ orbitals which make up the CBM is observed. The appearance of Ti^{3+} due to boron doping is accounted for by the increase in Ti^{3+} peaks in XPS measurements.[33,444] Interstitial B thus incorporates as B^{3+} where, B_i^{3+} forms a trigonal planar BO_3 configuration (as with B_i^{2+}). Most cationic boron species display a similar trigonal planar configuration such as BF_3, BH_3, H_3BO_3 and B_2O_3; this is due to the sp^2 hybridisation of the $2s$ and $2p$ orbitals. This configuration in boron doped TiO_2 is therefore not too surprising. A similarity in XPS binding energies of interstitial B to B_2O_3 exists in the experimental literature (191-192 eV) making this easy to identify.[441,444,473] It is unlikely that either the neutral, 1+ or 2+ charge states will be seen in B-doped TiO_2 due to the Fermi level being trapped around 0.19 eV and 1.19 eV below the CBM under *Ti-rich/O-poor* and *Ti-poor/O-rich* conditions respectively by compensation by both V_{Ti} and B_{Ti} defects.

B_{Ti}:

Under *Ti-rich/O-poor* conditions, B_{Ti} begins to form around 0.22 eV *below* the CBM leaving a net two electron donation from B_i. Under *Ti-poor/O-rich* conditions, this crossing point occurs deeper in the band gap ~ 1.19 eV below the CBM. B_{Ti} in the neutral charge state possesses formation energies of 5.01 eV and 4.01 eV under *Ti-rich/O-poor* and *Ti-poor/O-rich* conditions respectively. B_{Ti} is also a *deep* defect where the 0/1- transition level occurs at 0.84 eV above the VBM. B_{Ti} will therefore not contribute to any *p*-type conductivity in anatase TiO_2. Boron substituting a titanium has been proposed from previous DFT calculations[444,561,563,564] to be the *least* energetically favourable substitutional defect, however we find the opposite is true. Figure 8.9(d) shows the distortion and partial charge densities for

B^0_{Ti} where boron distorts from the Ti site by up to ~ 11% in the *b* directions forming trigonal planar BO_3 similar to B^{3+}_i.

Although the hole is *localised* it is localised on an adjacent O as shown in Figure 8.9(d) and not on the B defect indicating that it remains B^{3+} in this charge state. When the hole is filled (ie. the 1- charge state), B moves back towards the original Ti site, however, it forms tetrahedral BO_4 instead of octahedral BO_6 as would be expected.

B_O:

The final defect to be considered is substitutional, B_O. This defect species is considered to be the 'energetically favourable' substitutional acceptor from the theoretical and experimental consensus.[444,566] However, using HSE06, we find that under *Ti-rich/O-poor* and *Ti-poor/O-rich* conditions, B^0_O possesses a very high formation energies of 10.23 eV and 15.23 eV respectively. The probability of finding B_O in anatase under thermodynamic equilibrium is therefore slim. B_O acts as a *deep* donor with a 1+/0 transition level occurring at ~ 0.2 eV below the CBM. At Fermi levels just beyond the CBM, B_O rapidly becomes an acceptor transitioning to the 2- charge state (~ 0.1 eV above the CBM) then subsequently to the 4- charge state (~ 0.36 eV above the CBM). Both the neutral and 4- charge states are shown in Figures 8.9(e) and (f) respectively. For B^0_O the electron localisation is seen shared between the boron and titanium atom (beneath). The B atom distorts around 5% in the *c* direction whilst the Ti atom below shifts around 4% away from the B atom. In the 4- charge state the electron density is highly localised over the BTi_3 centre and the atoms shift back towards their original position by around 2% from B^0_{Ti}.

From our calculations, it is clear that both B_i and B_{Ti} will preferentially form. Under *Ti-rich/O-poor* (*n*-type favourable conditions) it is likely that more interstitial boron will form and likely causes the blue shifts in the band gap as seen in experiment. High *n*-type conductivities will not be realisable due to the Fermi level trapping around 0.19 eV below the CBM. Under *p*-type favourable *Ti-poor/O-rich* conditions, the Fermi level is trapped in the band gap around 1.19 eV below the CBM where it is likely that a larger concentration of B_{Ti} will be present. The possibility for self-passivated doping is therefore likely when the right growth conditions are used. The reasoning behind the lack of B_{Ti} seen in experiment can be due to the similarities in the coordination environments (trigonal planar) and oxidation states (3+) of both B_{Ti} and B_i. A simple analysis of the B core levels ($E^{shift}_{B_{core}}$) can be achieved using the B

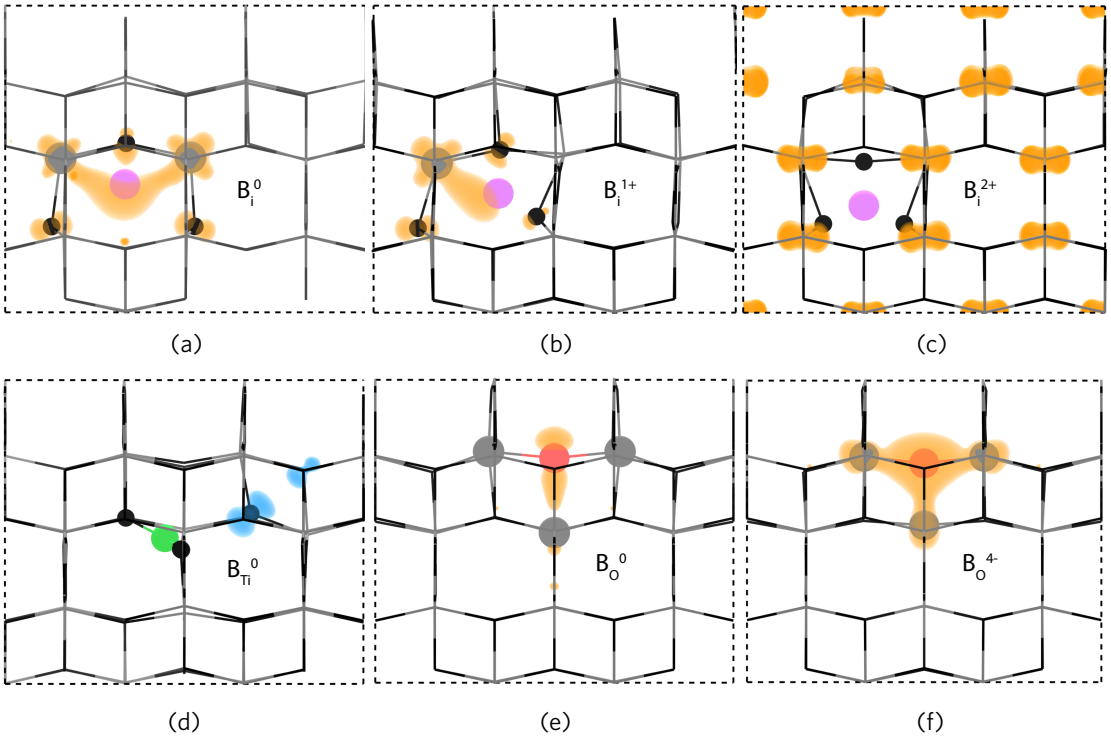

FIGURE 8.9: The partial charge densities for Bi in the neutral (a), 1+ (b) and 2+ (c) charge states, B_{Ti} in the neutral charge state (d) and B_O in both the neutral (e) and 4- (f) charge state. Each panel is viewed along the {100} direction and the isosurfaces for electrons (orange) and holes (blue) are plotted from 0-0.015 eV. The anatase lattice is displayed by the wire-frame model where Ti=grey and O=black and the boron atoms are colour coded according to Figure 8.8.

1s core levels ($\epsilon_{B\,1s}$) from the DFT output:

$$E^{\text{shift}}_{\text{B}_{\text{core}}} = \epsilon^{\text{VBM}} + \Delta v^{\text{pot}} - \epsilon^{\text{B}\,1s} \tag{8.3.1}$$

where E_{VBM} is the eigenvalue of the VBM of the defective cell which is aligned to the host supercell using Δv^{pot}. Analysis of the B core level shifts for both B^{1-}_{Ti} and B^{3+}_{i} shows that they both have the similar shifts of ~ 172.20 eV. In experiment a binding energy around 192.20 eV corresponding to interstitial B is seen and the similarity in oxidation states and environment is likely why the literature doesn't report substitutional B.[441,444,473] Although the amphoteric nature of B in anatase gives rise to a self-compensation mechanism, the larger formation energies and lattice distortions mean that small quantities of dopant concentrations will be

expected. Further work on B-doped TiO_2 will need to focus on B-related clusters and the formation of similar defects in *rutile* TiO_2. Mixed phase powders of TiO_2 are known to possess enhanced photocatalytic activity[34], which, when boron doped could be enhanced significantly.

8.4 Enhanced Carrier Lifetimes in Copper Doped TiO_2

Details of the theoretical methodology is included in Appendix C.1.
The work in this section is in preparation for publication.

Enhanced carrier lifetimes have been seen to occur in Cu doped anatase TiO_2 under visible light making it a promising dopant for use in photocatalysis.[492–495] Cu also has a range of oxidation states (1+, 2+, 3+) and small ionic radii that allow it to sit both substitutionally and interstitially. The ionic radii's however, are closer to those of Ti (Ti^{4+} = 0.61Å; Cu^{3+} = 0.54Å; Cu^{2+} = 0.73Å; Cu^{1+} = 0.77Å)[240] and as such, Cu should not cause as much distortion to the anatase lattice as boron does. Boron was also limited by its desire be three-coordinated due to the sp^2 hybridisation present. Cu possesses antibacterial properties making its incorporation into TiO_2 sought after for antimicrobial coatings.[568–572] The observed reduced recombination rates means that this antimicrobial process is enhanced and has been seen to exist in Cu-doped ZnO as well.[573] In TiO_2 as with ZnO, Cu incorporates as both Cu^{1+} and Cu^{2+} as seen in XPS results which could be indicative of multi site occupancy.[569,571,574] Few DFT studies have been carried out to determine the cause of: i) the species present in anatase TiO_2 or ii) the cause of the extended carrier lifetimes through bulk defects.[568,575–577] This chapter will assess the thermodynamic and *optical transitions* of Cu-doped anatase to answer these questions.

8.4.1 Cu-doping of TiO_2

The defect thermodynamic transition levels are displayed in Figure 8.10 for all intrinsic defects and and Cu-related species in anatase TiO_2 under *Ti-rich/O-poor* and *Ti-poor/O-rich* conditions.

Cu_{Ti}:

Substitutional Cu (Cu_{Ti}) incorporates as a fairly low formation energy acceptor defect under *p*-type preferable *Ti-poor/O-rich* conditions with a formation energy of 2.19 eV. Cu_{Ti} is a very

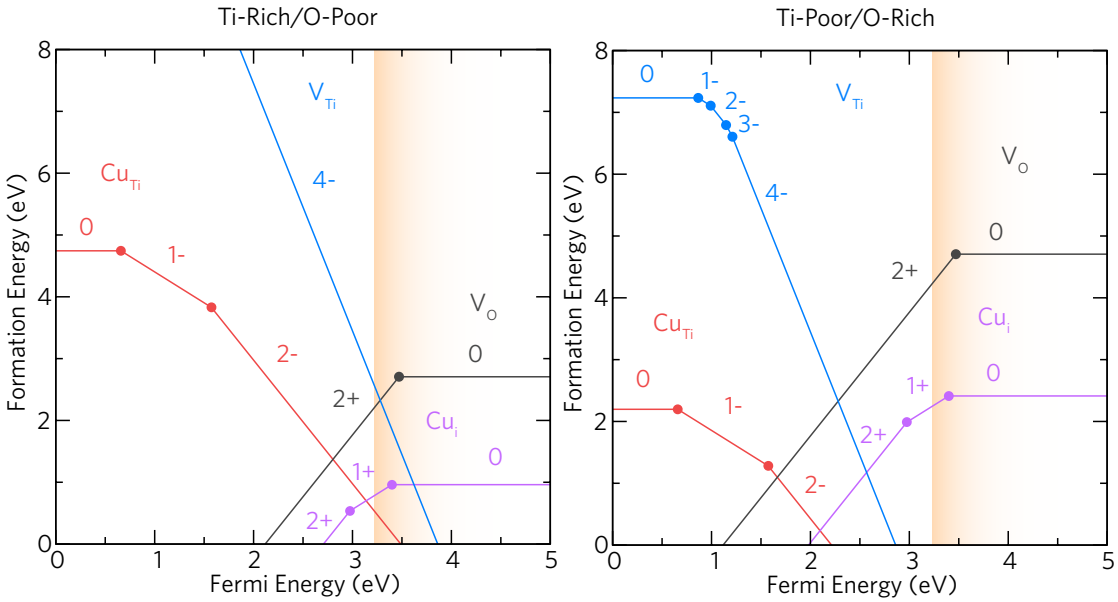

FIGURE 8.10: The thermodynamic transition levels for Cu-doped TiO_2 under *Ti-rich/O-poor* and *Ti-poor/O-rich* conditions. The Fermi energy ranges from the VBM (0 eV) to ~ 1.65 eV above the CBM (3.35 eV). The conduction band is shown by the graded orange area.

deep defect with the 0/1- transition level occurring around 0.66 eV above the VBM; as such, Cu_{Ti} will not be a source of *p*-type conductivity in anatase. A further transition level, 1-/2-, is observed at 1.57 eV above the VBM and the 3- charge state is not seen over the entirety of the band gap. Cu_{Ti}^{2-} becomes compensated for by V_O^{2+} around 1.67 eV above the VBM. Under *Ti-rich/O-poor* growth conditions, the formation energy of the neutral charge state (Cu_{Ti}^{0}) rises to 4.74 eV and the compensation by V_O^{2+} shifts the Fermi energy from 1.67 eV to 2.80 eV. Under the range of growth conditions Cu_{Ti} is in the 2- charge state signifying that it incorporates as Cu^{2+} and explains the presence of this oxidation state in experiment.[578,579]

Figure 8.11(a), (b) and (c) displays the hole localisations for Cu_{Ti}^{0}, Cu_{Ti}^{1-} and Cu_{Ti}^{2-} respectively. In the neutral charge state, one hole is localised in a *d* orbital on the Cu and the other two are delocalised on the six joining oxygens. In the 1- charge state, a hole is filled with an electron leaving one localised on the Cu and one delocalised on the adjacent O atoms as before. In the 2- charge state, the remaining hole is mostly localised on the Cu *d*orbital with some remaining density on the two equatorial (to the plane of the page) oxygen *p*-orbitals. A minimal distortion to the anatase lattice is observed with Cu remaining in the original octahedral Ti position over all charge states. Due to the delocalisation of hole density in the 0

and 1- charge states, the adjacent oxygens hardly shift from their positions, however in the 2- charge states, where the hole density is localised equatorially, there is a small shift of an oxygen by ~ 10% as seen in Figure 8.11(c).

Cu_i:

When copper sits interstitially in anatase, it acts as a *resonant* one-electron donor. Under favourable *Ti-rich/O-poor* conditions, it has a very low formation energy of 0.96 eV, whilst under *Ti-poor/O-rich* conditions the formation energy of the neutral charge state rises to 2.41 eV. The 1+/0 transition level occurs at around 0.05 eV above the CBM whilst the 1+/2+ transition level occurs around 0.37 eV *below* the CBM. Under *Ti-rich/O-poor* conditions Cu_i^{1+} becomes compensated by Cu_{Ti}^{2-} around 0.21 eV below the CBM. The Fermi level is expected to be trapped just below this point and so either negligible to no amounts of conductivity is to be observed in TiO_2:Cu. When the Fermi level is trapped here, Cu incorporates as Cu^{1+} accounting for the coexistence of Cu^{1+} and Cu^{2+} in the experimental literature.[578,579] Under *Ti-poor/O-rich* conditions the Fermi level becomes trapped when Cu_{Ti}^{2-} crosses Cu_i^{2+} around 2.1 eV above the VBM. In this scenario interstitial Cu will be Cu^{2+} and so the Cu oxidation states in anatase will be dependent on the synthesis conditions. Figure 8.11(d) and (e) shows the partial charge density of interstitial Cu in the 0 and 1+ charge state respectively. From our calculations, Cu moves from the perfect octahedral interstitial position to a distorted square planar position where it bonds to four oxygens. In general Cu^{2+} is well known to be Jahn-Teller active, thus preferring a square planar configuration. Little distortion is seen over the evolution of each charge state, as Cu_i retains the same position from $0 \rightarrow 1- \rightarrow 2-$ with the Cu–O distances retaining a length of 2.00 Å(similar to the 1.98 Å Ti–O bond length in anatase). The neighbouring four Ti ions shift away from the Cu defect by an average of 4%. The electron density in the 0 charge state is delocalised across the Ti 3*d* orbitals that make up the states at the CBM. In the 1+ charge state (Figure 8.11(e)) there is a localisation of the electron density on and around the Cu (indicative of Cu^{1+}). Previous GGA calculations[576] predict that Cu_i is in fact higher in energy than Cu_{Ti} and that the Fermi level is pinned close to the VBM. The likely explanation for this is due to GGA functionals not describing localised electrons or holes correctly, as well as the incorrect description of the band gap.

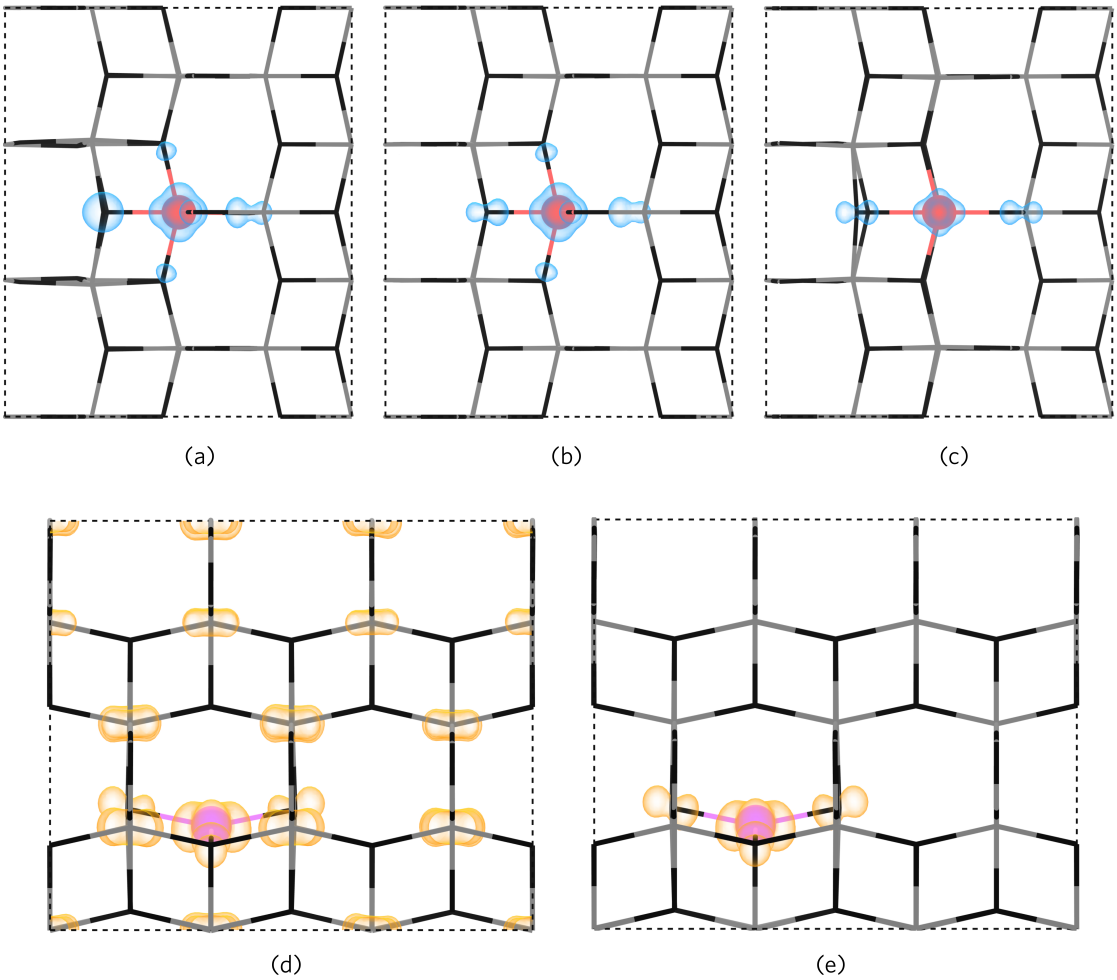

FIGURE 8.11: The partial charge densities for Cu_{Ti} in the 0 (a), 1- (b) and 2- (c) charge states as viewed along the {010} direction and for Cu_i in the 0 (d) and 1- (e) charge states as viewed along the {100} direction. For hole and electron charge densities are depicted in blue and orange and are plotted from 0–0.015 eV Å^{-1}. For each panel, the anatase lattice are depicted using a wire-frame model (Ti=grey; O=black) and the Cu species are colour coded to Figure 8.10.

8.4.2 Optical Absorption and Photoluminescence in TiO_2:Cu

The optical absorption and emissions for both Cu defects were evaluate and are shown using the one-dimensional configurational coordinate diagram in Figure 8.12.

Absorption:

Figure 8.12(a) demonstrates that Cu_{Ti} undergoes optical absorption from $2- \rightarrow 1- \rightarrow 0$ charge states within the near UV (490nm) and the UV (375nm) respectively for excitation to the CBM. These absorptions occur within the absorption edge of anatase TiO_2, thus it is not expected to be distinguishable experimentally. Cu_{Ti} can also undergo electron capture from the VBM (Figure 8.12(c)). Absorptions in this context occur in the near IR (886nm; $0 \rightarrow 1-$) and the green portion (525nm; $1- \rightarrow 2-$) of the visible spectrum. Figure 8.12(b) and (d) show the excitation and capture of an electron for Cu_i respectively. For CBM excitation, an absorption in the near-IR (969nm) is seen, whilst for excitation from the VBM an absorption of 369nm is observed, likely to be part of the band gap absorption. Due to the thermodynamic ionisation, it is not expected that the optical absorption from the 1+ to the 0 charge state will not occur and as such is omitted from this diagram.

Emission:

Cu_{Ti} undergoes emission in the visible and infrared portion of the electromagnetic spectrum and is shown in Figure 8.12(a) and (c). Emission following an absorption of an electron to the conduction band occurs at wavelengths of 634nm and 1252nm for $0 \rightarrow 1- \rightarrow 2-$ transitions. Upon the release of a hole to the VBM (Figure 8.12(c)) an emission of 1512nm and a possible non-radiative transition of 31μm. Cu_i shows an emission from $1+ \rightarrow 2+$ charge states emitting an electron to the VBM. Cu_i undergoes photoluminescence after the capture of an electron from the valence band as shown in Figure 8.12(d). This transition incurs the release of a photon of energy 2.07 eV (599nm) with a broad peak ($E_{rel} = 0.91$ eV). The capture of an electron from the CBM undergoes a *non-radiative* transition due to the thermodynamic resonance of Cu_i^{1+} in the conduction band. As such, interstitial Cu captures an electron (with an energy barrier of 0.005 eV) in order to return to Cu_i^{2+}.

The coexistence of interstitial and substitutional Cu in the anatase lattice therefore plays a role in the enhanced electron-hole separation lifetimes and thus the photocatalytic activity. Cu therefore plays a synergistic effect by producing shallow-donor/deep-acceptor pairs. Within this mechanism, the filled Cu_{Ti} defect can excite an electron to the CBM which can be readily accepted by an interstitial Cu (due to the small activation energy) and thus increase the separation. Visible light excitation is also enhanced as both Cu_{Ti} and Cu_i absorb photons at 886nm and 969nm respectively. Increased Cu incorporation may favour the formation of

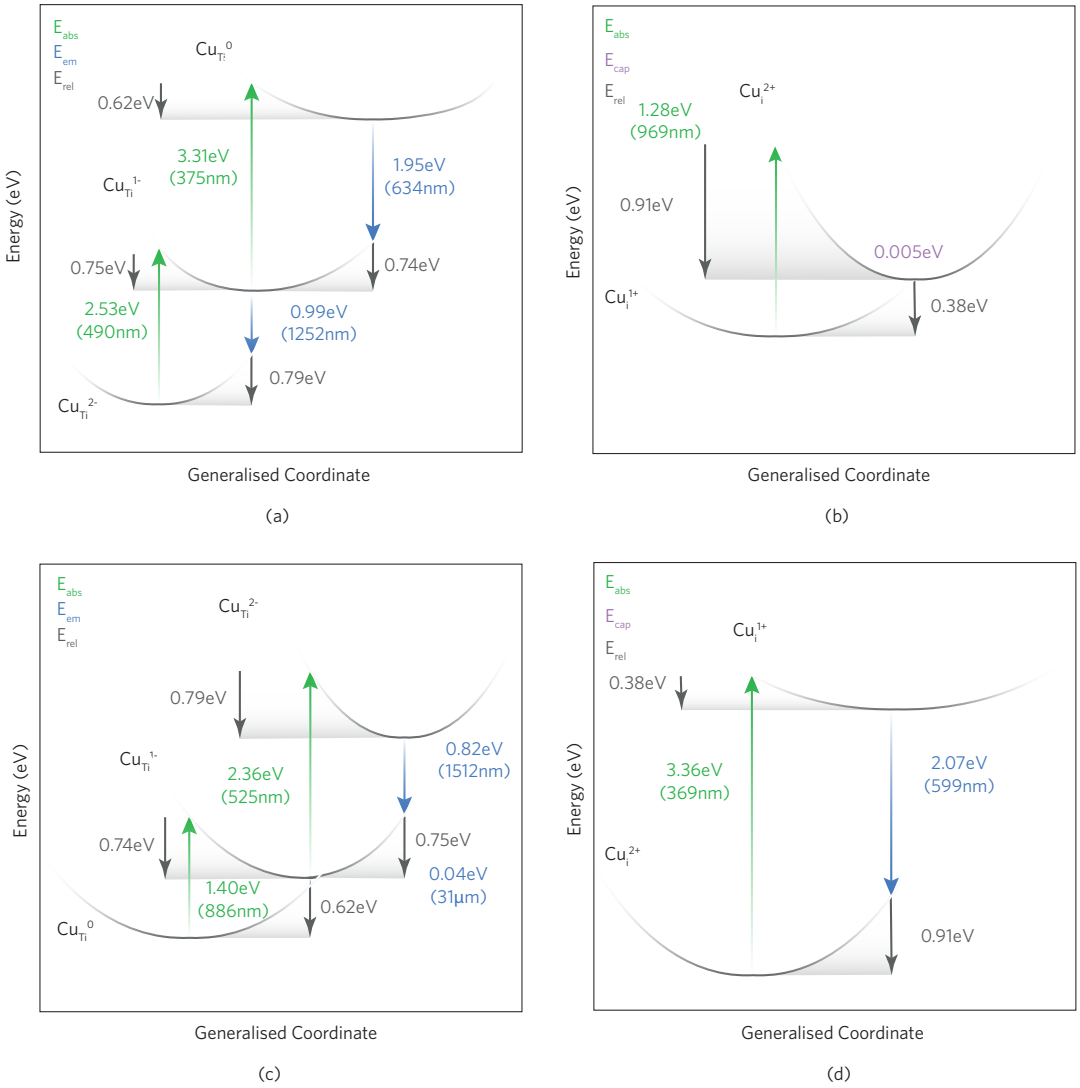

FIGURE 8.12: The one-dimensional configurational coordinate diagrams for Cu_{Ti} under excitation (a) and capture (c) of an electron to/from the CBM/VBM respectively. Similarly, the excitation (b) and capture (d) of electrons from/to Cu_i. In each example the absorption and emission energies are independent of the chemical potentials and thus the growth conditions.

interstitial Cu over substitutional Cu, however, thereby it is possible to lose this beneficial mechanism.

8.5 Conclusions

The work presented in this chapter extends the concept of *fully-passivated* codoping to single multi-site dopants; B and Cu. Codoping of TiO_2 with both [Ta+N] and [Nb+N] was tested using hybrid density functional theory. Despite binding energies between substitutional Nb(Ta) defects and N defects, the formation of *n*-type defects and dopants is still overwhelmingly preferable to *p*-type defects. The reasoning behind this is due to the large ionisation potentials and electron affinities in anatase TiO_2 (Section 7.1.1). Boron and copper doped anatase, however, give the ability to create a form of passivation through self-compensation and show remarkable photocatalytic properties in experiment. As an *amphoteric* defect, boron has the ability to act as an acceptor and donor in both substitutional positions as well as interstitially. From our calculations we find that the two dominant defect types are B_{Ti} and B_i, in contrast to the experimental literature which see B_O and B_i. The results presented in this chapter show that B incorporates exclusively as B^{3+} in preferential *trigonal-planar* configurations for both B_{Ti} and B_i. Calculated core level shifts show that these two defects will be *indistinguishable* from each other in XPS measurements and hence the reasoning behind the lack of appearance of B_{Ti} in the scientific literature. As B causes significant distortions to the anatase lattice, high formation energies are present meaning that under thermodynamic equilibrium conditions it would be expected that small dopant concentrations will be realised. Cu possesses ionic radii closer to that of Ti^{4+} as well as multiple oxidation states. From the work done herein a synergistic mechanism between interstitial Cu and substitutional Cu is found to exist. Hybrid DFT has accounted for the existence of both Cu^{1+} and Cu^{2+} oxidation states seen in experimentally synthesised Cu-doped TiO_2. Optical absorption and photoluminescence calculations show that visible light absorption is possible and a cooperation between the two defects allows for an enhanced electron-hole separation. From these results, the conclusion is that any form of *fully* passivated codoping in anatase TiO_2 is not achievable. An understanding of the mechanisms to enhance the carrier separation lifetimes and improve upon the photocatalytic properties of anatase has been gained which can be applied to similar materials such as ZnO or the other TiO_2 polymorphs.

Summary

The aims of this thesis were to explore and describe wide band gap semiconductors in terms of their thermodynamic and electronic properties. Three applications were covered in this work: *n*-type transparent conductors, *p*-type transparent conductors and TiO_2 photocatalysis. Despite a wealth of research into binary *n*-type transparent conducting oxides (TCOs), the use of In_2O_3 as the industry standard TCO in terms of conductivities and electron mobilities is hampered by the expense and scarcity of indium. Although SnO_2 has long been used for TCO purposes, in particular in photovoltaics and low-emissivity windows, high conductivities and mobilities to compete with and surpass In_2O_3 in electronics have yet to be realised. SnO_2 has conventionally been doped with either fluorine or antimony in an attempt to increase its desirable properties. The work in this thesis sought to understand the limitations of the current dopants in SnO_2 and offer an *optimum* dopant which do not possess the same mechanistic shortcomings. Chapter 4 detailed the self-compensation mechanism of F-doped SnO_2 and the propensity of Sb in SnO_2 to form Sb^{3+} instead of the desired Sb^{5+} for *n*-type conductivity. From our detailed analysis of potential dopant replacements, we found that tantalum acts as the optimum dopant in tin dioxide allowing higher dopant concentrations than either fluorine or antimony and remaining as Ta^{5+} within the rutile lattice. Our calculations also show that Ta does not perturb the conduction band minimum (as F and Sb do), thus accounting for the very high reported mobilities for Ta-doped SnO_2 in the experimental literature.

For truly transparent electronic devices as well as more efficient photovoltaics, a transparent *p*-type conductor is required. The current generation of materials used for this purpose tend to suffer from low optical transparency, poor conductivities as well as the inability to produce a *degenerately* acceptor doped material. The work carried out in Chapter 6 followed the established 'chemical modulation of the valence' band design principles seen in Cu^{1+}-based oxides such as the delafossite $CuAlO_2$. This principle has already been extended to

chalcogenides, in particular the layered *oxychalcogenide* $[Cu_2S_2][Sr_3Sc_2O_5]$ which has high reported mobilities and optical transparency. As a quinary material, it is possible to form many more compounds with the same structure and stoichiometry as $[Cu_2S_2][Sr_3Sc_2O_5]$ and gain structure-property relationships in order to produce other *p*-type transparent conductors. From our analysis we found that nine compounds will be stable relative to competing phases and that of these compounds, $[Cu_2S_2][Ba_3Sc_2O_5]$ was found to possess the lowest hole effective masses and largest optical transparency. Experimental powders of $[Cu_2S_2][Ba_3Sc_2O_5]$ were produced from our predictions with excellent agreement between the theory and experiment in terms of structural and electronic properties. In Section 6.2, Cu^{1+}-based phosphides were analysed ($M^{2+}CuP$; M = Mg, Ca, Sr, Ba) showing that the chemical modulation of the valence band can be extended to the pnictides. Although the largest optical band gap was found for CaCuP (2.71 eV), precluding its use as a transparent conductor, the low hole effective masses were competitive with and even surpassed the electron effective masses of the industry standard *n*-type TCOs. Synthesised powders of CaCuP were fabricated possessing an optical band gap of 2.78 eV and resistivities of $10^{-3}\,\Omega\,\text{cm}$ (for an undoped pellet) further concluding the theoretical findings. The trigonal planar Cu–P hexagonal network was elucidated to be the origin of the highly disperse VBM and thus the low hole effective masses for CaCuP. A tetrahedral coordination as seen in MgCuP was found to be detrimental to the conductivity and thus it was reasoned that for Cu^{1+}-based phosphide transparent conductors, trigonal planar Cu–P was optimal.

The final wide band gap application to be explored was photocatalysis, in particular, TiO_2 photocatalysis and an assessment of doping mechanisms that enhance this process. Anatase TiO_2 possesses a wide band gap ($\sim$ 3.2–3.4 eV) which means that only UV light is absorbed and not visible light, as is desired for efficient photocatalysis. Methods at reducing this band gap have been through high levels of acceptor doping, usually with nitrogen or carbon. This has the effect of producing states just above the VBM and reducing the band gap of anatase, however, doing so also creates localised hole states which act as recombination centres and have a negative impact on the photocatalytic efficiency. Compensated codoping was proposed to passivate these hole states by simultaneously codoping TiO_2 with a donor such as niobium or tantalum. Although a lot of research has been spent on creating codoped systems, full passivation has yet to be achieved. Chapter 8 involved the calculation of two popular codoping systems, Nb+N and Ta+N. The calculations proved that fully compensated codoping was not achievable due to the preference of *n*-type over *p*-type defects as TiO_2 is inher-

ently n-type due to the low ionisation potentials and high electron affinities. Boron and Copper were also explored for enhanced visible light photocatalysis due to their *amphoteric* nature meaning they are capable of sitting on multiple sites in the anatase lattice. It was found that in B-doped anatase, B sits interstitially and prefers a trigonal planar configuration, thus large distortions to the anatase lattice are seen when it is incorporated substitutionally. Due to the possible coexistence of B_{Ti} and B_i in the anatase lattice, a synergistic effect is possible which gives rise to the enhanced photocatalysis seen in experiment. Copper acts in much the same way, however the probability of finding both interstitial and substitutional Cu is heightened. This results in possible donor-acceptor pairs which absorb in the visible light giving rise to extended electron-hole separation lifetimes. This is particularly useful in photocatalysis where extended carrier lifetimes are necessary to facilitate the splitting of water or the destruction of microbes when used as an antimicrobial coating.

Appendices

Appendix A

n-Type Transparent Conductors

A.1 Introduction to *n*-Type Transparent Conductors

In Chapter 3.2.1 Figure 3.5, the band structures for In_2O_3, SnO_2, ZnO and $BaSnO_3$ are displayed. These were calculated within the VASP code.[105–108] and used the projector augmented wave method (PAW).[44] to describe the interactions between the core and valence electrons. Table A.1 displays the calculation parameters used to relax the compounds and thus calculate the band structures in Chapter 3.2.1. Each structure was relaxed until the forces acting on all the atoms was less than 0.01 eV Å^{-1}.

TABLE A.1: The calculation parameters for In_2O_3, SnO_2, ZnO and $BaSnO_3$. The space group, DFT functional, portion of Hartree-Fock exchange (α), Γ-centred *k*-point grid and plane-wave energy cutoff is tabulated.

Compound	Space Group	DFT Functional	α	*k*-point grid	Plane-wave cut-off / eV
In_2O_3	$Ia\bar{3}$	HSE06	0.25	$4\times4\times4$	450
SnO_2	$P4_2/mnm$	PBE0	0.25	$4\times4\times6$	400
ZnO	$P6_3mc$	HSE	0.375	$8\times8\times5$	450
$BaSnO_3$	$Pm\bar{3}m$	PBE0	0.25	$6\times6\times6$	450

A.2 The Search for the Optimum Dopant in SnO_2

Ab-initio calculations on SnO_2 were performed using hybrid density functional theory within the VASP code[105–108] The projector-augmented wave method (PAW)[44] was used to describe the interaction between the core electrons (Sn[Kr], O[He], F[He], Sb[Kr], P[Ne], Nb[Kr], Ta[Xe]) and the valence electrons. The hybrid functional PBE0 developed by Adamo and Barone[23,265] was used in order to reduce the *self-interaction error* allowing for an accurate description of the band gap of SnO_2. PBE0 has been shown to predict the properties for tin based TCOs with a high degree of accuracy.[24–26,264,266] PBE0 incorporates 25% of exact Fock exchange to the PBE (Perdew Burke and Ernzerhoff)[14] formalism. The conventional cell was relaxed using the parameters detailed in Table A.1, where convergence was deemed to be complete when the forces acting on all the atoms was < 0.01 eV Å^{-1}.

A.2.1 Defect Methodology

In order to assess the thermodynamic properties of the intrinsic and extrinsic defects in SnO_2, a 72 atom $2 \times 2 \times 2$ supercell was created from the bulk conventional cell. This was subjected to a geometry relaxation keeping all but the atoms within the cell constant. A 400 eV plane-wave cut-off and a $2 \times 2 \times 2$ Γ-centred k-point grid was used to achieve this. Each supercell relating to the defects and their charge states were created and relaxed until the forces on all the atoms was less than 0.01 eV Å^{-1}.

Thermodynamic Limits:

The chemical potentials (μ_i) can reflect the equilibrium growth conditions which can be varied to simulate the experimental partial pressures defining the conditions of n and p-type defect formation. This is all relative to the calculated enthalpy of the host material

$$\mu_{\mathrm{Sn}} + 2\mu_{\mathrm{O}} = \Delta H_f^{\mathrm{SnO_2}} = \text{-}5.27\ \mathrm{eV} \tag{A.2.1}$$

The experimentally determined standard enthalpy of formation for SnO_2 is -5.98 eV[425], which is in agreement with our calculated value at 0 K. Our calculations allow for the determination of two growth conditions, the *Sn-rich/O-poor* limit which typically favours the formation of

n-type defects which is determined by the formation of metallic Sn.

$$\Delta\mu_{Sn} = 0; \Delta\mu_{O} = -2.64\,\text{eV} \tag{A.2.2}$$

Likewise for *p*-type defect favourable formation conditions, *Sn-poor/O-rich*, is limited by the formation of O_2 gas.

$$\Delta\mu_{O} = 0; \Delta\mu_{Sn} = -5.27\,\text{eV} \tag{A.2.3}$$

Calculation of the Dopant Chemical Potentials:

Table A.2 displays all the dopant-related limiting phases alongside the the Γ-centred *k*-point grids used, enthalpies of formation (ΔH_f) and the defined chemical potentials for that particular dopant (μ_i; where i = F, Sb, P, Nb, Ta). Experimental values are given in parentheses. The dopant chemical potentials are defined within the formation of SnO_2 (equation A.2.1) and within the formation of each limiting phase. Figure A.1 displays the formation of each limiting phase *within* the μ_O range of SnO_2 (μ_O = -2.64 eV – 0 eV). The limiting phase is the compound with the lowest μ_i at a certain μ_O, such that under *Sn-rich/O-poor* the Sb and Nb chemical potentials are limited by the formation of $Sb_{(s)}$ and Nb_2O_5 respectively. Under *Sn-poor/O-rich* the limiting phases are Sb_2O_5 and Nb_2O_5 respectively.

TABLE A.2: The competing phases related to the different dopants (F, Sb, P, Nb, Ta). The Γ-centred *k*-points are tabulated with the enthalpies of formation relative to experiment (in parentheses) and the chemical potentials (μ_i, where i=F, Sb, P, Nb, Ta) under *Sn-rich/O-poor*, *Sn-poor/O-rich* conditions.

Dopant	Limit	Space Group	*k*-points	$\Delta H_f/eV$	$\Delta\mu_i^{O\text{-}poor}$ / eV	$\Delta\mu_i^{O\text{-}rich}$ / eV
F	SnF_4	*I4/mmm*	6 × 6 × 6	-12.43 (-12.14[580])	-3.11	-1.79
Sb	Sb_2O_5	*C2/c*	2 × 5 × 4	-9.60 (-9.97[425])	0.00	-4.80
	SbO_2	$Pna2_1$	5 × 4 × 2	-8.80 (-9.28[581])		
	Sb_2O_3	*Pccn*	5 × 4 × 2	-6.91 (-7.07[581])		
P	P_2O_5	*Fdd2*	4 × 4 × 6	-14.79 (-15.59[582])	-0.80	-7.40
Nb	Nb_2O_5	*I4/mmm*	2 × 2 × 2	-18.55 (-19.69[582])	-2.69	-9.28
	NbO_2	*C2/c*	3 × 3 × 3	-7.72 (-8.24[582])		
	NbO	*Pm3m*	6 × 6 × 6	-4.13 (-4.35[582])		
Ta	Ta_2O_5	$I4_1/amd$	6 × 6 × 1	-20.47 (-21.21[582])	-3.54	-10.23

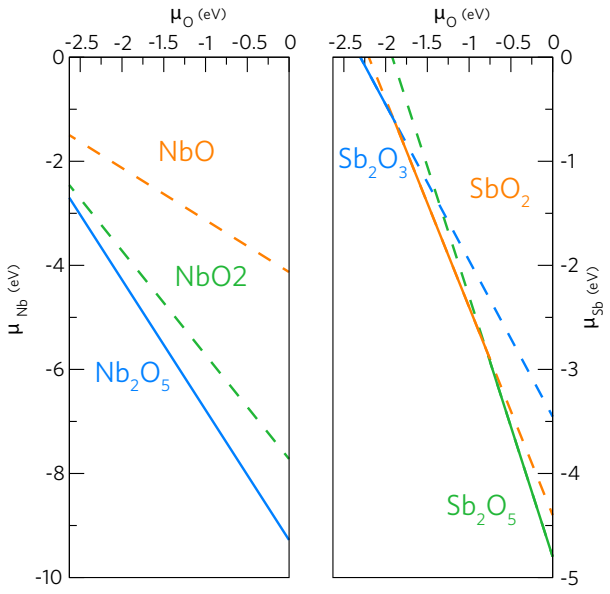

FIGURE A.1: The chemical potential limits as calculated for each Nb and Sb-related phase within the chemical potential bounds of SnO_2 (μ_O = -2.64 eV – 0 eV). (a) and (b) correspond to Nb and Sb-doped SnO_2 respectively. The solid lines correspond to the limiting phase at a particular μ_O. All phases are tabulated in Table A.2.

Band-Unfolding

Due to the shrinking of the Brillouin zone, supercell calculations result in folded band structures. In order to regain a representation of the *primitive* or *conventional* cell, the band unfolding code, *BandUp* was used. Band unfolding is a methodology described by Popescu and Zunger[583] and is implemented in a python package by Medeiros and Björk.[287,288]

A.3 F-doped SnO_2 Experimental Methodology

This section was written by and reproduced with permission by Jack E. N. Swallow and the group of Prof. Timothy Veal at the University of Liverpool. F-doped SnO_2 thin films were obtained by NSG Group.

FTO samples:

Fluorine-doped tin dioxide (FTO) thin films deposited on glass by APCVD were obtained from NSG Group. Samples consisted of a multi-layer structure with an undoped SnO_2 layer ~25 nm deposited directly on the glass substrate providing a rough surface for the subsequent layers to adhere to. A SiO_2 layer follows of thickness ~ 25 nm acting as a sodium diffusion barrier, and finally the electrically active F:SnO_2 layer is deposited. The tetragonal rutile structure associated with the SnO_2 was confirmed via x-ray diffraction (see Figure S5 in supporting information). The samples are polycrystalline in nature and no impurity phases were present. Samples were prepared for measurement by mechanically cleaning the surface with laboratory wipes and isopropyl alcohol to remove large particulates, as well as being treated in an ultrasonic bath submerged in diluted surface cleaner (decon 90 surface cleaning agent) and then isopropyl alcohol, and rinsed in deionized water.

Hall Effect Mobility:

Hall effect measurements were performed using the standard van der Pauw configuration at a field strength of 0.8 T to determine the free carrier concentration (n) and transport mobility (μ) of FTO samples. Measurements were performed at room temperature on the samples, all of which displayed n-type conductivity. The measured free carrier concentrations across the sample range varied from $(1.81 \pm 0.01) \times 10^{20}$ cm^{-3} to $(5.48 \pm 0.04) \times 10^{20}$ cm^{-3} and electron mobilities varied from 27.3 ± 0.2 cm^2/V·s to 38.2 ± 0.1 cm^2/V·s. Samples which displayed high carrier concentrations and low mobilities corresponded to those of high fluorine content. Temperature dependent Hall effect was also performed on some samples, with sample temperature being varied from 10 to 300 K (±0.5 K) (see Figure S1 in supporting information).

Supplementary Information: Scattering Mechanisms

Transport mobilities of the FTO samples as a function of carrier concentration, as measured primarily by Hall effect. For degenerately doped semiconductors, such as transparent conducting oxides, the dominant carrier scattering/mobility reducing mechanism in the majority of cases is ionised impurity scattering[282,584]. To simulate this effect, the degenerate form of the Brooks-Herring formula[584,585] has been implemented. All donors are assumed to be ionized and have a charge state of $Z_D = 1$, corresponding to substitutional fluorine, F_O. Other scattering mechanisms such as: acoustic deformation potential[162,586], longitudinal polar-optic phonons (we use here the formalism set out by Low and Pines[587] and adapted by Fonstad and Rediker for SnO_2 [162], however a number of other approaches do exist[588,589]) and grain boundary scattering for both degenerate[590] and non-degenerate[591] systems. The effects of neutral impurities, and other phonon effects were found to be negligible.

Appendix B

p-Type Transparent Conductors

B.1 Elemental Modulation of $[Cu_2S_2][Sr_3Sc_2O_5]$

B.1.1 Computational Methodology

Ab-initio calculations using VASP code[105–108]were performed using both standard and hybrid functionals. Variations of the $[Cu_2S_2][A_3B_2O_5]$ structure (Tetragonal,$I4/mmm$) were formed where A=**Sr**,Ca,Ba,Mg and B=**Sc**,Al,Ga,In,Sc,Y,La. This resulted in 24 compounds with the same stoichiometry as $[Cu_2S_2][Sr_3Sc_2O_5]$ and are named using the convention 'AB' eg. $[Cu_2S_2][Sr_3Sc_2O_5]$ is 'SrSc', $[Cu_2S_2][Ba_3Al_2O_5]$ is 'BaAl' and $[Cu_2S_2][Ca_3Ga_2O_5]$ is 'CaGa'. These compounds were relaxed using the PBEsol[16] (Perdew-Burke-Ernzerhoff) functional with a '+U' value of 6.15 eV for Cu.[330] The 24 compounds were relaxed using a plane wave energy cut-off of 500 eV to avoid Pulay stress[47] and a $6\times6\times2$ Γ-centred k-point mesh for accuracy. Convergence was deemed complete when the forces acting on *all* the ions was less than 0.01 eV Å^{-1}.

In order to screen the novel compounds in terms of their thermodynamic stability, all known competing phases and elements related to the quinary systems were also calculated using PBEsol+U. This resulted in the calculation of ~ 313 crystal structures from the ICSD[363] alongside the lowest energy determined magnetic configurations for the Cu^{2+}-based compounds. A standard 700 eV plane-wave energy cutoff was employed to allow for total convergence of these systems together with k-point meshes generated to allow a sampling density of 0.04 Å^{-1} which was found to be sufficiently accurate. The *Chemical Potential Limits*

Analysis Program (CPLAP)[592] code was used to assess the thermodynamic stability of the 24 SCSOS compounds as well as evaluating the energy above the convex hull for the unstable compounds.

The stable and metastable compounds were then subjected to an HSE06 (Heyd-Scuzeria-Ernzerhoff)[30–32] relaxation in order to glean accurate electronic and optical properties. The HSE06 hybrid functional has been shown to give a correct description of the band gap and optical properties of SCSOS[362] relative to experiment.[351]. The projector-augmented wave method (PAW)[44] was used to describe the interactions between the core electrons and valence electrons which are treated explicitely. The optical absorption spectra were calculated using the real and imaginary parts of the dielectric constant calculated using a Kramers-Kronig transformation and a summation over the unoccupied bands respectively using a method by Furthmüller and coworkers.[593] This sums the absorption spectrum over *all* direct valence band to conduction band transitions ignoring intraband and indirect absorptions.

B.1.2 Experimental Methodology

This section was written by and reproduced with permission by Mr Gregory J. Limburn In the Group of Dr Geoffrey Hyett at the University of Southampton.

Solid-State Synthesis:

Sc_2O_3 (99.99%, Alfa Aesar) and Cu_2S (99.5%, Alfa Aesar) were purchased and used as supplied. BaO was prepared via the thermal decomposition of $BaCO_3$ (99%. Alfa Aesar) under dynamic vacuum (1000°C, 14 h) in a silica tube closed at one end, before being stored in a nitrogen filled glove box. BaS was synthesised by reaction of CS_2 vapour with $BaCO_3$ (900°C, 8 h). The CS_2 vapour was generated by flowing argon (Pureshield, 99.998%, BOC) through a bubbler containing liquid CS_2 (99.9%, Sigma Aldrich). After the vapour exited the reactor it was passed through two bleach containing bubblers in order to oxidise any excess CS_2. The purity of these precursors was confirmed by powder X-ray diffraction. A 0.5 g powder sample of $[Cu_2S_2][Ba_3Sc_2O_5]$ was synthesised by reaction of BaO, BaS, Sc_2O_3 and Cu_2S in a 2:1:1:1 stoichiometric ratio. Desired precursor amounts were weighed, mixed and ground in an agate pestle and mortar under an inert atmosphere in a glovebox (Saffron). The precursor mixture was then loaded into a die (13mm, Specac), removed from the glove box, pressed into a pellet and immediately returned to the inert atmosphere. The pellet was loaded into an alumina crucible which was then sealed under vacuum in a silica ampoule. The sealed sample was heat treated at 800°C for 12 hours. The sample was ground, re-pelleted and resealed in an alumina crucible in a silica ampoule with 2 further heat treatments at 800°C for 12 hours. Sample purity was monitored using XRD, and once synthesized the sample was found to be air stable.

X-ray Diffraction:

The purity of precursors and initial phase identification of the targeted product was confirmed by X-ray diffraction using a Bruker D2 in Bragg-Brentano geometry with a Cu K X-ray source (20 kV; 10 mA). Full characterisation of the compound $[Cu_2S_2][Ba_3Sc_2O_5]$ was performed using synchrotron X-ray diffraction data collected from the I11 beamline, Diamond

Light Source, using 15 keV X-rays (0.82603Å) over a range 10<2<100°, with a step size of 0.001° and with a scan rate of 2.5° min^{-1}. Rietveld refinement of structural models against this data was carried out using the GSAS suite of software, with the EXPGUI interface.[594]

Spectrophotometry:

Diffuse reflectance measurements were collected using a UV-Vis-near IR Spectrophotometer (Perkin-Elmer Lambda 750 S) using deuterium and tungsten lamps and equipped with a 100 mm integrating sphere. Diffuse reflectance data were converted into the Kubelka-Munk function, f(R),[595] assumed proportional to the absorption coefficient throughout the visible region, which was used in the construction of a Tauc plot.[392,596] The band gap was estimated by determining the x-axis intercept of a linear fit of the absorption edge. This was fitted by the plotting of a linear function passing through the two data points between which the largest gradient was observed.

B.1.3 Supplementary Information: Thermodynamic Stability

Table B.1 shows the thermodynamic stability results for all 24 calculated compounds using PBEsol. This table provides the energy above the convex hull, the decomposition products (if E >0 eV atom^{-1}) and the enthalpy of formation ($\Delta H_f^{\text{synthesis}}$) of each compound as calculated using the synthesis route laid out in ref. [351] and equation 6.1.2 in Chapter 6.1. MgLa and CaLa did not relax using either PBEsol or HSE06 and thus are absent from this table.

Table B.2 provides the elemental reference energies per atom which were used in the calculation of the thermodynamic stabilities of each $[Cu_2S_2][A_3B_2O_5]$ compound. The calculated enthalpies of formation for each $[Cu_2S_2][A_3B_2O_5]$ are given in Table B.3 which are calculated relative to their constituent elements:

$$2Cu_{(s)} + 2S_{(s)} + 3A_{(s)} + 2B_{(s)} + \frac{5}{2}O_{2(g)} \rightarrow [Cu_2S_2][A_3B_2O_5]_{(s)} \tag{B.1.1}$$

Table B.4 lists the competing phases (321) together with their enthalpies of formation (calculated in the same way as equation B.1.1) and tabulating any magnetic orderings (where applicable) for the Cu^{2+}-based compounds. Any positive values of ΔH_f were disregarded in the calculation of the thermodynamic stability for each $[Cu_2S_2][A_3B_2O_5]$ compound.

TABLE B.1: The calculated compounds together with the energies above the convex hull (0 eV indicates stable), Decomposition Products and the enthalpies of formation of synthesis $\Delta H_f^{\text{synthesis}}$ from equation 6.1.2 in Chapter 6.1. Negative formation enthalpies are favourable.

Compound	E (above hull) /eV atom^{-1}	Decomposition Products	$\Delta H_f^{\text{synthesis}}$ /eV
MgAl	0.21	Cu_2S, MgS, Al_2O_3,MgO	+3.01
MgGa	0.30	Cu_2S, MgO, $CuGaS_2$, Ga_2O_3	+3.39
MgIn	0.66	Cu_7In_3, In_2S_3, $MgSO_4$, MgO, In_2O_3	+6.20
MgSc	0.38	Cu_2S, Sc_2SO_2, MgO	+5.30
MgY	0.56	Cu_2S, Y_2SO_2, MgO	+7.00
MgLa	-	.....	-
CaAl	0.00	.....	-12.17
CaGa	0.00	.....	-12.34
CaIn	0.32	In_3Cu_7, CaS, Cu, $CaSO_4$	-9.29
CaSc	0.05	$CaSO_4$, Cu, Ca_2CuO_3, Y_2O_3, CaS	-8.31
CaY	0.18	$CuSO_4$, Cu, Ca_2CuO_3, Y_2O_3, CaS	-8.25
CaLa	-	.....	-
SrAl	0.00	.....	-1.10
SrGa	0.00	.....	-1.83
SrIn	0.29	$SrIn_2O_4$, SrS, SrO, $SrSO_4$, Cu_7In_3	+0.42
SrSc	0.0005	Cu, SrS, $SrSc_2O_4$, $SrSO_4$	-0.61
SrY	0.12	Cu,SrS, SrY_2O_4, $SrSO_4$	+9.88
SrLa	0.42	SrO, SrS, $SrSO_4$, La_2O_3, $Cu_{13}La$	+9.08
BaAl	0.07	Cu, $BaAl_2O_4$, $BaSO_4$, BaS	-0.81
BaGa	0.00	.....	-2.15
BaIn	0.34	$BaSO_4$, $Ba_4In_2S_6$, BaO, Cu_7In_3, $Ba_3In_2O_6$	-0.83
BaSc	0.00	.....	-1.42
BaY	2.45	BaY_2O_4, ęBaSO4, Cu, BaS	-0.25
BaLa	0.31	La_2O_3, $Cu_{13}La$, $BaSO_4$, BaS, BaO	+7.18

TABLE B.2: The elemental reference energies for the calculation of the formation enthalpies of each SCSOS compound and competing phase (Tables B.3 and B.4 respectively). All values are calculated using PBEsol+U.

Element	Energy / eV atom^{-1}
Cu	-2.29
O	-4.55
Sr	-1.34
Sc	-6.45
S	-3.73
Al	-4.14
Ga	-2.86
In	-2.80
Y	-6.58
La	-5.03
Mg	-1.62
Ca	-1.94
Ba	-1.89
Se	-25.46
Te	-2.92

TABLE B.3: The formation energies (ΔH_f) of all SCSOS compounds (with $[Cu_2S_2][Mg_3La_2O_5]$ and $[Cu_2S_2][Ca_3La_2O_5]$ omitted due to inability to geometrically optimise). All values are calculated using PBEsol+U.

Compound	ΔH_f / eV
$[Cu_2S_2][Sr_3Sc_2O_5]$	-36.27
$[Cu_2S_2][Sr_3Al_2O_5]$	-33.39
$[Cu_2S_2][Sr_3Ga_2O_5]$	-28.87
$[Cu_2S_2][Sr_3In_2O_5]$	-25.31
$[Cu_2S_2][Sr_3Y_2O_5]$	-34.17
$[Cu_2S_2][Sr_3La_2O_5]$	-31.87
$[Cu_2S_2][Mg_3Sc_2O_5]$	-28.05
$[Cu_2S_2][Mg_3Al_2O_5]$	-26.96
$[Cu_2S_2][Mg_3Ga_2O_5]$	-21.34
$[Cu_2S_2][Mg_3In_2O_5]$	-17.22
$[Cu_2S_2][Mg_3Y_2O_5]$	-26.14
$[Cu_2S_2][Ca_3Sc_2O_5]$	-32.90
$[Cu_2S_2][Ca_3Al_2O_5]$	-33.39
$[Cu_2S_2][Ca_3Ga_2O_5]$	-28.32
$[Cu_2S_2][Ca_3In_2O_5]$	-23.96
$[Cu_2S_2][Ca_3Y_2O_5]$	-32.64
$[Cu_2S_2][Ba_3Sc_2O_5]$	-35.03
$[Cu_2S_2][Ba_3Al_2O_5]$	-31.04
$[Cu_2S_2][Ba_3Ga_2O_5]$	-27.14
$[Cu_2S_2][Ba_3In_2O_5]$	-24.50
$[Cu_2S_2][Ba_3Y_2O_5]$	-33.65
$[Cu_2S_2][Ba_3La_2O_5]$	-31.72

TABLE B.4: The enthalpies of formation (ΔH_f) of each competing phase calculated using PBEsol+U. The magnetic orderings for the Cu^{2+} compounds correspond to the lowest energy configuration orderings and are either AFM = antiferromagnetic or FM = Ferrimagnetic.

Compound	ΔH_f / eV	Magnetic Ordering	Compound	ΔH_f / eV	Magnetic Ordering
Cu_2S	-0.79		$Cu(SO_4)$	-7.52	AFM
Cu_5Sr	-0.28		$SrSc_2S_4$	-14.76	
SO_3	-4.74		$Sr_2Cu_3O_5$	-16.18	AFM
SrCu	-0.34		$SrCuO_3$	-8.92	
$CuScO_2$	-9.97		S_8O	-1.30	
S_3Sc_2	-9.88		$SrSc_2O_4$	-24.60	
Sc_2O_3	-18.42		Al_2O_3	-15.04	
$Sc_2(SO_4)_3$	-37.70		Al_2S_3	3440.83	
SO_2	-3.30		$Al_2(SO_4)_3$	-33.13	
SrO	-5.92		Al_4Sr	0.07	
SrS	-4.62		Al_2O	0.85	
SrS_3	-4.50		Al_2Sr	-0.35	
$SrSO_4$	-14.38		Al_3Cu_2	0.48	
Cu_2O	-1.56		Al_9Sr_5	-1.87	
Cu_2Sc	-0.51		$AlCu_3$	-0.28	
CuSc	-0.38		AlO	-2.24	
$CuScS_2$	-5.56		$Cu_2Al_4O_7$	-26.07	
Sc_2O_2S	-15.83		$CuAlO_2$	-8.44	
ScS	-4.01		$Sr_4(Al_6O_{12})(SO_4)$	-78.18	
SrO_2	-6.27		SrAl	-0.23	
SrS_2	-4.59		$SrAl_2S_4$	-9.87	
CuO_2	0.35	AFM	Al_2Cu	0.31	
CuS_2	-0.52	AFM	Al_2Sr_3	10.64	
Cu_4O_3	-4.53	AFM	Al_4Cu_9	-1.06	
$(Cu_2S_2)(Sr_2CuO_2)$	-13.68	AFM	Al_7Sr_8	-2.21	
CuS	-0.56	AFM	AlCu	-0.001	
CuO	-1.50	AFM	$AlCu_4$	-0.08	
$Cu_2Sc_2O_5$	-21.22	FM	$SrAl_2O_4$	-21.44	
$SrCuO_2$	-7.53	AFM	$Sr_8(Al_{12}O_{24})S_2$	-137.49	
$SrCu_2O_2$	-7.70		$CuAlS_2$	0.12	
$Cu_2(SO_4)$	-7.23		$CuAl_2O_4$	-15.80	FM
$(SrO)(Al_2O_3)_2$	-36.30		$Cu_{10}In_7$	-0.60	

Compound	ΔH_f / eV	Magnetic Ordering	Compound	ΔH_f / eV	Magnetic Ordering
$(SrO)_4(Al_2O_3)_7$	-131.25		$Cu_{11}In_9$	-0.56	
$SrAl_{12}O_{19}$	-96.91		Cu_2In	0.15	
$SrAl_4O_7$	-34.83		InS	-1.06	
$Sr_{10}Al_6O_{19}$	-106.19		In_2S_3	-2.90	
$Sr_2Al_6O_{11}$	-58.17		$In_{24}S_{32}$	-32.97	
$Sr_3Al_2O_6$	-36.23		In_5S_4	-3.33	
$SrO(Al_2O_3)_6$	-96.91		In_6S_7	-7.05	
$CuGa_2$	-0.27		$InSr_3$	-1.41	
$GaCu_2$	-0.09		In_2Sr	-1.80	
GaS	-1.30		SrIn	-1.19	
Ga_2S_3	-3.36		In_4Sr	-1.88	
Ga_2Sr	-1.81		$Sr_{11}In_7$	-9.54	
Ga_4Sr	-2.49		Sr_5In_3	-4.16	
Ga_2O_3	-9.80		In_2O_3	-8.49	
$CuGaS_2$	-2.62		$SrCu_7In_6$	-2.12	
Cu_2GaSr	-1.15		$CuInO_2$	-4.97	
$CuGaO_2$	-5.80		In_2CuO_4	-8.16	
$SrGa_2S_4$	-8.60		$CuInS_2$	-2.22	
$Ga_2(SO_4)_3$	-27.18		$SrIn_2S_4$	-7.78	
$SrGa_2O_4$	-16.50		$In_2(SO_4)_3$	-26.59	
$SrGa_4O_7$	-26.27		Cu_7In_3	-12.44	
$Sr_3Ga_4O_9$	-39.30		Sr_3In_{11}	-5.63	
$Sr_4Ga_2O_7$	-34.42		$SrIn_2O_4$	-14.87	
Cu_9Ga_4	-1.72		$Sr_2In_2O_5$	-20.35	
Ga_7Sr_8	-10.20		Cu_2Y	-0.49	
$Sr_{10}Ga_6O_{19}$	-93.34		Cu_5Y	-0.76	
$Sr_3Ga_2O_6$	-29.23		CuY	-0.31	
Sr_2CuGaO_3S	-17.38		$CuYO_2$	-9.83	
CuIn	0.10		SrY_2O_4	-24.18	
$CuIn_2$	0.47		SrY_2S_4	-15.41	
$Y_2(SO_4)_3$	-38.60		LaS_2	-5.79	
$Y_2Cu_2O_5$	-21.03	FM	Cu_2Mg	-0.28	

Compound	ΔH_f / eV	Magnetic Ordering	Compound	ΔH_f / eV	Magnetic Ordering
Y_2O_2S	-16.33		MgS	-2.95	
Y_2O_3	-18.20		MgSc	-5.75	
Y_2OS_2	-13.43		MgO	-5.60	
Y_2S_3	-10.54		MgO_2	-5.39	
Y_5S_7	-25.50		$MgCu_2O_3$	-8.36	FM
$YCuS_2$	-5.80		$MgSc_2S_4$	-12.73	
YS	-3.67		$MgSO_4$	-12.41	
YS_2	-0.61		$MgAl_2$	0.05	
$LaCu_5$	-0.39		Al_2MgO_4	-20.55	
$(LaO)_2(SO_4)$	-25.64		Al_2CuMg	-0.48	
Cu_2La	-0.30		$Al_{12}Mg_{17}$	3.81	
Cu_6La	-0.50		$Al_{14}Mg_{13}$	6.91	
$CuLaS_2$	-6.19		$Al_{30}Mg_{23}$	10.01	
$Cu_{13}La$	-22.01		$Al_{12}Cu_6Mg_{11}$	1.49	
$CuLa_2S_4$	-11.95	AFM	$Al_5Cu_6Mg_2$	-0.73	
$CuLaO_2$	-9.59		$MgAl_2S_4$	-12.34	
CuLa	-0.12		Ga_5Mg_2	-0.94	
La_2O_2S	-16.21		$Mg_2Cu_6Ga_5$	-3.84	
La_2CuO_4	-18.96	FM	Ga_2Mg	-1.03	
$La_2Cu_2O_5$	-20.46	AFM	$GaMg_2$	-0.44	
La_2O_3	-17.58		Ga_2Mg_5	-0.92	
$La_3CuO_2S_3$	-22.55		$MgGa_2S_4$	-6.41	
La_2S_3	-11.14		InMg	-0.25	
La_3CuLaS_7	-15.61	AFM	$InMg_2$	-0.34	
$LaCuO_3$	-10.56	AFM	In_2Mg_5	-0.70	
La_3S_4	-15.61		In_3Mg	-0.27	
$La_{10}OS_{14}$	-58.64		$MgIn_2O_4$	-13.84	
LaCuOS	-8.72		Cu_4InMg	-0.61	
LaS	-3.80		In_2MgS_4	-5.88	
MgY	-0.21		$Ca_{13}Al_{14}$	-6.56	
$Mg_{24}Y_5$	-1.59		Ca_8Al_3	-1.78	
Cu_9Mg_2Y	-1.48		$Al_7Ca_3Cu_2$	-3.50	

Compound	ΔH_f / eV	Magnetic Ordering	Compound	ΔH_f / eV	Magnetic Ordering
Mg_2Y	-0.25		$CaAl_2S_4$	-9.62	
YCuMg	-0.42		$CaAl_2O_4$	-21.40	
$YCuMg_4$	-0.55		$CaAl_4O_7$	-36.50	
YCu_4Mg	-0.98		$Ca_2Al_2O_5$	-27.82	
Y_2Cu_2Mg	-0.81		$Ca_3Al_2O_6$	-28.10	
$LaMg_{12}$	-0.64		$Ca_4O(Al_2O_4)_3$	-69.89	
La_2Mg_{17}	-1.24		$Ca_4Al_6O_{13}$	-70.74	
$LaCu_2Mg$	-0.38		Al_8CaCu_4	-0.28	
$LaCu_9Mg_2$	-1.25		$Ca_9(Al_2O_6)_3$	-100.45	
$LaCuMg_4$	-0.58		$Ca_{12}Al_{14}O_{33}$	-179.16	
LaMg	-0.18		$Ca_5Al_6O_{14}$	-76.87	
$LaMg_2$	-0.32		$Ca_8Al_{12}O_{24}S_2$	-137.20	
$LaMg_3$	-0.51		CaGa	-1.00	
La_2Cu_2Mg	4.65		$CaGa_2$	-1.70	
CaCu	-0.17		$CaGa_4$	-2.00	
$CaCu_5$	-0.44		$Ca_{11}Ga_7$	-7.56	
Ca_2Cu	-0.23		Ca_3Ga_5	-4.45	
CaS	-4.43		Ca_3Ga_8	-5.23	
CaO	-0.48		Ca_5Ga_3	-3.24	
CaO_2	-3.60		Ca_2Cu_2Ga	-1.33	
$CaCuO_2$	-7.40		$CaGa_2S_4$	-8.07	
$CaCu_2O_3$	-8.83	AFM	$Ca_2Ga_2O_5$	-22.53	
Ca_2CuO_3	-13.75		$Ca_5Ga_6O_{14}$	-61.41	
$CaSc_2S_4$	-14.35		$CaGa_2O_4$	-16.36	
$CaSO_4$	-14.04		$Ca_{28}Ga_{11}$	-16.62	
$CaSc_2O_4$	-24.69		$CaGa_4O_7$	-26.11	
Al_2Ca	-0.94		CaIn	-1.06	
Al_4Ca	-0.84		$CaIn_2$	-1.52	
Ca_2In	-1.27		Ba_7Al_{13}	-4.11	
Ca_3In	-1.10		$BaAl_4S_7$	-14.93	
Ca_8In_3	-4.26		$BaAl_2S_4$	-9.84	
$CaCuIn_2$	-1.40		$Ba_{21}Al_{40}$	-18.10	

Compound	ΔH_f / eV	Magnetic Ordering	Compound	ΔH_f / eV	Magnetic Ordering
$CaCu_4In$	-0.99		$Ba_{17}Al_3O_7$	-34.49	
$CaIn_2O_4$	-14.73		$BaAl_2O_4$	-21.29	
CaY_2S_4	-14.98		$Ba_4Al_2O_7$	-37.08	
CaY_2O_4	-19.63		$BaGa_2$	-1.43	
$CaLa_2O_4$	-22.87		$BaGa_4$	-2.35	
$BaCu_3O_4$	-9.55	AFM	$BaGa_4S_7$	-11.85	
$BaSO_4$	-13.72		$Ba_2Ga_2S_5$	-5.78	
$BaCu_2O_2$	-7.11		$Ba_5(GaS_4)_2$	-25.46	
$BaCu_2S_2$	-5.30		$Ba_4Ga_2S_7$	-21.12	
$BaCu_4S_3$	-6.16		$Ba_{10}Ga$	0.29	
BaCu	0.003		Ba_8Ga_7	-37.88	
Ba_2S_3	-8.29		$BaCu_2Ga$	-1.05	
BaS_2	-4.34		$Ba_3Ga_2S_6$	-16.92	
BaS_3	-4.50		$BaGa_2S_4$	-8.33	
$BaSc_2O_4$	-23.93		$Ba_4Ga_2O_7$	-32.15	
BaS	-4.18		BaIn	-0.92	
$BaScCuS_3$	-10.28		$BaIn_2$	-1.59	
$BaCu_{13}$	0.13		$BaIn_4$	-1.99	
BaO	-5.11		Ba_9In_4	-3.93	
BaO_2	-5.88		$BaIn_2S_4$	-7.66	
$Ba_3Cu_3Sc_4O_{12}$	-58.31	FM	$Ba_2In_2S_5$	-11.95	
$Al_{13}Ba_7$	-4.11		$Ba_4In_2S_6$	-27.99	
Al_2Ba	-0.63		$Ba_3In_2O_6$	-24.50	
Al_4Ba	-1.03		$BaIn_2O_4$	-13.20	
Ba_3Al_5	-1.61		$Ba_{11}In_6O_3$	-21.39	
Ba_4Al_5	-1.88		Ba_2In	-0.98	
Ba_7Al_{10}	-3.54		$Ba_4In_6O_{13}$	-46.56	
$Ba_2In_2O_5$	-19.24		$YBa_2Cu_4O_8$	-26.36	
BaY_2S_4	-15.20		Y_2BaCuO_5	-25.38	AFM
BaY_2O_4	-23.52		$Ba_2YCu_3O_6$	-23.74	AFM
$Ba_3Y_4O_9$	-51.54		$Y_2Ba_4Cu_6O_{13}$	-48.86	AFM
$BaYCuS_3$	-10.65		$La_4BaCu_5O_{12}$	-48.12	FM
$BaLaCuS_3$	-10.71				

B.1.4 Supplementary Information: Electronic Properties

Figure B.1 displays the combined total and partial density of states (DOS) for each stable SCSOS compound. below each graph, a zoom-in of the VBM and CBM is provided for clarity. The analysis of the DOS is given in Chapter 6.1.3 as well as a tabulation of the percentage of states at the band extrema (given in Tables 6.3 and B.1 for the VBM and CBM respectively).

Figure B.2 displays the first brillouin zone and associated unit cell of the $[Cu_2S_2][Sr_3Sc_2O_5]$ structure. The high symmetry points and coordinates were taken from the Bilbao Crystallographic server[597–599] and Bradley and Cracknell.[56] The associated band structures are provided in Chapter 6.1.3 Figure 6.5.

Figure B.3 shows the calculated absorption spectra for each stable compound. The optical absorption coefficient, α is displayed alongside α^2 which is proportional to the band gap using the Tauc relation ($E_g \propto \alpha^2$).[596]

B.1.5 Supplementary Information: Experimental XRD

The powder XRD diffraction pattern of $[Cu_2S_2][Ba_3Sc_2O_5]$ is shown in Figure B.4(a). A Rietveld refinement was carried out against this data using a starting model based on the previously reported and assumed isostructural $[Cu_2S_2][Sr_3Sc_2O_5]$ (SCSOS), but with replacement of strontium ions with barium ions and an appropriate expansion in lattice parameter. Refinement of this model against the data was carried out with refinement of the background function, the Lorentzian and Gaussian components of pseudo-Voight peak-profile functions, the lattice parameters, the atomic positions and their isotropic displacements. The refinement confirmed that $[Cu_2S_2][Ba_3Sc_2O_5]$ was single phase crystallising in the tetragonal I_4/mmm space group with lattice parameters of $a = 4.14462(2)$Å and $c = 27.12390(8)$Å, with a good fit to the data with $\chi^2 = 2.938$ and $R_p = 7.80\%$. All the structural parameters are given in Chapter 6.1.4 Table 6.6.

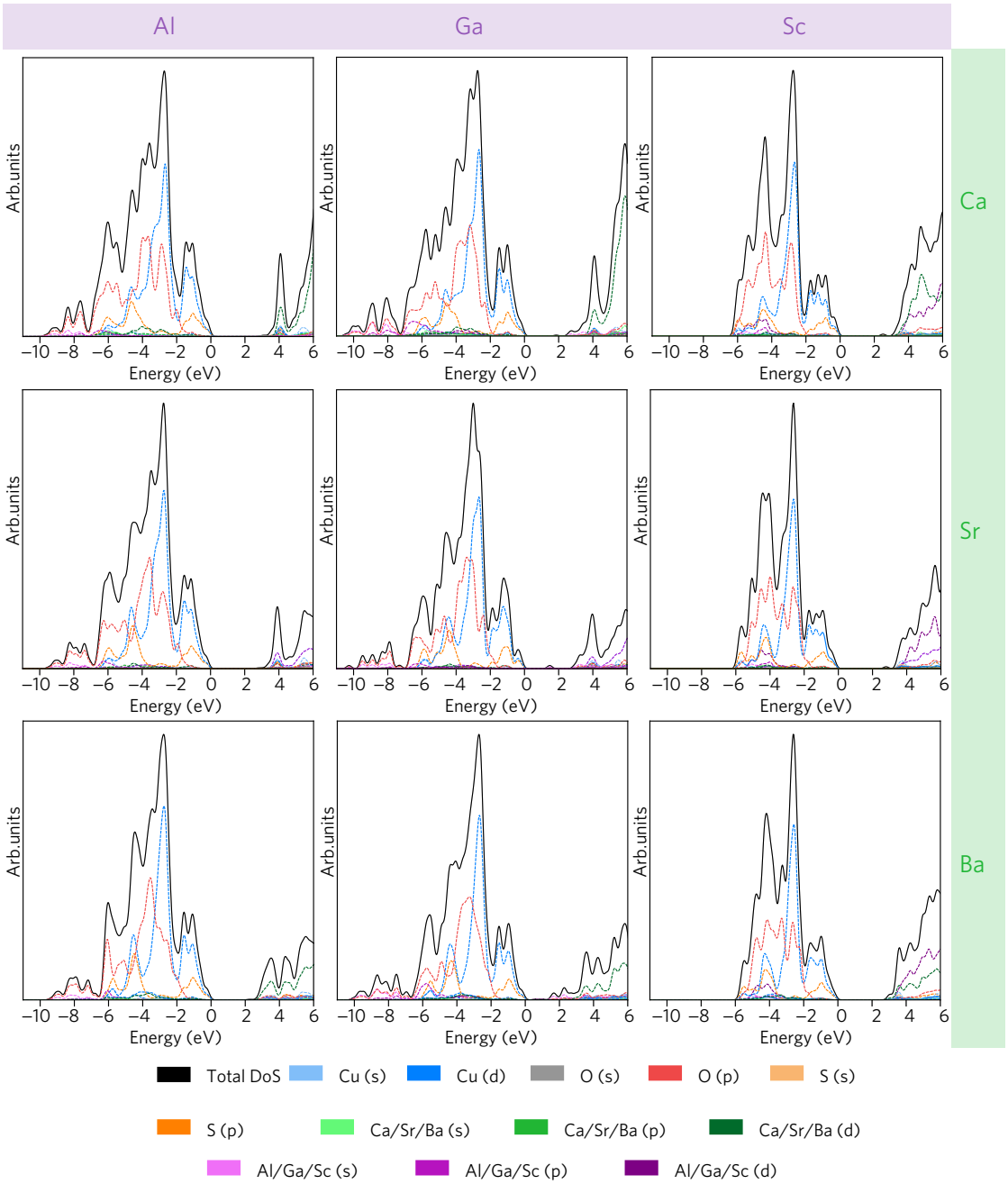

FIGURE B.1: The combined total and partial density of states (DOS) for all stable and metastable compounds as calculated using HSE06. The DOS are arrayed in a grid such that the top left corresponds to CaAl and the bottom right to BaSc. For each structure, a zoomed in portion of the VBM and CBM is provided for clarity and the VBM is set to 0 eV in each example.

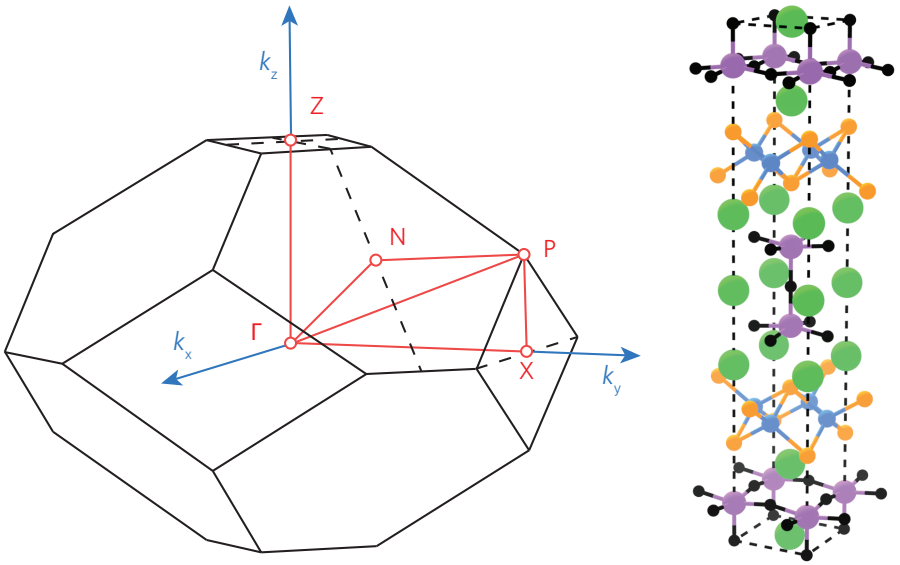

FIGURE B.2: The first Brillouin zone used to calculate the band structure of SCSOS, adapted from the Bilbao Crystallographic server[597–599] and Bradley and Cracknell[56]

B.1.6 Supplementary Information: Experimental Optical Absorption

Spectroscopic diffuse reflection data were recorded on the sample of $[Cu_2S_2][Ba_3Sc_2O_5]$, and used to produce a Tauc plot which can be seen in Figure B.4(b). This shows a strong absorption which can be attributed to a direct band gap of 3.24 eV. This puts the band gap in the UV, and therefore we would predict that the material should be transparent, which is contradicted by the observed light brown colour of the powder. However, there is an additional, less intense feature in the plot which can be related to a band gap of 2.26 eV, which is more consistent with the observed colour. The origin of this is still not clear, but could be due to an amorphous impurity or d–d transitions within Cu related defects.

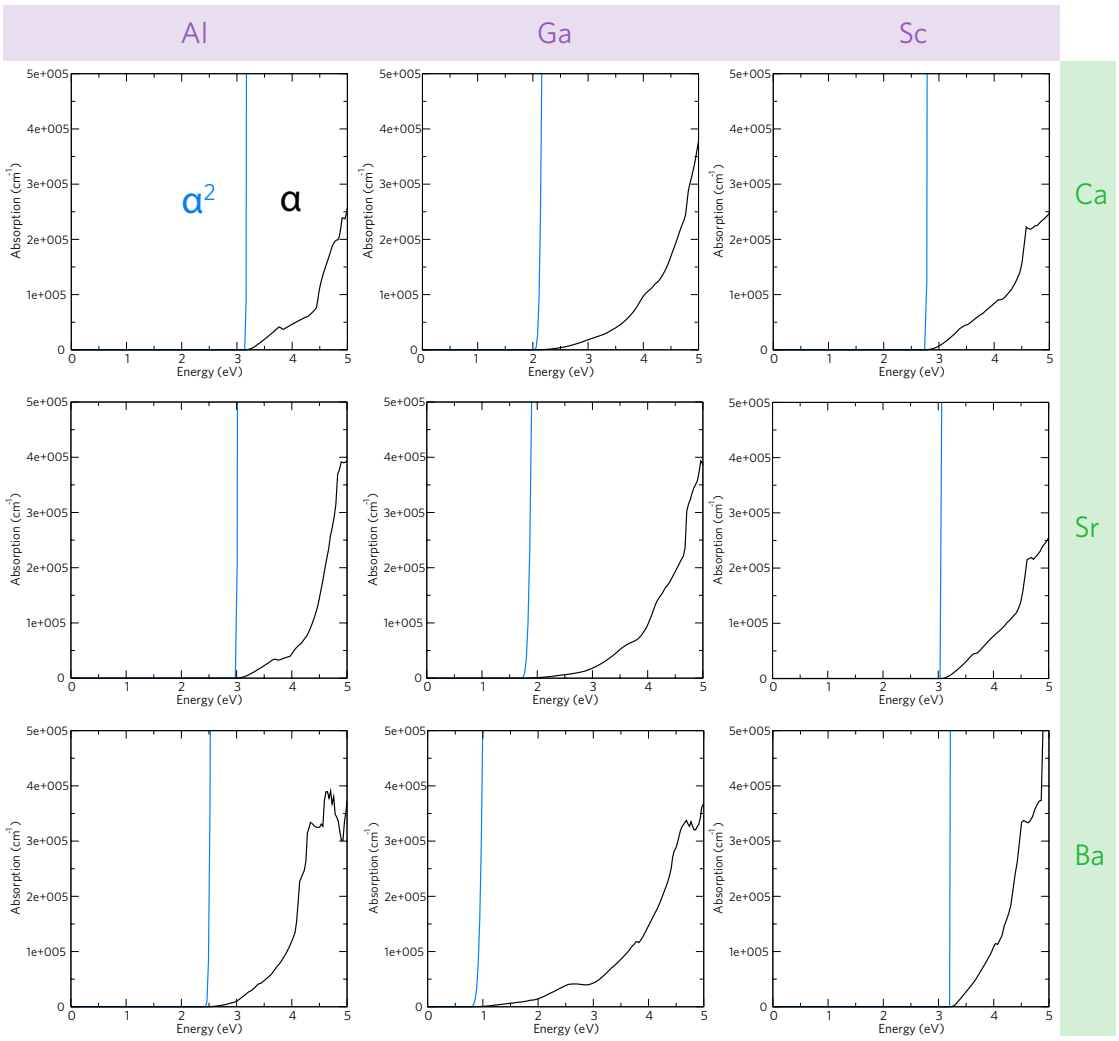

FIGURE B.3: The calculated optical absorption spectra (black=α and blue=α^2) for each of the 9 stable compounds.The DOS are arrayed in a grid such that the top left corresponds to CaAl and the bottom right to BaSc. Each spectrum is calculated over all possible direct valence to conduction band transitions.

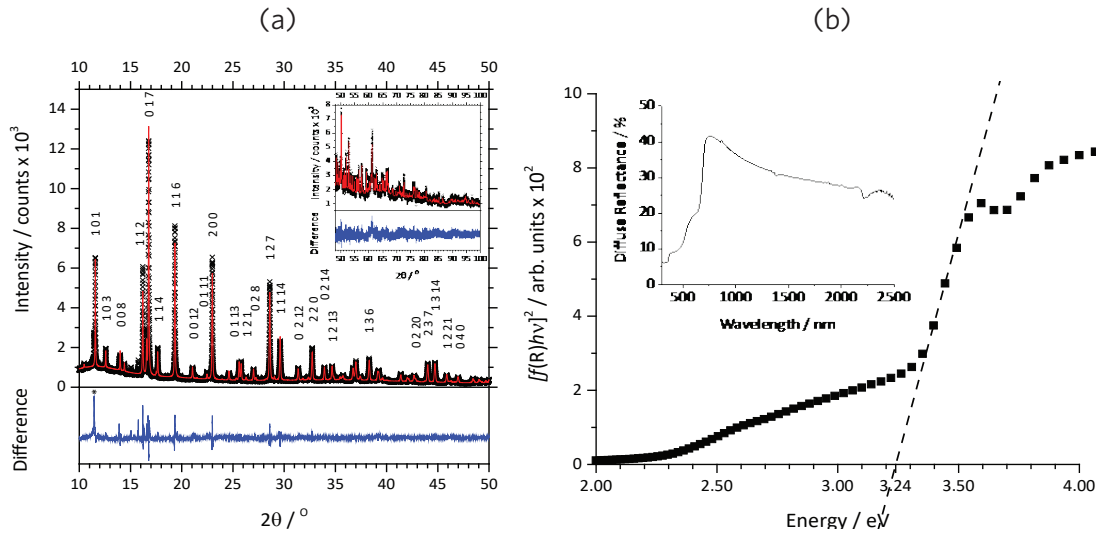

FIGURE B.4: (a) Indexed synchotron powder x-ray diffraction pattern collected using the I11 beamline at the Diamond Light Source, with a wavelength of 0.82603 Å. Black crosses represent the observed diffraction data; the red line, the calculated diffraction pattern and blue line, the difference between these values. Note that different scales are used on the intensity and difference plots. *The peak labelled by the asterisk at ~ 11.44° arises from diluting emulsion added to the sample to reduce x-ray absorption.
(b) Tauc plot, $[f(R)h\nu]^2$ vs. photon energy, derived from the raw diffuse reflectance spectrum (inset) collected over a range of 300–2500 nm at intervals of 5 nm. The dashed line extrapolated to the abscissa models the linear region of absorption edge for calculation of the band gap energy.

B.2 Engineering Valence Band Dispersion - CaCuP

B.2.1 Computational Methodology

The hybrid PBE0[23,265] functional using 25% exact Fock exchange was used for the electronic structure and total energy calculations as implemented in the VASP code.[105–108] Structural optimisations were carried out using a plane wave cut off energy of 400 eV and a k-point sampling of Γ-centred 7 x 7 x 4 for CaCuP, SrCuP and BaCuP and Γ-centred 8 x 5 x 4 for MgCuP. The projector-augmented wave method (PAW)[44,600] was utilised to describe the interactions between the valence and the core electrons (Ca:[Ar], Sr:[Kr], Ba:[Xe], Mg:[Ne], Cu:[Ar] and P:[Ne]) and the structures were deemed to be converged when the forces on all the atoms were less than 0.01 eVÅ^{-1}.

The calculated density of states (DOS) for CaCuP was weighted using the atomic orbital photoionisation cross-sections formulated by Yeh and Lindau[48] simulating valence band X-ray photoelectron spectroscopy (XPS) that can be compared directly with experiment. A Gaussian broadening of 0.47 eV was also applied to match experimental broadening.

The optical absorption spectra were calculated using the real and imaginary parts of the dielectric constant calculated using a Kramers-Kronig transformation and a summation over the unoccupied bands respectively using a method by Furthmüller and coworkers.[593] This sums the absorption spectrum over *all* direct valence band to conduction band transitions ignoring intraband and indirect absorptions.

B.2.2 Experimental Methodology

This section was written by and reproduced with permission by Dr Robert G. Palgrave at University College London.

Ca (99.0%), Cu (99.9%) and P (99.9%) were obtained from SigmaAldrich. CaCuP was synthesised from the elements with an addition of 5% P over the required stoichiometry which was necessary due to evaporation. The starting materials were ground in an agate mortar and pestle in a nitrogen glovebox, sealed in a quartz tube under reduced pressure (c. 10-3 mbar) and heated at 500 °C, with heating and cooling rates of 5 °C/min for a total of 24 hours with one intermittent regrinding which was carried out in the glovebox. Powder X-ray diffraction (XRD) was carried out on a STOE diffractometer in transmission geometry using Mo-Kα radiation over the 2θ range 2 to 40° with a step size of 0.05°. X-ray photoelectron spectroscopy (XPS) was carried out using a Thermo K-alpha spectrometer utilising Al K alpha radiation and run in constant analyser energy (CAE) mode. Survey and high resolution spectra were taken with a pass energy of 200 eV and 50 eV respectively. For high resolution scans, a binding energy step size of 0.1 eV was used. The spectral resolution, measured as the full width at half maximum (FWHM) of the Ag $3d_{5/2}$ peak on a clean Ag surface, was 0.9 eV under these conditions. In situ Ar ion etching was carried out using a 2000 eV Ar ion beam in a background Ar pressure of 2×10^{-7} mbar. The binding energy scale was corrected for charging by adjusting the adventitious C 1s peak to 284.6 eV. Optical measurements were taken using a Perkin Elmer Fourier Transform Lambda 950 UV-vis spectrophotometer in diffuse reflectance geometry. Powder samples were packed into a holder presenting a surface area significantly larger than the incident beam and with sufficient thickness to ensure no transmission. Reflected light was measured using an integrating sphere and reflectance values were converted using the Kubelka-Munk function to yield values proportional to absorption.[595] Conductivity measurements were carried out using an Ecopia HMS-3000 instrument and a van der Pauw electrode geometry.

B.2.3 Supplementary Information: XRD and XPS results

The powder XRD pattern from the sample of CaCuP was recorded and the published structural model in the $P6_3/mmc$ space group[377] was used as a basis for Rietveld refinement using the EXPGUI and GSAS software and is shown in Figure B.5.[594,601] The initial fitting was carried out using the CaCuP phase alone, which led to a satisfactory fit of all intense peaks but some small peaks remained unaccounted for. A two phase refinement containing CaCuP and $CaCu_{3.8}P_2$ yielded an improvement in fit and accounted for several of the unknown peaks.[602] The CaCuP unit cell was refined in the $P6_3/mmc$ space group yielding lattice parameters of a = 4.070(1) Å and c = 7.826(2) Å which compare well with the reported structure.[377] The literature structure of $CaCu_{3.8}P_2$ was used without refinement of its unit cell. In the final refinement an Rwp value of 0.081 was obtained and the impurity level of $CaCu_{3.8}P_2$ phase was 1.6(2) weight % .

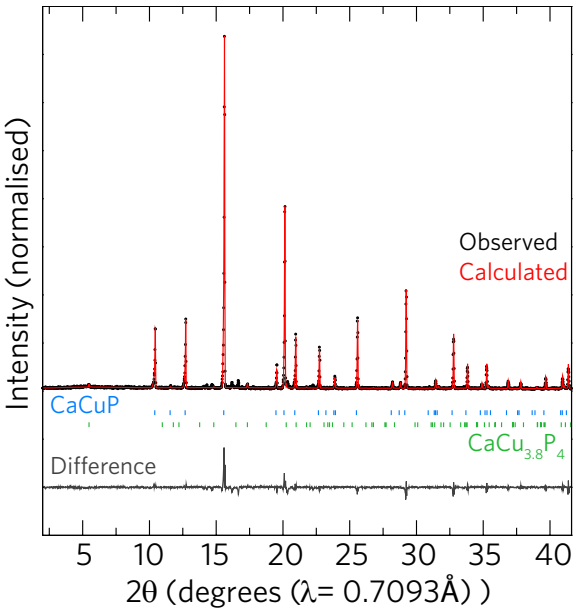

FIGURE B.5: Powder X-ray diffraction pattern from CaCuP synthesised here (black) and calculated from the standard structure (red) with the difference between the calculated and observed intensities shown underneath in grey. The phase ticks for CaCuP and $CaCu_{3.8}P_4$ are shown in blue and green respectively.

Figure B.6 displays the XPS spectra for the Cu *2p*, Ca *2p*, P *2p* regions alongside the valence band (VB) XPS. The surface of the as synthesised powder contained a significant amount of oxygen. Ar ion etching for 60 s using a 2000 eV Ar ion beam was able to reduce the level of

oxygen suggesting that the oxidation was localised on the surface. High resolution spectra showed a symmetrical Cu $2p_{3/2}$ peak at 933.2 eV, corresponding to Cu^{1+}. This assignment is supported by the lack of strong, sharp satellite peaks that typically accompany Cu^{2+} spectra.[603] Such satellite peaks arise from a $3d^9$ initial state that results on photemission in a series of screened and unscreened final states,[604] and are detectable even with low concentrations of Cu^{2+} within a predominantly Cu^{1+} matrix.[605] The spectral region between the Cu *2p* spin orbit doublet that we measure in CaCuP does shows a very broad feature centred on 949.4 eV with FWHM of 8 eV. The origin of this feature is unknown, but it is unlike previously reported Cu^{2+} satellites, which are typically much sharper.[603–605] The feature may, therefore, be due to an as yet unassigned loss process. Given its position some 16 eV above the Cu $2p_{3/2}$ peak, the feature may be due to valence band plasmon loss, which is typically seen in materials with similar valence band electron density at c. 20 eV to the high binding energy side of the main photoemission peak.[606] Unfortunately the corresponding Cu $2p_{1/2}$ loss peak (if it were present) would be obscured by the O Auger line which overlaps on the binding energy scale at this photon energy. Further study is needed to ascertain the nature of the loss feature present in the Cu *2p* spectrum.

Ca *2p* spectra showed two overlapping doublets. The lower binding energy component has Ca $2p_{3/2}$ component at 346.3 eV (red trace, Figure B.6b). We could find no reference of the XPS binding energy of Ca phosphide compounds. Ca_3P_2 itself is highly toxic and unstable, which may have precluded its measurement. However, CaS has been reported with a Ca $2p_{3/2}$ binding energy of 346.5 eV, very similar to our observed value.[607] Therefore we assign the Ca $2p_{3/2}$ environment at 346.3 eV to Ca within the CaCuP structure. The other observed Ca *2p* component, with Ca $2p_{3/2}$ binding energy of 347.8 eV (blue trace, Figure B.6b) corresponds well to $Ca_3(PO_4)_2$ or $CaHPO_4$.[608] This indicates a level of oxidation of the surface as discussed above. No crystalline $Ca_3(PO_4)_2$ or $CaHPO_4$ was observed in XRD, again suggesting this is surface limited oxidation.

The P *2p* region again was composed of overlapping peaks. Deconvolution showed that the principal chemical component (representing 66% of the P signal) was associated with a P $2p_{3/2}$ peak at 128.7 eV (red trace, Figure B.6c), corresponding to phosphide compounds: for example InP is reported with the same P $2p_{3/2}$ binding energy.[609] A higher binding energy component (representing 18% of the P signal) is also observed with a P $2p_{3/2}$ peak at 133.4 eV (blue trace , Figure B.6c), corresponding to phosphate groups,[610] and consistent with the interpretation of the Ca *2p* region given above. The remainder (c. 16% of the observed P

signal) was fitted with a P $2p_{3/2}$ component at 130.5 eV (purple trace, Figure B.6c), and may originate from elemental P, which may be located at the sample surface due to evaporation during synthesis.

The valence band was recorded up to 30 eV binding energy. The main feature at low binding energy is a spectral maximum at 3.9 eV corresponding to Cu *3d* electrons, which confirmed by the excellent agreement with our simulated XPS (red dashed lines). The onset of the valence band begins immediately at the Fermi level (BE = 0 eV), indicating filled states immediately below the Fermi level, i.e. a *p*-type semiconductor or a metal. However, no Fermi edge was observed, meaning that if this is a metal the density of states at the Fermi level is low. This fits with our calculations of a very disperse valence band, with the Fermi level found near to the VBM, most likely through Cu deficiency. The Ca *3p* shallow core line appears at 25.5 eV. The Ca *3p* shallow core line appears at 25.5 eV.

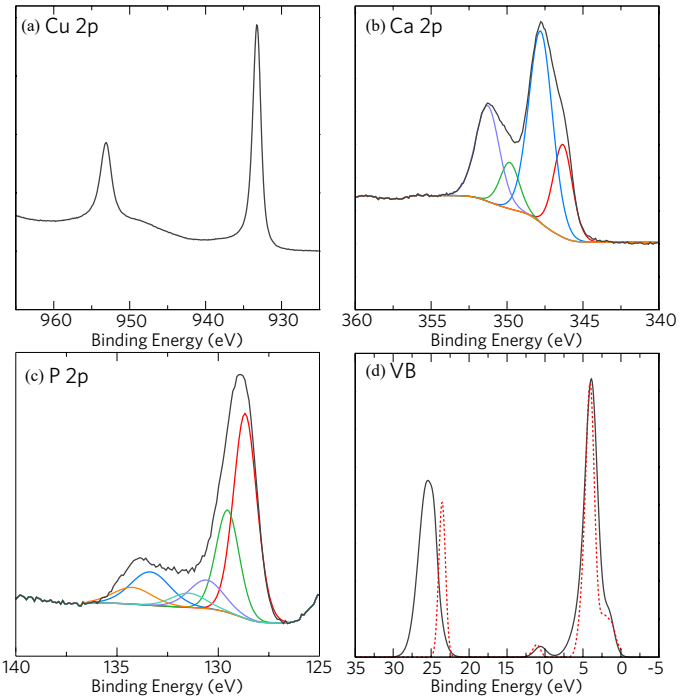

FIGURE B.6: X-ray photoelectron spectra of CaCuP. (a): Cu *2p*, (b): Ca *2p* and (c): P *2p* regions are shown, with curve fitting as described in the text. The valence band region up to 35 eV binding energy is shown in (c) with the simulated VB XPS overlaid (red dashed line) taken from the PBE0 calculated DoS for CaCuP.

B.2.4 Supplementary Information: Optical Properties

Diffuse reflectance optical spectra were recorded in the interval 1.5 – 3.5 eV. The Kubelka Munk function, F(R) is taken to be proportional to absorption; this is valid if scattering is constant throughout the wavelength range used, which is a reasonable assumption.[595] There appears to be an absorption edge towards the higher energy range. Recently Poeppelmeier and co workers have proposed a method for accurate determination of the band gap in degenerately doped semiconductors.[393] This is similar to the well established Tauc method,[392] but takes into account the presence of a large concentration of charge carriers. Using the Poeppelmeier method, plots of F(R) and $F(R)^2$ against energy were made and are displayed in Figure B.7(a) alongside the simulated PBE0 optical absorption spectrum (b). The absorption edge of each plot was extrapolated to the x-axis (y=0). For the F(R) plot the extrapolated value, E_1 = 2.66 eV. For the $F(R)^2$ the extrapolated value E_2 = 2.72 eV. According to the Poeppelmeier method, the band gap $Eg = 2E_2\text{-}E_1$, which in this case gives 2.78 eV. Below the absorption edge there are two strong absorption peaks located at 1.8 eV and 2.2 eV. The origin of these peaks is not clear. Cu^{2+} d-d transitions can occur in this energy range,[611] but XPS detects no Cu^{2+}. While XPS detects calcium phosphate impurities at the surface, these are not expected to give rise to visible light absorption. The weight percentage of crystalline impurities (c. 1.7 weight %) is too low to effect strong absorption bands as seen here. The absorptions likely arise from as-yet unidentified defects within the CaCuP structure.

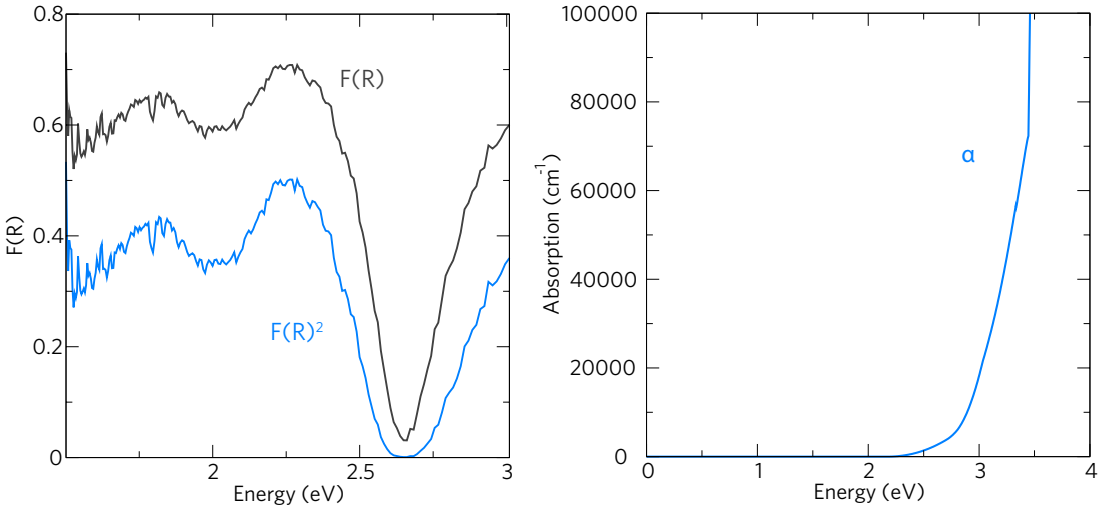

FIGURE B.7: The diffuse reflectance optical spectra showing the Kubelka-Munk function F(R) and $F(R)^2$ is displayed in (a). The direct band gap calculated from the Poeppelmeier method is shown to be 2.78 eV. (b) Shows the calculated optical absorption spectrum using the PBE0 functional where a weak absorption onset at 2.17 eV and a strong absorption at 2.71 eV are seen.

Conductivity measurements were carried out by forming a 12 mm diameter pellet, which was prepared by biaxial pressing at 1 tonne pressure followed by annealing at 300 °C for 4 hours under nitrogen to sinter the particles. This yielded a pellet approximately 3 mm thick with a density of approximately 70%. The surface was polished to remove surface oxidation, and gold electrodes were sputtered in a van der Pauw geometry. Conductivity was then measured using a four point probe. A resistivity of $2 \times 10^{-3} \pm 0.2 \times 10^{-3}\,\Omega\,\text{cm}$ was measured in this way. We were unable to record reliable Hall Effect data on the pellet.

Appendix C

Understanding TiO_2 Photocatalysis

C.1 Understanding the Role of Defects and Dopants in Anatase

The properties of bulk TiO_2 were calculated using the hybrid HSE06[30,31] functional within density functional theory (DFT) using VASP.[105–108] HSE06 provides a markedly improved description of the electronic and structural properties of all the known polymorphs of TiO_2, and hybrid functionals are, in general, an improvement on standard DFT functionals which contain a systematic *self-interaction* error owing to the underestimation of band gaps in semiconductors.[33,35–37,39,40] All the bulk geometric, electronic, intrinsic and extrinsic defects were calculated. A geometry optimisation of the bulk primitive cell was carried out minimising the volume, lattice parameters, cell angles and the ions within the cell until the forces acting on all the atoms was less than 0.01 eV Å^{-1}. A 450 eV plane-wave energy cut-off and a Γ-centred $7 \times 7 \times 5$ k-point mesh was used in order to calculate the electronic and structural properties accurately. The projector augmented wave method (PAW)[44] was utilised to describe the interactions between the valence and core electrons (Ti[Ar], O[He], N[He], Nb[Kr], Ta[Xe], B[He], Cu[Ar]).

C.1.1 Defect Methodology

In order to calculate the defect thermodynamics of TiO_2 a $3 \times 3 \times 2$ supercell containing 108 atoms was formed from the bulk. A geometric optimisation of the defective supercells in-

volved calculating the relaxation of only the ions within the cell, keeping the cell volume, lattice parameters and angles fixed. A plane wave energy cut-off of 450 eV, Γ-centred $2 \times 2 \times 2$ k-point mesh were used to relax the supercells to the same force convergence as for the primitive bulk. All defect calculations were spin-polarised.

Section 2.3.5 (Chapter 2) provides details on the calculation of the chemical potential limits of TiO_2. The chemical potential range of TiO_2 is limited by the formation of Ti_2O_3 thus creating an upper bound on μ_{Ti} .Equations C.1.1 and C.1.2 show the formation enthalpies of TiO_2 and Ti_2O_3 respectively as a function of their chemical potentials.

$$\Delta H_f^{TiO_2} = \mu_{Ti} + 2\mu_O = -9.14\,\text{eV} \tag{C.1.1}$$

$$\Delta H_f^{Ti_2O_3} = 2\mu_{Ti} + 3\mu_O = -14.76\,\text{eV} \tag{C.1.2}$$

Solving these simultaneously results in the chemical potentials of μ_{Ti} and μ_O under *Ti-rich/O-poor* conditions:

$$\mu_{Ti} = -2.11\,\text{eV}; \mu_O = -3.51\,\text{eV} \tag{C.1.3}$$

and for *Ti-poor/O-rich* conditions:

$$\mu_{Ti} = -9.14\,\text{eV}; \mu_O = 0\,\text{eV} \tag{C.1.4}$$

Calculation of the Dopant Chemical Potentials:

The dopant states are restricted by the formation of limiting phases and are tabulated in Table C.1. Table C.1 displays the plane-wave energy cutoffs and k-point meshes used in the geometry optimisations (forces <10meVÅ^{-1}) and the calculated enthalpies of formation (ΔH_f). These enthalpies of formation are in good agreement with the standard temperature and pressure experimental results, with differences expected due to the difference in temperature (DFT formation energies are calculated at 0K). Figure C.1 displays the evolution of dopant chemical potentials, N:(a), Nb:(b), B:(c), Cu:(d), with respect to the oxygen chemical potential of TiO_2 (μ_O = -3.51–0 eV). The dashed grey line indicates the *Ti-rich/O-poor*† point, μ_O = -2 eV ($\mu_{Ti} = -5.14$ eV) which is within experimental viability as rationalised by Agoston et al.[28,90]. These chemical potentials, for example, correspond to a pressure and temperature of $p_{O_2} < p_{O_2}^{\text{ambient}}$ and $T = 600$ K which can be calculated using equations 2.3.18 and 2.3.19 in Section 2.3.5 (Chapter 2).

TABLE C.1: The competing phases related to the different dopants (N, Nb, Ta, B, Cu). The Γ-centred *k*-points are tabulated with the enthalpies of formation relative to experiment (in parentheses) and the chemical potentials (μ_i, where i=N, Nb, Ta, B, Cu) under *Ti-rich/O-poor*†, *Ti-poor/O-rich* conditions. †*O-poor* limit is defined as -2 eV rather than the *absolute O-poor* limit in the Nb, Ta and N systems.

Dopant	Limit	Space Group	*k*-points	$\Delta H_f/eV$	$\Delta\mu_i^{O\text{-}poor}$ / eV	$\Delta\mu_i^{O\text{-}rich}$ / eV
N	TiN	$Fm\bar{3}m$	$8\times8\times8$	-3.49 (-3.50[582])	0	-0.26
	Ti_2N	$P42/mnm$	$5\times5\times8$	-4.07 (N/A)		
	NO_2	$R\bar{3}$	$4\times4\times4$	-0.26 (N/A)		
	N_2O_5	Cm	$5\times5\times4$	-0.13 (N/A)		
Nb	Nb_2O_5	$I4/mmm$	$2\times2\times2$	-18.48 (-19.69[582])	-4.24	-9.24
	NbO_2	$C2/c$	$3\times3\times3$	-7.64 (-8.24[582])		
	NbO	$Pm3m$	$6\times6\times6$	-4.10 (-4.35[582])		
Ta	Ta_2O_5	$I4_1/amd$	$6\times6\times1$	-20.31 (-21.21[582])	-5.16	-10.27
B	B_2O_3	$P3_121$	$6\times6\times3$	-13.09 (-13.20[582])	-1.28	-6.54
	TiB_2	$P6/mmm$	$8\times8\times8$	-3.89 (-2.90[582])		
Cu	CuO	$C2/c$	$6\times6\times6$	-1.45 (-1.62[582])	0	-1.45
	Cu_2O	$Pn\bar{3}m$	$6\times6\times6$	-1.56 (-1.77[582])		
	Cu_2O_3	$Ia3$	$3\times3\times3$	-0.62 (N/A[582])		

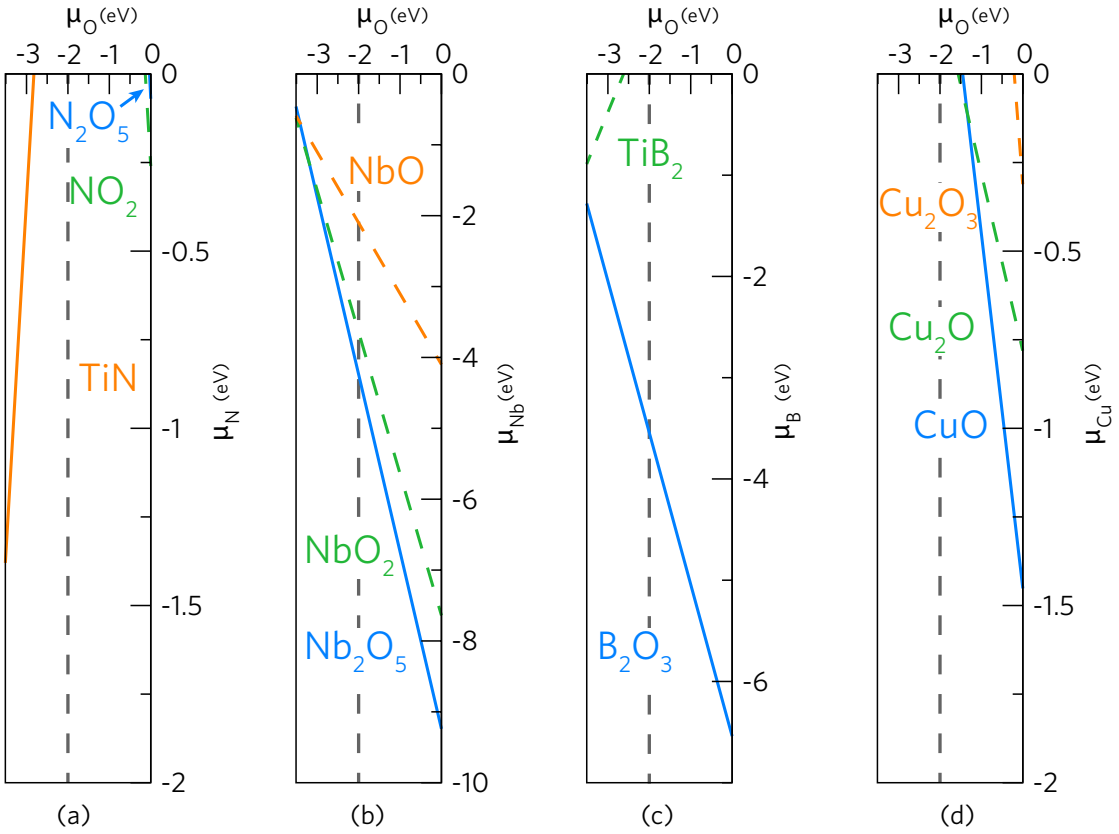

FIGURE C.1: The chemical potential limits as calculated for (a) N (b) Nb (c) B and (d) Cu dopants within the chemical potential bounds of TiO_2 (μ_O = -3.51 eV – 0 eV). The solid lines correspond to the limiting phase at a particular μ_O. All phases are tabulated in Table A.2. The grey line in the (a) and (b) corresponds to μ_O = -2 eV which is used as the *Ti-rich/O-poor* limit in those systems.

Indexes and Bibliography

Acronyms and Abbreviations

Computational Theory and Methods

HF	Hartree-Fock theory
SCF	Self-Consistent Field
UEG	Uniform Electron Gas
DFT	Density Functional Theory
DFPT	Density Functional Perturbation Theory
DFT+U	Density Functional Theory + Hubbard U correction
SIE	Self-Interaction Error
PAW	Projector Augmented Wave Method
DOS	Density of States
pDOS	Partial Density of States
QM/MM	Quantum Mechanics / Molecular Mechanics
GW	Greens Function (G) and Coulomb Interaction (W)
LDA	Local Density Approximation
GGA	Generalised Gradient Approximation
LYP	Lee-Yang-Parr Functional
PBE	Perdew-Burke-Ernzerhof Functional
PBEsol	Perdew-Burke-Ernzerhof Functional optimised for solids
PW91	Perdew-Wang-1991 Functional
PBE0	Perdew-Burke-Ernzerhof Hybrid functional
HSE06	Heyd-Scuseria-Ernzerhof Hybrid functional (25% HF exchange)
FNV	Freysoldt-Neugebauer-Van de Walle Correction
SPL	Single Particle Level
VASP	Vienna *Ab-initio* Simulation Package

Experimental Methods

DLTS	Deep Level Transient Spectroscopy
PL	Photoluminescence
PLE	Photoluminescence Excitation
XPS	X-ray Photoelectron Spectroscopy
VB-XPS	Valence Band X-ray Photoelectron Spectroscopy
HAXPES	Hard X-ray Photoelectron Spectroscopy
CVD	Chemical Vapour Deposition
MOCVD	Metal Organic Chemical Vapour Deposition
APCVD	Atmospheric Pressure Chemical Vapour Deposition
AACVD	Aerosol Assisted Chemical Vapour Deposition
PLD	Pulsed Laser Deposition
MBE	Molecular Beam Epitaxy
EXAFS	Extended X-ray Absorption Fine Structure
XRD	X-ray Diffraction
TAS	Transient Absorption Spectroscopy
NMR	Nuclear Magnetic Resonance
UVVis	Ultraviolet-Visible Spectroscopy

Miscellaneous

ICSD	Inorganic Crystal Structures Database
FWHM	Full Width Half Maximum
FLOPS	Floating Operations Per Second
NHE	Normal Hydrogen Electronde

MATERIALS

ITO	Tin-doped Indium Oxide
IMO	Molybdenum-doped Indium Oxide
FTO	Fluorine-doped Tin Dioxide
ATO	Antimony-doped Tin Dioxide
AZO	Aluminium-doped Zinc Oxide
IGZO	Indium and Gallium Zinc Oxide
SCSOS (also SrSc)	$[Cu_2S_2][Sr_3Sc_2O_5]$

THEORY

HOMO	Highest Occupied Molecular Orbital
LUMO	Lowest Unoccupied Molecular Orbital
VBM	Valence Band Maximum
CBM	Conduction Band Minimum
CBM+1	The band directly above the Conduction Band Minimum
UV	UltraViolet
IR	InfraRed
CMVB	Chemical Modulation of the Valence Band
redox	Reduction-Oxidation

APPLICATIONS

TC	Transparent Conductor
TCO	Transparent Conducting Oxide
LCD	Liquid Crystal Display
LED	Light Emitting Diode
OLED	Organic Light Emitting Diode
Low-E	Low-Emissivity (Glass Coating)
PV	Photovoltaic
PC	Photocatalyst

List of Equations

1.1.1 THEORY: Time-independent Schrödinger Equation 6
1.1.2 THEORY: Kinetic and potential energy contributions to the Hamiltonian . . 6
1.1.3 THEORY: Born-Oppenheimer approximation applied to the Hamiltonian . . 7
1.1.4 THEORY: The kinetic energy contribution and nuclear-electron potential energy interactions 7
1.1.5 THEORY:Variational principle applied to the Hamiltonian 7
1.2.1 THEORY: Sum of one-electron Hamiltonians in Hartree-Fock theory 8
1.2.2 THEORY: One-electron Hamiltonian in Hartree-Fock theory 8
1.2.3 THEORY: The Hartree Product 8
1.2.4 THEORY: Electrostatic repulsion in Hartree-Fock theory 9
1.2.5 THEORY: Exchange integral in Hartree-Fock theory 9
1.2.6 THEORY: Total HF energy 9
1.3.1 THEORY:Total energy using the density ($[\rho(r)]$) to describe an inhomogeneous electron gas 10
1.3.2 THEORY: The universal functional in DFT for an inhomogeneous electron gas 10
1.3.3 THEORY: The Kohn-Sham kinetic energy function in DFT 11
1.3.4 THEORY: The Kohn-Sham total energy and exchange correlation functional in DFT 11
1.3.5 THEORY: The exchange and correlation functional in DFT 12
1.3.6 THEORY: Hubbard-like 'U' parameter in DFT 13
1.3.7 THEORY: Exchange-correlation of hybrid functionals in DFT 13
1.3.8 THEORY: Exchange-correlation PBE0 functional in DFT 13
1.3.9 THEORY: Exchange-correlation HSE06 functional in DFT 14
2.2.1 METHODOLOGY: The parabolic effective mass 20
2.2.2 METHODOLOGY: The Kramers-Kronig relationship for the real part of the dielectric function 20

2.2.3 METHODOLOGY:The complex refractive index 20
2.2.4 METHODOLOGY:The absorption coefficient, α 20
2.3.1 METHODOLOGY: The enthalpy of formation for a neutral defect ($q = 0$) . . . 22
2.3.2 METHODOLOGY: The enthalpy of formation for a charged defect ($q \neq 0$) . . . 23
2.3.3 METHODOLOGY: The Madelung energy for the image charge correction . . . 25
2.3.4 METHODOLOGY:The Makov and Payne image charge correction 25
2.3.5 METHODOLOGY: The second radial moment, Q, of the Makov and Payne image charge correction 25
2.3.6 METHODOLOGY: The Lany and Zunger image charge correction formalism. 25
2.3.7 METHODOLOGY: The approximate reduction of the Lany and Zunger image charge correction 26
2.3.8 METHODOLOGY: The band filling correction for a donor defect 26
2.3.9 METHODOLOGY: The band filling correction for an acceptor defect 26
2.3.10 METHODOLOGY: The enthalpy of formation of TiO_2 27
2.3.11 METHODOLOGY: The enthalpy of formation of Ti_2O_3 27
2.3.12 METHODOLOGY: The chemical potentials of TiO_2 under *Ti-rich/O-poor* conditions 27
2.3.13 METHODOLOGY: The chemical potentials of TiO_2 under *Ti-poor/O-rich* conditions 27
2.3.14 METHODOLOGY: The enthalpy of formation of NbO 27
2.3.15 METHODOLOGY: The enthalpy of formation of NbO_2 27
2.3.16 METHODOLOGY: The enthalpy of formation of Nb_2O_5 27
2.3.17 METHODOLOGY: The Nb chemical potentials in Nb-doped TiO_2 28
2.3.18 METHODOLOGY: The dependence of μ_O on $O_{2(g)}$ partial pressure and temperature 29
2.3.19 METHODOLOGY: The dependence of μ_O on varying $O_{2(g)}$ partial pressure at a fixed temperature 29
2.4.1 METHODOLOGY: Thermodynamic transition levels 31
2.4.2 METHODOLOGY: The Beer-Lambert equation 33
2.4.3 METHODOLOGY: The optical defect transitions relating to a defect in charge state 'q' 34
3.2.1 *n*-TYPE INTRO.: Moss-Burstein Shift 45

3.2.2 *n*-TYPE INTRO.: The combined hole-electron effective masses for the Moss-Burstein Shift . . . 45
3.2.3 *n*-TYPE INTRO.: The optical band gap due to a Moss-Burstein shift . . . 46
3.2.4 *n*-TYPE INTRO.: The plasmon frequency . . . 47
3.2.5 *n*-TYPE INTRO.:Conductivity, mobility and carrier concentration relation . . . 47
3.2.6 *n*-TYPE INTRO.: The activation energy of a polaron . . . 51
3.2.7 *n*-TYPE INTRO.: The Mott criterion . . . 52
3.2.8 *n*-TYPE INTRO.: The effective Bohr radius (a_0^*) . . . 52
4.3.1 SnO_2: The binding energy of [Sb_{Sn}+V_O] . . . 68
4.5.1 SnO_2: The formation of $Nb(Ta)_{Sn}$ in the presence of V_O . . . 81
4.5.2 SnO_2: The formation of V_O in the presence of $Nb(Ta)_{Sn}$ . . . 81
6.1.1 [Cu_2S_2][$A_3B_2O_5$]: SrSc decomposition pathway . . . 99
6.1.2 [Cu_2S_2][$A_3B_2O_5$]:Experimental synthesis route . . . 100
7.1.1 PHOTOCATALYSIS INTRO: The oxidation half equation of $H_2O_{(l)}$ . . . 136
7.1.2 PHOTOCATALYSIS INTRO: The reduction half equation of $H_2O_{(l)}$ . . . 136
8.2.1 TiO_2: The binding energy of [$Nb(Ta)_{Ti}$+N_O] . . . 157
8.2.2 TiO_2: The binding energy of [$3Nb(Ta)_{Ti}$+N_i] . . . 158
8.3.1 TiO_2: Boron doped TiO_2 core level shifts . . . 164
B.1.1 APPENDIX B:Enthalpy of formation of each SCSOS compound relative to their constituent elements . . . 192

List of Figures

2.1 METHODOLOGY: Primitive cell, unit cell and supercell schematic 16
2.2 METHODOLOGY: Depiction of a pseudopotential 17
2.3 METHODOLOGY: The first Brillouin zone, band structure and DOS of wurtzite ZnO 19
2.4 METHODOLOGY: The post processing corrections used in calculating the enthalpy of formation of a defect 24
2.5 METHODOLOGY: The evolution of phases that limit μ_{Nb} in TiO_2 28
2.6 METHODOLOGY: Example defect thermodynamic transition level diagrams . 32
2.7 METHODOLOGY:Example configurational coordinate diagrams for optical defect transition levels 36
3.1 *n*-TYPE INTRO.:The cost versus abundance of indium and tin 41
3.2 *n*-TYPE INTRO.: The common applications of TCOs 43
3.3 *n*-TYPE INTRO.: The comparison between fundamental and optical band gap 45
3.4 *n*-TYPE INTRO.: A schematic showing the Moss-Burstein shift 46
3.5 *n*-TYPE INTRO.: The calculated band structures of In_2O_3, SnO_2, ZnO, $BaSnO_3$ 49
3.6 *n*-TYPE INTRO.:The simplified molecular orbital diagrams for In_2O_3, SnO_2, ZnO, $BaSnO_3$ 50
3.7 *n*-TYPE INTRO.: Resonant, shallow and deep defects 51
4.1 SnO_2: The structure of rutile SnO_2 56
4.2 SnO_2: The bulk DOS and band structure of SnO_2 57
4.3 SnO_2: The thermodynamic transition levels for V_O and V_{Sn} 58
4.4 SnO_2: The partial charge densities for V_O and V_{Sn} 59
4.5 SnO_2: The thermodynamic transition levels for F-doped SnO_2 61
4.6 SnO_2: The partial charge densities for F_O^{1+} and F_i^{1-} 63
4.7 SnO_2:The experimental hall mobility vs carrier concentration and optical absorption data of F-doped SnO_2 64

4.8 SnO_2: The thermodynamic transition level diagrams for Sb-doped SnO_2 . . 66
4.9 SnO_2: The partial charge densities for Sb^{0}_{Sn} and Sb^{1-}_{Sn} 67
4.10 SnO_2: The partial charge densities for (Sb_{Sn}+V_O) 69
4.11 SnO_2: The thermodynamic transition level diagrams for P-doped SnO_2 . . . 71
4.12 SnO_2: The partial electron charge densities for P^{1-}_{Sn}, P^{0}_{O} and P^{1-}_{O} 73
4.13 SnO_2: The partial charge densities for P^{3+}_{i} and P^{3-}_{i} 74
4.14 SnO_2: The partial charge densities for (P_{Sn}+V_O) 75
4.15 SnO_2: The thermodynamic transition levels for Nb and Ta-doped SnO_2 . . . 77
4.16 SnO_2: The partial charge densities for Nb^{0}_{Sn} and $Ta^{0\text{ or }1-}_{Sn}$ 79
4.17 SnO_2: The partial charge densities for ($Nb(Ta)_{Sn}$ + V_O) 82
4.18 SnO_2: The unfolded band structures for Nb^{0}_{Sn} 83
4.19 SnO_2: The unfolded band structures for Ta^{0}_{Sn} 84
5.1 *p*-TYPE INTRO: The upper valence band of In_2O_3 92
5.2 *p*-TYPE INTRO: The crystal structures of Cu_2O, Al_2O_3 and $CuAlO_2$ 93
5.3 *p*-TYPE INTRO: The crystal structures of LaCuOCh (Ch = S, Se, Te) 96
6.1 $[Cu_2S_2][A_3B_2O_5]$: The $[Cu_2S_2][Sr_3Sc_2O_5]$ crystal structure 99
6.2 $[Cu_2S_2][A_3B_2O_5]$: The stable and metastable SCSOS compounds within 0–0.02 eV atom^{-1} 100
6.3 $[Cu_2S_2][A_3B_2O_5]$: The bond lengths and angles relating to the valence band 104
6.4 $[Cu_2S_2][A_3B_2O_5]$: Representative DOS for each different B^{3+} group: SrAl, SrGa and SrSc 109
6.5 $[Cu_2S_2][A_3B_2O_5]$: The combined band structures for the stable SCSOS compounds 110
6.6 $[Cu_2S_2][A_3B_2O_5]$: The comparison between a and the direct fundamental band gap and the hole effect mass 112
6.7 CaCuP: The structures of MgCuP (*Pnma*) and CaCuP ($P6_3/mmc$) 119
6.8 CaCuP: The band structure and DOS for MgCuP 121
6.9 CaCuP: The band structures for CaCuP, SrCuP and BaCuP 122
6.10 CaCuP: The DOS for CaCuP, SrCuP and BaCuP 123
6.11 CaCuP: The experimental optical spectra and calculated optical absorption using PBE0 for CaCuP 127
7.1 PHOTOCATALYSIS INTRO: The anatase, rutile and brookite structures 135

7.2 PHOTOCATALYSIS INTRO: The AM1.5 solar spectrum and ideal photocatalyst band structure . . . 137
7.3 PHOTOCATALYSIS INTRO: The band alignment of anatase, rutile and brookite 138
7.4 PHOTOCATALYSIS INTRO: The band structures of anatase, rutile and brookite 139
7.5 PHOTOCATALYSIS INTRO: A schematic of passivated codoping . . . 143
8.1 TiO_2: The DOS and band structure for anatase TiO_2 . . . 146
8.2 TiO_2: The transition levels for V_O and V_{Ti} . . . 147
8.3 TiO_2: The partial charge densities for V_O and V_{Ti} . . . 149
8.4 TiO_2: The configurational coordinate diagrams for V_O and V_{Ti} . . . 152
8.5 TiO_2: The thermodynamic transition levels for Nb and Ta-doped anatase TiO_2 154
8.6 TiO_2: The partial charge densities for N_O,$(NO)_O$ and $Nb(Ta)_{Ti}$ . . . 156
8.7 TiO_2: The partial charge densities for ($Nb(Ta)_{Ti}$+N_O) and ($3Nb(Ta)_{Ti}$+$(NO)_O$) 158
8.8 TiO_2: The thermodynamic transition level diagrams for B-doped anatase TiO_2 161
8.9 TiO_2: The partial charge densities for B_i, B_{Ti} and B_O . . . 164
8.10 TiO_2: The thermodynamic transition levels for Cu-doped anatase TiO_2 . . . 167
8.11 TiO_2: The partial charge densities for Cu_{Ti} and Cu_i . . . 169
8.12 TiO_2: The configurational coordinate diagrams for Cu_{Ti} and Cu_i . . . 171
A.1 APPENDIX A: The chemical potential limits as calculated for each Nb and Sb-related phase within SnO_2 . . . 184
B.1 APPENDIX B: The DOS for all stable SCSOS compounds . . . 202
B.2 APPENDIX B: The first Brillouin zone and structure of SCSOS . . . 203
B.3 APPENDIX B: The calculated optical absorption for each stable SCSOS compound . . . 204
B.4 APPENDIX B: The XRD and optical absorption spectra of $[Cu_2S_2][Ba_3Sc_2O_5]$ 205
B.5 APPENDIX B: The XRD of CaCuP . . . 208
B.6 APPENDIX B:The XPS of CaCuP together with experimental and simulated VB-XPS of CaCuP . . . 210
B.7 APPENDIX B: The diffuse reflectance optical spectra of CaCuP and the calculated optical absorption spectrum using PBE0 . . . 212
C.1 APPENDIX C: The chemical potential limits for N, Nb, B and Cu in anatase TiO_2 216

List of Tables

2.1 METHODOLOGY: Oxygen chemical potentials at varying temperatures (500K–1200K) and fixed pressure (1 atm) . . . 29

2.2 METHODOLOGY: Oxygen chemical potentials at varying oxygen partial pressures (0.001–1000 atm) and fixed temperature (900K) . . . 30

3.1 *n*-TYPE INTRO: The average effective electron and hole masses for In_2O_3, SnO_2, ZnO and $BaSnO_3$ . . . 48

4.1 SnO_2:Calculated structural and electronic properties of SnO_2 . . . 55

6.1 $[Cu_2S_2][A_3B_2O_5]$: Enthalpies of formation calculated from synthesis . . . 101

6.2 $[Cu_2S_2][A_3B_2O_5]$:Structural parameters and bond lengths for all stable SCOS compounds . . . 105

6.3 $[Cu_2S_2][A_3B_2O_5]$: The percentage of states at the VBM for each stable SCSOS compound . . . 107

6.4 $[Cu_2S_2][A_3B_2O_5]$: The percentage of states at the CBM for each stable SCSOS compound . . . 108

6.5 $[Cu_2S_2][A_3B_2O_5]$:The fundamental and optical band gaps and effective masses . . . 114

6.6 $[Cu_2S_2][A_3B_2O_5]$:The experimentally derived structural parameters and optical band gap of $Cu_2S_2Ba_3Sc_2O_5$ . . . 115

6.7 CaCuP: Calculated structural parameters for M^{2+}CuP (M^{2+} = Mg,Ca,Sr,Ba) . 120

6.8 The effective masses of electrons at the CBM and holes at the VBM. The values in *italics* correspond to light hole effective masses. . . . 123

6.9 CaCuP: The percentage of states at the VBM and CBM . . . 123

8.1 TiO_2: Calculated structural parameters for bulk anatase TiO_2 . . . 145

A.1 APPENDIX A The calculation parameters for In_2O_3, SnO_2, ZnO and $BaSnO_3$. 181

A.2 APPENDIX A The competing phases related to the different dopants (F, Sb, P, Nb, Ta) . . . 184

B.1 APPENDIX B: The calculated energies above hull, decomposition products and formation enthalpies of the SCSOS compounds 193
B.2 APPENDIX B: The elemental reference energies for the SCSOS compounds . 194
B.3 APPENDIX B: The formation energies of all SCSOS compounds relative to the elemental reference energies 195
B.4 APPENDIX B: The formation energies of each competing phase 196
C.1 APPENDIX C: The competing phases related to the different dopants (N, Nb, Ta, B, Cu) in TiO_2 215

Acknowledgement of Resources and Figures

Section Text, Figures and Tables:

CHAPTER 3 SECTION 3.2.1:

Figure 3.3 and Figure 3.4 were adapted with permission from Mr A. M. Ganose.

CHAPTER 4 SECTION 4.2:

Figure 4.7 was reproduced with permission from ref. [275] by Mr J.E.N Swallow et al.

CHAPTER 6 SECTION 6.1.4:

Table 6.6 was compiled with data obtained from Mr Greg J. Limburn et al.

CHAPTER 6 SECTION 6.2:

Figure 6.11 and subsequent analysis was reused from ref. [54] with permission from Dr R. G. Palgrave et al.

APPENDIX A:

Section A.3 was reproduced and adapted with permission from ref. [275] by Mr J.E.N Swallow et al.

APPENDIX B:

Section B.1.2 and Sections B.1.5 and B.1.6 together with Figure B.4 was obtained and reproduced with permission from Mr Greg J. Limburn et al.

APPENDIX B:

Section B.2.2 and Sections B.2.3 and B.2.4 together with Figures B.5, B.6 and B.7 were reproduced and adapted with permission from ref. [54] with permission from Dr R. G. Palgrave et al.

BACKPAGE:

The periodic table was adapted with permission from Mr A. M. Ganose.

Computing Resources:

Work in this thesis made use of the ARCHER UK National Supercomputing Service (http://www.archer.ac.uk) via membership of the UK's HEX Materials Chemistry Consortium, funded by EPSRC (EP/L00202).

The Legion (Legion@UCL) and Grace (Grace@UCL) High Performance Computing Facility located at University College London.

Analysis and Figure Production:

Creation of DOS, band structures and optical absorption figures were created using the in-house code: vaspy (https://github.com/SMTG-UCL/vaspy) written and updated by Mr A. M. Ganose.

The software used for plotting graphs were;

XMGrace (http://plasma-gate.weizmann.ac.il/Grace/) and Matplotlib (https://matplotlib.org/)

Adobe Illustrator (http://adobe.com/uk/illustrator) was used to create schematic diagrams and edit plots where necessary.

This thesis was typeset using LaTeX.

Bibliography

[1] Fock, V. *Zeitschrift für Physik* **1930**, *62*, 795–805.

[2] Hartree, D. R. *Mathematical Proceedings of the Cambridge Philosophical Society* **1928**, *24*, 426.

[3] Slater, J. C. *Physical Review* **1929**, *34*, 1293–1322.

[4] Löwdin, P.-O. *Physical Review* **1955**, *97*, 1474–1489.

[5] Thomas, L. H. *Mathematical Proceedings of the Cambridge Philosophical Society* **1927**, *23*, 542.

[6] Dirac, P. A. M. *Mathematical Proceedings of the Cambridge Philosophical Society* **1930**, *26*, 376.

[7] Fermi, E. *Zeitschrift für Physik* **1928**, *48*, 73–79.

[8] Teller, E. *Review of Modern Physics* **1962**, *34*, 627–631.

[9] Hohenberg, P. Kohn, W. *Physical Review B* **1964**, *136*, 864–871.

[10] Kohn, W.; Sham, L. J. *Physical Review* **1965**, *140*, A1133–A1138.

[11] Ceperley, D. M.; Alder, B. J. *Physical Review Letters* **1980**, *45*, 566–569.

[12] Burke, K. *The Journal of Chemical Physics* **2012**, *136*, 150901.

[13] Lee, C.; Yang, W.; Parr, R. G. *Physical Review B* **1988**, *37*, 785–789.

[14] Perdew, J. P.; Burke, K.; Ernzerhof, M. *Physical Review Letters* **1996**, *77*, 3865–3868.

[15] Perdew, J. P.; Wang, Y. *Physical Review B* **1992**, *45*, 13244–13249.

[16] Perdew, J. P.; Ruzsinszky, A.; Csonka, G. I.; Vydrov, O. A.; Scuseria, G. E.; Constantin, L. A.; Zhou, X.; Burke, K. *Physical Review Letters* **2008**, *100*, 136406.

[17] Anisimov, V. I.; Zaanen, J.; Andersen, O. K. *Physical Review B* **1991**, *44*, 943 –954.

[18] Anisimov, V. I.; Solovyev, I. V.; Korotin, M. A.; Czyżyk, M. T.; Sawatzky, G. A. *Physical Review B* **1993**, *48*, 16929–16934.

[19] Dudarev, S. L.; Botton, G. A.; Savrasov, S. Y.; Humphreys, C. J.; Sutton, A. P. *Physical Review B* **1998**, *57*, 1505–1509.

[20] Löwdin, P.-O. *Physical Review* **1955**, *97*, 1509–1520.

[21] Li, S. F.; Lu, H.; Li, P.; Yang, Z.; Guo, Z. X. *The Journal of Chemical Physics* **2008**, *128*, 164718.

[22] Perdew, J. P.; Ernzerhof, M.; Burke, K. *The Journal of Chemical Physics* **1996**, *105*, 9982–9985.

[23] Adamo, C.; Barone, V. *Journal or Chemical Physics* **1999**, *110*, 6158.

[24] Ganose, A. M.; Scanlon, D. O. *Journal of Materials Chemistry C* **2016**, *4*, 1467–1475.

[25] Scanlon, D. O.; Watson, G. W. *Journal of Materials Chemistry* **2012**, *22*, 25236.

[26] Scanlon, D. O. *Physical Review B* **2013**, *87*, 161201.

[27] Sallis, S.; Scanlon, D. O.; Chae, S. C.; Quackenbush, N. F.; Fischer, D. A.; Woicik, J. C.; Guo, J.-H.; Cheong, S. W.; Piper, L. F. J. *Applied Physics Letters* **2013**, *103*, 042105.

[28] Ágoston, P.; Körber, C.; Klein, A.; Puska, M. J.; Nieminen, R. M.; Albe, K. *Journal of Applied Physics* **2010**, *108*, 053511.

[29] 'Agoston, P.; Albe, K.; Nieminen, R. M.; Puska, M. J. *Physical Review Letters* **2009**, *103*, 245501.

[30] Paier, J.; Marsman, M.; Hummer, K.; Kresse, G.; Gerber, I. C.; Ángyán, J. G. *The Journal of Chemical Physics* **2006**, *124*, 154709.

[31] Heyd, J.; Scuseria, G. E.; Ernzerhof, M. *The Journal of Chemical Physics* **2003**, *118*, 8207–8215.

[32] Heyd, J.; Scuseria, G. E.; Ernzerhof, M. *The Journal of Chemical Physics* **2006**, *124*, 219906.

[33] Bhachu, D. S.; Sathasivam, S.; Sankar, G.; Scanlon, D. O.; Cibin, G.; Carmalt, C. J.; Parkin, I. P.; Watson, G. W.; Bawaked, S. M.; Obaid, A. Y.; Al-Thabaiti, S.; Basahel, S. N. *Advanced Functional Materials* **2014**, *24*, 5075–5085.

[34] Scanlon, D. O.; Dunnill, C. W.; Buckeridge, J.; Shevlin, S. a.; Logsdail, A. J.; Woodley, S. M.; Catlow, C. R. a.; Powell, M. J.; Palgrave, R. G.; Parkin, I. P.; Watson, G. W.; Keal, T. W.; Sherwood, P.; Walsh, A.; Sokol, A. a. *Nature Materials* **2013**, *12*, 798–801.

[35] Buckeridge, J.; Butler, K. T.; Catlow, C. R. A.; Logsdail, A. J.; Scanlon, D. O.; Shevlin, S. A.; Woodley, S. M.; Sokol, A. A.; Walsh, A. *Chemistry of Materials* **2015**, *27*, 3844–3851.

[36] Çelik, V.; Mete, E. *Physical Review B* **2012**, *86*, 205112.

[37] Huy, H. A.; Aradi, B.; Frauenheim, T.; Deák, P. *Physical Review B* **2011**, *83*, 155201.

[38] Varley, J. B.; Janotti, A.; de Walle, C. G. V. *Physical Review B* **2010**, *81*, 245216.

[39] Matsubara, M.; Saniz, R.; Partoens, B.; Lamoen, D. *Physical Chemistry Chemical Physics* **2017**, *19*, 1945–1952.

[40] Boonchun, A.; Reunchan, P.; Umezawa, N. *Physical Chemistry Chemical Physics* **2016**, *18*, 30040–30046.

[41] Wimmer, E.; Freeman, A. J.; Weinert, M. *Physical Review Letters* **1982**, *48*, 1128–1131.

[42] Bloch, F. *Zeitschrift für Physik* **1929**, *52*, 555–600.

[43] King-Smith, R. D.; Vanderbilt, D. *Physical Review B* **1993**, *47*, 1651–1654.

[44] Blochl, P. *Physical Review B* **1994**, *50*, 17953–17979.

[45] Feynman, R. P. *Physical Review* **1939**, *56*, 340–343.

[46] *Hans Hellmann: Einführung in die Quantenchemie*; Springer Berlin Heidelberg, 2015.

[47] Pulay, P. *Molecular Physics* **2002**, *100*, 57–62.

[48] Yeh, J.; Lindau, I. *Atomic Data and Nuclear Data Tables* **1985**, *32*, 1–155.

[49] Scofield, J. H. *Lawrence Livermore Laboratory* **1973**,

[50] Savory, C. N.; Ganose, A. M.; Travis, W.; Atri, R. S.; Palgrave, R. G.; Scanlon, D. O. *Journal of Materials Chemistry A* **2016**, *4*, 12648–12657.

[51] Bhachu, D. S.; Moniz, S. J. A.; Sathasivam, S.; Scanlon, D. O.; Walsh, A.; Bawaked, S. M.; Mokhtar, M.; Obaid, A. Y.; Parkin, I. P.; Tang, J.; Carmalt, C. J. *Chemical Science* **2016**, *7*, 4832–4841.

[52] Körber, C.; Krishnakumar, V.; Klein, A.; Panaccione, G.; Torelli, P.; Walsh, A.; Da Silva, J. L. F.; Wei, S.-H.; Egdell, R. G.; Payne, D. J. *Physical Review B* **2010**, *81*, 165207.

[53] Sathasivam, S.; Williamson, B. A. D.; Kafizas, A.; Althabaiti, S. A.; Obaid, A. Y.; Basahel, S. N.; Scanlon, D. O.; Carmalt, C. J.; Parkin, I. P. *The Journal of Physical Chemistry C* **2017**, *121*, 202–210.

[54] Williamson, B. A. D.; Buckeridge, J.; Brown, J.; Ansbro, S.; Palgrave, R. G.; Scanlon, D. O. *Chemistry of Materials* **2016**, *29*, 2402–2413.

[55] Sathasivam, S.; Arnepalli, R. R.; Bhachu, D. S.; Lu, Y.; Buckeridge, J.; Scanlon, D. O.; Kumar, B.; Singh, K. K.; Visser, R. J.; Blackman, C. S.; Carmalt, C. J. *Journal of Physical Chemistry C* **2016**, *120*, 7013–7019.

[56] Bradley, C. J. *The Mathematical Theory of Symmetry in Solids: Representation Theory for Point Groups and Space Groups*; Oxford University Press, 2010.

[57] Gibbs, Z. M.; Ricci, F.; Li, G.; Zhu, H.; Persson, K.; Ceder, G.; Hautier, G.; Jain, A.; Snyder, G. J. *npj Computational Materials* **2017**, *3*.

[58] Gajdoš, M.; Hummer, K.; Kresse, G.; Furthmüller, J.; Bechstedt, F. *Physical Review B* **2006**, *73*, 045112.

[59] Yu, P. Y.; Cardona, M. *Fundamentals of Semiconductors*; Springer Berlin Heidelberg, 2010.

[60] Ramos, L. E.; Paier, J.; Kresse, G.; Bechstedt, F. *Physical Review B* **2008**, *78*, 195423.

[61] Paier, J.; Marsman, M.; Kresse, G. *Physical Review B* **2008**, *78*, 121201.

[62] R W Grimes, C. R. A. C.; Stoneham, A. M. *Journal of Physics, Condensed Matter* **1989**, *1*, 7367.

[63] Mott, N. F.; Littleton, M. J. *Transactions of the Faraday Society* **1938**, *34*, 485.

[64] Logsdail, A. J.; Downing, C. A.; Keal, T. W.; Sherwood, P.; Sokol, A. A.; Catlow, C. R. A. *Physical Chemistry Chemical Physics* **2016**, *18*, 28648–28660.

[65] Xie, Z.; Sui, Y.; Buckeridge, J.; Catlow, C. R. A.; Keal, T. W.; Sherwood, P.; Walsh, A.; Scanlon, D. O.; Woodley, S. M.; Sokol, A. A. *physica status solidi (a)* **2016**, *214*, 1600445.

[66] Walsh, A.; Buckeridge, J.; Catlow, C. R. a.; Jackson, A. J.; Keal, T. W.; Miskufova, M.; Sherwood, P.; Shevlin, S. a.; Watkins, M. B.; Woodley, S. M.; Sokol, A. a. *Chemistry of Materials* **2013**, *25*, 2924–2926.

[67] Buckeridge, J.; Catlow, C. R. A.; Scanlon, D. O.; Keal, T. W.; Sherwood, P.; Miskufova, M.; Walsh, A.; Woodley, S. M.; Sokol, A. A. *Physical Review Letters* **2015**, *114*, 016405.

[68] Needs, R. J. *Topics in Applied Physics*; Springer Berlin Heidelberg, pp 141–164.

[69] Foulkes, W. M. C.; Mitas, L.; Needs, R. J.; Rajagopal, G. *Reviews of Modern Physics* **2001**, *73*, 33–83.

[70] Parker, W. D.; Wilkins, J. W.; Hennig, R. G. *physica status solidi (b)* **2010**, *248*, 267–274.

[71] Nieminen, R. M. *Modelling and Simulation in Materials Science and Engineering* **2009**, *17*, 084001.

[72] Hine, N. D. M.; Frensch, K.; Foulkes, W. M. C.; Finnis, M. W. *Physical Review B* **2009**, *79*, 024112.

[73] Komsa, H.-P.; Rantala, T. T.; Pasquarello, A. *Physical Review B* **2012**, *86*, 045112.

[74] Van De Walle, C. G.; Neugebauer, J. *Journal of Applied Physics* **2004**, *95*, 3851–3879.

[75] Janak, J. F. *Physical Review B* **1978**, *18*, 7165–7168.

[76] Freysoldt, C.; Grabowski, B.; Hickel, T.; Neugebauer, J.; Kresse, G.; Janotti, A.; de Walle, C. G. V. *Reviews of Modern Physics* **2014**, *86*, 253–305.

[77] Lany, S.; Zunger, A. *Physical Review B* **2008**, *78*, 235104.

[78] Murphy, S. T.; Hine, N. D. M. *Physical Review B* **2013**, *87*, 094111.

[79] Freysoldt, C.; Neugebauer, J.; de Walle, C. G. V. *Physical Review Letters* **2009**, *102*, 016402.

[80] Leslie, M.; Gillan, N. J. *Journal of Physics C: Solid State Physics* **1985**, *18*, 973–982.

[81] Makov, G.; Payne, M. C. *Physical Review B* **1995**, *51*, 4014–4022.

[82] Kumagai, Y.; Oba, F. *Physical Review B* **2014**, *89*, 195205.

[83] Lany, S.; Zunger, A. *Modelling and Simulation in Materials Science and Engineering* **2009**, *17*, 084002.

[84] Persson, C.; Zhao, Y.-J.; Lany, S.; Zunger, A. *Physical Review B* **2005**, *72*, 035211.

[85] Yin, W.-J.; Ma, J.; Wei, S.-H.; Al-Jassim, M. M.; Yan, Y. *Physical Review B* **2012**, *86*, 045211.

[86] Hellström, M.; Spångberg, D.; Hermansson, K.; Broqvist, P. *Journal of Chemical Theory and Computation* **2013**, *9*, 4673–4678.

[87] Reuter, K.; Scheffler, M. *Physical Review B* **2001**, *65*, 035406.

[88] Taylor, F. H.; Buckeridge, J.; Catlow, C. R. A. *Chemistry of Materials* **2016**, *28*, 8210–8220.

[89] Morgan, B. J.; Watson, G. W. *The Journal of Physical Chemistry C* **2010**, *114*, 2321–2328.

[90] Stull, D. R.; Prophet, H. *NSRDS-NBS (Book 37) ; National Bureau of Standards U.S: Washington, DC* **1971**,

[91] Pilkington NSG:. `https://www.pilkington.com/`.

[92] Drabold D.A., E. S. *Theory of Defects in Semiconductors*; Springer-Verlag GmbH, 2006.

[93] Watkins, G. D. *Advances in Solid State Physics*; Springer Berlin Heidelberg, pp 163–189.

[94] Lany, S.; Zunger, A. *Physical Review B* **2005**, *72*, 035215.

[95] Lyons, J. L.; Janotti, A.; de Walle, C. G. V. *Physical Review B* **2014**, *89*, 035204.

[96] Varley, J. B.; Janotti, A.; de Walle, C. G. V. *Advanced Materials* **2011**, *23*, 2343–2347.

[97] Weber, J. R.; Koehl, W. F.; Varley, J. B.; Janotti, A.; Buckley, B. B.; de Walle, C. G. V.; Awschalom, D. D. *Proceedings of the National Academy of Sciences* **2010**, *107*, 8513–8518.

[98] Johann Heinrich Lambert, E. A. *Liepzig* **1760**,

[99] Beer, *Annalen der Physik und Chemie* **1852**, *162*, 78–88.

[100] Alkauskas, A.; McCluskey, M. D.; de Walle, C. G. V. *Journal of Applied Physics* **2016**, *119*, 181101.

[101] Matthew D. McCluskey, E. E. H. *Dopants and Defects in Semiconductors*; CRC PR INC, 2012.

[102] Franck, J.; Dymond, E. G. *Transactions of the Faraday Society* **1926**, *21*, 536.

[103] Condon, E. *Physical Review* **1926**, *28*, 1182–1201.

[104] Alkauskas, A.; Buckley, B. B.; Awschalom, D. D.; de Walle, C. G. V. *New Journal of Physics* **2014**, *16*, 073026.

[105] Kresse, G.; Hafner, J. *Physical Review B* **1993**, *47*, 558–561.

[106] Kresse, G.; Hafner, J. *Physical Review B* **1994**, *49*, 14251–14269.

[107] Kresse, G.; Furthmüller, J. *Physical Review B* **1996**, *54*, 11169–11186.

[108] Kresse, G.; Furthmüller, J. *Computational Materials Science* **1996**, *6*, 15–50.

[109] Burbano, M.; Scanlon, D. O.; Watson, G. W. *Journal of the American Chemical Society* **2011**, *133*, 15065–15072.

[110] Kılıç, Ç.; Zunger, A. *Physical Review Letters* **2002**, *88*, 095501.

[111] Baedeker, K. *Annals of Physics* **1909**, *334*, 566–584.

[112] Wang, A.; Babcock, J. R.; Edleman, N. L.; Metz, A. W.; Lane, M. A.; Asahi, R.; Dravid, V. P.; Kannewurf, C. R.; Freeman, A. J.; Marks, T. J. *Proceedings of the National Academy of Sciences* **2001**, *98*, 7113–7116.

[113] Lany, S.; Zakutayev, A.; Mason, T. O.; Wager, J. F.; Poeppelmeier, K. R.; Perkins, J. D.; Berry, J. J.; Ginley, D. S.; Zunger, A. *Physical Review Letters* **2012**, *108*, 016802.

[114] Gordon, R. G. *MRS Bulletin* **2000**, *25*, 52–57.

[115] Dixon, S. C.; Scanlon, D. O.; Carmalt, C. J.; Parkin, I. P. *Journal of Materials Chemistry C* **2016**, *4*, 6946–6961.

[116] Zhang, K. H. L.; Xi, K.; Blamire, M. G.; Egdell, R. G. *Journal of Physics: Condensed Matter* **2016**, *28*, 383002.

[117] Minami, T. *Semiconductor Science and Technology* **2005**, *20*, S35–S44.

[118] Hada, T.; Wasa, K.; Hayakawa, S. *Thin Solid Films* **1971**, *7*, 135–145.

[119] Luo, X.; Oh, Y. S.; Sirenko, A.; Gao, P.; Tyson, T. A.; Char, K.; Cheong, S.-W. *Applied Physics Letters* **2012**, *100*, 172112.

[120] Kim, H. J.; Kim, U.; Kim, H. M.; Kim, T. H.; Mun, H. S.; Jeon, B.-G.; Hong, K. T.; Lee, W.-J.; Ju, C.; Kim, K. H.; Char, K. *Applied Physics Express* **2012**, *5*, 061102.

[121] Granqvist, C.; Hultåker, A. *Thin Solid Films* **2002**, *411*, 1–5.

[122] Bhachu, D. S.; Scanlon, D. O.; Sankar, G.; Veal, T. D.; Egdell, R. G.; Cibin, G.; Dent, A. J.; Knapp, C. E.; Carmalt, C. J.; Parkin, I. P. *Chemistry of Materials* **2015**, *27*, 2788–2796.

[123] Moss, R.; Tzimas, E.; Kara, H.; Willis, P.; Kooroshy, J. *JRC-scientific and strategic reports, European Commission Joint Research Centre Institute for Energy and Transport* **2011**,

[124] The London Metal Exchange. `https://www.lme.com/en-gb/metals/`.

[125] Future Market Insights, Global Flat Panel Display Market: 2017–2027.

[126] www.sharp-world.com/igzo/.

[127] Potter, D. B.; Powell, M. J.; Parkin, I. P.; Carmalt, C. J. *Journal of Materials Chemistry C* **2018**,

[128] Ginley, D. S.; Bright, C. *MRS Bulletin* **2000**, *25*, 15–18.

[129] Advani, G.; Jordan, A. *Solar Energy* **1983**, *30*, 71–73.

[130] Peng, J.; Lu, L.; Yang, H. *Renewable and Sustainable Energy Reviews* **2013**, *19*, 255–274.

[131] Ganose, A. M.; Savory, C. N.; Scanlon, D. O. *Chemical Communications* **2017**, *53*, 20–44.

[132] Yang, W. S.; Park, B.-W.; Jung, E. H.; Jeon, N. J.; Kim, Y. C.; Lee, D. U.; Shin, S. S.; Seo, J.; Kim, E. K.; Noh, J. H.; Seok, S. I. *Science* **2017**, *356*, 1376–1379.

[133] Granqvist, C. G. *Solar Energy Materials and Solar Cells* **2007**, *91*, 1529–1598.

[134] Heo, Y. H.; You, D. J.; Lee, H.; Lee, S.; Lee, H.-M. *Solar Energy Materials and Solar Cells* **2014**, *122*, 107–111.

[135] Strano, V.; Smecca, E.; Depauw, V.; Trompoukis, C.; Alberti, A.; Reitano, R.; Crupi, I.; Gordon, I.; Mirabella, S. *Applied Physics Letters* **2015**, *106*, 013901.

[136] Kambe, M.; Takahashi, A.; Taneda, N.; Masumo, K.; Oyama, T.; Sato, K. Fabrication of A-Si:H Solar cells on high haze SnO_2:F thin films. 2008 33rd IEEE Photovolatic Specialists Conference. 2008.

[137] Walsh, A.; Ahn, K.-S.; Shet, S.; Huda, M. N.; Deutsch, T. G.; Wang, H.; Turner, J. a.; Wei, S.-H.; Yan, Y.; Al-Jassim, M. M. *Energy Environmental Science* **2009**, *2*, 774.

[138] Walsh, A.; Silva, J. L. F. D.; Wei, S.-H.; Körber, C.; Klein, A.; Piper, L. F. J.; DeMasi, A.; Smith, K. E.; Panaccione, G.; Torelli, P.; Payne, D. J.; Bourlange, A.; Egdell, R. G. *Physical Review Letters* **2008**, *100*, 167402.

[139] Hamberg, I.; Granqvist, C. G.; Berggren, K. F.; Sernelius, B. E.; Engström, L. *Physical Review B* **1984**, *30*, 3240–3249.

[140] Köstlin, H.; Jost, R.; Lems, W. *Physica Status Solidi (a)* **1975**, *29*, 87–93.

[141] Sathasivam, S.; Williamson, B. A. D.; Althabaiti, S. A.; Obaid, A. Y.; Basahel, S. N.; Mokhtar, M.; Scanlon, D. O.; Carmalt, C. J.; Parkin, I. P. *ACS Applied Materials & Interfaces* **2017**, *9*, 18031–18038.

[142] Koffyberg, F. P. *Physical Review B* **1976**, *13*, 4470–4476.

[143] Jefferson, P. H.; Hatfield, S. A.; Veal, T. D.; King, P. D. C.; McConville, C. F.; Zúñiga–Pérez, J.; Muñoz–Sanjosé, V. *Applied Physics Letters* **2008**, *92*, 022101.

[144] Farahani, S. K. V.; Veal, T. D.; King, P. D. C.; Zúñiga-Pérez, J.; Muñoz-Sanjosé, V.; McConville, C. F. *Journal of Applied Physics* **2011**, *109*, 073712.

[145] Speaks, D. T.; Mayer, M. A.; Yu, K. M.; Mao, S. S.; Haller, E. E.; Walukiewicz, W. *Journal of Applied Physics* **2010**, *107*, 113706.

[146] Piper, L.; Jefferson, P.; Veal, T.; McConville, C.; Zuñiga-Pérez, J.; Muñoz-Sanjosé, V. *Superlattices and Microstructures* **2007**, *42*, 197–200.

[147] Jin, S.; Yang, Y.; Medvedeva, J. E.; Ireland, J. R.; Metz, A. W.; Ni, J.; Kannewurf, C. R.; Freeman, A. J.; Marks, T. J. *Journal of the American Chemical Society* **2004**, *126*, 13787–13793.

[148] Piper, L. F. J.; Colakerol, L.; King, P. D. C.; Schleife, A.; Zúñiga Pérez, J.; Glans, P.-A.; Learmonth, T.; Federov, A.; Veal, T. D.; Fuchs, F.; Muñoz Sanjosé, V.; Bechstedt, F.; McConville, C. F.; Smith, K. E. *Physical Review B* **2008**, *78*, 165127.

[149] Moss, T. S. *Proceedings of the Physical Society: Section B* **1954**, *67*, 775–782.

[150] Burstein, E. *Physical Review* **1954**, *93*, 632–633.

[151] Walsh, A.; Kehoe, A. B.; Temple, D. J.; Watson, G. W.; Scanlon, D. O. *Chemical Communications* **2013**, *49*, 448–450.

[152] Ha, V.-A.; Waroquiers, D.; Rignanese, G.-M.; Hautier, G. *Applied Physics Letters* **2016**, *108*, 201902.

[153] Ginley, D. S., Ed. *Handbook of Transparent Conductors*; Springer Nature, 2011.

[154] Young, D. L.; Coutts, T. J.; Kaydanov, V. I.; Gilmore, A. S.; Mulligan, W. P. *Journal of Vacuum Science & Technology A: Vacuum, Surfaces, and Films* **2000**, *18*, 2978–2985.

[155] Walsh, A.; Silva, J. L. F. D.; Wei, S.-H. *Physical Review B* **2008**, *78*, 075211.

[156] Wei, S.-H.; Zunger, A. *Physical Review B* **1988**, *37*, 8958–8981.

[157] Raghavan, S.; Schumann, T.; Kim, H.; Zhang, J. Y.; Cain, T. A.; Stemmer, S. *APL Materials* **2016**, *4*, 016106.

[158] Oshima, M.; Yoshino, K. *Japanese Journal of Applied Physics* **2011**, *50*, 05FB15.

[159] Fan, J. C. C.; Bachner, F. J.; Foley, G. H. *Applied Physics Letters* **1977**, *31*, 773–775.

[160] Agura, H.; Suzuki, A.; Matsushita, T.; Aoki, T.; Okuda, M. *Thin Solid Films* **2003**, *445*, 263–267.

[161] Singh, A. K.; Janotti, A.; Scheffler, M.; de Walle, C. G. V. *Physical Review Letters* **2008**, *101*, 055502.

[162] Fonstad, C. G.; Rediker, R. H. *Journal of Applied Physics* **1971**, *42*, 2911–2918.

[163] Nagasawa, M.; Shionoya, S. *Japanese Journal of Applied Physics* **1971**, *10*, 727–731.

[164] Samson, S.; Fonstad, C. G. *Journal of Applied Physics* **1973**, *44*, 4618–4621.

[165] Jarzebski, Z. M. *Journal of The Electrochemical Society* **1976**, *123*, 299C.

[166] de Walle, C. G. V. *Physical Review Letters* **2000**, *85*, 1012–1015.

[167] Janotti, A.; de Walle, C. G. V. *Applied Physics Letters* **2005**, *87*, 122102.

[168] Bjørheim, T. S.; Kotomin, E. *The Journal of Physical Chemistry Letters* **2014**, *5*, 4238–4242.

[169] Goyal, A.; Gorai, P.; Peng, H.; Lany, S.; Stevanovic, V.

[170] Liu, J.; Liu, T.; Liu, F.; Li, H. *RSC Advances* **2014**, *4*, 36983–36989.

[171] Noguchi, S.; Sakata, H. *Journal of Physics D: Applied Physics* **1980**, *13*, 1129–1133.

[172] Batzill, M.; Diebold, U. *Progress in Surface Science* **2005**, *79*, 47–154.

[173] Kılıç, Ç.; Zunger, A. *Applied Physics Letters* **2002**, *81*, 73–75.

[174] Li, H.; Robertson, J. *Journal of Applied Physics* **2014**, *115*, 203708.

[175] Meléndez, J. J.; Wierzbowska, M. *The Journal of Physical Chemistry C* **2016**, *120*, 4007–4015.

[176] King, P. D. C.; Lichti, R. L.; Celebi, Y. G.; Gil, J. M.; Vilão, R. C.; Alberto, H. V.; Duarte, J. P.; Payne, D. J.; Egdell, R. G.; McKenzie, I.; McConville, C. F.; Cox, S. F. J.; Veal, T. D. *Physical Review B* **2009**, *80*, 081201.

[177] Eschrig, H. *Crystal Research and Technology* **1991**, *26*, 788–788.

[178] Azo Materials: www.azom.com.

[179] Gordon, R. *Journal of Non-Crystalline Solids* **1997**, *218*, 81–91.

[180] Thangaraju, B. *Thin Solid Films* **2002**, *402*, 71–78.

[181] Baek, W.-H.; Choi, M.; Yoon, T.-S.; Lee, H. H.; Kim, Y.-S. *Applied Physics Letters* **2010**, *96*, 133506.

[182] Parkin, I. P.; Manning, T. D. *Journal of Chemical Education* **2006**, *83*, 393.

[183] Snaith, H. J.; Ducati, C. *Nano Letters* **2010**, *10*, 1259–1265.

[184] Tiwari, A. N.; Khrypunov, G.; Kurdzesau, F.; Bätzner, D. L.; Romeo, A.; Zogg, H. *Progress in Photovoltaics: Research and Applications* **2004**, *12*, 33–38.

[185] Lewis, B. G.; Paine, D. C. *MRS Bulletin* **2000**, *25*, 22–27.

[186] Das, S.; Jayaraman, V. *Progress in Materials Science* **2014**, *66*, 112–255.

[187] Wang, Y.; Jiang, X.; Xia, Y. *Journal of the American Chemical Society* **2003**, *125*, 16176–16177.

[188] Sheel, D.; Yates, H.; Evans, P.; Dagkaldiran, U.; Gordijn, a.; Finger, F.; Remes, Z.; Vanecek, M. *Thin Solid Films* **2009**, *517*, 3061–3065.

[189] Aliyu, M. M.; Hossain, S.; Husna, J.; Dhar, N.; Huda, M. Q.; Sopian, K.; Amin, N. High quality indium tin oxide (ITO) film growth by controlling pressure in RF magnetron sputtering. 2012 38th IEEE Photovoltaic Specialists Conference. 2012.

[190] Suzuki, M.; Taga, Y. *Journal of Applied Physics* **2001**, *90*, 5599–5605.

[191] Deng, W.; Ohgi, T.; Nejo, H.; Fujita, D. *Applied Physics A Materials Science & Processing* **2001**, *72*, 595–601.

[192] Mason, M. G.; Hung, L. S.; Tang, C. W.; Lee, S. T.; Wong, K. W.; Wang, M. *Journal of Applied Physics* **1999**, *86*, 1688–1692.

[193] woo Lee, S.; Kim, Y.-W.; Chen, H. *Applied Physics Letters* **2001**, *78*, 350–352.

[194] Nakao, S.; Yamada, N.; Hitosugi, T.; Hirose, Y.; Shimada, T.; Hasegawa, T. *Applied Physics Express* **2010**, *3*, 031102.

[195] Noor, N.; Parkin, I. P. *Thin Solid Films* **2013**, *532*, 26–30.

[196] Rey, G.; Ternon, C.; Modreanu, M.; Mescot, X.; Consonni, V.; Bellet, D. *Journal of Applied Physics* **2013**, *114*, 183713.

[197] Isono, T.; Fukuda, T.; Nakagawa, K.; Usui, R.; Satoh, R.; Morinaga, E.; Mihara, Y. *SID Symposium Digest of Technical Papers* **2006**, *37*, 1874.

[198] Nguyen, T. B.; Le, T. T. B.; Nguyen, N. L. *Advances in Natural Sciences: Nanoscience and Nanotechnology* **2010**, *1*, 025002.

[199] Park, S.-M.; Ikegami, T.; Ebihara, K. *Thin Solid Films* **2006**, *513*, 90–94.

[200] Geoffroy, C.; Campet, G.; Menil, F.; Portier, J.; Salardenne, J.; Couturier, G. *Active and Passive Electronic Components* **1991**, *14*, 111–118.

[201] Bhachu, D. S.; Waugh, M. R.; Zeissler, K.; Branford, W. R.; Parkin, I. P. *Chemistry - A European Journal* **2011**, *17*, 11613–11621.

[202] Feng, H.; Zhuo, R.; Chen, J.; Yan, D.; Feng, J.; Li, H.; Cheng, S.; Yan, P. *Physica E: Low-dimensional Systems and Nanostructures* **2009**, *41*, 1640–1644.

[203] Bae, J. W.; Lee, S. W.; Yeom, G. Y. *Journal of The Electrochemical Society* **2007**, *154*, D34.

[204] Yusnidar, M. N.; Fauzia, V.; Handoko, D.; Hanum, L. *Journal of Physics: Conference Series* **2017**, *817*, 012031.

[205] Heiras-Trevizo, A.; Amézaga-Madrid, P.; Corral-Bustamante, L.; Antúnez-Flores, W.; Ruiz, P. P.; Miki-Yoshida, M. *Thin Solid Films* **2017**, *638*, 22–27.

[206] Sawada, Y.; Hashimoto, Y.; Hoshi, Y.; Uchida, T.; Kobayashi, S.; Sun, L.; Yue, B. *IOP Conference Series: Materials Science and Engineering* **2017**, *250*, 012021.

[207] Yu, S.; Zheng, H.; Li, L.; Chen, S. *Ceramics International* **2017**, *43*, 5654–5660.

[208] Kim, H.; Auyeung, R.; Piqué, a. *Thin Solid Films* **2008**, *516*, 5052–5056.

[209] Marcel, C.; Hegde, M.; Rougier, A.; Maugy, C.; Guéry, C.; Tarascon, J.-M. *Electrochimica Acta* **2001**, *46*, 2097–2104.

[210] Shen, Q.; Yang, P.; Li, N.; Li, M.; Chen, F.; Zhang, L. *Journal of Wuhan University of Technology-Mater. Sci. Ed.* **2016**, *31*, 20–26.

[211] Zhi, X.; Zhao, G.; Zhu, T.; Li, Y. *Surface and Interface Analysis* **2008**, *40*, 67–70.

[212] Bisht, H.; Eun, H.-T.; Mehrtens, A.; Aegerter, M. *Thin Solid Films* **1999**, *351*, 109–114.

[213] Zhang, B.; Tian, Y.; Zhang, J.; Cai, W. *Materials Letters* **2011**, *65*, 1204–1206.

[214] Acosta, D.; Zironi, E.; Montoya, E.; Estrada, W. *Thin Solid Films* **1996**, *288*, 1–7.

[215] Terrier, C.; Chatelon, J.; Roger, J. *Thin Solid Films* **1997**, *295*, 95–100.

[216] Terrier, C.; Chatelon, J.; Berjoan, R.; Roger, J. *Thin Solid Films* **1995**, *263*, 37–41.

[217] Han, C.-H.; Han, S.-D.; Gwak, J.; Khatkar, S. *Materials Letters* **2007**, *61*, 1701–1703.

[218] Banerjee, A.; Kundoo, S.; Saha, P.; Chattopadhyay, K. *Journal of Sol-Gel Science and Technology* **2003**, *28*, 105–110.

[219] Kurz, A.; Brakecha, K.; Puetz, J.; Aegerter, M. *Thin Solid Films* **2006**, *502*, 212–218.

[220] Rajpure, K.; Kusumade, M.; Neumann-Spallart, M. N.; Bhosale, C. *Materials Chemistry and Physics* **2000**, *64*, 184–188.

[221] Suffner, J.; Ágoston, P.; Kling, J.; Hahn, H. *Journal of Nanoparticle Research* **2010**, *12*, 2579–2588.

[222] Peng, H.; Perkins, J. D.; Lany, S. *Chemistry of Materials* **2014**, *26*, 4876–4881.

[223] Fantini, M.; Torriani, I. *Thin Solid Films* **1986**, *138*, 255–265.

[224] Canestraro, C. D.; Roman, L. S.; Persson, C. *Thin Solid Films* **2009**, *517*, 6301–6304.

[225] Canestraro, C. D.; Oliveira, M. M.; Valaski, R.; da Silva, M. V. S.; David, D. G. F.; Pepe, I.; Silva, a. F. D.; Roman, L. S.; Persson, C. *Applied Surface Science* **2008**, *255*, 1874–1879.

[226] Elangovan, E.; Ramamurthi, K. *Applied Surface Science* **2005**, *249*, 183–196.

[227] Agashe, C.; Major, S. S. *Journal of Materials Science* **1996**, *31*, 2965–2969.

[228] Berry, F. J.; Holbourn, P. E.; Woodhams, F. W. D. *Journal of the Chemical Society, Dalton Transactions* **1980**, 2241–2245.

[229] Berry, F. J.; Laundy, B. J. *Journal of the Chemical Society, Dalton Transactions* **1981**, 1442–1444.

[230] Gržeta, B.; Tkalčec, E.; Goebbert, C.; Takeda, M.; Takahashi, M.; Nomura, K.; Jakšić, M. *Journal of Physics and Chemistry of Solids* **2002**, *63*, 765–772.

[231] Terrier, C.; Chatelon, J.; Roger, J.; Berjoan, R.; Dubois, C. *Journal of Sol-Gel Science and Technology* **1997**, *10*, 75–81.

[232] Montilla, F.; Morallon, E.; Battisti, A.; Barison, S.; Daolio, S.; Vazquez, J. *Journal of Physical Chemistry B* **2004**, *108*, 15976–15981.

[233] Egdell, R.; Flavell, W.; Tavener, P. *Journal of Solid State Chemistry* **1984**, *51*, 345–354.

[234] Rockenberger, J.; zum Felde, U.; Tischer, M.; Tröger, L.; Haase, M.; Weller, H. *The Journal of Chemical Physics* **2000**, *112*, 4296–4304.

[235] Geraldo, V.; Briois, V.; Scalvi, L.; Santilli, C. *Journal of the European Ceramic Society* **2007**, *27*, 4265–4268.

[236] Agashe, C.; Major, S. S. *Journal of Physics D: Applied Physics* **1996**, *29*, 2988–2991.

[237] Abass, A. *Solid State Communications* **1987**, *61*, 507–510.

[238] Abass, A. K.; Al-Liabi, N. A.; Taha, W. A. *Physica Status Solidi (a)* **1988**, *106*, 613–618.

[239] Cheng, H.-E.; Wen, C.-H.; Hsu, C.-M. *Journal of Vacuum Science & Technology A: Vacuum, Surfaces, and Films* **2016**, *34*, 01A112.

[240] Shannon, R. D. *Acta Crystallographica Section A* **1976**, *32*, 751–767.

[241] Upadhyay, J.; Vishwakarma, S.; Prasad, H. *Thin Solid Films* **1989**, *169*, 195–204.

[242] Ren, X.; Yang, D.; Yang, Z.; Feng, J.; Zhu, X.; Niu, J.; Liu, Y.; Zhao, W.; Liu, S. F. *ACS Applied Materials & Interfaces* **2017**, *9*, 2421–2429.

[243] Suzuki, A. Y.; Nose, K.; Ueno, A.; Kamiko, M.; Mitsuda, Y. *Applied Physics Express* **2012**, *5*, 011103.

[244] Turgut, G.; Keskenler, E. F.; Aydın, S.; Sönmez, E.; Doğan, S.; Düzgün, B.; Ertuğrul, M. *Superlattices and Microstructures* **2013**, *56*, 107–116.

[245] Kikuchi, N.; Kusano, E.; Kishio, E.; Kinbara, A. *Vacuum* **2002**, *66*, 365–371.

[246] Behtash, M.; Joo, P. H.; Nazir, S.; Yang, K. *Journal of Applied Physics* **2015**, *117*, 175101.

[247] Turgut, G.; Keskenler, E. F.; Aydın, S.; Yılmaz, M.; Doğan, S.; Düzgün, B. *Physica Scripta* **2013**, *87*, 035602.

[248] Guagliardo, P. R.; Vance, E. R.; Zhang, Z.; Davis, J.; Williams, J. F.; Samarin, S. N. *Journal of the American Ceramic Society* **2012**, *95*, 1727–1731.

[249] Zhang, G.; Qin, G.; Yu, G.; Hu, Q.; Fu, H.; Shao, C. *Thin Solid Films* **2012**, *520*, 5965–5970.

[250] Wang, Y.; Brezesinski, T.; Antonietti, M.; Smarsly, B. *ACS Nano* **2009**, *3*, 1373–1378.

[251] Gokulakrishnan, V.; Parthiban, S.; Jeganathan, K.; Ramamurthi, K. *Journal of Materials Science* **2011**, *46*, 5553–5558.

[252] Seo, Y. J.; Kim, G. W.; Sung, C. H.; Anwar, M.; Lee, C. G.; Koo, B. H. *Current Applied Physics* **2011**, *11*, S310–S313.

[253] Slassi, A. *Optical and Quantum Electronics* **2016**, *48*.

[254] Stefik, M.; Cornuz, M.; Mathews, N.; Hisatomi, T.; Mhaisalkar, S.; Grätzel, M. *Nano Letters* **2012**, *12*, 5431–5435.

[255] Toyosaki, H.; Kawasaki, M.; Tokura, Y. *Applied Physics Letters* **2008**, *93*, 132109.

[256] Kim, Y.-W.; Lee, S. W.; Chen, H. *Thin Solid Films* **2002**, *405*, 256–262.

[257] Lee, S.; Daga, A.; Xu, Z.; Chen, H. *Materials Science and Engineering: B* **2003**, *99*, 134–137.

[258] Nakao, S.; Yamada, N.; Hitosugi, T.; Hirose, Y.; Shimada, T.; Hasegawa, T. *Thin Solid Films* **2010**, *518*, 3093–3096.

[259] Turgut, G. *Thin Solid Films* **2015**, *594*, 56–66.

[260] Muto, Y.; Nakatomi, S.; Oka, N.; Iwabuchi, Y.; Kotsubo, H.; Shigesato, Y. *Thin Solid Films* **2012**, *520*, 3746–3750.

[261] Nguyen, N. M.; Luu, M. Q.; Nguyen, M. H.; Nguyen, D. T.; Bui, V. D.; Truong, T. T.; Pham, V. T.; Nguyen-Tran, T. *Journal of Electronic Materials* **2017**, *46*, 3667–3673.

[262] Weidner, M.; Jia, J.; Shigesato, Y.; Klein, A. *physica status solidi (b)* **2016**, *253*, 923–928.

[263] Weidner, M.; Brötz, J.; Klein, A. *Thin Solid Films* **2014**, *555*, 173–178.

[264] Graužinytė, M.; Goedecker, S.; Flores-Livas, J. A. *Chemistry of Materials* **2017**, *29*, 10095–10103.

[265] Paier, J.; Hirschl, R.; Marsman, M.; Kresse, G. *Journal of Chemical Physics* **2005**, *122*, 234102.

[266] Fritsch, D.; Morgan, B. J.; Walsh, A. *Nanoscale Research Letters* **2017**, *12*.

[267] Haines, J.; Léger, J. M. *Physical Review B* **1997**, *55*, 11144–11154.

[268] Yamanaka, T.; Kurashima, R.; Mimaki, J. *Zeitschrift für Kristallographie - Crystalline Materials* **2000**, *215*.

[269] Nagasawa, M.; Shionoya, S. *Physics Letters* **1966**, *22*, 409–410.

[270] Arlinghaus, F. *Journal of Physics and Chemistry of Solids* **1974**, *35*, 931–935.

[271] Farahani, S. K. V.; Veal, T. D.; Mudd, J. J.; Scanlon, D. O.; Watson, G. W.; Bierwagen, O.; White, M. E.; Speck, J. S.; McConville, C. F. *Physical Review B* **2014**, *90*, 155413.

[272] Nagasawa, M.; Shionoya, S.; Makishima, S. *Journal of the Physical Society of Japan* **1965**, *20*, 1093.

[273] Button, K. J.; Fonstad, C. G.; Dreybrodt, W. *Physical Review B* **1971**, *4*, 4539–4542.

[274] Feneberg, M.; Lidig, C.; Lange, K.; White, M. E.; Tsai, M. Y.; Speck, J. S.; Bierwagen, O.; Goldhahn, R. *physica status solidi (a)* **2013**, *211*, 82–86.

[275] Swallow, J. E. N.; Williamson, B. A. D.; Whittles, T. J.; Birkett, M.; Featherstone, T. J.; Peng, N.; Abbott, A.; Farnworth, M.; Cheetham, K. J.; Warren, P.; Scanlon, D. O.; Dhanak, V. R.; Veal, T. D. *Advanced Functional Materials* **2017**, 1701900.

[276] Oba, F.; Togo, A.; Tanaka, I.; Paier, J.; Kresse, G. *Physical Review B* **2008**, *77*, 245202.

[277] Dixon, S. C.; Sathasivam, S.; Williamson, B. A. D.; Scanlon, D. O.; Carmalt, C. J.; Parkin, I. P. *Journal of Materials Chemistry C* **2017**, *5*, 7585–7597.

[278] Janotti, A.; de Walle, C. G. V. *Physical Review B* **2007**, *76*, 165202.

[279] Frodason, Y. K.; Johansen, K. M.; Bjørheim, T. S.; Svensson, B. G.; Alkauskas, A. *Physical Review B* **2017**, *95*, 094105.

[280] Kafizas, A.; Noor, N.; Carmichael, P.; Scanlon, D. O.; Carmalt, C. J.; Parkin, I. P. *Advanced Functional Materials* **2014**, *24*, 1758–1771.

[281] Kang, Y.; de Walle, C. G. V. *Applied Physics Letters* **2017**, *111*, 152107.

[282] Ellmer, K. *Journal of Physics D Applied Physics* **2001**, *34*, 3097–3108.

[283] Look, D. C.; Leedy, K. D.; Vines, L.; Svensson, B. G.; Zubiaga, A.; Tuomisto, F.; Doutt, D. R.; Brillson, L. J. *Physical Review B* **2011**, *84*, 115202.

[284] Haitjema, H.; Elich, J.; Hoogendoorn, C. J. *Solar Energy Materials* **1989**, *18*, 283–297.

[285] Fauzia, V.; Yusnidar, M.; Lalasari, L. H.; Subhan, A.; Umar, A. A. *Journal of Alloys and Compounds* **2017**, *720*, 79–85.

[286] Lyons, J. L.; Janotti, A.; de Walle, C. G. V. *Applied Physics Letters* **2009**, *95*, 252105.

[287] Medeiros, P. V. C.; Stafström, S.; Björk, J. *Physical Review B* **2014**, *89*, 041407.

[288] Medeiros, P. V. C.; Tsirkin, S. S.; Stafström, S.; Björk, J. *Physical Review B* **2015**, *91*, 041116.

[289] Minami, T. *MRS Bulletin* **2000**, *25*, 38–44.

[290] Banerjee, A.; Chattopadhyay, K. *Progress in Crystal Growth and Characterization of Materials* **2005**, *50*, 52–105.

[291] Chen, L.; Yang, J.; Klaus, S.; Lee, L. J.; Woods-Robinson, R.; Ma, J.; Lum, Y.; Cooper, J. K.; Toma, F. M.; Wang, L.-W.; Sharp, I. D.; Bell, A. T.; Ager, J. W. *Journal of the American Chemical Society* **2015**, *137*, 9595–9603.

[292] Fortunato, E.; Ginley, D.; Hosono, H.; Paine, D. C. *MRS Bulletin* **2007**, *32*, 242–247.

[293] Kim, H.-J.; Lee, J.-H. *Sensors and Actuators B: Chemical* **2014**, *192*, 607–627.

[294] Sawatzky, G. A.; Allen, J. W. *Physical Review Letters* **1984**, *53*, 2339–2342.

[295] Antolini, E. *Materials Chemistry and Physics* **2003**, *82*, 937–948.

[296] Shin, S.; Shin, J.; Park, K.; Ishida, T.; Tabata, O.; Kim, H. *Thin Solid Films* **1999**, *341*, 225–229.

[297] Chen, Z.; Li, W.; Li, R.; Zhang, Y.; Xu, G.; Cheng, H. *Langmuir* **2013**, *29*, 13836–13842.

[298] Utsumi, K.; Matsunaga, O.; Takahata, T. *Thin Solid Films* **1998**, *334*, 30–34.

[299] Ishibashi, S.; Higuchi, Y.; Ota, Y.; Nakamura, K. *Journal of Vacuum Science & Technology A: Vacuum, Surfaces, and Films* **1990**, *8*, 1403–1406.

[300] Fan, J.; Sreekanth, K.; Xie, Z.; Chang, S.; Rao, K. *Progress in Materials Science* **2013**, *58*, 874–985.

[301] Brauer, G.; Kuriplach, J.; Ling, C. C.; Djurišić, A. B. *Journal of Physics: Conference Series* **2011**, *265*, 012002.

[302] Suja, M.; Bashar, S. B.; Morshed, M. M.; Liu, J. *ACS Applied Materials & Interfaces* **2015**, *7*, 8894–8899.

[303] Pan, H.; Meng, X.; Cai, J.; Li, S.; Qin, G. *RSC Advances* **2015**, *5*, 19353–19361.

[304] Tsay, C.-Y.; Liang, S.-C. *Journal of Alloys and Compounds* **2015**, *622*, 644–650.

[305] Pan, S. S.; Li, G. H.; Wang, L. B.; Shen, Y. D.; Wang, Y.; Mei, T.; Hu, X. *Applied Physics Letters* **2009**, *95*, 222112.

[306] Pan, S. S.; Wang, S.; Zhang, Y. X.; Luo, Y. Y.; Kong, F. Y.; Xu, S. C.; Xu, J. M.; Li, G. H. *Applied Physics A* **2012**, *109*, 267–271.

[307] Asbalter, J.; Subrahmanyam, A. *Journal of Vacuum Science & Technology A: Vacuum, Surfaces, and Films* **2000**, *18*, 1672–1676.

[308] Li, Y.; Sun, J.; Singh, D. J. *Applied Physics Letters* **2017**, *110*, 051904.

[309] Hsin, C. L.; He, J. H.; Lee, C. Y.; Wu, W. W.; Yeh, P. H.; Chen, L. J.; Wang, Z. L. *Nano Letters* **2007**, *7*, 1799–1803.

[310] *Materials Science Research Trends*; Nova Science Publishers Inc, 2007.

[311] Walsh, A.; Silva, J. L. F. D.; Wei, S.-H. *Chemistry of Materials* **2009**, *21*, 5119–5124.

[312] Ievtushenko, A.; Khyzhun, O.; Shtepliuk, I.; Bykov, O.; Jakieła, R.; Tkach, S.; Kuzmenko, E.; Baturin, V.; O.Karpenko,; Olifan, O.; Lashkarev, G. *Journal of Alloys and Compounds* **2017**, *722*, 683–689.

[313] Li, J.; Liu, Y.; Mei, Z.; Vines, L.; Kuznetsov, A.; Du, X. *Materials Science in Semiconductor Processing* **2017**, *69*, 28–31.

[314] Sharma, P.; Bhardwaj, R.; Singh, R.; Kumar, S.; Mukherjee, S. *Applied Physics Letters* **2017**, *111*, 091604.

[315] Erdem, E. *Nanoscale* **2017**, *9*, 10983–10986.

[316] Guziewicz, E.; Przezdziecka, E.; Snigurenko, D.; Jarosz, D.; Witkowski, B. S.; Dluzewski, P.; Paszkowicz, W. *ACS Applied Materials & Interfaces* **2017**, *9*, 26143–26150.

[317] He, H.; Xie, Z.; Li, Q.; Li, J.; Zhang, Q. *Journal of Alloys and Compounds* **2017**, *714*, 258–262.

[318] Huang, X.; Feng, M.; Gao, C. *Journal of Materials Science: Materials in Electronics* **2017**, *28*, 12139–12146.

[319] Bae, S.-D.; Kwon, S.-H.; Jeong, H.-S.; Kwon, H.-I. *Semiconductor Science and Technology* **2017**, *32*, 075006.

[320] Le, T.; Dang, H. P.; Luc, Q. H.; Le, V. H. *Journal of Physics D: Applied Physics* **2017**, *50*, 145102.

[321] Le, T.; Dang, H. P.; Le, V. H. *Journal of Alloys and Compounds* **2017**, *696*, 1314–1322.

[322] Kawazoe, H.; Yasukawa, M.; Hyodo, H.; Kurita, M.; Yanagi, H.; Hosono, H. *Nature* **1997**, *389*, 939–942.

[323] Li, B.; Akimoto, K.; Shen, A. *Journal of Crystal Growth* **2009**, *311*, 1102–1105.

[324] Scanlon, D. O.; Godinho, K. G.; Morgan, B. J.; Watson, G. W. *The Journal of Chemical Physics* **2010**, *132*, 024707.

[325] Yanagi, H.; Inoue, S.-i.; Ueda, K.; Kawazoe, H.; Hosono, H.; Hamada, N. *Journal of Applied Physics* **2000**, *88*, 4159.

[326] Kawazoe, H.; Yanagi, H.; Ueda, K.; Hosono, H. *MRS Bulletin* **2000**, *25*, 28–36.

[327] Marquardt, M. a.; Ashmore, N. a.; Cann, D. P. *Thin Solid Films* **2006**, *496*, 146–156.

[328] Ueda, K.; Hase, T.; Yanagi, H.; Kawazoe, H.; Hosono, H.; Ohta, H.; Orita, M.; Hirano, M. *Journal of Applied Physics* **2001**, *89*, 1790.

[329] Nagarajan, R.; Draeseke, a. D.; Sleight, a. W.; Tate, J. *Journal of Applied Physics* **2001**, *89*, 8022–8025.

[330] Scanlon, D. O.; Watson, G. W. *Chemistry of Materials* **2009**, *21*, 5435–5442.

[331] Snure, M.; Tiwari, A. *Applied Physics Letters* **2007**, *91*, 092123.

[332] Shi, L.-J.; Fang, Z.-J.; Li, J. *Journal of Applied Physics* **2008**, *104*, 073527.

[333] Godinho, K. G.; Carey, J. J.; Morgan, B. J.; Scanlon, D. O.; Watson, G. W. *Journal of Materials Chemistry* **2010**, *20*, 1086–1096.

[334] Kudo, A.; Yanagi, H.; Hosono, H.; Kawazoe, H. *Applied Physics Letters* **1998**, *73*, 220.

[335] Hiramatsu, H.; Ueda, K.; Ohta, H.; Orita, M.; Hirano, M.; Hosono, H. *Applied Physics Letters* **2002**, *81*, 598.

[336] Scanlon, D. O.; Watson, G. W. *Physical Chemistry Chemical Physics* **2011**, *13*, 9667.

[337] Dekkers, M.; Rijnders, G.; Blank, D. H. A. *Applied Physics Letters* **2007**, *90*, 021903.

[338] Kim, S.; Cianfrone, J. A.; Sadik, P.; Kim, K.-W.; Ivill, M.; Norton, D. P. *Journal of Applied Physics* **2010**, *107*, 103538.

[339] Mansourian-Hadavi, N.; Wansom, S.; Perry, N. H.; Nagaraja, A. R.; Mason, T. O.; hui Ye, L.; Freeman, A. J. *Physical Review B* **2010**, *81*, 075112.

[340] Bhatia, A.; Hautier, G.; Nilgianskul, T.; Miglio, A.; Sun, J.; Kim, H. J.; Kim, K. H.; Chen, S.; Rignanese, G.-M.; Gonze, X.; Suntivich, J. *Chemistry of Materials* **2016**, *28*, 30–34.

[341] Kashida, S.; Shimosaka, W.; Mori, M.; Yoshimura, D. *Journal of Physics and Chemistry of Solids* **2003**, *64*, 2357–2363.

[342] Wu, Y.; Wadia, C.; Ma, W.; Sadtler, B.; Alivisatos, A. P. *Nano Letters* **2008**, *8*, 2551–2555.

[343] Scanlon, D. O.; Buckeridge, J.; Catlow, C. R. a.; Watson, G. W. *Journal of Materials Chemistry C* **2014**, *2*, 3429.

[344] Liu, M. L.; Wu, L. B.; Huang, F. Q.; Chen, L. D.; Ibers, J. A. *Journal of Solid State Chemistry* **2006**, *180*, 62–69.

[345] Ueda, K.; Hosono, H.; Hamada, N. *Journal of Physics: Condensed Matter* **2004**, *16*, 5179–5186.

[346] Hiramatsu, H.; Ueda, K.; Ohta, H.; Hirano, M.; Kikuchi, M.; Yanagi, H.; Kamiya, T.; Hosono, H. *Applied Physics Letters* **2007**, *91*, 012104.

[347] Hiramatsu, H.; Ueda, K.; Ohta, H.; Hirano, M.; Kamiya, T.; Hosono, H. *Applied Physics Letters* **2003**, *82*, 1048–1050.

[348] Hiramatsu, H.; Ueda, K.; Takafuji, K.; Ohta, H.; Hirano, M.; Kamiya, T.; Hosono, H. *Journal of Applied Physics* **2003**, *94*, 5805–5808.

[349] Ueda, K.; Inoue, S.; Hirose, S.; Kawazoe, H.; Hosono, H. *Applied Physics Letters* **2000**, *77*, 2701.

[350] Clarke, S. J.; Adamson, P.; Herkelrath, S. J. C.; Rutt, O. J.; Parker, D. R.; Pitcher, M. J.; Smura, C. F. *Inorganic Chemistry* **2008**, *47*, 8473–86.

[351] Liu, M.-L.; Wu, L.-B.; Huang, F.-Q.; Chen, L.-D.; Chen, I.-W. *Journal of Applied Physics* **2007**, *102*, 116108.

[352] Otzschi, K.; Ogino, H.; Shimoyama, J.-i.; Kishio, K. *Journal of Low Temperature Physics* **1999**, *117*, 729–733.

[353] Caskey, C. M.; Richards, R. M.; Ginley, D. S.; Zakutayev, A. *Mater. Horizons* **2014**, *1*, 424.

[354] Walsh, A.; Chen, S.; Wei, S.-H.; Gong, X.-G. *Advanced Energy Materials* **2012**, *2*, 400–409.

[355] Zakutayev, A.; Caskey, C. M.; Fioretti, A. N.; Ginley, D. S.; Vidal, J.; Stevanovic, V.; Tea, E.; Lany, S. *Journal of Physical Chemistry Letters* **2014**, *5*, 1117–1125.

[356] Birkett, M.; Savory, C. N.; Fioretti, A. N.; Thompson, P.; Muryn, C. A.; Weerakkody, A. D.; Mitrovic, I. Z.; Hall, S.; Treharne, R.; Dhanak, V. R.; Scanlon, D. O.; Zakutayev, A.; Veal, T. D. *Physical Review B* **2017**, *95*, 115201.

[357] Yang, M.; Zakutayev, A.; Vidal, J.; Zhang, X.; Ginley, D. S.; DiSalvo, F. J. *Energy Environmental Science* **2013**, *6*, 2994.

[358] Walsh, A.; Zunger, A. *Nature Materials* **2017**, *16*, 964–967.

[359] Palgrave, R. G.; Borisov, P.; Dyer, M. S.; McMitchell, S. R. C.; Darling, G. R.; Claridge, J. B.; Batuk, M.; Tan, H.; Tian, H.; Verbeeck, J.; Hadermann, J.; Rosseinsky, M. J. *Journal of the American Chemical Society* **2012**, *134*, 7700–7714.

[360] Haeni, J. H.; Theis, C. D.; Schlom, D. G.; Tian, W.; Pan, X. Q.; Chang, H.; Takeuchi, I.; Xiang, X.-D. *Applied Physics Letters* **2001**, *78*, 3292.

[361] Tian, W.; Pan, X. Q.; Haeni, J. H.; Schlom, D. G. *Journal of Materials Research* **2001**, *16*, 2013–2026.

[362] Scanlon, D. O.; Walsh, A.; Watson, G. W. *Chemistry of Materials* **2009**, *21*, 4568–4576.

[363] icsd.cds.rsc.org.

[364] Sun, W.; Dacek, S. T.; Ong, S. P.; Hautier, G.; Jain, A.; Richards, W. D.; Gamst, A. C.; Persson, K. A.; Ceder, G. *Science Advances* **2016**, *2*, e1600225–e1600225.

[365] Gotsis, H. J.; Barnes, A. C.; Strange, P. *Journal of Physics: Condensed Matter* **1992**, *4*, 10461–10468.

[366] Evans, H. T. *Zeitschrift für Kristallographie* **1979**, *150*, 299–320.

[367] Cava, R.; Reidinger, F.; Wuensch, B. *Solid State Ionics* **1981**, *5*, 501–504.

[368] Ueda, K.; Hosono, H. *Thin Solid Films* **2002**, *411*, 115–118.

[369] Fuchs, F.; Bechstedt, F. *Physical Review B* **2008**, *77*, 155107.

[370] Llanos, J.; Peña, O. *Journal of Solid State Chemistry* **2005**, *178*, 957–960.

[371] Yanagi, H.; Park, S.; Draeseke, A.; Keszler, D.; Tate, J. *Journal of Solid State Chemistry* **2003**, *175*, 34–38.

[372] Park, C.-H.; Keszler, D. A.; Yanagi, H.; Tate, J. *Thin Solid Films* **2003**, *445*, 288–293.

[373] Park, C.-H.; Kykyneshi, R.; Yokochi, A.; Tate, J.; Keszler, D. A. *Journal of Solid State Chemistry* **2007**, *180*, 1672–1677.

[374] Zhu, W. J.; Hor, P. H. *Inorganic Chemistry* **1997**, *36*, 3576–3577.

[375] Evans, J. S. O.; Brogden, E. B.; Thompson, A. L.; Cordiner, R. L. *Chemical Communications* **2002**, 912–913.

[376] Mewis, A. *Zeitschrift fuer Naturforschung, Teil B. Anorganische Chemie, Organische Chemie* **1979**, *33*, p1373–p1376.

[377] Mewis, A. *Zeitschrift fuer Naturforschung, Teil B. Anorganische Chemie, Organische Chemie* **1978**, *33*, p983–p986.

[378] Preissler, N.; Bierwagen, O.; Ramu, A. T.; Speck, J. S. *Physical Review B* **2013**, *88*, 085305.

[379] Button, K. J.; Cohn, D. R.; Von Ortenbert, M.; Lax, B.; Mollwo, E.; Helbig, R. *Physical Review Letters* **1972**, *28*, 1637–1639.

[380] Zuo, J. M.; Kim, M.; O'Keeffe, M.; Spence, J. C. H. *Nature* **1999**, *401*, 49–52.

[381] Scanlon, D. O.; Watson, G. W. *Journal of Physical Chemistry Letters* **2010**, *1*, 3195–3199.

[382] Hahn, U.; Weber, W. *Physical Review B* **1996**, *53*, 12684–12693.

[383] Orgel, L. *Journal of Chemical Science* **1958**, 4186–4190.

[384] Omata, T.; Nagatani, H.; Suzuki, I.; Kita, M.; Yanagi, H.; Ohashi, N. *Journal of the American Chemical Society* **2014**, *136*, 3378–3381.

[385] Scanlon, D. O.; Walsh, A. *Acta Crystallographica Section B* **2015**, *71*, 702–706.

[386] Morgan, B. J.; Watson, G. W. *Physical Review B* **2009**, *80*, 233102.

[387] Shin, D. et al. *Physical Review B* **2009**, *80*, 233105.

[388] Scanlon, D. O.; Walsh, A.; Morgan, B. J.; Watson, G. W.; Payne, D. J.; Egdell, R. G. *Physical Review B* **2009**, *79*, 035101.

[389] Tossell, J. A.; Vaughan, D. J. *Inorganic Chemistry* **1981**, *20*, 3333–3340.

[390] Gaudin, E. *Journal of Solid State Chemistry* **2001**, *160*, 212–221.

[391] Savelsberg, G.; Schäfer, H. *Zeitschrift für Naturforschung B* **1978**, *33*, 370–373.

[392] Tauc, J.; Grigorovici, R.; Vancu, A. *physica status solidi (b)* **1966**, *15*, 627–637.

[393] Dolgonos, A.; Mason, T. O.; Poeppelmeier, K. R. *Journal of Solid State Chemistry* **2016**, *240*, 43–48.

[394] Zhang, J.; Song, L.; Madsen, G. K. H.; Fischer, K. F. F.; Zhang, W.; Shi, X.; Iversen, B. B. *Nature Communications* **2016**, *7*, 10892.

[395] Mizuguchi, Y.; Nishida, A.; Omachi, A.; Miura, O. *Cogent Physics* **2016**, *3*.

[396] Hautier, G.; Miglio, A.; Ceder, G.; Rignanese, G.-M.; Gonze, X. *Nature Communications* **2013**, *4*, 2292.

[397] Aksit, M.; Kolli, S. K.; Slauch, I. M.; Robinson, R. D. *Applied Physics Letters* **2014**, *104*, 161901.

[398] Arca, E.; Fleischer, K.; Shvets, I. V. *Applied Physics Letters* **2011**, *99*, 111910.

[399] Wei, R.; Tang, X.; Hu, L.; Hui, Z.; Yang, J.; Luo, H.; Luo, X.; Dai, J.; Song, W.; Yang, Z.; Zhu, X.; Sun, Y. *Chemical Communications* **2014**, *50*, 9697.

[400] Zhang, K. H. L.; Du, Y.; Papadogianni, A.; Bierwagen, O.; Sallis, S.; Piper, L. F. J.; Bowden, M. E.; Shutthanandan, V.; Sushko, P. V.; Chambers, S. A. *Advanced Materials* **2015**, *27*, 5191–5195.

[401] Johnson, R. W.; Hultqvist, A.; Bent, S. F. *Materials Today* **2014**, *17*, 236–246.

[402] Su, G.; Hadjiev, V. G.; Loya, P. E.; Zhang, J.; Lei, S.; Maharjan, S.; Dong, P.; Ajayan, P. M.; Lou, J.; Peng, H. *Nano Letters* **2015**, *15*, 506–513.

[403] Harrison, A.; Walton, M. *Solar Energy* **1978**, *20*, 185–188.

[404] Chemours, www.chemours.com. `www.chemours.com`.

[405] Osmond-McLeod, M. J.; Oytam, Y.; Rowe, A.; Sobhanmanesh, F.; Greenoak, G.; Kirby, J.; McInnes, E. F.; McCall, M. J. *Particle and Fibre Toxicology* **2015**, *13*.

[406] Jacobs, J. F.; van de Poel, I.; Osseweijer, P. *NanoEthics* **2010**, *4*, 103–113.

[407] Ropers, M.-H.; Terrisse, H.; Mercier-Bonin, M.; Humbert, B. *Application of Titanium Dioxide*; Intech, 2017.

[408] Weir, A.; Westerhoff, P.; Fabricius, L.; Hristovski, K.; von Goetz, N. *Environmental Science & Technology* **2012**, *46*, 2242–2250.

[409] Lu, Y.; Sathasivam, S.; Song, J.; Crick, C. R.; Carmalt, C. J.; Parkin, I. P. *Science* **2015**, *347*, 1132–1135.

[410] Holtzinger, C.; Niparte, B.; Wächter, S.; Berthomé, G.; Riassetto, D.; Langlet, M. *Surface Science* **2013**, *617*, 141–148.

[411] Sathasivam, S.; Bhachu, D. S.; Lu, Y.; Chadwick, N.; Althabaiti, S. A.; Alyoubi, A. O.; Basahel, S. N.; Carmalt, C. J.; Parkin, I. P. *Scientific Reports* **2015**, *5*.

[412] Takeuchi, M.; Sakamoto, K.; Martra, G.; Coluccia, S.; Anpo, M. *The Journal of Physical Chemistry B* **2005**, *109*, 15422–15428.

[413] Nakata, K.; Fujishima, A. *Journal of Photochemistry and Photobiology C: Photochemistry Reviews* **2012**, *13*, 169–189.

[414] Schneider, J.; Matsuoka, M.; Takeuchi, M.; Zhang, J.; Horiuchi, Y.; Anpo, M.; Bahnemann, D. W. *Chemical Reviews* **2014**, *114*, 9919–9986.

[415] Linsebigler, A. L.; Lu, G.; Yates, J. T. *Chemical Reviews* **1995**, *95*, 735–758.

[416] Web of Knowledge. `http://wok.mimas.ac.uk/`.

[417] Fujishima, A.; Honda, K. *Nature* **1972**, *238*, 37–38.

[418] Yamauchi, M.; Abe, R.; Tsukuda, T.; Kato, K.; Takata, M. *Journal of the American Chemical Society* **2011**, *133*, 1150–1152.

[419] Kudo, A.; Miseki, Y. *Chemical Society Review* **2009**, *38*, 253–278.

[420] Ni, M.; Leung, M. K.; Leung, D. Y.; Sumathy, K. *Renewable and Sustainable Energy Reviews* **2007**, *11*, 401–425.

[421] Hanaor, D. A. H.; Sorrell, C. C. *Journal of Materials Science* **2010**, *46*, 855–874.

[422] Monai, M.; Montini, T.; Fornasiero, P. *Catalysts* **2017**, *7*, 304.

[423] Luttrell, T.; Halpegamage, S.; Tao, J.; Kramer, A.; Sutter, E.; Batzill, M. *Scientific Reports* **2014**, *4*, 4043.

[424] Gai, Y.; Li, J.; Li, S.-S.; Xia, J.-B.; Wei, S.-H. *Physical Review Letters* **2009**, *102*, 036402.

[425] Haynes, W. *CRC Handbook of Chemistry and Physics*, 97th ed.; CRC, 2016.

[426] NREL, Reference Solar Spectral Irradiance: Air Mass 1.5. `http://rredc.nrel.gov/solar/spectra/am1.5/`.

[427] Walter, M. G.; Warren, E. L.; McKone, J. R.; Boettcher, S. W.; Mi, Q.; Santori, E. A.; Lewis, N. S. *Chemical Reviews* **2010**, *110*, 6446–6473.

[428] Rouse, L. *Materials Research Bulletin* **1978**, *13*, 861–868.

[429] Kandiel, T. A.; Robben, L.; Alkaim, A.; Bahnemann, D. *Photochemical and Photobiological Sciences* **2013**, *12*, 602–609.

[430] Paola, A. D.; Cufalo, G.; Addamo, M.; Bellardita, M.; Campostrini, R.; Ischia, M.; Ceccato, R.; Palmisano, L. *Colloids and Surfaces A: Physicochemical and Engineering Aspects* **2008**, *317*, 366–376.

[431] Paola, A. D.; Bellardita, M.; Palmisano, L. *Catalysts* **2013**, *3*, 36–73.

[432] Pan, H.; Qiu, X.; Ivanov, I. N.; Meyer, H. M.; Wang, W.; Zhu, W.; Paranthaman, M. P.; Zhang, Z.; Eres, G.; Gu, B. *Applied Catalysis B: Environmental* **2009**, *93*, 90–95.

[433] Zhang, J.; Zhou, P.; Liu, J.; Yu, J. *Physical Chemistry Chemical Physics* **2014**, *16*, 20382–20386.

[434] Xu, M.; Gao, Y.; Moreno, E. M.; Kunst, M.; Muhler, M.; Wang, Y.; Idriss, H.; Wöll, C. *Physical Review Letters* **2011**, *106*, 138302.

[435] Wang, X.; Kafizas, A.; Li, X.; Moniz, S. J. A.; Reardon, P. J. T.; Tang, J.; Parkin, I. P.; Durrant, J. R. *The Journal of Physical Chemistry C* **2015**, *119*, 10439–10447.

[436] Kafizas, A.; Wang, X.; Pendlebury, S. R.; Barnes, P.; Ling, M.; Sotelo-Vazquez, C.; Quesada-Cabrera, R.; Li, C.; Parkin, I. P.; Durrant, J. R. *The Journal of Physical Chemistry A* **2016**, *120*, 715–723.

[437] Furubayashi, Y.; Hitosugi, T.; Yamamoto, Y.; Inaba, K.; Kinoda, G.; Hirose, Y.; Shimada, T.; Hasegawa, T. *Applied Physics Letters* **2005**, *86*, 252101.

[438] Hitosugi, T.; Furubayashi, Y.; Ueda, A.; Itabashi, K.; Inaba, K.; Hirose, Y.; Kinoda, G.; Yamamoto, Y.; Shimada, T.; Hasegawa, T. *Japanese Journal of Applied Physics* **2005**, *44*, L1063–L1065.

[439] Mazzolini, P.; Acartürk, T.; Chrastina, D.; Starke, U.; Casari, C. S.; Gregori, G.; Bassi, A. L. *Advanced Electronic Materials* **2016**, *2*, 1500316.

[440] Bhachu, D. S.; Egdell, R. G.; Sankar, G.; Carmalt, C. J.; Parkin, I. P. *Journal of Materials Chemistry C* **2017**, *5*, 9694–9701.

[441] Quesada-González, M.; Boscher, N. D.; Carmalt, C. J.; Parkin, I. P. *ACS Applied Materials & Interfaces* **2016**, *8*, 25024–25029.

[442] Wang, B.; Zhao, F.; Du, G.; Porter, S.; Liu, Y.; Zhang, P.; Cheng, Z.; Liu, H. K.; Huang, Z. *ACS Applied Materials & Interfaces* **2016**, *8*, 16009–16015.

[443] Grabowska, E.; Zaleska, A.; Sobczak, J.; Gazda, M.; Hupka, J. *Procedia Chemistry* **2009**, *1*, 1553–1559.

[444] Finazzi, E.; Valentin, C. D.; Pacchioni, G. *The Journal of Physical Chemistry C* **2009**, *113*, 220–228.

[445] Yang, Y.; Ni, D.; Yao, Y.; Zhong, Y.; Ma, Y.; Yao, J. *RSC Advances* **2015**, *5*, 93635–93643.

[446] Wu, G.; Nishikawa, T.; Ohtani, B.; Chen, A. *Chemistry of Materials* **2007**, *19*, 4530–4537.

[447] Park, Y.; Kim, W.; Park, H.; Tachikawa, T.; Majima, T.; Choi, W. *Applied Catalysis B: Environmental* **2009**, *91*, 355–361.

[448] Wu, X.; Yin, S.; Dong, Q.; Guo, C.; Li, H.; Kimura, T.; Sato, T. *Applied Catalysis B: Environmental* **2013**, *142-143*, 450–457.

[449] Asahi, R. *Science* **2001**, *293*, 269–271.

[450] Sakthivel, S.; Janczarek, M.; Kisch, H. *The Journal of Physical Chemistry B* **2004**, *108*, 19384–19387.

[451] Sathish, M.; Viswanathan, B.; Viswanath, R. P.; Gopinath, C. S. *Chemistry of Materials* **2005**, *17*, 6349–6353.

[452] Cong, Y.; Zhang, J.; Chen, F.; Anpo, M. *The Journal of Physical Chemistry C* **2007**, *111*, 6976–6982.

[453] Gopal, N. O.; Lo, H.-H.; Ke, T.-F.; Lee, C.-H.; Chou, C.-C.; Wu, J.-D.; Sheu, S.-C.; Ke, S.-C. *The Journal of Physical Chemistry C* **2012**, *116*, 16191–16197.

[454] Sotelo-Vazquez, C.; Noor, N.; Kafizas, A.; Quesada-Cabrera, R.; Scanlon, D. O.; Taylor, A.; Durrant, J. R.; Parkin, I. P. *Chemistry of Materials* **2015**, *27*, 3234–3242.

[455] Shi, J.; Chen, S.; Wang, S.; Ye, Z. *Procedia Engineering* **2012**, *27*, 564–569.

[456] Ai, H.-Y.; Shi, J.-W.; Duan, R.-X.; Chen, J.-W.; Cui, H.-J.; Fu, M.-L. *International Journal of Photoenergy* **2014**, *2014*, 1–9.

[457] Quesada-Cabrera, R.; Sotelo-Vázquez, C.; Quesada-González, M.; Melián, E. P.; Chadwick, N.; Parkin, I. P. *Journal of Photochemistry and Photobiology A: Chemistry* **2017**, *333*, 49–55.

[458] Kim, S. J.; Xu, K.; Parala, H.; Beranek, R.; Bledowski, M.; Sliozberg, K.; Becker, H.-W.; Rogalla, D.; Barreca, D.; Maccato, C.; Sada, C.; Schuhmann, W.; Fischer, R. A.; Devi, A. *Chemical Vapor Deposition* **2013**, *19*, 45–52.

[459] Sarantopoulos, C.; Gleizes, A. N.; Maury, F. *Thin Solid Films* **2009**, *518*, 1299–1303.

[460] Chen, S.-Z.; Zhang, P.-Y.; Zhuang, D.-M.; Zhu, W.-P. *Catalysis Communications* **2004**, *5*, 677–680.

[461] Prabakar, K.; Takahashi, T.; Nezuka, T.; Takahashi, K.; Nakashima, T.; Kubota, Y.; Fujishima, A. *Renewable Energy* **2008**, *33*, 277–281.

[462] Pandiyan, R.; Delegan, N.; Dirany, A.; Drogui, P.; Khakani, M. A. E. *The Journal of Physical Chemistry C* **2016**, *120*, 631–638.

[463] Chen, H.; Dawson, J. A. *The Journal of Physical Chemistry C* **2015**, *119*, 15890–15895.

[464] Finazzi, E.; Valentin, C. D.; Selloni, A.; Pacchioni, G. *The Journal of Physical Chemistry C* **2007**, *111*, 9275–9282.

[465] Livraghi, S.; Paganini, M. C.; Giamello, E.; Selloni, A.; Valentin, C. D.; Pacchioni, G. *Journal of the American Chemical Society* **2006**, *128*, 15666–15671.

[466] Valentin, C. D.; Finazzi, E.; Pacchioni, G.; Selloni, A.; Livraghi, S.; Paganini, M. C.; Giamello, E. *Chemical Physics* **2007**, *339*, 44–56.

[467] Valentin, C. D.; Pacchioni, G.; Selloni, A.; Livraghi, S.; Giamello, E. *The Journal of Physical Chemistry B* **2005**, *109*, 11414–11419.

[468] Bharti, B.; Kumar, S.; Lee, H.-N.; Kumar, R. *Scientific Reports* **2016**, *6*.

[469] Li, Y.; Hwang, D.-S.; Lee, N. H.; Kim, S.-J. *Chemical Physics Letters* **2005**, *404*, 25–29.

[470] Valentin, C. D.; Pacchioni, G.; Selloni, A. *Chemistry of Materials* **2005**, *17*, 6656–6665.

[471] Sun, Y.-Y.; Zhang, S. *Physical Chemistry Chemical Physics* **2016**, *18*, 2776–2783.

[472] Sakthivel, S.; Kisch, H. *Angewandte Chemie International Edition* **2003**, *42*, 4908–4911.

[473] Quesada-González, M.; Baba, K.; Sotelo-Vázquez, C.; Choquet, P.; Carmalt, C. J.; Parkin, I. P.; Boscher, N. D. *Journal of Materials Chemistry A* **2017**, *5*, 10836–10842.

[474] Park, M. S.; Kwon, S. K.; Min, B. I. *Physical Review B* **2002**, *65*, 161201.

[475] Zaleska, A.; Grabowska, E.; Sobczak, J. W.; Gazda, M.; Hupka, J. *Applied Catalysis B: Environmental* **2009**, *89*, 469–475.

[476] Carmichael, P.; Hazafy, D.; Bhachu, D. S.; Mills, A.; Darr, J. A.; Parkin, I. P. *Physical Chemistry Chemical Physics* **2013**, *15*, 16788.

[477] Yang, K.; Dai, Y.; Huang, B. *The Journal of Physical Chemistry C* **2010**, *114*, 19830–19834.

[478] Sharma, S. D.; Singh, D.; Saini, K.; Kant, C.; Sharma, V.; Jain, S.; Sharma, C. *Applied Catalysis A: General* **2006**, *314*, 40–46.

[479] Janisch, R.; Gopal, P.; Spaldin, N. A. *Journal of Physics: Condensed Matter* **2005**, *17*, R657–R689.

[480] Tian, J.; Gao, H.; Deng, H.; Sun, L.; Kong, H.; Yang, P.; Chu, J. *Journal of Alloys and Compounds* **2013**, *581*, 318–323.

[481] AL-Jawad, S. M.; Taha, A. A.; Salim, M. M. *Optik - International Journal for Light and Electron Optics* **2017**, *142*, 42–53.

[482] Mathews, N. R.; Jacome, M. A. C.; Morales, E. R.; Antonio, J. A. T. *physica status solidi (c)* **2009**, *6*, S219–S223.

[483] Wang, X.; Gong, W. *Journal of Wuhan University of Technology-Mater. Sci. Ed.* **2008**, *23*, 155–158.

[484] Alexandrescu, R.; Morjan, I.; Scarisoreanu, M.; Birjega, R.; Popovici, E.; Soare, I.; Gavrila-Florescu, L.; Voicu, I.; Sandu, I.; Dumitrache, F.; Prodan, G.; Vasile, E.; Figgemeier, E. *Thin Solid Films* **2007**, *515*, 8438–8445.

[485] Sadanandam, G.; Lalitha, K.; Kumari, V. D.; Shankar, M. V.; Subrahmanyam, M. *International Journal of Hydrogen Energy* **2013**, *38*, 9655–9664.

[486] Iwasaki, M.; Hara, M.; Kawada, H.; Tada, H.; Ito, S. *Journal of Colloid and Interface Science* **2000**, *224*, 202–204.

[487] Miao, Y.; Zhai, Z.; Jiang, L.; Shi, Y.; Yan, Z.; Duan, D.; Zhen, K.; Wang, J. *Powder Technology* **2014**, *266*, 365–371.

[488] Ould-Chikh, S.; Proux, O.; Afanasiev, P.; Khrouz, L.; Hedhili, M. N.; Anjum, D. H.; Harb, M.; Geantet, C.; Basset, J.-M.; Puzenat, E. *ChemSusChem* **2014**, *7*, 1361–1371.

[489] Peng, Y.-H.; Huang, G.-F.; Huang, W.-Q. *Advanced Powder Technology* **2012**, *23*, 8–12.

[490] Dholam, R.; Patel, N.; Adami, M.; Miotello, A. *International Journal of Hydrogen Energy* **2009**, *34*, 5337–5346.

[491] Jun, T. H.; Lee, K. S. *Materials Letters* **2010**, *64*, 2287–2289.

[492] You, M.; Kim, T. G.; Sung, Y.-M. *Crystal Growth & Design* **2010**, *10*, 983–987.

[493] Colón, G.; Maicu, M.; Hidalgo, M.; Navío, J. *Applied Catalysis B: Environmental* **2006**, *67*, 41–51.

[494] Choudhury, B.; Dey, M.; Choudhury, A. *International Nano Letters* **2013**, *3*.

[495] Park, H. S.; Kim, D. H.; Kim, S. J.; Lee, K. S. *Journal of Alloys and Compounds* **2006**, *415*, 51–55.

[496] Choi, W.; Termin, A.; Hoffmann, M. R. *The Journal of Physical Chemistry* **1994**, *98*, 13669–13679.

[497] Fagan, R.; McCormack, D. E.; Dionysiou, D. D.; Pillai, S. C. *Materials Science in Semiconductor Processing* **2016**, *42*, 2–14.

[498] Zaleska, A. *Recent Patents on Engineering* **2008**, *2*, 157–164.

[499] Kafizas, A.; Dunnill, C. W.; Parkin, I. P. *Journal of Materials Chemistry* **2010**, *20*, 8336.

[500] Alim, M. A.; Bak, T.; Atanacio, A. J.; Ionescu, M.; Kennedy, B.; Price, W. S.; Plessis, J. D.; Pourmahdavi, M.; Zhou, M.; Torres, A.; Nowotny, J. *Ionics* **2017**,

[501] Znad, H.; Ang, M. H.; Tade, M. O. *International Journal of Photoenergy* **2012**, *2012*, 1–9.

[502] Kelly, P.; West, G.; Ratova, M.; Fisher, L.; Ostovarpour, S.; Verran, J. *Molecules* **2014**, *19*, 16327–16348.

[503] Moon, J.; Takagi, H.; Fujishiro, Y.; Awano, M. *Journal of Materials Science* **2001**, *36*, 949–955.

[504] Luo, L.; Li, T.; Ran, X.; Wang, P.; Guo, L. *Journal of Nanomaterials* **2014**, *2014*, 1–6.

[505] Putta, T.; Lu, M.-C.; Anotai, J. *Journal of Environmental Management* **2011**, *92*, 2272–2276.

[506] Sheppard, L. R.; Hager, S.; Holik, J.; Liu, R.; Macartney, S.; Wuhrer, R. *The Journal of Physical Chemistry C* **2014**, *119*, 392–400.

[507] Yin, W.-J.; Tang, H.; Wei, S.-H.; Al-Jassim, M. M.; Turner, J.; Yan, Y. *Physical Review B* **2010**, *82*, 045106.

[508] Zhang, P.; Yin, S.; Sekino, T.; Lee, S. W.; Sato, T. *Research on Chemical Intermediates* **2012**, *39*, 1509–1515.

[509] Chadwick, N. P.; Glover, E. N. K.; Sathasivam, S.; Basahel, S. N.; Althabaiti, S. A.; Alyoubi, A. O.; Parkin, I. P.; Carmalt, C. J. *Journal of Materials Chemistry A* **2016**, *4*, 407–415.

[510] Lim, J.; Murugan, P.; Lakshminarasimhan, N.; Kim, J. Y.; Lee, J. S.; Lee, S.-H.; Choi, W. *Journal of Catalysis* **2014**, *310*, 91–99.

[511] Breault, T. M.; Bartlett, B. M. *The Journal of Physical Chemistry C* **2012**, *116*, 5986–5994.

[512] Breault, T. M.; Bartlett, B. M. *The Journal of Physical Chemistry C* **2013**, *117*, 8611–8618.

[513] Zhao, Y. F.; Li, C.; Hu, J. Y.; Gong, Y. Y.; Niu, L. Y.; Liu, X. J. *Physics Letters A* **2016**, *380*, 910–916.

[514] Obata, K.; Irie, H.; Hashimoto, K. *Chemical Physics* **2007**, *339*, 124–132.

[515] McDonnell, K. A.; English, N. J.; Rahman, M.; Dowling, D. P. *Physical Review B* **2012**, *86*, 115306.

[516] Dong, P.; Liu, B.; Wang, Y.; Pei, H.; Yin, S. *Journal of Materials Research* **2010**, *25*, 2392–2400.

[517] Yang, F.; Yang, H.; Tian, B.; Zhang, J.; He, D. *Research on Chemical Intermediates* **2012**, *39*, 1685–1699.

[518] Zhang, J.; Pan, C.; Fang, P.; Wei, J.; Xiong, R. *ACS Applied Materials & Interfaces* **2010**, *2*, 1173–1176.

[519] Zhe-Peng, Z.; Biao, Y.; Hai-Bo, F.; Xin-Liang, Z.; He-Bao, Y. *Journal of Physics and Chemistry of Solids* **2015**, *87*, 53–57.

[520] Li, Z.; Wang, X.; Xing, X.; Wang, Y. *Journal of the Korean Physical Society* **2017**, *70*, 286–291.

[521] Ren, D.; Cheng, J.; Cheng, X. *Journal of Solid State Chemistry* **2016**, *238*, 83–87.

[522] Choi, H.; Shin, D.; Yeo, B. C.; Song, T.; Han, S. S.; Park, N.; Kim, S. *ACS Catalysis* **2016**, *6*, 2745–2753.

[523] Rimoldi, L.; Ambrosi, C.; Liberto, G. D.; Presti, L. L.; Ceotto, M.; Oliva, C.; Meroni, D.; Cappelli, S.; Cappelletti, G.; Soliveri, G.; Ardizzone, S. *The Journal of Physical Chemistry C* **2015**, *119*, 24104–24115.

[524] Gong, J.; Yang, C.; Zhang, J.; Pu, W. *Applied Catalysis B: Environmental* **2014**, *152-153*, 73–81.

[525] Patel, N.; Jaiswal, R.; Warang, T.; Scarduelli, G.; Dashora, A.; Ahuja, B.; Kothari, D.; Miotello, A. *Applied Catalysis B: Environmental* **2014**, *150-151*, 74–81.

[526] Fang, Y.; Cheng, D.; Niu, M.; Yi, Y.; Wu, W. *Chemical Physics Letters* **2013**, *567*, 34–38.

[527] Huang, J.; Wen, S.; Liu, J.; He, G. *Journal of Natural Gas Chemistry* **2012**, *21*, 302–307.

[528] Kurtoglu, M. E.; Longenbach, T.; Sohlberg, K.; Gogotsi, Y. *The Journal of Physical Chemistry C* **2011**, *115*, 17392–17399.

[529] Liu, L.; Chen, S.; Sun, W.; Xin, J. *Journal of Molecular Structure* **2011**, *1001*, 23–28.

[530] Valentin, C. D.; Finazzi, E.; Pacchioni, G.; Selloni, A.; Livraghi, S.; Czoska, A. M.; Paganini, M. C.; Giamello, E. *Chemistry of Materials* **2008**, *20*, 3706–3714.

[531] Long, R.; English, N. J. *Chemical Physics Letters* **2009**, *478*, 175–179.

[532] Long, R.; English, N. J. *Chemistry of Materials* **2010**, *22*, 1616–1623.

[533] Burdett, J. K.; Hughbanks, T.; Miller, G. J.; Richardson, J. W.; Smith, J. V. *Journal of the American Chemical Society* **1987**, *109*, 3639–3646.

[534] Rao, K. V. K.; Naidu, S. V. N.; Iyengar, L. *Journal of the American Ceramic Society* **1970**, *53*, 124–126.

[535] Deák, P.; Aradi, B.; Frauenheim, T. *Physical Review B* **2011**, *83*, 155207.

[536] Landmann, M.; Rauls, E.; Schmidt, W. G. *Journal of Physics: Condensed Matter* **2012**, *24*, 195503.

[537] Dou, M.; Persson, C. *Journal of Applied Physics* **2013**, *113*, 083703.

[538] Tang, H.; Prasad, K.; Sanjinès, R.; Schmid, P. E.; Lévy, F. *Journal of Applied Physics* **1994**, *75*, 2042–2047.

[539] Tang, H.; Lévy, F.; Berger, H.; Schmid, P. E. *Physical Review B* **1995**, *52*, 7771–7774.

[540] Patrick, C. E.; Giustino, F. *Journal of Physics: Condensed Matter* **2012**, *24*, 202201.

[541] Kang, W.; Hybertsen, M. S. *Physical Review B* **2010**, *82*, 085203.

[542] Gong, S.; Liu, B.-G. *Chinese Physics B* **2012**, *21*, 057104.

[543] Chiodo, L.; Salazar, M.; Romero, A. H.; Laricchia, S.; Sala, F. D.; Rubio, A. *The Journal of Chemical Physics* **2011**, *135*, 244704.

[544] Mattioli, G.; Alippi, P.; Filippone, F.; Caminiti, R.; Bonapasta, A. A. *The Journal of Physical Chemistry C* **2010**, *114*, 21694–21704.

[545] Oba, F.; Nishitani, S. R.; Isotani, S.; Adachi, H.; Tanaka, I. *Journal of Applied Physics* **2001**, *90*, 824–828.

[546] Na-Phattalung, S.; Smith, M. F.; Kim, K.; Du, M.-H.; Wei, S.-H.; Zhang, S. B.; Limpijumnong, S. *Physical Review B* **2006**, *73*, 125205.

[547] Kernazhitsky, L.; Shymanovska, V.; Gavrilko, T.; Naumov, V.; Fedorenko, L.; Kshnyakin, V.; Baran, J. *Journal of Luminescence* **2014**, *146*, 199–204.

[548] Santara, B.; Giri, P. K.; Imakita, K.; Fujii, M. *The Journal of Physical Chemistry C* **2013**, *117*, 23402–23411.

[549] Wang, X.; Feng, Z.; Shi, J.; Jia, G.; Shen, S.; Zhou, J.; Li, C. *Physical Chemistry Chemical Physics* **2010**, *12*, 7083.

[550] L., L. K.; Shymanovska, V.; Gavrilko, T.; Naumov, V.; Fedorenko, L.; Kshnyakin, V. *Journal of Nano and Electronic Physics* **2013**, *5*, 03047.

[551] Stefan, M.; Pana, O.; Leostean, C.; Bele, C.; Silipas, D.; Senila, M.; Gautron, E. *Journal of Applied Physics* **2014**, *116*, 114312.

[552] Abazović, N. D.; Čomor, M. I.; Dramićanin, M. D.; Jovanović, D. J.; Ahrenkiel, S. P.; Nedeljković, J. M. *The Journal of Physical Chemistry B* **2006**, *110*, 25366–25370.

[553] Mathew, S.; Prasad, A. K.; Benoy, T.; Rakesh, P. P.; Hari, M.; Libish, T. M.; Radhakrishnan, P.; Nampoori, V. P. N.; Vallabhan, C. P. G. *Journal of Fluorescence* **2012**, *22*, 1563–1569.

[554] Wang, W.; Lu, C.; Ni, Y.; Su, M.; Huang, W.; Xu, Z. *Applied Surface Science* **2012**, *258*, 8696–8703.

[555] Li, H.; Yin, S.; Wang, Y.; Sato, T. *Applied Catalysis B: Environmental* **2013**, *132-133*, 487–492.

[556] Morgan, B. J.; Scanlon, D. O.; Watson, G. W. *Journal of Materials Chemistry* **2009**, *19*, 5175.

[557] Osorio-Guillén, J.; Lany, S.; Zunger, A. *Physical Review Letters* **2008**, *100*, 036601.

[558] Janotti, A.; de Walle, C. G. V. *Reports on Progress in Physics* **2009**, *72*, 126501.

[559] Tian, H.; Hu, L.; Zhang, C.; Chen, S.; Sheng, J.; Mo, L.; Liu, W.; Dai, S. *Journal of Materials Chemistry* **2011**, *21*, 863–868.

[560] Chen, D.; Yang, D.; Wang, Q.; Jiang, Z. *Industrial & Engineering Chemistry Research* **2006**, *45*, 4110–4116.

[561] Zhao, W.; Ma, W.; Chen, C.; Zhao, J.; Shuai, Z. *Journal of the American Chemical Society* **2004**, *126*, 4782–4783.

[562] Yang, K.; Dai, Y.; Huang, B. *Physical Review B* **2007**, *76*, 195201.

[563] Geng, H.; Yin, S.; Yang, X.; Shuai, Z.; Liu, B. *Journal of Physics: Condensed Matter* **2005**, *18*, 87–96.

[564] Gopal, N. O.; Lo, H.-H.; Ke, S.-C. *Journal of the American Chemical Society* **2008**, *130*, 2760–2761.

[565] Feng, N.; Zheng, A.; Wang, Q.; Ren, P.; Gao, X.; Liu, S.-B.; Shen, Z.; Chen, T.; Deng, F. *The Journal of Physical Chemistry C* **2011**, *115*, 2709–2719.

[566] Lin, Y.; Jiang, Z.; Zhu, C.; Hu, X.; Zhang, X.; Zhu, H.; Fan, J.; Lin, S. H. *Journal of Materials Chemistry A* **2013**, *1*, 4516.

[567] Yu, J.; Zhou, P.; Li, Q. *Physical Chemistry Chemical Physics* **2013**, *15*, 12040.

[568] Yadav, H. M.; Otari, S. V.; Koli, V. B.; Mali, S. S.; Hong, C. K.; Pawar, S. H.; Delekar, S. D. *Journal of Photochemistry and Photobiology A: Chemistry* **2014**, *280*, 32–38.

[569] Weerachai Sangchay, K. K., Lek Sikong *Walailak Journal of Science and Technology* **2013**, *10*, 19–27.

[570] Yousef, A.; El-Halwany, M.; Barakat, N. A.; Al-Maghrabi, M. N.; Kim, H. Y. *Journal of Industrial and Engineering Chemistry* **2015**, *26*, 251–258.

[571] Leyland, N. S.; Podporska-Carroll, J.; Browne, J.; Hinder, S. J.; Quilty, B.; Pillai, S. C. *Scientific Reports* **2016**, *6*.

[572] Zhang, L.; Guo, J.; Huang, X.; Zhang, Y.; Han, Y. *Journal of Materials Chemistry B* **2016**, *4*, 3788–3800.

[573] Hassan, I. A.; Sathasivam, S.; Nair, S. P.; Carmalt, C. J. *ACS Omega* **2017**, *2*, 4556–4562.

[574] Karunakaran, C.; Abiramasundari, G.; Gomathisankar, P.; Manikandan, G.; Anandi, V. *Journal of Colloid and Interface Science* **2010**, *352*, 68–74.

[575] Navas, J.; Sánchez-Coronilla, A.; Aguilar, T.; Hernández, N. C.; de los Santos, D. M.; Sánchez-Márquez, J.; Zorrilla, D.; Fernández-Lorenzo, C.; Alcántara, R.; Martín-Calleja, J. *Physical Chemistry Chemical Physics* **2014**, *16*, 3835.

[576] Assadi, M. H. N.; Hanaor, D. A. H. *Journal of Applied Physics* **2013**, *113*, 233913.

[577] Guo, M.; Du, J. *Physica B: Condensed Matter* **2012**, *407*, 1003–1007.

[578] Hu, Q.; Huang, J.; Li, G.; Jiang, Y.; Lan, H.; Guo, W.; Cao, Y. *Applied Surface Science* **2016**, *382*, 170–177.

[579] Tsai, C.-Y. *Aerosol and Air Quality Research* **2013**,

[580] *Advances in Inorganic Chemistry and Radiochemistry*; Elsevier Science, 1981.

[581] Aspiala, M.; Sukhomlinov, D.; Taskinen, P. *Solid State Ionics* **2014**, *265*, 80–84.

[582] Chase, M. W. *Journal of Physical and Chemical Reference Data* **1996**, *25*, 551–603.

[583] Popescu, V.; Zunger, A. *Physical Review B* **2012**, *85*, 085201.

[584] Look, D. C.; Stutz, C. E.; Molnar, R. J.; Saarinen, K.; Liliental-Weber, Z. *Solid State Communications* **2001**, *117*, 571–575.

[585] Brooks, H. *Advances in Electronics and Electron Physics* **1955**, *7*, 85–182.

[586] Bardeen, J.; Shockley, W. *Physical Review* **1950**, *80*, 72–80.

[587] Low, F. E.; Pines, D. *Physical Review* **1955**, *1953*, 414–418.

[588] Frohlich, H.; Mott, N. F. *Proceedings of the Royal Society A: Mathematical, Physical and Engineering Sciences* **1939**, *171*, 496–504.

[589] Howarth, D. J.; Sondheimer, E. H. *Proceedings of the Royal Society A: Mathematical, Physical and Engineering Sciences* **1953**, *219*, 53–74.

[590] Bruneaux, J.; Cachet, H.; Froment, M.; Messad, A. *Thin Solid Films* **1991**, *197*, 129–142.

[591] Seto, J. Y. W. *Journal of Applied Physics* **1975**, *46*, 5247–5254.

[592] Buckeridge, J.; Scanlon, D. O.; Walsh, A.; Catlow, C. R. A. *Computational Physics Communication* **2014**, *185*, 330–338.

[593] Adolph, B.; Furthmüller, J.; Bechstedt, F. *Physical Review B* **2001**, *63*, 125108.

[594] Toby, B. H. *Journal of Applied Crystallography* **2001**, *34*, 210–213.

[595] Kubelka, P. *Journal of the Optical Society of America* **1948**, *38*, 448.

[596] Tauc, J. *Materials Research Bulletin* **1968**, *3*, 37–46.

[597] Aroyo, M. I.; Perez-Mato, J. M.; Capillas, C.; Kroumova, E.; Ivantchev, S.; Madariaga, G.; Kirov, A.; Wondratschek, H. *Zeitschrift für Kristallographie - Crystalline Materials* **2006**, *221*.

[598] Aroyo, M. I.; Kirov, A.; Capillas, C.; Perez-Mato, J. M.; Wondratschek, H. *Acta Crystallographica Section A Foundations of Crystallography* **2006**, *62*, 115–128.

[599] Aroyo, M.; Perez-Mato, J.; Orobengoa, D.; Tasci, E.; De La Flor, G.; Kirov, A. *Bulgarian Chemical Communications* **2011**, *43*, 183–197, cited By 135.

[600] Kresse, G.; Joubert, D. *Physical Review B* **1999**, *59*, 1758–1775.

[601] Larson, A.; Dreele, R. V. *Los Alamos National Laboratory Report* **2000**, 86–748.

[602] Mewis, A. *Zeitschrift für Naturforschung B* **1980**, *35*.

[603] Ghijsen, J.; Tjeng, L. H.; van Elp, J.; Eskes, H.; Westerink, J.; Sawatzky, G. A.; Czyzyk, M. T. *Physical Review B* **1988**, *38*, 11322–11330.

[604] Shin, D.; Foord, J. S.; Egdell, R. G.; Walsh, A. *Journal of Applied Physics* **2012**, *112*, 113718.

[605] Deuermeier, J.; Gassmann, J.; Brötz, J.; Klein, A. *Journal of Applied Physics* **2011**, *109*, 113704.

[606] Egdell, R. G.; Henrich, V. E.; Bowdler, R.; Sekine, T. *Journal of Applied Physics* **2003**, *94*, 6611.

[607] Franzen, H.; Merrick, J.; Umaña, M.; Khan, A.; Peterson, D.; McCreary, J.; Thorn, R. *Journal of Electron Spectroscopy and Related Phenomena* **1977**, *11*, 439–443.

[608] Demri, B.; Muster, D. *Journal of Materials Processing Technology* **1995**, *55*, 311–314.

[609] Clark, D.; Fok, T.; Roberts, G.; Sykes, R. *Thin Solid Films* **1980**, *70*, 261–283.

[610] Streubel, P.; Franke, R.; Chassé, T.; Fellenberg, R.; Szargan, R. *Journal of Electron Spectroscopy and Related Phenomena* **1991**, *57*, 1–13.

[611] Jianmin, L.; Yugeng, Z. *Crystal Research and Technology* **1991**, *26*, 331–337.

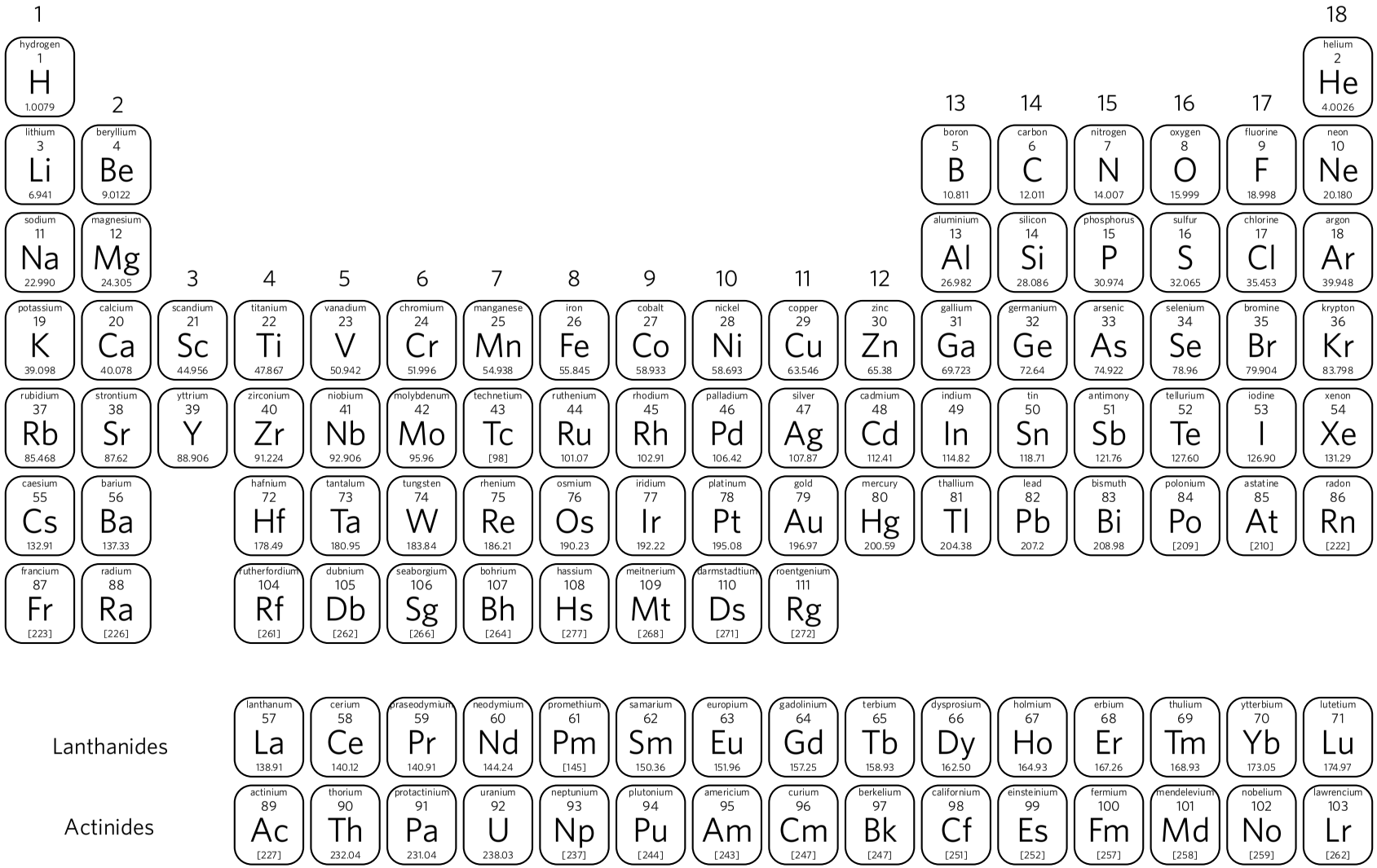
1
18
hydrogen 1 H 1.0079
helium 2 He 4.0026
2
13
14
15
16
17
lithium 3 Li 6.941
beryllium 4 Be 9.0122
boron 5 B 10.811
carbon 6 C 12.011
nitrogen 7 N 14.007
oxygen 8 O 15.999
fluorine 9 F 18.998
neon 10 Ne 20.180
sodium 11 Na 22.990
magnesium 12 Mg 24.305
3
4
5
6
7
8
9
10
11
12
aluminium 13 Al 26.982
silicon 14 Si 28.086
phosphorus 15 P 30.974
sulfur 16 S 32.065
chlorine 17 Cl 35.453
argon 18 Ar 39.948
potassium 19 K 39.098
calcium 20 Ca 40.078
scandium 21 Sc 44.956
titanium 22 Ti 47.867
vanadium 23 V 50.942
chromium 24 Cr 51.996
manganese 25 Mn 54.938
iron 26 Fe 55.845
cobalt 27 Co 58.933
nickel 28 Ni 58.693
copper 29 Cu 63.546
zinc 30 Zn 65.38
gallium 31 Ga 69.723
germanium 32 Ge 72.64
arsenic 33 As 74.922
selenium 34 Se 78.96
bromine 35 Br 79.904
krypton 36 Kr 83.798
rubidium 37 Rb 85.468
strontium 38 Sr 87.62
yttrium 39 Y 88.906
zirconium 40 Zr 91.224
niobium 41 Nb 92.906
molybdenum 42 Mo 95.96
technetium 43 Tc [98]
ruthenium 44 Ru 101.07
rhodium 45 Rh 102.91
palladium 46 Pd 106.42
silver 47 Ag 107.87
cadmium 48 Cd 112.41
indium 49 In 114.82
tin 50 Sn 118.71
antimony 51 Sb 121.76
tellurium 52 Te 127.60
iodine 53 I 126.90
xenon 54 Xe 131.29
caesium 55 Cs 132.91
barium 56 Ba 137.33
hafnium 72 Hf 178.49
tantalum 73 Ta 180.95
tungsten 74 W 183.84
rhenium 75 Re 186.21
osmium 76 Os 190.23
iridium 77 Ir 192.22
platinum 78 Pt 195.08
gold 79 Au 196.97
mercury 80 Hg 200.59
thallium 81 Tl 204.38
lead 82 Pb 207.2
bismuth 83 Bi 208.98
polonium 84 Po [209]
astatine 85 At [210]
radon 86 Rn [222]
francium 87 Fr [223]
radium 88 Ra [226]
rutherfordium 104 Rf [261]
dubnium 105 Db [262]
seaborgium 106 Sg [266]
bohrium 107 Bh [264]
hassium 108 Hs [277]
meitnerium 109 Mt [268]
darmstadtium 110 Ds [271]
roentgenium 111 Rg [272]
Lanthanides
lanthanum 57 La 138.91
cerium 58 Ce 140.12
praseodymium 59 Pr 140.91
neodymium 60 Nd 144.24
promethium 61 Pm [145]
samarium 62 Sm 150.36
europium 63 Eu 151.96
gadolinium 64 Gd 157.25
terbium 65 Tb 158.93
dysprosium 66 Dy 162.50
holmium 67 Ho 164.93
erbium 68 Er 167.26
thulium 69 Tm 168.93
ytterbium 70 Yb 173.05
lutetium 71 Lu 174.97
Actinides
actinium 89 Ac [227]
thorium 90 Th 232.04
protactinium 91 Pa 231.04
uranium 92 U 238.03
neptunium 93 Np [237]
plutonium 94 Pu [244]
americium 95 Am [243]
curium 96 Cm [247]
berkelium 97 Bk [247]
californium 98 Cf [251]
einsteinium 99 Es [252]
fermium 100 Fm [257]
mendelevium 101 Md [258]
nobelium 102 No [259]
lawrencium 103 Lr [262]

University College London

April, 2018